



HAL
open science

Modeling and development of new materials for fuel cells solid electrolyte

Yangzhou Ma

► **To cite this version:**

Yangzhou Ma. Modeling and development of new materials for fuel cells solid electrolyte. Other. Université de Technologie de Belfort-Montbéliard, 2016. English. NNT : 2016BELF0286 . tel-01872968

HAL Id: tel-01872968

<https://theses.hal.science/tel-01872968>

Submitted on 12 Sep 2018

HAL is a multi-disciplinary open access archive for the deposit and dissemination of scientific research documents, whether they are published or not. The documents may come from teaching and research institutions in France or abroad, or from public or private research centers.

L'archive ouverte pluridisciplinaire **HAL**, est destinée au dépôt et à la diffusion de documents scientifiques de niveau recherche, publiés ou non, émanant des établissements d'enseignement et de recherche français ou étrangers, des laboratoires publics ou privés.

SPIM

Thèse de Doctorat

Thèse N°286

Année 2016



école doctorale sciences pour l'ingénieur et microtechniques
UNIVERSITÉ DE TECHNOLOGIE BELFORT-MONTBÉLIARD

THÈSE

Présentée pour obtenir le grade de

Docteur de l'Université de Technologie de Belfort-Montbéliard

en

Science des Matériaux

Par

■ **Yangzhou MA**

**Modeling and development of new materials for fuel cells
solid electrolyte**

Soutenance publique le 25 mars 2016

Jury:

Mme. Ghislaine BERTRAND, Prof.	Reviewer	ENSIACET, Toulouse
M. Sofiane GUESSASMA, HDR.	Reviewer	INRA, Nantes
M. Hanlin LIAO, Prof.	Examiner	UTBM, Belfort
M. Nouredine FENINECHE, HDR.	Supervisor	UTBM, Belfort
M. Omar ELKEDIM, HDR.	Supervisor	UTBM, Belfort
M. Salim-Mourad CHERIF, Prof.	Examiner	Université Paris 13, Paris

Acknowledgement

As this thesis work is mainly done in the laboratories IRTES - LERMPS and Femto- ST- MN2S, as well as supported by China Scholarship Council and UTBM in the framework of UT-INSA (2012), my thanks first go to all the collaborating parties which made this work possible at all.

I would express my greatest gratitude to my thesis supervisors Prof. FENINECHE Nouredine and Prof. ELKEDIM Omar, who have been extremely supportive along this journey of scientific research, where difficulties are only the stairs for one to climb up. It is not only the knowledge I could learn from them, but also the confident and cheerful attitude toward obstacles is of great inspiration to me on this road of science in the future. I would also like to say thanks to them for their patience to guide me through all this work.

I am very thankful for Mrs. BERTRAND Ghislaine and Mr. GUESSASMA Sofiane to take the time to be the reviewers and help improve the thesis.

I feel honored to have Mr. LIAO Hanlin and Mr. CHERIF Salim Mourad to be present in the jury of the thesis defense session.

I would also like to extend my deep appreciation to M. MOLIERE Michel, who has contributed a lot to this work in the first place. I was already lucky enough to meet him in person in a laboratory seminar, but he also kindly provided much assistance to improve my work with both the methods and technologies. Today I can still recall his detailed teachings from chemical reaction mechanisms to the experimental equipment design. In addition, we had spent very good time when we found some nice bistros in the city. His enthusiasm toward science and the passion for life will always be my inspiration and spur me to pursue excellence when doing science.

I must appreciate the collaboration with M. BRIOIS Pascal on co-completing this work with the measurement of the electrical properties. Contribution from you is invaluable to this work. Many thanks go to the recommendations and assistances from the professors: M. Hanlin Liao, M. Pierre Bertrand, M. Joel Chauvelot and Mrs. Pascale Hoog.

I have received countless help from many nice working fellows, my colleagues in our lab. They are: Soumia Lardjane, Nicolas Bruno, Jean-Baptiste Devillers, Emilie Aubignat, Xinkun Suo, Taikai Liu, Min Yu, Xiaohua Feng, Jiangwei Liu, Duo Yi, Amal Masmoudi, Chunjie Huang, Zexin Yu, Bilel Hosni et al. and peers from different sections: Hui Wang-Liao, Marc Cescutti et al. Especially our “scientific interest group”: Shuo Yin, Chaoyue Chen, Zhao Zhang and Yingchun Xie, thank you for giving some academic discussions, yielding us steady progress.

My thanks go to all the people that make my life in France a wonderful experience. Especially, M. Chengzhong Zhou, thank you for giving me the opportunity to have all the pleasant time with my dear brothers and sisters. It will always be the best memory to recall.

Most importantly, I would like to thank my wife. Her support, encouragement, “quiet patience” and unwavering love were undeniably the bedrock upon which the past two years of my life have been built.

Finally, I owe to my parents at the moment, who have been the ones standing firmly behind my back, despite the physical distance between us. Like always, during my study in France, they have been giving me wise advice and are always helping me to be a better person. My sisters deserve my wholehearted thanks as well for their endless love, support and encouragement.

Contents

Introduction	1
CHAPTER I Overview of the solid oxide fuel cells (SOFC) and apatite-type materials as electrolyte in SOFC	5
I.1 Solid Oxide Fuel Cells (SOFCs)	7
I.1.1 Historic	7
I.1.2 Fuel cell structure and operation	9
I.1.3 Comparison of some alternative fuel cells.....	22
I.2 Materials used in the SOFCs	23
I.2.1 Cathode materials	23
I.2.2 Anode materials	29
I.2.3 Interconnect materials.....	32
I.2.4 Materials for electrolytes	33
I.3 Encountered difficulties of operating temperature.....	40
I.4 Apatite-type phase lanthanum silicate electrolyte.....	41
I.4.1 Structure.....	41
I.4.2 Electrical properties	43
I.4.3 Conduction pathway	45
I.4.4 Influence of doping and substitution	49
I.5 Summary	50
I.6 References	51
CHAPTER II. Fundamentals of Experimental, Calculation and Characterization	59
II.1. Synthesis methods.....	61
II.1.1 Dry pressing	61
II.1.2 Casting.....	62
II.1.3 Screen printing	63
II.1.4 Physical vapor deposition (PVD).....	64
II.1.5 Chemical vapor deposition (CVD).....	65
II.1.6 Thermal spray.....	65
II.1.7 Chemical methods	66
II.2 Characterization	70
II 2.1 Density	70

II.2.2 Phase.....	71
II 2.3 Microstructure	74
II 2.4 Conductivity	75
II 2.5 TGA.....	80
II.3. Ab initio calculations modeling	81
II.3.1 Introduction of ab initio calculation	81
II.3.2 Density functional theory (DFT).....	83
II.3.3 The pseudopotentials.....	91
II.3.4 Computational application	93
II.3.5 Vienna Ab initio Simulation Package (VASP)	94
II.4 References.....	96
CHAPTER III. Ab initio study of $\text{La}_{10-x}\text{Sr}_x(\text{Si,Ge})_6\text{O}_{27-0.5x}$ apatite for SOFC electrolyte	101
III.1 Introduction	103
III.2 $\text{La}_{10-x}\text{Sr}_x(\text{Si,Ge})_6\text{O}_{27-0.5x}$ apatite study	104
III.2.1 Calculation details.....	105
III.2.2 Structure properties	107
III.3 Sr-doped LSO study	107
III.3.1 electronic properties.....	107
III.3.2 Density of states and band structure	110
III.4 Ge-doped LSO study	114
III.5 Effect of doping on activation energy	115
III.6 Influence of doping positions on lattice parameters.....	117
III.7 Summary.....	118
III.8 References	120
Chapter IV: Preliminary experimental exploration for synthesizing pure $\text{La}_{10}\text{Si}_6\text{O}_{27}$ apatites	123
IV.1 Co-precipitation method.....	125
IV.1.1 Sample preparation	125
IV.1.2 Co-precipitation process and calcination.....	126
IV.1.3 Sintering process and characterization	132
IV.1.4 Electrical characterization.....	135
IV.2 Sr, Mn-doping LSO with co-precipitation method design	137
IV.2.1 Sr-doping LSO.....	137
IV.2.2 Mn-doping LSO.....	139
IV.3 Molten salt	143

IV.4 Homogeneous deposition precipitation (HDP)	151
IV.5 Summary	153
IV.6 References	154
Chapter V Synthesis of Pure $\text{La}_{10-x}\text{Sr}_x\text{Si}_6\text{O}_{27-0.5x}$ Apatites Using an Optimized Sol-Gel Process	155
V.1 Parameters investigation	157
V.1.1 Synthesis process	157
V.1.2 Effect of Sr-doping.....	159
V.1.3 Study of the influence of pH	160
V.1.4 Effect of the calcination condition	163
V.2 Optimized synthesis study	164
V.2.1 Calcination study.....	164
V.2.2 Sintering study	170
V.2.3 Conductivity study	175
V.3 Summary.....	180
V.4 References.....	182
Conclusion.....	183
Annex I. List of publications and conferences	187

Index of Figures and Tables

Figure I. 1. William Grove's 1839 gas voltaic battery diagram, pioneer of modern fuel cell	7
Figure I. 2. Schematic diagram of the operation of a fuel cell (This work has been released into the public domain by its author, Sakurambo.).....	10
Figure I. 3. the input and output of the fuel cell	11
Figure I. 4. The energy and power properties of the fuel cell compared to other energy conversion devices (A. Comparison of the specific power between the present SOFC $\sim 2\text{W} / \text{cm}^2$ at 650°C and multiple energy conversion devices as a function of the power density. B. Ragone plot, specific energy versus specific power, for various energy devices in relation to the present SOFC) [41].	14
Figure I. 5. Changes in oxygen reduction activity plotted as a function of the oxygen binding energy [42]	16
Figure I. 6. The types of oxygen adsorption process in the cathode	16
Figure I. 7. The logarithm of the exchange current density ($\log i_0$) against the force of the metal-hydrogen bond formed during the reaction itself.	18
Figure I. 8. Schematic of diffusion mechanisms in solid state structures: (a) vacancy diffusion; (b) Interstitial diffusion; (c) ions exchange- direct and circle.....	19
Figure I. 9. Schematic representation of the diffusion of an atom from its original position into another lattice site. Activation energy E_m has to be supplied to the atom so that it could break inter-atomic bonds and to move into the new position.	20
Figure I. 10. Arrhenius plot of $\ln D$ vs. $1/T$ with a slop of $-Q_d/R$ and an intercept of $\ln D_0$	21
Figure I. 11. Cross-sectional views SEM micrographs of (a) a single cell, (b) the porous Ni-GDC (gadolinia-doped ceria) anode, (c) the dense GDC electrolyte, and (d) the porous SSC (Sm _{0.5} Sr _{0.5} CoO ₃) -GDC cathode.....	22
Figure I. 12. A diagram of the reactions in the cathode of SOFC	24
Figure I. 13. Schematic of the lattice structure of a perovskite- ABO_3	25
Figure I. 14. Variation of electrical conductivity (σ) of $\text{La}_{1-x}\text{Sr}_x\text{MnO}_{3-\delta}$ (x is 0 to 0.7) at different temperature (at pure oxygen $P_{\text{O}_2} = 1$ bar).....	26
Figure I. 15. Schematic view of the crystal structures of: (a) Simple perovskite, (b) Double perovskite and (c) Ruddlesden-Popper K_2NiF_4 type phase. Sites for water insertion are shown: oxygen vacancies for the perovskites and interstitials for $\text{Ln}_2\text{MO}_{4+\delta}$	27
Figure I. 16. Transmission electron micrographs showing the anode (a) operated with hydrogen fuel (b) operated with syngas for 15min; (c) operated under same gas mixture for 2h (the ingredient of synthesis gas: CH_4 23.64% ; CO 7.60% ; CO_2 14.27% ; H_2 49.48% ; H_2O 5.00%) [64].....	29
Figure I. 17. the three views of the pyrochlore structure $\text{A}_2\text{B}_2\text{O}_6\text{O}'$ (a) showing the relation between the structures of fluorite and pyrochlore in where an octant of the cell of the pyrochlore unit is represented by the large cube, (b) octahedral connectivity $\langle\text{BO}_6\rangle$ units with A sites and O' anions as "extra-framework ions," (c) the A sublattice as a network of corner-shared O'-centered tetrahedra, with B and O atoms omitted. A - purple, B - green, O - yellow and O' - orange.....	31
Figure I. 18. Schematic diagram of the components of a planar cell to show the interconnect	32
Figure I. 19. Schematic showing selection of phases in Fe-Co-Ni based alloys as metallic interconnect materials [86].....	33
Figure I. 20. Cubic fluorite structure of ceria	34
Figure I. 21. Schematic of the $\delta\text{-Bi}_2\text{O}_3$ polymorph crystal structures	35
Figure I. 22. Structures of pyrochlore - One eighth of the unit cell of the ordered pyrochlore structure showing specific positions of the cations and anions (B^{4+} cation at the origin). [101].....	37
Figure I. 23. Arrangement of B-O octahedra and tetrahedra in the ideal brownmillerite structure, $\text{A}_2\text{B}_2\text{O}_5$ (A cations removed for clarity)	39

Figure I. 24. The apatite structure, $A_{10}(MO_4)_6X_{2-y}$, and alternative representation of the apatite structure: illustration of the “microporous” $A_4(MO_4)_6$ framework: The cavities are where the remaining A_6X_{2-y} units would occupy. (original figure from ref [116])	42
Figure I. 25. Schematic diagram of lanthanum-silicon apatite structure	43
Figure I. 26. Conductivities of selected electrolyte materials at intermediate temperature (LSO series lies at shaded part, original figure from ref [124])	45
Figure I. 27. The interstitial oxygen site (brown sphere) at the periphery of the channels, and associated lattice relaxation (blue spheres = La, green spheres = Si).....	46
Figure I. 28. ^{29}Si NMR spectra (left) and Raman spectra results (right) for (a) $\text{La}_8\text{Sr}_2(\text{SiO}_4)_6\text{O}_2$, (b) $\text{La}_9\text{Sr}(\text{SiO}_4)_6\text{O}_{2.5}$, (c) deconvolution of the latter. [127, 128]	47
Figure I. 29. O5 oxygen vacancy migration along the O5 oxide channel (a), and interstitial oxygen migration viewed perpendicular to the O5 channel, showing a non-linear (sinusoidal-like) pathway (b), suggested for $\text{La}_8\text{Sr}_2(\text{SiO}_4)_6\text{O}_2$ and $\text{La}_{9.33}(\text{SiO}_4)_6\text{O}_2$ respectively.....	47
Figure I. 30. Proposed conduction pathway between adjacent oxide-ion channels via two “ $\text{S}_\text{N}2$ ”-type processes, with accompanying rotation of the silicate tetrahedra, obtained from computer simulation results of $\text{La}_{9.33}(\text{SiO}_4)_6\text{O}_2$. The incorporation of a periphery interstitial oxide-ion (yellow) (a) forces a silicate oxygen (orange) in between the two SiO_4 units forming an Si_2O_9 unit (b), the top silicate unit rotates to form an Si_2O_9 unit with a neighboring silicate unit (c), and an oxygen on the top silicate unit (green) is released as an interstitial in a different channel (d).....	48
Figure I. 31. Comparison of the conductivities (500 °C) of oxygen stoichiometric samples with the same level of cation vacancies (a) and same level of oxygen excess – $\text{O}_{2.5}$ (b) [116]	49
Figure II. 1. A schematic diagram for showing dry pressing process, devices and the electrolyte obtained by this technique.	62
Figure II. 2. SEM micrographs of tape casting electrolyte using in SOFC and voltage-current, impedance spectrum characteristics of the cell operating at 800 °C.	63
Figure II. 3. (a) SEM micrographs of electrolyte layer on the left and porous Ni–YSZ cermet on the right. (b) Specific resistance at different temperatures in comparison with YSZ pellet.....	64
Figure II. 4. SEM micrographs of YSZ films grown by RMS (reactive magnetron sputtering) on (100) Si substrate at room temperature under 1 Pa: a) top view, b) cross-section.....	64
Figure II. 5. Experimental setup of ultrasonic aerosol assisted chemical vapor deposition at atmospheric pressure and the morphology of as obtained electrolyte	65
Figure II. 6. Micrographs of fracture surface of the $\text{La}_{10}\text{Si}_{5.8}\text{Mg}_{0.2}\text{O}_{26.8}$ coating deposited by VLPPS (a) and APS (b).	66
Figure II. 7. A schematic diagram of sol-gel process and its application ways (https://str.llnl.gov/str/May05/Satcher.html)	68
Figure II. 8. Flowchart of the process used in the preparation of doped and undoped lanthanum silicates.	69
Figure II. 9. Density and relative density of sintered samples at different temperatures [39].....	71
Figure II. 10. Photography and X-ray diffraction mechanism of Bruker-AXS D8 FOCUS Advanced Bragg-Brentano X-ray Powder Diffractometer	72
Figure II. 11. Stick pattern of high intensity diffraction for Lanthanum silicate (ref. 00-049-0443)....	73
Figure II. 12. JSM-7800F field emission scanning electron microscope	74
Figure II. 13. Diagram of the four-point method.....	75
Figure II. 14. Representation of an electric circuit impedance diagram. (a) Electrical circuit, (b)Complex impedance diagram corresponding to a Nyquist plot and (c) in a Bode plot.	77
Figure II. 15. Schematic of an impedance plot for an electroded polycrystalline sample with an analog equivalent electric circuit.	78
Figure II. 16. Devices for measuring the conductivity (the inset is the structure of sample furnace)...	79
Figure II. 17. Schematic of DSC and TG technique.....	80
Figure II. 18. Schematic illustration of the simulation methods for different length and time scales... ..	82
Figure II. 19. Flowchart of a self-consistent calculation in a method based on the DFT calculation	91

Figure II. 20. Material properties studies with DFT calculation	94
Figure III. 1. Schematic diagram of the input files for VASP	107
Figure III. 2. Schematic diagram of lanthanum-silicon apatite structure	108
Figure III. 3. Different Sr dopant ratio effects on the electronic properties compared to ionic conductivity	109
Figure III. 4. Effect of Sr dopant on the Fermi level	110
Figure III. 5. Total DOS (left) and partial DOS (right) of LSO with different Sr dopant ratios in (a) La:Sr = 10:0 (b) La:Sr = 9:1 (c) La:Sr = 8:2	111
Figure III. 6. Comparison among the different Sr-doping ratios	112
Figure III. 7. PDOS curves analysis for different La and Sr doping ratios	113
Figure III. 8. Calculated band structure of $\text{La}_{10}\text{Si}_6\text{O}_{27}$	113
Figure III. 9. The DOS comparison between LSO and LGO	114
Figure III. 10. The calculated electron density of LSO and LGO	115
Figure III. 11. The calculated energy barriers along c-axis for activation energy of LSO with different Sr doping ratios and positions (a ~ b, $\text{La}_9\text{SrSi}_6\text{O}_{26.5}$ with Sr position near to (a) and far from (b) migration channel; c ~ e, $\text{La}_8\text{Sr}_2\text{Si}_6\text{O}_{26}$ with two Sr positions near-near to (c), near-far from (d) and far-far from (e) migration channel; f, $\text{La}_{10}\text{Si}_6\text{O}_{27}$)	116
Figure III. 12. The calculated energy barriers along c-axis for activation energy of LGO (a) and the activation energy of each group (b)	117
Figure III. 13. $\text{La}_{10-x}\text{Sr}_x(\text{Si,Ge})_6\text{O}_{27-0.5x}$ XRD patterns: (a) modeled and (b) experimental, versus different doping ratios	118
Figure IV. 1. co-precipitation reaction equipment design (Acid burette – left; alkaline burette – right)	126
Figure IV. 2. X-ray diffraction patterns of different groups of compounds synthesized with different calcination temperature	128
Figure IV. 3. X-ray diffraction patterns the group of compounds synthesized with 1000°C calcination temperature (the miller indices of lanthanum silicate is shown in the figure)	129
Figure IV. 4. TG/DSC curves of precipitant to analyze the calcination process	130
Figure IV. 5. The morphologies of samples with different calcination temperatures treatment by SEM analysis	131
Figure IV. 6. The grain sizes of samples treated with different temperatures by analyzing SEM photos	131
Figure IV. 7. EDX analysis curve of the obtained sample in three different zones (1000°C group as an example)	132
Figure IV. 8. X-ray diffraction patterns of different groups with further sintering treatment at 1500°C for 2h	133
Figure IV. 9. Typical SEM micrographs of samples sintered at 1500°C for 2h	134
Figure IV. 10. Impedance diagram in Nyquist representation registered at 773 K under static air on apatite pellet. Frequency logarithms are represented	136
Figure IV. 11. Arrhenius plot of ionic conductivity	137
Figure IV. 12. Sr-doping LSO co-precipitation reaction equipment design	139
Figure IV. 13. Experimental equipment and process of Mn-doping LSO with co-precipitation	140
Figure IV. 14. the phase diagram of the $\text{MnO-Mn}_2\text{O}_3\text{-MnO}_2$ system[5]	141
Figure IV. 15. The XRD diffraction patterns of the powder before calcination and the sample after calcination (the inset shows the sample appearance)	142
Figure IV. 16. Flow chart of molten salt method for LSO synthesis	143
Figure IV. 17. XRD diffraction pattern of the composition synthesized by molten NH_4NO_3 method	144
Figure IV. 18. The phase equilibrium diagram of the KCl-NaCl system	145
Figure IV. 19. XRD results of the product with NaCl-KCl eutectic method by multiple temperature	146
Figure IV. 20. The diffraction pattern of the 850°C group before and after the citric acid washing ...	147
Figure IV. 21. The phase equilibrium diagram of the KCl-LiCl system	148

Figure IV. 22. XRD results of the product with LiCl-KCl eutectic method at 450°C for 10h	149
Figure IV. 23. The phase equilibrium diagram of the $\text{Li}_2\text{SO}_4\text{-K}_2\text{SO}_4$ system (data from FTsalt)	150
Figure IV. 24. XRD results of the product with $\text{Li}_2\text{SO}_4\text{-K}_2\text{SO}_4$ eutectic method at 700°C and 900°C	150
Figure IV. 25. Schematic diagram of homogeneous deposition precipitation method equipment for synthesizing LSO compounds	151
Figure IV. 26. XRD results of the product with HDP method with calcination temperature of 800°C for 2h	152
Figure IV. 27. The morphologies of the powder with HDP method calcined at 800°C for 2h by SEM analysis	153
Figure V. 1. Flow chat of the process used for the preparation of doped and undoped lanthanum silicates	157
Figure V. 2. TG/DSC curves of $\text{La}(\text{NO}_3)_3 \cdot x\text{H}_2\text{O}$ as raw material to verify the number of crystal water in a molecular	158
Figure V. 3. Diffraction patterns of lanthanum silicates corresponding to the three Sr-doping ratios after sintering (1500°C, 4h). The inset shows the pattern of dry gel before sintering	159
Figure V. 4. The mechanism of lanthanum silicates sol-gel formation process (the features of the three obtained sols are shown by the inset)	161
Figure V. 5. SEM figures or the morphologies of the obtained compounds with optimized process (a, dry gel before calcination with unsuitable pH; b, dry gel before calcination with optimized pH.)....	163
Figure V. 6. Diffraction patterns of the obtained powders for the sintering time (a) and temperature (b) studies	164
Figure V. 7. Typical XRD pattern of a dry gel before calcination	166
Figure V. 8. XRD patterns obtained with different calcination temperature and Sr doping (no sintering)	166
Figure V. 9. Local XRD patterns corresponding to three Sr doping ratios (a) and three calcination temperatures (b) (no sintering)	167
Figure V. 10. SEM micrographs of calcined (no sintering) samples (a, 900 °C-3; b, 1000 °C-3; c, 1000 °C-3)	169
Figure V. 11. The sample density of each group by the optimized process	170
Figure V. 12. The size change of the sample before and after sintering at 1500°C	171
Figure V. 13. XRD patterns of the sintered samples (groups 1 to 3 having different calcination temperatures and Sr doping)	171
Figure V. 14. Local XRD patterns of the group 1 to 3 having different Sr doping proportion (a); influence of sintering temperature (b)	172
Figure V. 15. SEM micrographs of samples sintered at 1500°C for 2h	173
Figure V. 16. EDS spectra of sintered samples with different Sr doping ratios	174
Figure V. 17. Ionic conductivities of the groups obtained with different Sr dopings and pre-calcination temperatures	176
Figure V. 18. Ionic conductivities for different Sr ratios, measured at 500°C (a) and 600°C (b)	177
Figure V. 19. Arrhenius plots of samples calcined at three temperatures ($\text{La}_9\text{Sr}_2\text{Si}_6\text{O}_{27}$ as an example) (a) with different Sr doping ratios (1000-1: $\text{La}_{10}\text{Si}_6\text{O}_{27}$, 1000-2: $\text{La}_9\text{SrSi}_6\text{O}_{27}$ and 1000-3: $\text{La}_9\text{Sr}_2\text{Si}_6\text{O}_{27}$) (b)	178
Table I. 1. The electromotive forces and the ideal efficiency of a fuel cell at different temperatures ..	13
Table I. 2. The characteristics comparison of fuel cells classified according to the electrolyte	23
Table I. 3. Summary of the properties and performance of multiple cathode materials	28
Table I. 4. Wyckoff Positions and symmetry sites of Group 176 ($\text{P6}_3/\text{m}$) (quote from the Bilbao Crystallographic Server)	41
Table I. 5. The atoms coordinate of lanthanum-silicon apatite structure	43

Table I. 6. The undoped ionic conductivities of lanthanum silicates reported in literature.....	44
Table I. 7. The apatite type LSO electrical properties doped by various elements	50
Table II. 1. The PDF files of the compounds involved in this work	73
Table II. 2. Some elements' characteristic X-ray energy for EDX characterization	75
Table III. 1. Experimental ionic conductivities and activation energy of Ge, Sr substitution LSO apatite. ($\text{La}_{10-x}\text{Sr}_x(\text{Si},\text{Ge})_6$ in the table represents $\text{La}_{10-x}\text{Sr}_x(\text{Si},\text{Ge})_6\text{O}_{27-0.5x}$ for short, similarly hereinafter)	105
Table III. 2. The atoms coordinate of lanthanum-silicon apatite structure.....	107
Table III. 3. Calculated and experimental lattice constants and internal parameters of LSOs and LGO	108
Table IV. 1. The pH and temperature values during the co-precipitation process	127
Table V. 1. XRD analyses of powders obtained with different Sr doping ratios and calcination temperatures	165
Table V. 2. Composition estimates based on the results of EDS	175
Table V. 3. Density and conductivity properties of the LSOs obtained after sintering.....	179

Introduction

The desire to develop alternative energy sources, along with the ever-diminishing fossil fuel supply results in a present push for new energy conversion technology. With various advantages to directly and efficiently convert chemical energy to electrical energy, fuel cells have been investigated and applied in many fields. Fuel cells are direct chemical to electrical energy conversion devices that operate via an electrochemical reaction involving a fuel source (e.g. any hydrogen containing gas such as gasified coal and various hydrocarbons) and an oxygen source (e.g. oxygen and air). Among them, solid oxide fuel cell (SOFC) is one type of fuel cell which are defined by their ceramic and oxide electrolyte and it has an eliminate corrosion or leakage problems comparing to some other liquid electrolyte fuel cells. There are three basic components in a SOFC, namely, porous anode, cathode and dense electrolyte. The electrolyte material plays a very important role in the SOFC to transport oxygen ions and isolate airflow.

Recently, the SOFC draws much attention in commercial application with a solid material, most commonly a ceramic material named Yttria-Stabilized Zirconia (YSZ), as the electrolyte. This type of electrolyte has excellent ionic conductivity negligible electronic conduction over a wide range of oxygen partial pressure. Nevertheless, the operating temperature of this type SOFC is too high (800°C-1000°C). The high temperature causes many problems, such as the ageing of constituent components, the choice of the matched interconnectors or electrodes, and the maintenance of high temperature itself will cost much which would restrict the application in many fields.

At present, IT-SOFC (intermediate temperature SOFC) holds great promise of meeting the commercial needs to overcome the high temperature problems, attributing to the development of high ionic conductivity materials as the electrolyte. The electrolyte plays a very important role to transport the ions, which directly affects the power and energy density of a cell.

Nowadays, apatite type ionic conductors, rare earths silicates and germ with the chemical formula $RE_x(MO_4)_6O_y$, RE = rare earth, M = Si and Ge, $x = 9.33 \sim 10$, $y = 2 \sim 3$, attract many interests due to the superior transport properties with high ionic conductivity and low activation energy. They can operate stably at intermediate temperature over a wide oxygen partial pressure range and maintain excellent performances, being considered as a candidate for IT-SOFC electrolytes. Among this series of conductors, the La-Si-O type has a higher conductivity and the performance would be improved with different doping elements.

To modify the apatite $La_{10}Si_6O_{27}$ performance as an electrolyte, various doping elements influences also have been studied. Generally, there are two doping sites: La site with doping elements, such as Mg, Sr, Ba alkaline earth metal elements, and Si site with doping elements Ge, Mn, Al, Fe, etc. Because of the similar chemical properties with La, Sr has been chosen as suitable element doping at La site. Recently, Sr-doped LSO $La_9Sr_1Si_6O_{26.5}$ has been synthesized by Bonhomme et al with solid state reaction and the ionic conductivity is $2.4\text{--}2.6 \text{ mS}\cdot\text{cm}^{-1}$ at 700°C . L. Zhang et al has improved the synthesized process with a water-based gel-casting route and obtained $La_9Sr_1Si_6O_{26.5}$ with the highest ionic conductivity of $0.57 \text{ mS}\cdot\text{cm}^{-1}$ at 500°C , however, the calcination temperature is as high as 1400°C . As for the influence of different doping ratios, A. Orera et al. has investigated the ionic conductivity of $La_{8+x}Sr_{2-x}(SiO_4)_6O_{2+0.5x}$ ($0 \leq x \leq 1.0$) with ^{29}Si NMR and Raman technologies.

On one hand, many synthesis methods have been employed to obtain the pure phase composition, including some traditional methods: solid state reaction, freeze drying, and some new process with auxiliary chemicals: DEA precipitation, sol-gel, etc. High calcination temperature (around 1700°C) is necessary to reduce the secondary products and incomplete reacted chemicals with the traditional synthesis methods. The new processes are widely applied to improve the calcination condition and reduce the production cost. In recent years, the sol-gel

method becomes a research focus for its low cost and relatively simple realization in the synthesis fields with TEOS and La_2O_3 .

On the other hand, to reduce the cost of the experiment, more and more researchers choose the calculation to predict the characteristics of materials. Among these methods of calculation, DFT (Density functional theory) is one of the highest precision results so it has been widely used. We chose the VASP (Vienna Ab initio Simulation Package) package to start the calculation of its high efficiency and precision results.

The main goal of the present work focuses on the calculation, characterization and optimization of the apatite-type $\text{La}_{10-x}\text{Sr}_x\text{Si}_6\text{O}_{27-0.5x}$ (LSO) as the electrolyte material in IT-SOFC. We use a dual approach: a simulation approach and an experimental approach to optimize the electrolyte materials for fuel cells at an intermediate temperature.

We have divided the thesis into four stages as follows:

- Study the fundamental properties of Sr, Ge doping $\text{La}_{10}\text{Si}_6\text{O}_{27}$ using the DFT methods;
- Check the results of the simulation by the realization of these materials;
- Study and compare different synthesis methods to obtain an efficient, simple approach;
- Investigation of the experimental impact factor to achieve pure phase products (with and without Sr doping) for fine ionic conductivity.

Chapter I gives a review on SOFC work mechanism and its component materials, especially the apatite-type phase lanthanum silicates electrolyte materials.

Chapter II presents the synthesis methods for our electrolyte materials, characterization involving in this work and the theoretical foundation of ab initio calculations, particularly for the ceramic calculation.

Chapter III is composed with the calculation study of the apatite-type LSO. We investigated the influence of Sr doping, as well as discovering the relationship between electric properties and crystal microstructures.

Chapter IV gives preliminary experimental exploration of co-precipitation, molten salts and HDP (homogenous deposition precipitation) methods. The co-precipitation method has been presented as a high efficiency, alternative way to obtain the apatite-type lanthanum silicate as an electrolyte in SOFC. With which the apatite phase can be achieved with facile procedure at low temperature.

Chapter V contains experimental methods to synthesize pure phase, high crystallization LSO. We developed the traditional sol-gel method, reduced the synthesis process and cost. The relevant synthesis parameters have been investigated to get pure, highly crystalline powders. The mechanisms occurring in the sol-gel reactions are discussed. The electrical performance indicates that the obtained LSO has the possibility to be a considerable candidate as electrolyte material in IT-SOFC.

Annex I illustrates the publications and conferences list.

CHAPTER I Overview of the solid oxide fuel cells
(SOFC) and apatite-type materials as electrolyte in
SOFC

This chapter gives a brief review for principles of solid oxide fuel cell (SOFC) system to the material involved in their construction. This review will include its history, principle, structure and materials as well as the apatite type materials that will be introduced as promising electrolytes in SOFC's and as the subject of the present thesis study.

I.1 Solid Oxide Fuel Cells (SOFCs)

I.1.1 Historic

The Fuel cells (FC) [1-5] are the energy conversion devices able to produce electric energy from chemical energy directly with high efficiency. The original idea of FC was firstly proposed by a Welsh physicist *William Grove* in the mid-nineteenth century. [6, 7] At the time, the mechanism of electrical conduction investigation just started by some pioneers (e.g. Benjamin Franklin, Georg Simon Ohm, Andre Marie Ampere et al.). Almost simultaneously, the operating principle of fuel cells was discovered by *Christian Friedrich Schönbein*. [8]

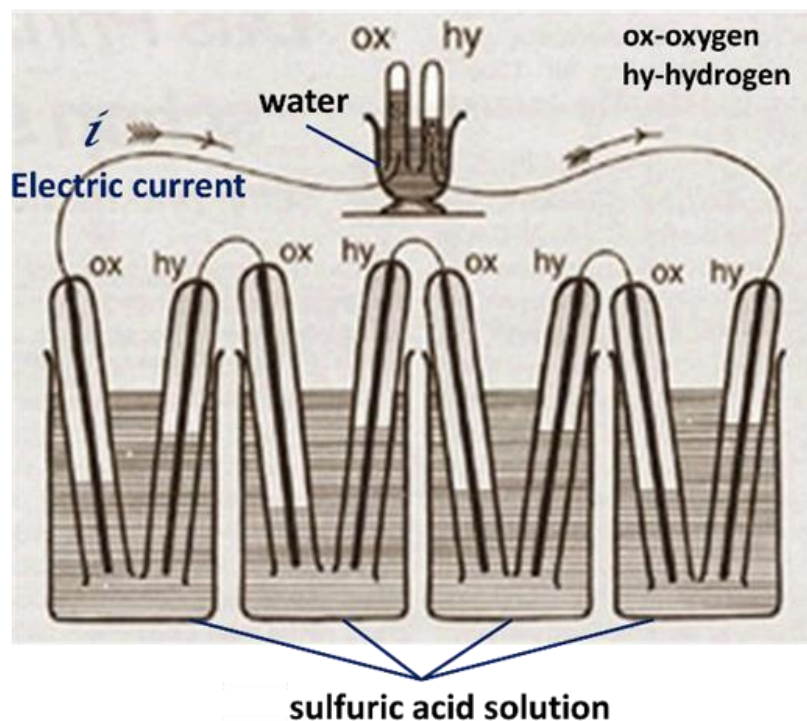


Figure I. 1. William Grove's 1839 gas voltaic battery diagram, pioneer of modern fuel cell

In 1842 *Grove* [9] sketched a design of fuel cell stack and it has the similar materials with today's phosphoric acid fuel cell. This system used sulfuric acid as the electrolyte and platinum as electrode material. The diagram of the first fuel cell is shown in Figure I.1.

From then, fuel cells came in many varieties. Originally the concept and basic materials on solid electrolyte were proposed by *Nernst* and his colleagues at Göttingen in late nineteenth century [10-12]. But considerable progress in the theory and experiment came out still in 110 years. Composition of 85% zirconia and 15% yttrium oxide by mass, as said by Nernst, was first used to improve the ionic conductivity. Zirconia based ceramics were used initially in the fuel cell, which was the first attempt of making a high operating temperature solid oxide fuel cell (SOFCs) in 1937 by *Baur* and *Preis* [13, 14].

In 1960s, *Kiukkola* and *Wagner* [15] reported thermodynamic investigations on metal / metal oxide systems, and the paper stimulated numerous activities [16, 17] in the field of solid state electrochemistry in various regions of the world. With the development of the conductive properties of the stabilized zirconia, SOFCs were being extensively studied. A growing number of patents and papers on SOFC appeared in several countries.

In United States, Westinghouse Electric Corporation had developed industrial SOFC stacks [18]. Planar and tubular cells with platinum electrodes were produced and connected in pack, using a gold / nickel solder. In Europe, after *Palguyev* and *Volchenkova* [19, 20] had published conductivity measurements on $3\text{ZrO}_2 \cdot 2\text{CeO}_2 + 10\text{wt}\% \text{CaO}$ and other systems, research programs addressing cells with solid oxide electrolytes blossomed. The researchers have substantially contributed a lot of work and developed the electrolyte in solid form on Ca-Zr-Y system. During this period, some institutes and universities have produced numerous valuable results on SOFC that deserves recognition: the Battelle Institute in Geneva and Frankfurt, Universities of Grenoble, Nagoya and Greifswald et al.[21-23]. In Asia, *Takahashi* [24,

25]investigated with electrolytes of alkaline carbonate in Japan, which began SOFC research there.

In the mid-1990s, the development of SOFC had a rapid increase since the new materials, oxides of the lanthanide ion conductor were found using as electrolyte in SOFC by *Ishihara* in 1994 [26]. This form of doped lanthanum and gallium oxide provided an excellent conductivity at intermediate temperature, which started the studying intermediate temperature solid oxide fuel cells (IT-SOFC). It partly solved the problems of high operating temperature that was faced hitherto as it will be discussed in Section I.3. At the same time, polarization losses and importance of the electrode catalysis reactions increased. A large variety of new design concepts and cellular systems were being pursued and new solid electrolyte materials were imminent [27-29]. To some extent, it can be stated that the development of the SOFC technology is linked with the improvement of high performance solid electrolytes.

Recently, the search for improved electrolyte materials has attracted much attention to enlarge the application range of the SOFC. So far, fuel cells have been widely used in power plants [30, 31], automobiles [32, 33], domestic use [34, 35] and even digital products [36]. Such promising future is tied with the numerous advantages offered by the power generation equipment, namely in terms of conversion efficiencies, reduced environmental impact, low noise emissions and moderate cost.

I.1.2 Fuel cell structure and operation

I.1.2.1 Principle of operation

Fuel cells [37-39] have many pack types with multiple geometries and packing: i) tubular fuel cell firstly designed by Westinghouse co.; ii) planar fuel cell which has higher power density than the tubular one; iii) micro tubular fuel cell which possess higher energetic density, better

resistance to thermal stresses, and smaller starting times as compared with conventional planar stacks . Figure I.2 shows a schematic diagram of the solid oxide fuel cell in the planar form.

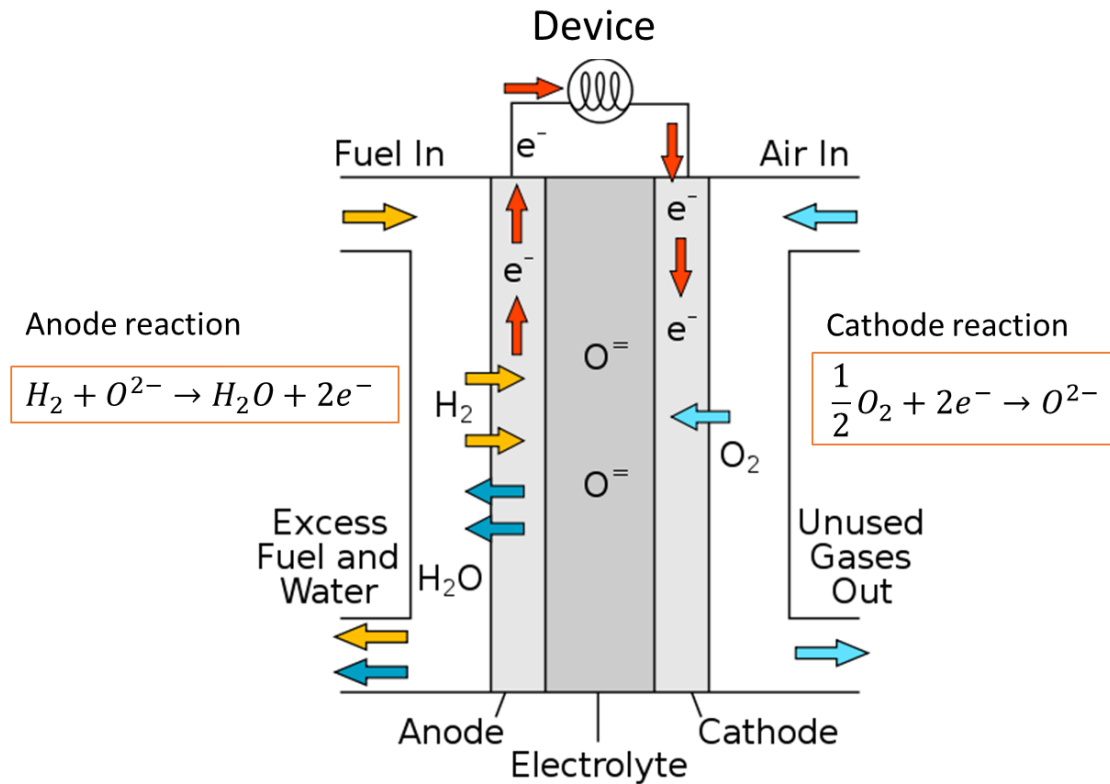


Figure I. 2. Schematic diagram of the operation of a fuel cell (This work has been released into the public domain by its author, *Sakurambo*.)

In this diagram, hydrogen is taken as fuel. The hydrogen comes into the anode (the oxidation electrode), to be absorbed by the material, in which it undergoes a catalytic dissociation that generates protons. Meanwhile, the adsorption and catalytic dissociation of oxygen molecules at the cathode (the reduction electrode) lead to the generation of oxygen ions. These ions pass through the electrolyte, meet the hydrogen ions at the anode. Both ions are consumed at the same time, and combined to generate water. In addition, this formation of water promotes the consumption reaction in both electrodes. Since the electrolyte is designed for electronic insulation, electrons can only pass through an external circuit from the anode to the cathode, whereby generating the wanted current.

- Chemical thermodynamics

Figure I.3 sketches the input and output of the fuel cell. The voltage/intensity characteristics are determined by the chemical energy contained in the fuel as shown by a simple thermodynamic analysis.

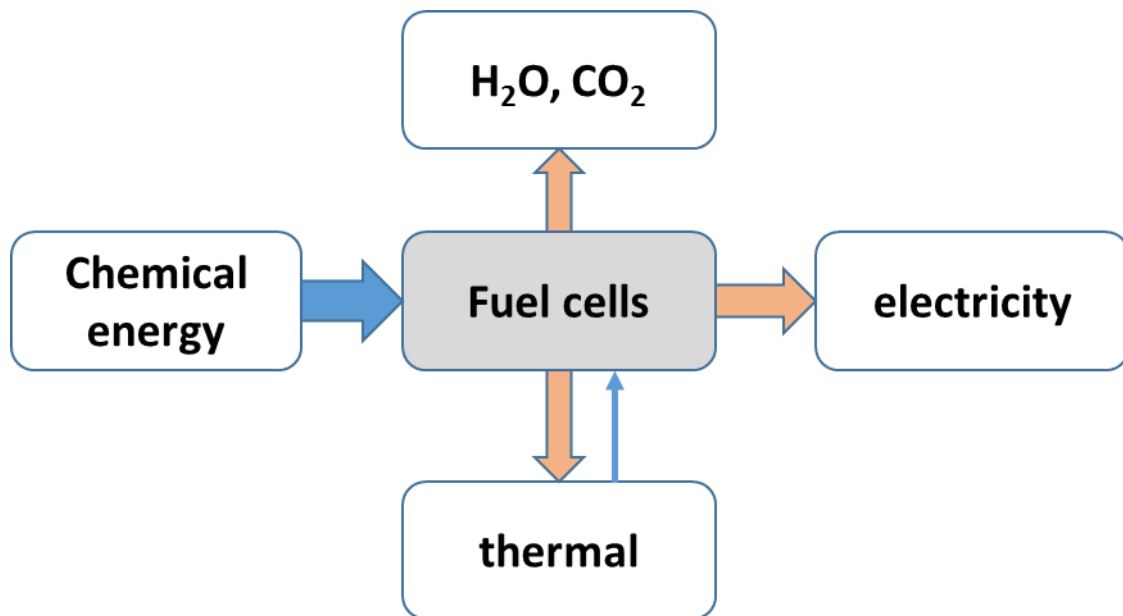


Figure I. 3. The input and output of the fuel cell

To simplify the discussion, hydrogen and oxygen are chosen as an example for the reaction taking place in the SOFC. The overall chemical reaction is given by equation I.1.



In this reaction, the change of energy can be expressed in Gibbs free energy ΔG , which depends only on the state before and after the chemical reaction, regardless of the process. It is defined by the equation I.2.

$$\Delta G = \Delta H - T\Delta S = \Delta U + \Delta(PV) - T\Delta S \quad \text{EQN I.2}$$

Among them, ΔH , T , ΔS , ΔU , P et V are the enthalpy change, the temperature, the entropy change, the internal energy change, pressure and volume, respectively.

The internal energy change ΔU includes the heat absorbed or released ΔQ and external work W . Both variables can be defined by equations I.3 and I.4 respectively.

$$\Delta Q = T\Delta S \quad \text{EQN I.3}$$

$$W = W' - P\Delta V \quad \text{EQN I.4}$$

The external work W included two parties: (i) the work of volume $\Delta(PV)$, which can be expressed as $P\Delta V$ in the stack under thermostatic condition and constant pressure; (ii) the non-volume work W' .

One draws the equation I.5 from equation I.4 using equation I.2 and I.3.

$$\Delta G = W' \quad \text{EQN I.5}$$

In the cells, the non-volume work W' , which is the electrical work, is equal to the change in the Gibbs energy under isothermal and isobaric conditions.

We assume that there is 1 mol hydrogen involved in the chemical reaction of equation I.1, thus 2 moles of electrons pass through the external circuit. The electrical work is given in the equation I.6.

$$W' = -2F \cdot E = \Delta G \quad \text{EQN I.6}$$

Then,

$$E = \frac{\Delta G}{-2F} \quad \text{EQN I.7}$$

where E is the electromotive force of the fuel cell and F is the Faraday constant that represents the total electricity of the charges of one mole elementary, and the value is 96 485 C/mol;

For example, when the product of the hydrogen fuel cell is vapor at the operating temperature of 200°C, the value of ΔG is -220.82 kJ/mol. the electromotive force is 1.14V.

- Fuel cells efficiency

First of all, we compare the energy conversion efficiency of the engine which is a traditional device commonly used for the conversion of chemical energy. According to the second law of thermodynamics, efficiency of work is to follow the Carnot efficiency, and it is given in equation I.8.

$$\eta = \frac{-W}{Q} = 1 - \frac{T_2}{T_1} \quad \text{EQN I.8}$$

Where, W , Q , T_1 and T_2 are the work function, heat absorbing from the high temperature source, the high temperature and low temperature. The temperature difference between inside and outside of engine is high, then there is more effectively. Currently, the limit of the theoretical efficiency of the car engine is about 50%, while the actual efficacy is much lower.

The theoretical efficiency[40] of the cell is defined as the equation I.9 showing:

$$\eta_{max} = \frac{\Delta G}{\Delta H} = \frac{\Delta H - T\Delta S}{\Delta H} = 1 - T \frac{\Delta S}{\Delta H} \quad \text{EQN I.9}$$

where ΔH is the enthalpy change, which is the heat emission by burning the same amount of fuel.

Table I. 1. The electromotive forces and the ideal efficiency of a fuel cell at different temperatures

The reaction in cells	298 K		600 K		1000 K	
	E ⁰ (V)	η_{max} (%)	E ⁰ (V)	η_{max} (%)	E ⁰ (V)	η_{max} (%)
$H_2 + \frac{1}{2}O_2 = H_2O(g)$	1.18	94	1.11	88	1.00	78
$CH_4 + 2O_2 = CO_2 + H_2O(g)$	1.04	100	1.04	100	1.04	100
$CO + \frac{1}{2}O_2 = CO_2$	1.34	91	1.18	81	1.01	69
$C + \frac{1}{2}O_2 = CO$	0.74	124	0.86	148	1.02	178

In some reactions, such as oxidation of Carbon, the Gibbs free energy is even higher than the enthalpy change. That is to say, the reactions in cell absorb heat during the conversion process

from chemical energy to electrical energy. Compared to combustion, the efficiency is even higher than 100%. Table I.1 shows the electromotive forces and the efficiency of common fuel cells.

- The energy density and power density

Figure I.4 shows the energy density and the power density of the fuel cell among the energy conversion and storage devices[41].

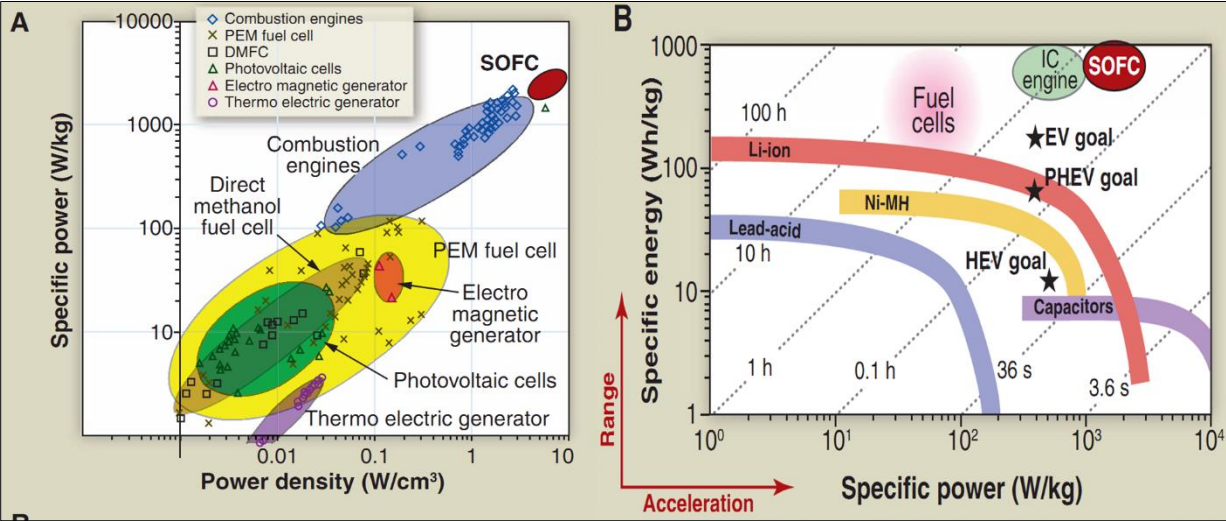


Figure I. 4. The energy and power properties of the fuel cell compared to other energy conversion devices (A. Comparison of the specific power between the present SOFC ~ 2W / cm² at 650°C and multiple energy conversion devices as a function of the power density. B. Ragone plot, specific energy versus specific power, for various energy devices in relation to the present SOFC) [41].

According to Figure I.4, it can be seen that the fuel cells provide higher energy density than other similar utility devices, such as batteries (Li-ion batteries, lead-acid ...), capacitors, and even internal combustion engines. In this perspective, the fuel cell including the SOFC may be the most promising devices for converting energy with high efficiency. As shown in Figure I.4 (A), even in the family of fuel cells, the SOFC has the highest power that can be used in the instantaneous high-energy output field. Furthermore, with liquid hydrocarbon fueling, SOFCs and internal combustion engines have essentially the same specific energy, that of the fuel (~

1kWh / kg). Thus, because our SOFC essentially has the same power and energy density as an internal combustion engine (Figure I.4 (B)), it could potentially transform the automotive sector as, for example, a range extender for plug-in hybrid electric vehicles (PHEVs) operating on conventional fuels. The corresponding 10 kW stack would only be a small cube of 10 cm per edge.

I.1.2.2 Structure of fuel cell

In this section, the three most important parts are presented by their uses and conditions to be fulfilled.

- An oxygen electrode (cathode)

This is a place for the reduction reaction of oxygen. It must match a porous structure (a porosity about 30% ~ 40%) to increase specific surface, as well as to permit the oxidant to reach the interface between cathode and electrolyte. In addition, it needs to have the properties:

- Chemical compatibility with the other contact components (usually the electrolyte and interconnect) in operating conditions;
- A thermal expansion coefficient (TEC) corresponding to those of other components;
- The chemical stability and microstructure in an oxidizing atmosphere during fabrication and operation;
- Adhesion to the surface of the electrolyte.

It is an electric and ion conductor. Meanwhile, it needs to have the ability of oxygen adsorption and catalytic cracking. The most common materials of the cathode are metals which can form the oxygen adsorption bonds easily. Figure I.5 shows evolution of the oxygen reduction activity of the different metals [42]. Among them, Pt shows the best performance.

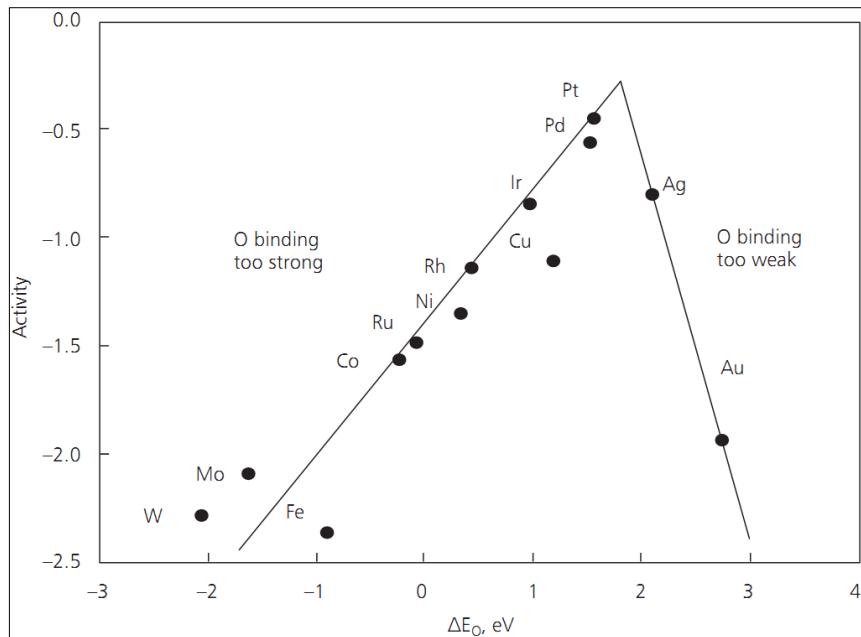


Figure I. 5. Changes in oxygen reduction activity plotted as a function of the oxygen binding energy [42]

The most important reaction in the cathode is the oxygen adsorption process. Generally, there are three types of adsorption and they are shown in Figure I.6.

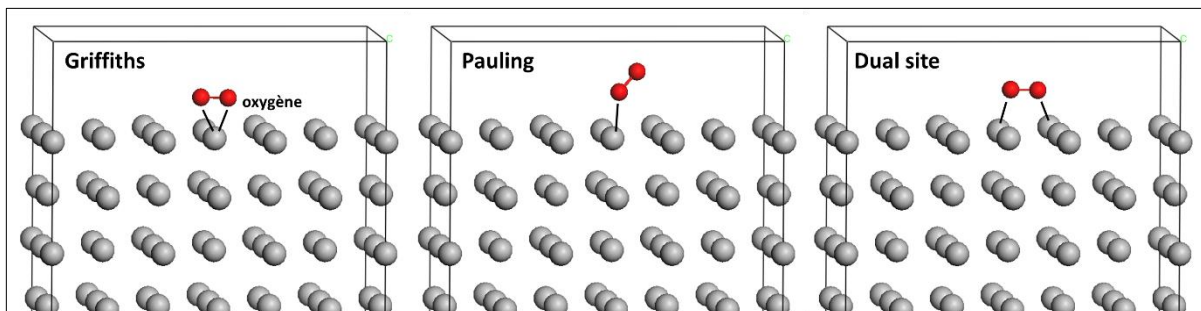


Figure I. 6. The types of oxygen adsorption process in the cathode

Generally, the three types of adsorption are Griffiths, Pauling and Dual Site model. In the Griffiths model, the oxygen molecule is hit by an atom of the cathode materials. The formation of the bond between the oxygen atom and the cathode atom leads to weaken the bond strength

between the two oxygen atoms, even to crack the oxygen molecule. This phenomenon contributes to the reduction of oxygen.

In the Pauling model, one of the oxygen atoms, which has a stronger activation in the molecule, gets combined to the atom of the cathode. The oxygen reduction in this mode achieved in most of electrode materials. In appropriate circumstances, adsorption takes place according to the Dual site model in which the oxygen molecule gets adsorbed on two atoms of cathode material at the same time, which leads to more favorable condition for the reduction of oxygen.

- A fuel electrode (anode)

This is a place for the oxidation reaction of the fuel. It must exhibit a porous structure to allow the fuel to reach the interface between anode and electrolyte. It is an electron and ion conductor. Meanwhile, it needs to have the possibility of processing hydrogen (or other fuel) adsorption and catalytic cracking.

Hydrogen oxidation reaction as the easiest, but the most typical reaction in the anode is shown as an example to explain the catalytic oxidation process. The oxidation of hydrogen molecules takes place on the surface of noble metals. Figure I.7 shows the exchange current density on the different metals as the anode materials [43-45]. The density largely depends on the metal-hydrogen bond: if the bond is very strong, it is difficult for the products separating from the metal, thereby interfering with the reaction continuation. And if the bond is very weak, the bond formation is not so stable that the hydrogen molecules are easy to be desorbed. Among them, Pt shows the best performance, and Pt was used as an electrode material of test electrolyte.

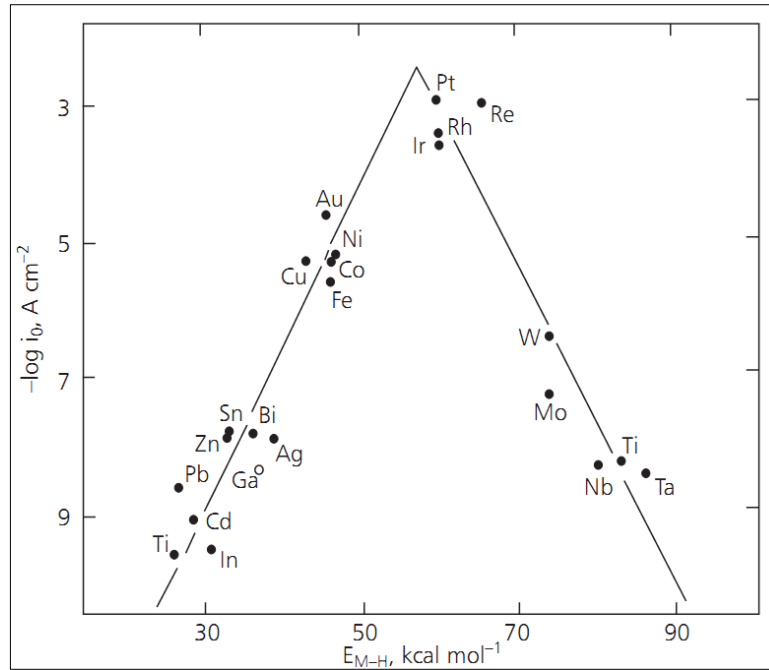
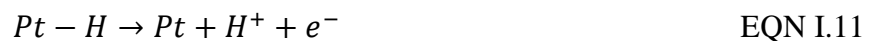


Figure I. 7. The logarithm of the exchange current density ($\log i_0$) against the force of the metal-hydrogen bond formed during the reaction itself.

At room temperature, the hydrogen ionization process on the surface of non-oxidized Pt comprises: Hydrogen dissociative adsorption and electron transfer. They are shown in the equations I.10 and I.11.



- A solid electrolyte

It is a component for transmitting oxygen ions. It must match a thin and impervious layer to separate the fuel from the anode side and oxidant on the cathode side during the operation of the stack. It must be electrical insulation and capable of conducting oxygen ions.

Due to crystal defects or their particular structures, these substances provide channels for rapid ion transition. At certain temperatures, they have high ion conductivity ($> 1 \sim 10^{-6} S \cdot cm^{-1}$),

also called as fast oxygen ion conductors. The performance of ionic conduction is dependent by the ion diffusion efficiency in the substances [46-48]. Figure I.8 gives some representative diffusion mechanisms for ion effective transmission. They have the potential to form an effective transportation.

- **Vacancy diffusion.** This diffusion takes place among the lattice sites, and it is based on the vacancies in crystal defects. To jump from lattice site to lattice site, atoms need energy to break bonds with neighbors, and to cause the necessary lattice distortions during jump. This energy comes from the thermal energy of atomic vibrations and electric field force in some cases.
- **Interstitial diffusion.** Interstitial diffusion is generally faster than vacancy diffusion because bonding of interstitials to the surrounding atoms is normally weaker and there are many more interstitial sites than vacancy sites to jump to. Requires small impurity atoms (e.g. C, H, O) to fit into interstices in host.
- **Ions exchange.** An ion exchanges with another neighbor ion. This mechanism creates very important local distortions repulsion. However this does not assume an existence of permanent point defects in the crystal.

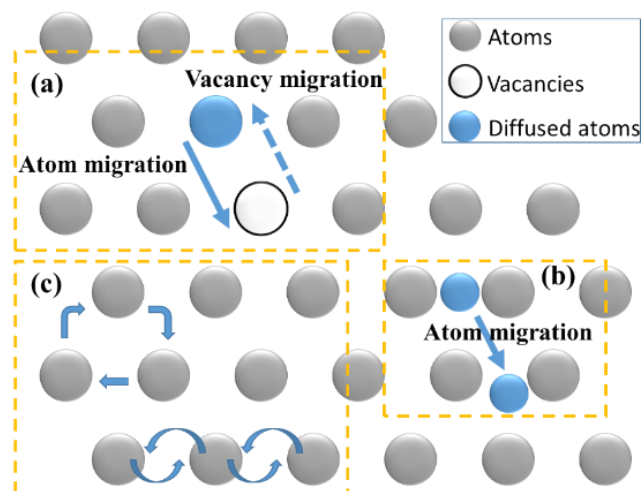


Figure I. 8. Schematic of diffusion mechanisms in solid state structures: (a) vacancy diffusion; (b) Interstitial diffusion; (c) ions exchange- direct and circle.

To further understand the factors that influence diffusion, thermally activated process is discussed in this part. First of all, the activation energy has to be drawn into the conception to describe the diffusion, even the conductivity. Figure I.9 gives a schematic to represent the definition of activation energy.

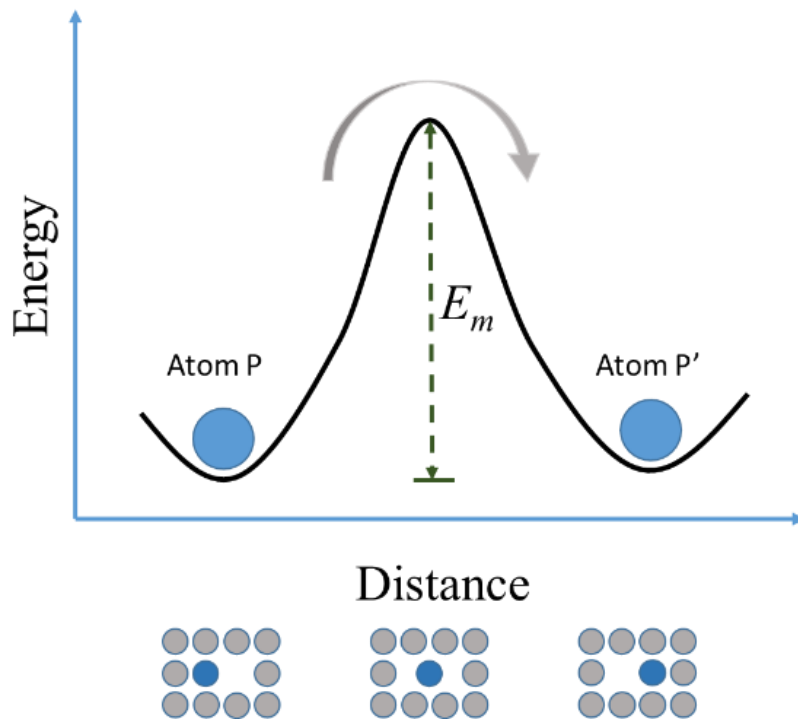


Figure I. 9. Schematic representation of the diffusion of an atom from its original position into another lattice site. Activation energy E_m has to be supplied to the atom so that it could break inter-atomic bonds and to move into the new position.

To jump from lattice site to lattice site, atoms need energy to break bonds with neighbors, and to cause the necessary lattice distortions during jump. The energy necessary for motion, E_m , is called the activation energy.

The probability of such fluctuation or frequency of jumps, R_j , depends exponentially on temperature and can be described by equation I.12 that is attributed to Swedish chemist Arrhenius:

$$R_j = R_0 \exp\left(-E_m/k_B T\right) \quad \text{EQN I.12}$$

Where R_0 is so-called “attempt frequency” proportional to the frequency of atomic vibrations. Correspondingly, Diffusion coefficient, which is the measure of mobility of diffusing species, can be given in equation I.13

$$D = D_0 \exp\left(-Q_d/RT\right) \quad \text{EQN I.13}$$

Where D_0 – temperature independent pre-exponential (m^2/s)

Q_d – the activation energy for diffusion (J/mol or eV)

R – the gas constant (8.31 J/mol•K or 8.62×10^{-5} eV/ K)

T – absolute temperature (K)

The above equation can be written as:

$$\ln D = \ln D_0 - \frac{Q_d}{R} \left(\frac{1}{T}\right) \quad \text{EQN I.14}$$

The activation energy Q_d and pre-exponential D_0 , therefore, can be estimated by plotting $\ln D$ versus $1/T$. Such plots are called Arrhenius plots, as shown in figure I.10.

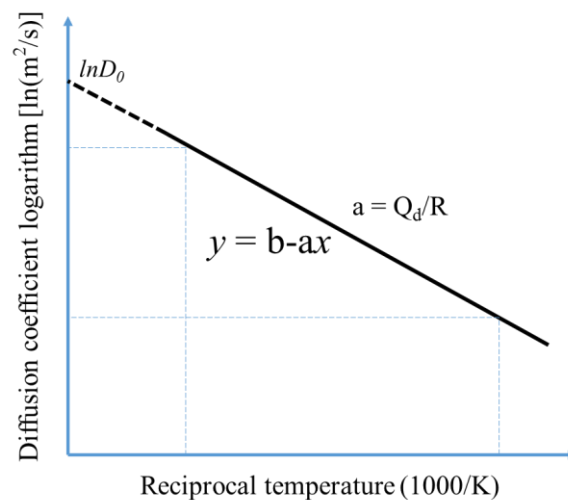


Figure I. 10. Arrhenius plot of $\ln D$ vs. $1/T$ with a slop of $-Q_d/R$ and an intercept of $\ln D_0$

These three components are the most important parties of the fuel cell. Figure I.11 shows the typical morphology of the three parts: a porous anode, a dense electrolyte and a porous cathode.[49]

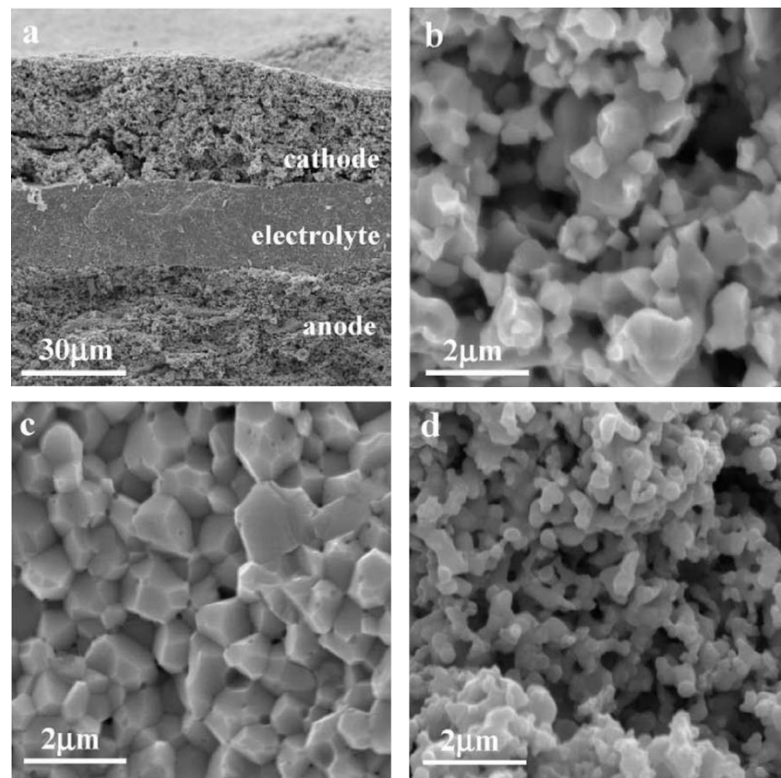


Figure I. 11. Cross-sectional views SEM micrographs of (a) a single cell, (b) the porous Ni–GDC (gadolinia-doped ceria) anode, (c) the dense GDC electrolyte, and (d) the porous SSC (Sm_{0.5}Sr_{0.5}CoO₃)–GDC cathode. [49]

I.1.3 Comparison of some alternative fuel cells

According to different types of electrolyte, fuel cells can be classified into multiple categories. Some relatively important alternatives or competitive fuel cells have to be presented here in order to further understand the features of SOFC. Table I.2 illustrates the comparison of fuel cell technologies.[50] They are Alkaline Fuel Cell (AFC), Phosphoric Acid Fuel Cell (PAFC), Molten Carbonate Fuel Cell (MCFC), Solid oxide Fuel Cell (SOFC) and Proton Exchange Methanol Fuel Cell (PEMFC). It is indicted that SOFC has many advantages for various application and most of the disadvantages is derived from the high operation temperature. The development of IT-SOFC is necessary to improve this situation.

Table I. 2. The characteristics comparison of fuel cells classified according to the electrolyte

Fuel cell type	AFC	PAFC	MCFC	SOFC	PEMFC
Common electrolyte	KOH	H ₃ PO ₄	Li ₂ CO ₃ -K ₂ CO ₃	YSZ	PEM
fuel	Hydrogen	Natural gas, methanol, gasoline	Natural gas, methanol, gasoline	Natural gas, methanol, gasoline	Hydrogen, methanol
Operating temperature	90-100°C	150-200°C	600-700°C	700-1000°C	50-100°C
Conductive ions	OH ⁻	H ⁺	CO ₃ ²⁻	O ²⁻	H ⁺
Typical stack size	10-100kW	200-400kW	300-3000kW	1-2000kW	<1-100kW
Life (h)	10000	15000	15000	7000	5000
Efficiency	60%	40%	45-50%	60%	35%-60%
Advantages	<ul style="list-style-type: none"> • Cathode reaction faster in alkaline electrolyte, leads to high performance • Low cost components 	<ul style="list-style-type: none"> • Higher temperature enables CHP • Increased tolerance to fuel impurities 	<ul style="list-style-type: none"> • High efficiency • Fuel flexibility • Can use a variety of catalysts • Suitable for CHP 	<ul style="list-style-type: none"> • High efficiency • Fuel flexibility • Can use a variety of catalysts • Solid electrolyte • Suitable for CHP & CHHP • Hybrid/GT cycle 	<ul style="list-style-type: none"> • Solid electrolyte reduces corrosion & electrolyte management problems • Low temperature • Quick start-up
Disadvantages	<ul style="list-style-type: none"> • Sensitive to CO₂ in fuel and air • Electrolyte management 	<ul style="list-style-type: none"> • Pt catalyst • Long start up time • Low current and power 	<ul style="list-style-type: none"> • High temperature corrosion and breakdown of cell components • Long start up time • Low power density 	<ul style="list-style-type: none"> • High temperature corrosion and breakdown of cell components • High temperature operation requires long start up time and limits 	<ul style="list-style-type: none"> • Expensive catalysts • Sensitive to fuel impurities • Low temperature waste heat
Application	<ul style="list-style-type: none"> • Military • Space 	<ul style="list-style-type: none"> • Distributed generation 	<ul style="list-style-type: none"> • Electric utility • Distributed generation 	<ul style="list-style-type: none"> • Auxiliary power • Electric utility • Distributed generation 	<ul style="list-style-type: none"> • Backup power • Portable power • Distributed generation • Transportation • Specialty vehicles

* CHP- combined heat and power; CHHP- combined heat, hydrogen, and power

I.2 Materials used in the SOFCs

I.2.1 Cathode materials

The oxygen reduction process occurs at the interface of electrode and electrolyte and the reaction is shown in Figure I.12. There are three ways to transfer oxygen and among them, TPB (triple phase boundary) is a very important reaction place [2, 51]. The cathode materials should have the properties: adsorption, catalytic cracking of oxygen, and conversion from the atoms to

ions. Thus, the electro catalytic activity of the cathode material is a very important reference to evaluate the cathode performance.

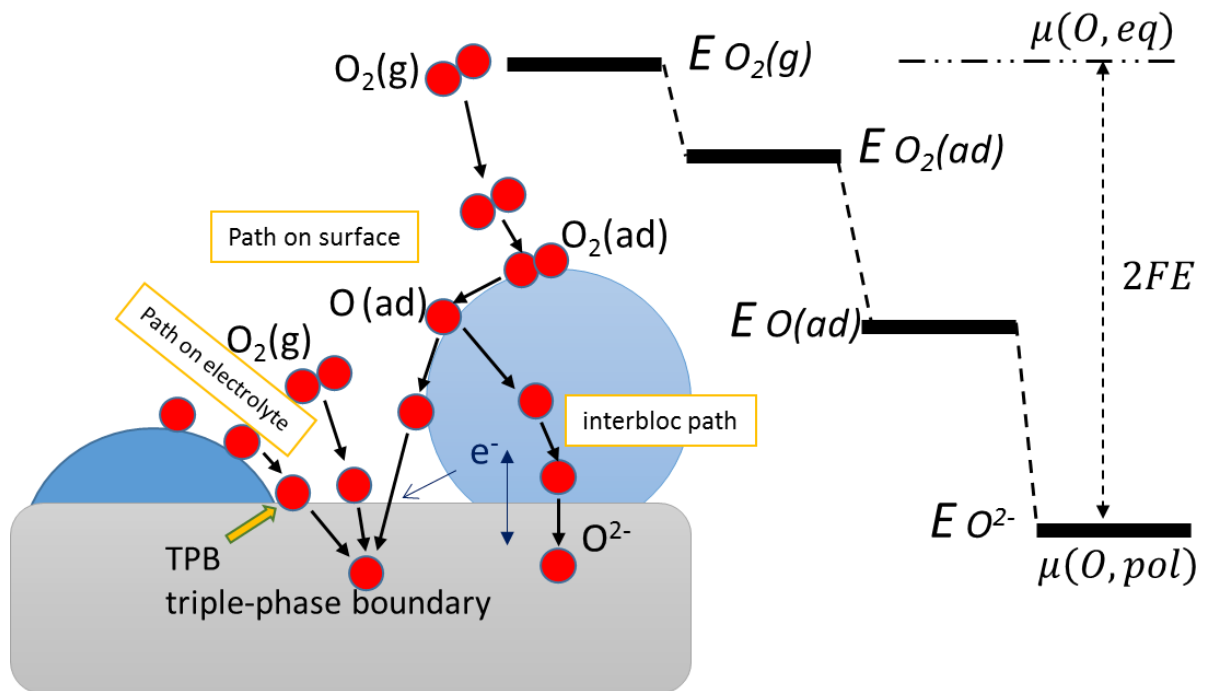


Figure I. 12. A diagram of the reactions in the cathode of SOFC

The cubic perovskite type oxides with general formula ABO_3 are mainly used as cathode materials[52]. These materials, with the electronic and the oxide ionic conductivity, are known with the name MIEC (Mixed Ionic-Electronic Conducting oxides). Figure I.13 shows a schematic of the typical structure of perovskite.

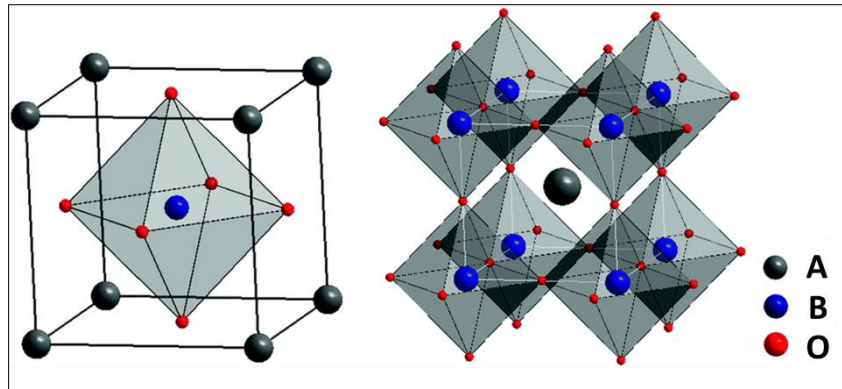
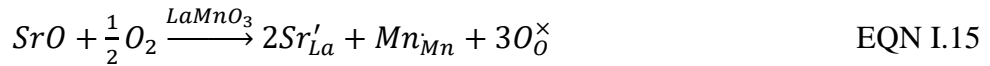


Figure I. 13. Schematic of the lattice structure of a perovskite– ABO_3

In the structure, *A* and *B* cations together possess a net charge of +6. The *A* sites are occupied by lower valence cations (eg, La, Sr, Ca, Pb, etc.). They are larger and are coordinated to 12 oxygen ions. Type *B* cations (such as, Ti, Cr, Ni, Fe, Co, Zr, etc.) occupy much smaller spaces and are coordinated to six oxygen ions. Most non-doped perovskite materials are poor conductor of oxide ions in the air.

In 1966, $La_{1-x}Sr_xCoO_{3-\delta}$ (LSC) was the first perovskite-type material, reported by *Button* and *Archer*, to be used as cathodes for SOFCs [53]. This was followed by synthesis of several perovskite materials which were subsequently tested for their usability. From 1973, $La_{1-x}Sr_xMnO_{3-\delta}$ (LSM) has been used exclusively for the purposes of the cathode, and until today it remains the most studied cathode material for SOFCs [54, 55]. In the case of $LaMnO_3$, Sr^{2+} cation dopant is most widely used because of the small difference in ionic size between Sr^{2+} and La^{3+} . However, on substitution of La^{3+} with Sr^{2+} cations, instead of compensation by the formation of positively charged oxygen vacancy, an oxidation of manganese cations occurs, which effectively increases the electron-hole concentration and improves electrical conductivity[56]. This process is similar to p-type doping in the p-type semiconductor. The defect reaction can be given in the form of Kröger–Vink notation as shown in EQN I.15.



A linear increase in the electron conductivity of $\text{La}_{1-x}\text{Sr}_x\text{MnO}_{3-\delta}$ with the increase of x has been reported by *Mizusaki* et al[57]. However, the conductivity reaches a maxima at $x = 0.5$. Zhang et al. and Li et al. have also reported an increase of the electric conductivity up to 200-485 S/cm ($x = 0.5$ at 1000 °C). A plot of $\log(\sigma T)$ vs $1/T$ for $\text{La}_{1-x}\text{Sr}_x\text{MnO}_{3-\delta}$ in the condition of pure oxygen ($P_{\text{O}_2} = 1$ bar) is shown in Figure I.14.

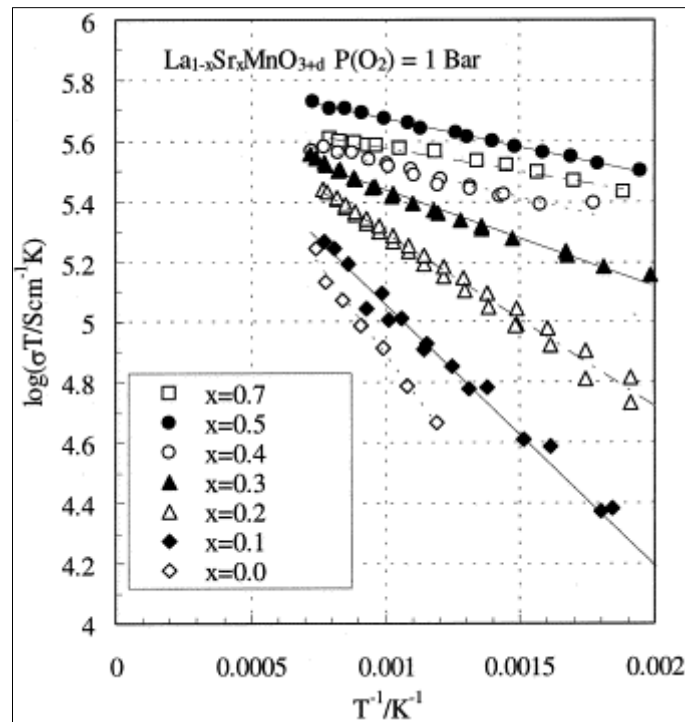


Figure I. 14. Variation of electrical conductivity (σ) of $\text{La}_{1-x}\text{Sr}_x\text{MnO}_{3-\delta}$ (x is 0 to 0.7) at different temperature (at pure oxygen $P_{\text{O}_2} = 1$ bar). [57]

Elements doping led to the emergence of new structures, more recently, double perovskite structure[58] has become a hot topic. A. *Grimaud* et al[59] summarized the change of the structure with the different doping elements shown in Figure I.15. With respect to the anisotropic oxygen diffusivity in these “layered structures,” quite different from the one in

simple perovskites in which oxygen vacancies are randomly distributed, one can expect anisotropic water insertion and peculiar protonic conduction.

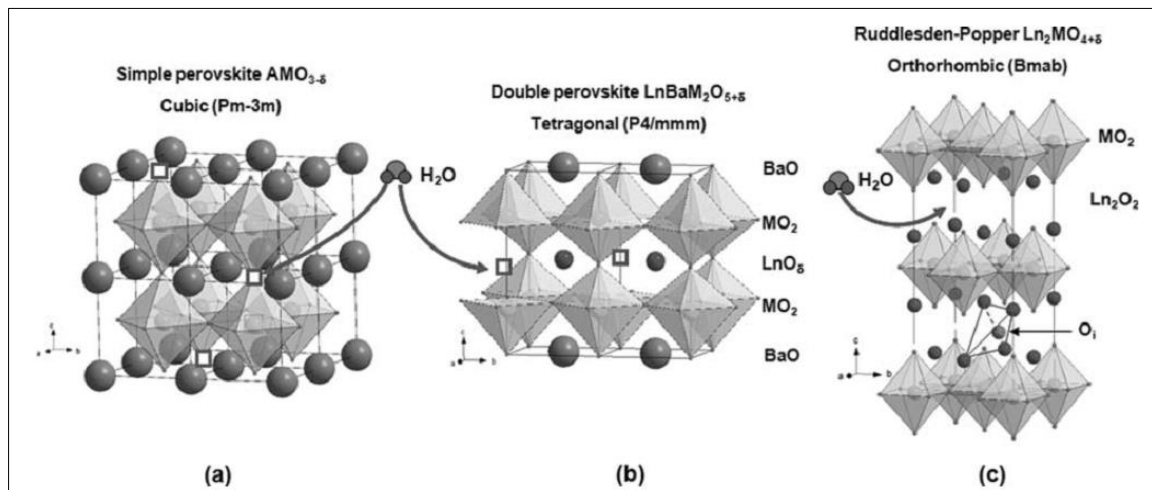


Figure I. 15. Schematic view of the crystal structures of: (a) Simple perovskite, (b) Double perovskite and (c) Ruddlesden-Popper K_2NiF_4 type phase. Sites for water insertion are shown: oxygen vacancies for the perovskites and interstitials for $Ln_2MO_{4+\delta}$. [59]

The performance of the existed cathode materials is listed in the Table I.3.[2] However, most of the reported performances vary tremendously because of several unknown variable factors during the operation/testing. The materials remain amount of work to clearly understand short- and long-term degradation problems with optimization and calculated predictions.

The compatibility of cathode on the electrolyte was first studied in 1969 by *Tedmon* et al[60]., with the porous $LaCoO_3$ cathode on YSZ electrolyte. From then on, this field study became a hot point till today.

Table I. 3. Summary of the properties and performance of multiple cathode materials

composition	TEC ($\times 10^{-6}/K$)	σ_e (S/cm)	σ_i (S/cm)	D_O (cm ² /s)	k (cm/s)	Temp.
Non-ABO₃ structure						
8YSZ	10.2-10.5	0.17	0.003-0.02			1000°C
YSZ-40% wt. LSM			3×10^{-3}	$1-6 \times 10^{-9}$	$7-1 \times 10^{-7}$	900°C
LSGM	10.4		0.08			700°C
Pt				4.1×10^{-6}	5×10^{-2} -1.6	
ABO₃ structure						
A=La, B=Mn	11.33-12.4	40-485	poor	2.45×10^{-13}	7.45×10^{-8}	1000°C
A=La, B=Co	20-22	50-201		5.31×10^{-9}	3.47×10^{-7}	900°C
A=La, B=Fe				5.28×10^{-12}	1.67×10^{-7}	1000°C
A_{1-x}A'_xBO₃						
A=La, A'=Sr, B=Mn	12.4 (x=0.2)	200-485	5.76×10^{-6}	1.33×10^{-11}		1000°C
A=La, A'=Sr, B=Co	20 (x=0.4)	2000	1.2	1.4×10^{-8}	4×10^{-4}	900°C
A=La, A'=Sr, B=Fe	x=0.1-0.4		8.3×10^{-4}	2.65×10^{-9}	5×10^{-4}	800°C
A=La, A'=Ba, B=Fe	x=0.2		3.1×10^{-4}			800°C
A=Y, A'=Ca, B=Mn	7-12 (x=0.3)					
A=Y, A'=Ca, B=Fe	x=0.1		3.9×10^{-2}			1000°C
A=Pr, A'=Sr, B=Co	18.3-29.6	1000	(x=0-0.5)			
A=Pr, A'=Sr, B=Mn	12.2 (x=0.5)	250				600°C
A=Sm, A'=Ba,Sr, B=Co	20-25	1280,280	(50°C, 900°C)			
AB_{1-y}B'_yO₃						
A=La, B=Ga, B'=Co	15.5	$\leftarrow y=0.2$	3.4×10^{-3}	$\leftarrow y=0.4$		800°C
A=La, B=Ni, B'=Fe	11.4 (y=0.4)	580				800°C
A=La, B=Ni, B'=Co	11.9-14.3	1200-1500	$\leftarrow y=0.4-0.6$			1000°C
A=Sr, B=Co, B'=Sb	y=0.1	300				400°C
A_{1-x}A'_xB_{1-y}B'_yO₃ (L-La, S-Sr, C-Co, F-Fe, N-Ni, G-Gd, M-Mn, B-Ba)						
LSCF	15,3 (x=0.4, y=0.8)	875 (y=0.2)	0.18 (x=0.4, y=0.2)	3×10^{-7} (x=0.4, y=0.2)	4×10^{-5} (x=0.4, y=0.2)	900 °C
LSCN	15.6	x=0.2, y=0.2	3.16	x=0.4, y=0.2		900°C
LSCM	x=0.2, y=0.8			2×10^{-7}		900°C
LSFN	12.8	x=0.2, y=0.2				
GSCM	24	x=0.2, y=0.1				
BSCF	x=0.5, y=0.2			1.3×10^{-4} (900°C)	1×10^{-6} (500°C)	
(L _{0.75} S _{0.25}) _{0.95} Cr _{0.5} M _{0.5}				3×10^{-8}		1000°C

* TEC – thermal expansion coefficient; σ_e – the electronic conductivity; σ_i – the ionic conductivity; D_O – diffusion coefficient of the oxygen ; k –oxygen surface exchange coefficient

I.2.2 Anode materials

- Ni-cermet

As mentioned before, certain metals can be candidates as the anode materials of SOFCs for their catalytic ability. No doubts, Pt has very good performance in hydrogen catalytic field, however the high cost and volatile feature under high operating temperature are big obstacles for the application in SOFC. Ni becomes the most commonly used anode metallic material due to its low overvoltage and low price. Considering the effective combination of metal and ceramic electrolyte, the optimization of metal electrodes, cermet (e.g. Ni-YSZ) and the metal oxide has been introduced. Ni-based cermet, particularly Ni-YSZ has been applied in various ways as commercial anode materials due to its high electrical conductivity [61, 62]. However, these materials have high sulfur poisoning [63] and carbon deposition [64] problems. This phenomenon can lead to the loss of material activity, reducing the cell life.

Fig. I.16 shows the carbon deposition on Ni-YSZ anode material with the cell of different work duration [65].

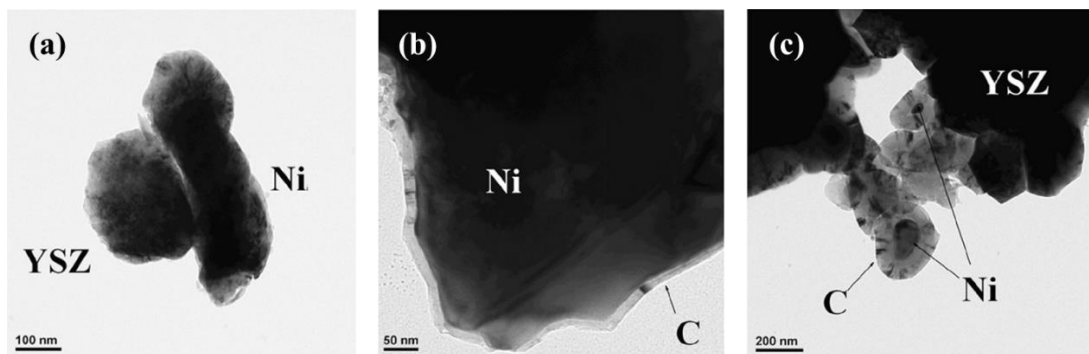


Figure I. 16. Transmission electron micrographs showing the anode (a) operated with hydrogen fuel (b) operated with syngas for 15min; (c) operated under same gas mixture for 2h (the ingredient of synthesis gas: CH₄ 23.64% ; CO 7.60% ; CO₂ 14.27% ; H₂ 49.48% ; H₂O 5.00%) [65].

- Cu-cermet

Cu cermet was found inactive to the carbon deposition in the reforming of hydrocarbon fuels, such as CH₄ and syngas [66]. However, Cu has a lower melting point (1083°C) relative to that of Ni (1453°C), therefore, sintering at elevated temperatures is impractical. Beside them, Lu et al [67]. studied that Cu does not give any catalytic activity for cracking hydrocarbons in the anode, however, it acts only as electronic conductors to the anode. Thus, some high catalytic activation of metals are used in Cu-based anode to improve the performance.

- Ceria

Cerium oxide and its compounds are introduced as anode materials due to their high electron-ionic conductivity in reducing atmosphere. Its ionic conductivity can be controlled by adding acceptor dopant oxides such as CaO, Y₂O₃, GdO₃ and Sm₂O₃. In addition, it acts as a catalyst for the direct oxidation of hydrocarbon-containing fuels. Further, it also has a good compatibility with the component materials of adjacent cells. M-CeO₂ or M-CeO₂-Y₂O₃ are very common forms of anode materials [68-72].

- perovskite structure, double-perovskite

In a quest to develop sulfur tolerant materials of anode, other than Ni-based structures, nickel free conductive metal oxide based perovskites were proposed.[73] The common chemical formula for these materials is ABO₃ (A = La, Sr, Ce, Mg and B = Ti, V, Mn, Mo, Nb high valence elements). The conductivity of SrTiO₃ has been found to increase to 100 S/cm (at 800 °C) when the lanthanides and yttrium replaces strontium [74, 75]. Nb doping in the Ti site has also been reported to increase the conductivity of 120 S/cm [76]. These materials have good chemical stability, thus many doping elements are employed to improve the conductivity.

- pyrochlores

Pyrochlores are $A_2B_2O_7$ type oxides usually with A^{III}/B^{IV} and A^{II}/B^V , which displays diverse electrical, magnetic, dielectric and catalytic properties [77-79]. The different composition of A and B results in a lack of oxygen or excess stoichiometric. Fig. I.17 shows the three views of the typical structure of pyrochlore $A_2B_2O_6O'$ [80]. The crystal structure of these compounds can accommodate high oxygen content and allow flexible combinations of cations on the two sites A and B. This allows to make changes in the combination of cations A and B to adapt the stability and electrical properties from the structure, especially the stability at high temperatures to satisfy the practical requirements of SOFC.

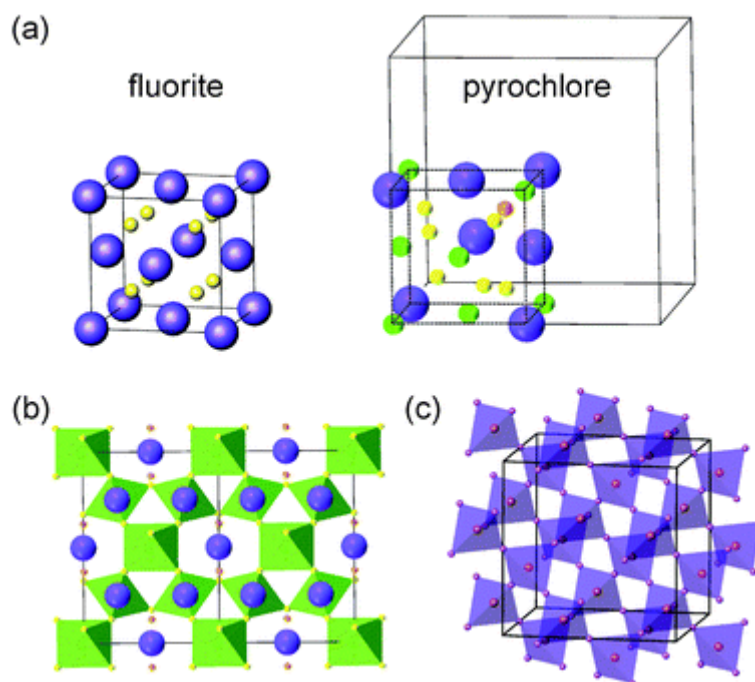


Figure I. 17. the three views of the pyrochlore structure $A_2B_2O_6O'$ (a) showing the relation between the structures of fluorite and pyrochlore in where an octant of the cell of the pyrochlore unit is represented by the large cube, (b) octahedral connectivity $\langle BO_6 \rangle$ units with A sites and O' anions as "extra-framework ions," (c) the A sublattice as a network of corner-shared O' -centered tetrahedra, with B and O atoms omitted. A - purple, B - green, O - yellow and O' - orange [80]

Pyrochlores $(Ln_{0.9}Ca_{0.1})_2Ti_2O_7$ ($Ln = Gd, Y$ and Yb) are reported to exhibit good ionic conductivity at high temperatures [81, 82]. Under reductive condition, $Gd_2(Ti_{1-x}Mo_x)_2O_7$ ($0.1 \leq x \leq 0.7$) with Mo (+IV) exhibits high electronic conductivity (> 10 S/cm) [83].

I.2.3 Interconnect materials

The interconnect corresponds to a metal or ceramic layer which is used to assemble the cell units in series or in parallel and finally to constitute the stack. It must separate the fuel gas from the oxygen. Interconnect materials must be stable under reduction and oxidization atmospheres, and must possess a predominant electrical conductivity. Figure I. 18 shows the position of interconnect in a fuel cell.

- Ceramic interconnect materials

The most commonly used ceramics as interconnects are lanthanum chromite (LaCrO_3) based materials which are among most stable perovskite-type oxides [84, 85]. LaCrO_3 has high electrical conductivity ($\sim 1 \text{ S/cm}$ à 1000°C) compared to other ceramics, high melting point (2510°C), low CTE disagreement with YSZ ($\text{CTE}_{\text{LaCrO}_3} \sim 9,5 \times 10^{-6}/\text{K}$ et $\text{CTE}_{\text{YSZ}} \sim 10,5 \times 10^{-6}/\text{K}$) [86] and relatively good compatibility with the other components of the cell, making it be a suitable interconnect. One or some elements of Ca, Mg, V, Co et al are selected to be doped in the material to improve its performance.

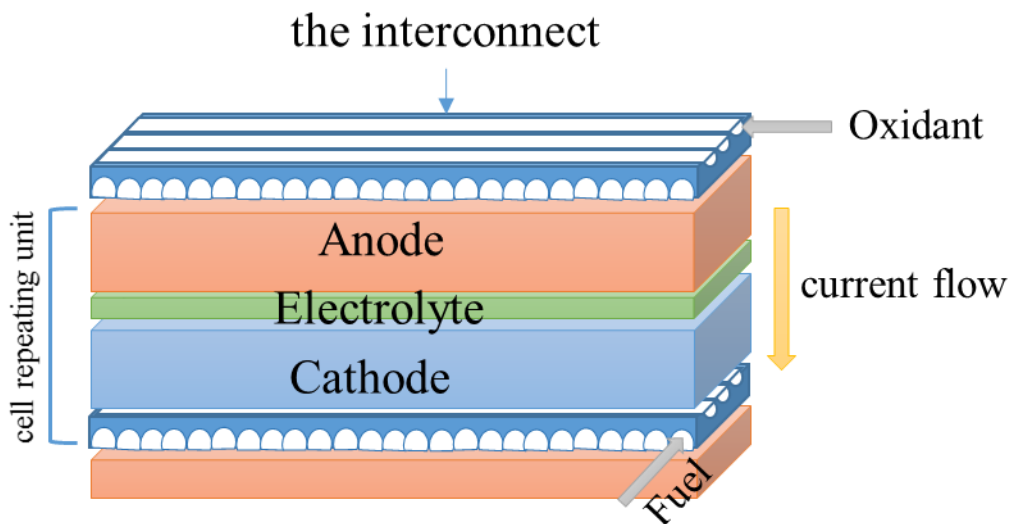


Figure I. 18. Schematic diagram of the components of a planar cell to show the interconnect

- Metal alloys for interconnect materials

Low cost, availability and easy manufacture make metal alloys more attractive than ceramics as interconnect materials. In this category, Ni, Cr and Fe-based oxidation-resistant alloys and precious metals such as Ag were used as interconnection material. Among the metallic alloys, the Fe-Cr alloys, Cr-based alloys, the Ni - Cr (Fe) based heat-resistant alloys, austenitic and ferritic stainless steels are widely used as materials for interconnect (as shown in Fig. I.19) [87].

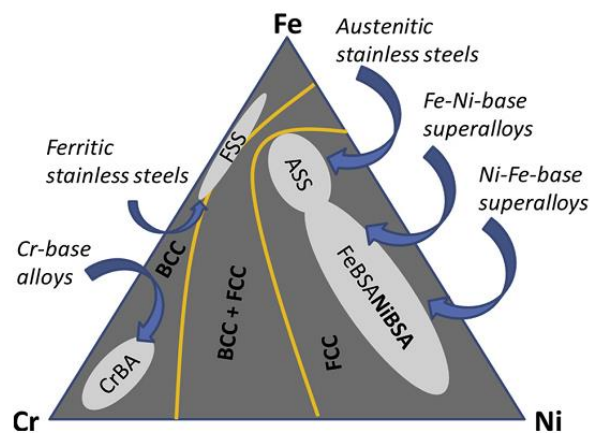


Figure I. 19. Schematic showing selection of phases in Fe–Co–Ni based alloys as metallic interconnect materials [87]

I.2.4 Materials for electrolytes

To achieve high ion conductivity of the electrolyte materials, their crystal structure must have a large open space or defects that allows high level of point defect disorder, and low migration enthalpy $\leq 1\text{eV}$ [88]. In these compounds, the metal cations have a certain level of vibration around their site due to their sizes are much smaller than of the oxide ion, as well as the metal cations also possess high valence charge, which does not allow the free movement within the network. This phenomenon leads to local defect to allow the ions crossing the structure.

- Fluorite structure oxides

Fluorite structure oxides belong to face centered of cubic lattice system. Figure I.20 exhibits a typical fluorite structure of ceria as an example. Generally, the fluorite structure has a common formula MO_2 , where M is high valence metal elements, for example CeO_2 , ZrO_2 , HfO_2 , and ThO_2 . There are still some special formulas, such as M_2O_3 , which possess two oxygen defects in a single cell of fluorite structure. Among these oxides, only ZrO_2 , CeO_2 and Bi_2O_3 have been of interest to researchers as an electrolyte material in SOFC.

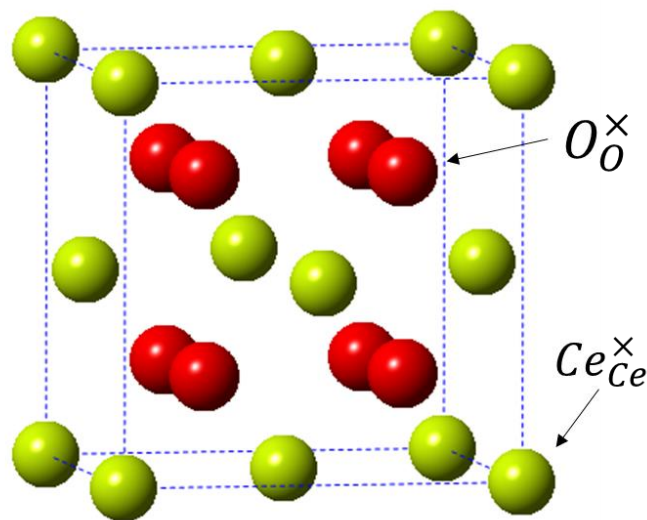


Figure I. 20. Cubic fluorite structure of ceria

To obtain sufficient amount of oxygen vacancies for exhibiting appreciable ionic conductivity, oxygen vacancies are introduced into the structure via substitution of host M^{4+} by low valence acceptor cations, such as, Gd^{3+} , Sm^{3+} , or Y^{3+} . This can be represented by defect equation using Kröger Vink notation shown below.



It is experimentally observed that the ionic conductivity reaches a maximum at dopant concentration of about 10–20 mol% depending on the type of dopant. Based on this

phenomenon, some composite oxides have been investigated as promising candidates of electrolyte.

As mentioned, Y_2O_3 stabilized ZrO_2 (YSZ) materials are typical commercial electrolytes owing to their high oxide ion conductivity. Among them, 8mol% Y_2O_3 - ZrO_2 (8YSZ) is reported to have highest ionic conductivity of 0.1S/cm at 1000°C [17]. Besides Y_2O_3 , the Sc_2O_3 also has been adopted as dopant in ZrO_2 (ScSZ), and 11ScSZ is reported to exhibit quite high ionic conductivity, close to 1.5 S/cm at 850°C [89]. It can be used in intermediate temperature SOFC as well as considering its wide range of oxygen partial pressures and good thermochemical properties. However, some obstacles should be addressed before commercial application, for example, phase transitions with the working temperature changes and high market price.

- δ - Bi_2O_3 based ceramics

In fact, Bi_2O_3 structure is attributed to fluorite category, while it has particular defects differing from common MO_2 fluorite structure. This results in its high ionic conductivity, as well as good electro catalytic activity for O_2 conversion at low temperature [90, 91]. Bi_2O_3 has four different polymorphs, denoted as monoclinic α , tetragonal β , body-centered cubic γ , and face-centered cubic δ . where the high conductivity is shown by δ -phase, whose structure is presented in Figure I.21.

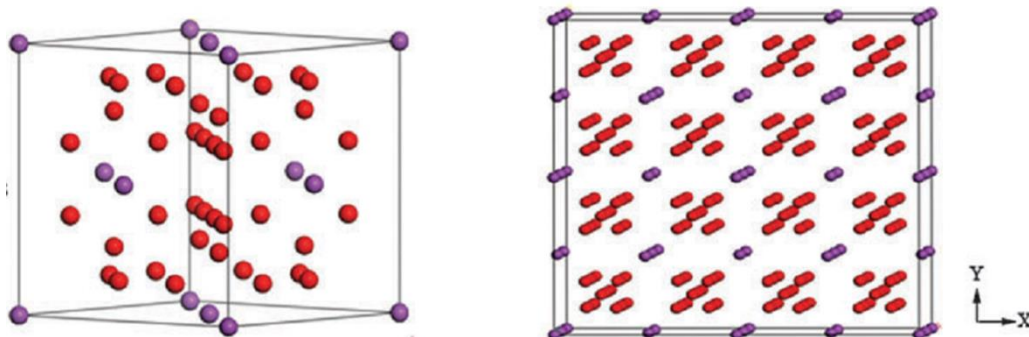


Figure I. 21. Schematic of the δ - Bi_2O_3 polymorph crystal structures

Although no elements doping δ -Bi₂O₃ shows high conductivity, it requires addition of certain dopant cations, .e., Y³⁺, La³⁺, Er³⁺, etc. to be stabilized at room temperature. They have been investigated by various researchers [92-95]. For example, Er- and Y-doped Bi₂O₃, namely, Bi_{1-x}Er_xO_{1.5} (x~0.20) and Bi_{1-x}Y_xO_{1.5}(x = 0.23–0.25) exhibit high ionic conductivity of $\sim 3.7 \times 10^{-1}$ S/cm and $\sim 2.3 \times 10^{-2}$ S/cm at 700 °C and 500 °C, respectively [96, 97].

Other Bi oxide based electrolyte materials BiMeVO_x, obtained by partial substitution of V in γ -Bi₄V₂O₁₁ by additive metal (Me = Co, Cu, Ta), exhibit high ionic conductivity.[98, 99] The conductivity of BiCuVO_x which corresponds to the partial substitution of V in Bi₄V₂O₁₁ by 10% of Cu is reported of two orders of magnitude higher than YSZ at 400°C. Unfortunately, at high temperature, bismuth oxide is easily reduced into bismuth metal which is liquid at 271 °C.[100, 101]

- Pyrochlores based ceramics

Pyrochlore structure with a general formula of A(III)₂B(IV)₂O₇ structure have been actively investigated for ionic conduction for long time. Pyrochlore is a superstructure of fluorite structure (MO₂) where A- and B-site cations are ordered and one eighth of the anions are missing (to form vacant sites as show in figure I.22 [102], the letter for showing position is called Wyckoff letter). It is reported that on reducing the size of A-site cations, pyrochlore to fluorite transition is favored (at elevated temperatures up to 1370–2227 °C). On reducing the size of the cation, a structural transformation is induced from a fully ordered pyrochlore lattice A₂B₂O₇ to a completely disordered anion deficient defective fluorite M₄O₇ (where M can be A or B).

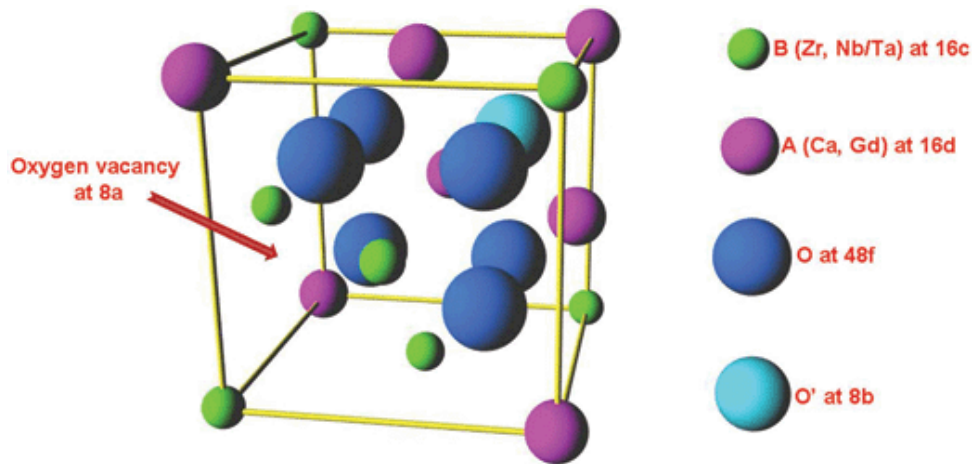


Figure I. 22. Structures of pyrochlore - One eighth of the unit cell of the ordered pyrochlore structure showing specific positions of the cations and anions (B^{4+} cation at the origin). [102]

The ionic conductivity of pyrochlore based oxides (e.g., $Gd_2Zr_2O_7 \sim 5 \times 10^{-2}$ S/cm) exhibits considerable performance, and the ionic conduction in these materials can be tailored either by chemical substitution [82]. Among various pyrochlore compositions, $Gd_{1.8}Ca_2Ti_2O_{7-\delta}$ ($x = 0.20$) is reported to exhibit the highest conductivity [81]. The substitution increases the p-type conductivity and lowers the n-type electronic conductivity of the material.

- Perovskite-based ceramics

As a typical perovskite ceramic, $LaGaO_3$ was investigated as ionic conductors by various groups [26, 103]. The migrating ion is expected to migrate through the center of triangle formed by two La^{3+} A-site cations and one Ga^{3+} B-site cation. The ionic radii ratio of the A- and B-site cations becomes an important factor, which significantly influences the ionic conductivity in the perovskite material. The ionic conductivity can be enhanced by either decreasing the size of A-site cation (minimum 0.95 Å) or increasing the size of B-site cation [104].

Addition of acceptor dopant cation to $LaGaO_3$ oxides, such as, Sr^{2+} , Ca^{2+} , Mg^{2+} or Ba^{2+} at La^{3+} or Ga^{3+} sites have been reported to enhance the catalytic activity and ionic conductivity. [2, 105, 106] These dopant cations create oxygen vacancies as a compensating defect, which, in turn,

increase the ionic conductivity. Typically, with Sr^{2+} , Mg^{2+} at La^{3+} , Ga^{3+} sites respectively, $\text{La}_{1-x}\text{Sr}_x\text{Ga}_{1-y}\text{Mg}_y\text{O}_{3-\delta}$ (LSGM) series have maximum ionic transport with x and y lying in the range of 0.10–0.20 and 0.15–0.20.[107]

Some trivalent elements (such as Al^{3+} , In^{3+} , Sc^{3+} and Y^{3+}) have also been used to occupy at B sites of LnBO_3 . These materials offer good mechanical compatibility during fabrication and good stability to reduction and volatilization. However, they possess relatively low ionic conductivity and high p-type electronic conduction in oxidizing atmosphere. Doping Sr^{2+} at A-site is a common way to enhance the conductivity and lower vacancy-association. $\text{La}_{0.9}\text{Sr}_{0.1}\text{AlO}_3$ has been reported has the maximum conductivity value, being close to 100 mS/cm at 1000°C [108].

- Brownmillerite – type ceramics

Oxides having a brownmillerite structure (with the chemical formula of $\text{A}_2\text{B}_2\text{O}_5$) consists of alternating layers of perovskite sharing corner with BO_6 octahedra and BO_4 tetrahedra, as shown in figure I.23.[109, 110] These materials are considered as oxygen deficient perovskites, thus oxygen vacancies are observed to order along (0 1 0) direction which can be good candidate as ionic transport channel. As the most common material of this series, $\text{Ba}_2\text{In}_2\text{O}_5$ exhibits high ionic conductivity in dry air, as well as the electronic conductivity existing [111, 112]. The disordered cubic perovskite phase can be stabilized by substituting In-sites with higher-valance cations, e.g., Zr^{4+} , Ce^{4+} , Sn^{4+} or Hf^{4+} that can enhance intermediate temperature ionic conduction [113]. La^{3+} , Sr^{2+} are also used to dope in Ba sites to modify the conductivity performance [114]. At 800°C, the maximum conductivity of ~ 0.12 S/cm is reported in $(\text{Ba}_{0.3}\text{Sr}_{0.2}\text{La}_{0.5})_2\text{In}_2\text{O}_{5.5}$ composition, which exceeds that of Y_2O_3 stabilized ZrO_2 .

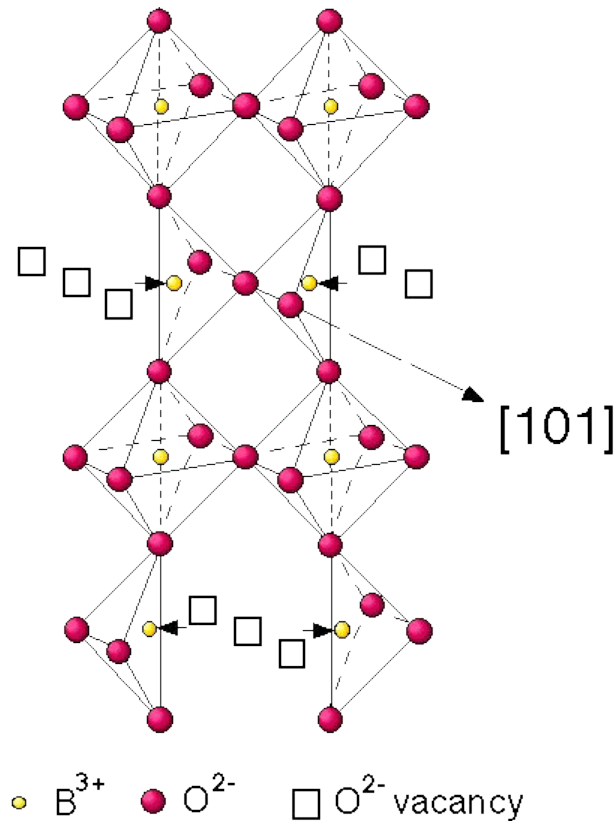


Figure I. 23. Arrangement of B-O octahedra and tetrahedra in the ideal brownmillerite structure, $A_2B_2O_5$ (A cations removed for clarity)

- $\text{La}_2\text{Mo}_2\text{O}_9$ (LAMO_X) based electrolyte materials

The oxide ion conductivity in LAMO_X was found to be $\sim 6 \times 10^{-2}$ S/cm, firstly reported by Lacorre et al. in year 2000 [115]. Doping with W to form $\text{La}_2\text{Mo}_{2-x}\text{W}_x\text{O}_9$ solid solutions (with $x \leq 1.6$) were reported to exhibit ionic conductivity of ~ 0.11 S $\cdot\text{cm}^{-1}$ ($x = 0$) to 0.05 S $\cdot\text{cm}^{-1}$ ($x = 1.5$) at 750 °C [116].

- Apatite structure

Apatite based materials have a general formula of $A_{10}(\text{MO}_4)_6\text{X}_{2\pm\delta}$ (where A is a rare earth or alkaline earth cation or Pb, M is a p-block element, such as, Si, Ge, P or V and X is OH⁻, O²⁻ or halides). The structure comprises of isolated MO_4 tetrahedra arranged in a way to form distinct anion and La channels running parallel to the c-axis. The oxide ion channels being in central

position participate in ionic conductivity [117]. This series of materials will be presented in details in section I.4.

I.3 Encountered difficulties of operating temperature

Comparing with some other electrolytes using for PAFC (Phosphoric Acid Fuel Cell), PEMFC (Proton Exchange Membrane Fuel Cell) and MCFC (Molten Carbonate Fuel Cell) etc., solid state electrolyte has lower ionic conductivity. In order to achieve a considerable conductivity, SOFC inevitably should work at high operating temperature.

Too high operating temperature leads some disadvantages in application:

- extended startup time;
- high thermal stress;
- weak components compatibility and the ageing of constituent components;
- the difficult choice of the matched interconnectors or electrodes
- high maintenance cost.

This will lead to the usage restriction in various fields, e.g., military and transportation, and also limit the application of some good performance materials as components in SOFC. Thus, more attention is paid to intermediate operating temperature (IT-SOFC), which results in many benefits: reducing manufacture costs and increase the selection range of materials. Meanwhile, the operation of FCs becomes environment-friendly, as well as decreasing the implementation difficulties of sealing technology.

The realization of IT-SOFC heavily depends on the development of electrolyte materials. The oxide ionic conductivity of traditional electrolyte materials decreases rapidly by reducing the operation temperature.

Recently, some new solid electrolyte materials have been developed to overcome these problems. These materials have common feature: high ionic conductivity and intermediate operating temperature. Among these materials, apatite rare-earth silicates, with a common formula $RE_{10}Si_6O_{27}$ ($RE=La, Pr, Nd, Sm, Gd, Dy$), have been considered as a promising solid electrolyte for IT-SOFC since they were firstly reported to have higher conductivity than YSZ below $600^\circ C$ by S. Nakayama et al [118, 119].

I.4 Apatite-type phase lanthanum silicate electrolyte

I.4.1 Structure

The lanthanum silicates using as electrolyte of IT-SOFC are apatite-type phase which has a general formula $(A^{2+})_{10}(MO_4^{3-})_6(X^{1-})_2$, belonging to $P6_3/m$ space group of hexagonal crystal system. The symmetry sites and atoms positions in a single cell are shown in Table I.4.

Table I. 4. Wyckoff Positions and symmetry sites of Group 176 ($P6_3/m$) (quote from the Bilbao Crystallographic Server)

sites	Multiplicity and Wyckoff letter	Site symmetry	Coordinates
A2	4f	3..	$(1/3, 2/3, z)$ $(2/3, 1/3, z+1/2)$ $(2/3, 1/3, -z)$ $(1/3, 2/3, -z+1/2)$
A1			
M	6h	m..	$(x, y, 1/4)$ $(-y, x-y, 1/4)$ $(-x+y, -x, 1/4)$ $(-x, -y, 3/4)$
O1			$(y, -x+y, 3/4)$ $(x-y, x, 3/4)$
O2			
O3	12i	1	(x, y, z) $(-y, x-y, z)$ $(-x+y, -x, z)$ $(-x, -y, z+1/2)$ $(y, -x+y, z+1/2)$ $(x-y, x, z+1/2)$ $(-x, -y, -z)$ $(y, -x+y, -z)$ $(x-y, x, -z)$ $(x, y, -z+1/2)$ $(-y, x-y, -z+1/2)$ $(-x+y, -x, -z+1/2)$
X	2a	-6..	$(0, 0, 1/4)$ $(0, 0, 3/4)$

Figure I.24 shows a schema of apatite structure: it consists of tetrahedron MO_4 , cation A and anion X. The M ions are in the center of MO_4 tetrahedron colored in green in the figure.

There are two types of parallel tunnels along the c axis [120]:

-the first one is occupied by A1 cations.

-the second one which has larger diameters than the previous ones, contain the six A2 cations and X anion. It can be the major channel for this ionic conductor.

In the case of using apatite as the solid electrolyte for IT-SOFC, the anion X^- will be substituted by O^{2-} ion in order to raise the electrical conductivity, the element A^{2+} is rare earth or alkali metal element and M represents P block element (P, Si or Ge).

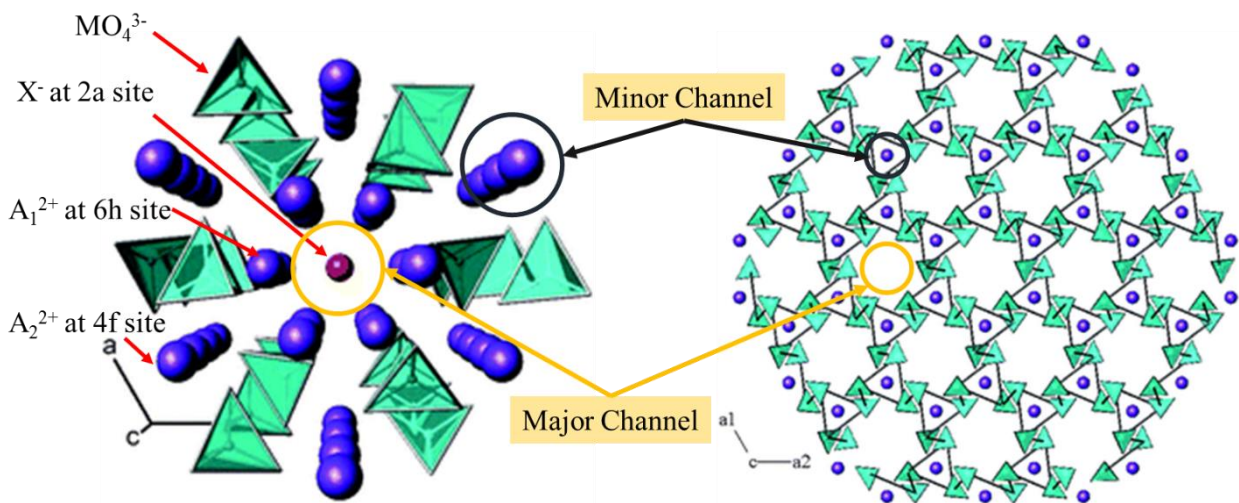


Figure I. 24. The apatite structure, $A_{10}(MO_4)_6X_{2\pm y}$, and alternative representation of the apatite structure: illustration of the “microporous” $A_4(MO_4)_6$ framework: The cavities are where the remaining $A_6X_{2\pm y}$ units would occupy. [117]

The solid electrolyte material has a common formula $La_{10}Si_6O_{27}$, Figure I.25 gives the schema of LSO apatite structure and the oxygen migration channel. As it can be seen, there is a large number of atoms in each single cell of the apatite structure. Lanthanum (La) occupies two different sites: La1-6h site (near the migration channel) and La2-4f site (far from the migration channel). Silicon (Si) located at 6h site around by four oxygen atoms (6h, 12i), forming a tetrahedron structure SiO_4 . The 2a site oxygen (O) atoms lie at the oxygen channel.

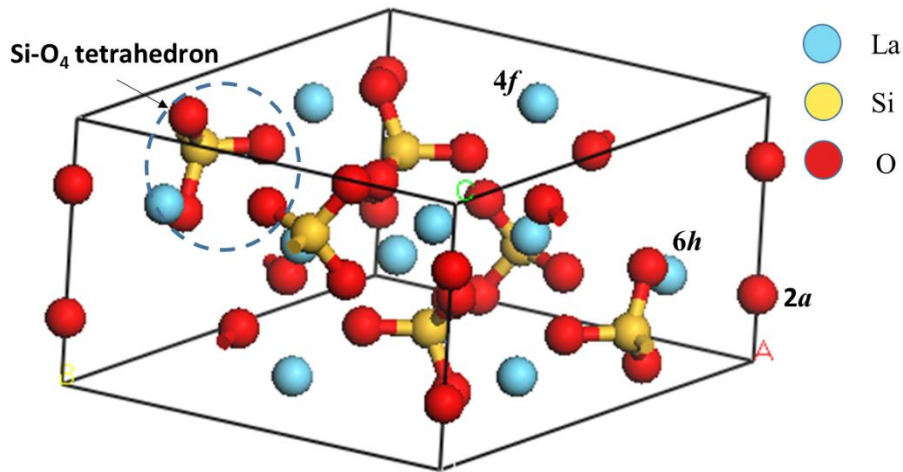


Figure I. 25. Schematic diagram of lanthanum-silicon apatite structure

The composition in actual material has an alternative formula $\text{La}_{9.33}(\text{SiO}_4)_6\text{O}_2$, which has the same structure as described in the preceding paragraph. This is due to the cation valence change causing by ions substitution. To keep the balance valence, the substitution, $\text{A}^{2+} \rightarrow \text{La}^{3+}$ and $\text{XO}_4^{3-} \rightarrow \text{SiO}_4^{4-}$, leads to a 0.67 vacancy at A site.

Table I.5 gives the atoms coordinates of this structure [121]. The single cell is built by some symmetry operations of these initial coordinates.

Table I. 5. The atoms coordinate of lanthanum-silicon apatite structure

Coordinate	La1-6h	La2-4f	Si-6h	O1-6h	O2-6h	O3-12i	O4-2a
x	0.2289	0.3333	0.4020	0.3224	0.5965	0.3443	0
y	-0.0125	0.6667	0.3718	0.4847	0.4731	0.2549	0
z	0.2500	-0.0007	0.2500	0.2500	0.2500	0.0701	0.2500

I.4.2 Electrical properties

$\text{Ln}_{9.33+x}(\text{SiO}_4)_6\text{O}_{2+3x/2}$ ($\text{Ln} = \text{La}, \text{Pr}$ and Nd) shows the high oxide ion conductivities by the initial work of Nakayama et al.[118, 119, 122] The conductivities were shown to be enhanced in

samples containing oxygen excess ($x > 0$), (*e.g.* $\sigma(500\text{ }^\circ\text{C}) = 1.1 \times 10^{-4} \text{ Scm}^{-1}$ for $\text{La}_{9.33}(\text{SiO}_4)_6\text{O}_2$, vs $1.3 \times 10^{-3} \text{ Scm}^{-1}$ for $\text{La}_{9.67}(\text{SiO}_4)_6\text{O}_{2.5}$). [123] These initial results suggested that interstitial oxide-ions were important in promoting high oxide-ion conductivity in these apatite systems.

Typically non-stoichiometry ranges of $0 \leq x \leq 0.34$ are possible for the larger rare earth elements before impurities such as Ln_2SiO_5 appear. For the smaller rare earths, *e.g.* Gd, lower non-stoichiometry ranges are observed, which suggests that less space is available to accommodate the extra interstitial oxide-ions as the unit cell size is reduced. In addition a general decrease in conductivity and increase in activation energy is observed as the size of the rare earth is reduced.[117]

Table I.6 shows different conductivities at 500°C of lanthanum silicates containing various oxygen excess [124]. To some extent, oxygen excess visibly affects the ionic conductivity. However, the synthesis process has an influential function to accurate the formula of the products. Anyway, this series materials have much higher ionic conductivities than commercial electrolyte material YSZ at intermediate temperature.

Table I. 6. The undoped ionic conductivities of lanthanum silicates reported in literature

Formula	$\text{La}_{10}(\text{SiO}_4)_6\text{O}_3$	$\text{La}_{9.67}(\text{SiO}_4)_6\text{O}_{2.5}$	$\text{La}_{9.60}(\text{SiO}_4)_6\text{O}_{2.4}$	$\text{La}_{9.56}(\text{SiO}_4)_6\text{O}_{2.34}$	$\text{La}_{9.33}(\text{SiO}_4)_6\text{O}_2$
Conductivity	$1.8 \times 10^{-4} \text{ S/cm}$	$1.3 \times 10^{-3} \text{ S/cm}$	$6 \times 10^{-4} \text{ S/cm}$	$1.4 \times 10^{-3} \text{ S/cm}$	$1.5 \times 10^{-4} \text{ S/cm}$

Figure I.26 gives the ionic conductivity comparison of some selected typical electrolyte materials at intermediate temperature. Lanthanum silicates apatites lie in the middle of the chart which means their ionic conductivity is placed in the middle among all the candidates (higher than YSZ). Remarkably, non-toxic, low-cost features make them a research focus. Moreover, the conductivity performance can be enhanced by a wide range of doping studies.

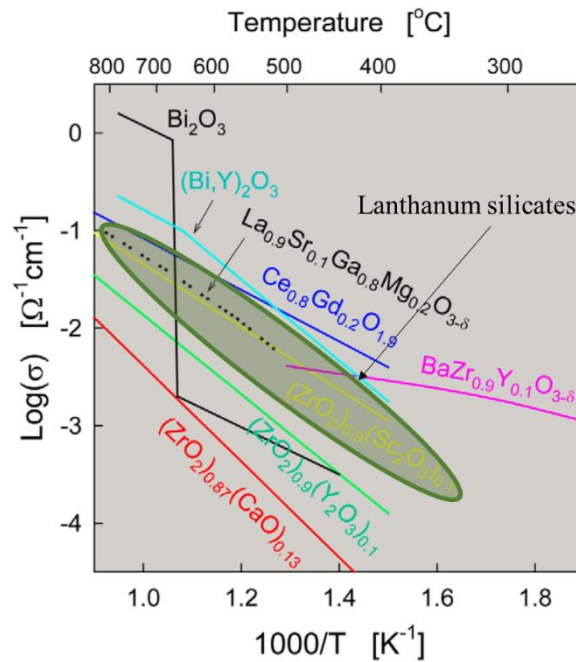


Figure I. 26. Conductivities of selected electrolyte materials at intermediate temperature (LSO series lies at shaded part, original figure from ref [125])

I.4.3 Conduction pathway

The first work with modeling methods of interstitial site and conduction pathway of this material has been investigated by *M. S. Islam* et al [117, 126, 127]. By their discussion, the interstitial oxide-ions, which lie upon the ions migration channel, are important to affect the conductivity. These interstitial ions are not located down the center of the oxide ion channels due to the high anisotropic thermal displacement parameter. Figure I.27 gives the principal result of atomistic modeling studies on two systems: $\text{La}_{9.33}(\text{SiO}_4)_6\text{O}_2$ and $\text{La}_8\text{Sr}_2(\text{SiO}_4)_6\text{O}_2$. The brown site in the figure is the location of a new energetically favorable oxygen interstitial site: it is accommodated at the channel periphery, rather than the channel center.

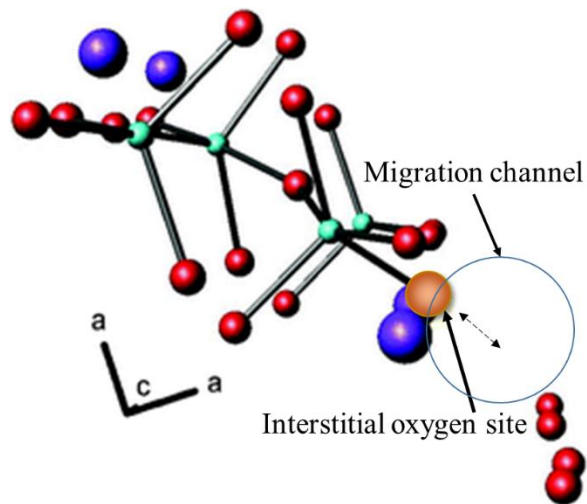


Figure I. 27. The interstitial oxygen site (brown sphere) at the periphery of the channels, and associated lattice relaxation (blue spheres = La, green spheres = Si)

Additional support for this interstitial oxide-ion site has come from ^{29}Si NMR and Raman spectra studies by *A. Orera* et al. [128, 129] shown in figure I.28. These studies have shown a correlation between the ^{29}Si NMR spectra and the conductivity, with poorly conducting samples demonstrating a single NMR resonance, whereas in fast ion conducting compositions, an extra peak was apparent, attributed to a silicate group adjacent to an interstitial oxygen site. For the Raman results of the samples containing oxygen excess, the fitting clearly needs the incorporation of a new band at 360 cm^{-1} . This is contributed to the interstitial oxygen.

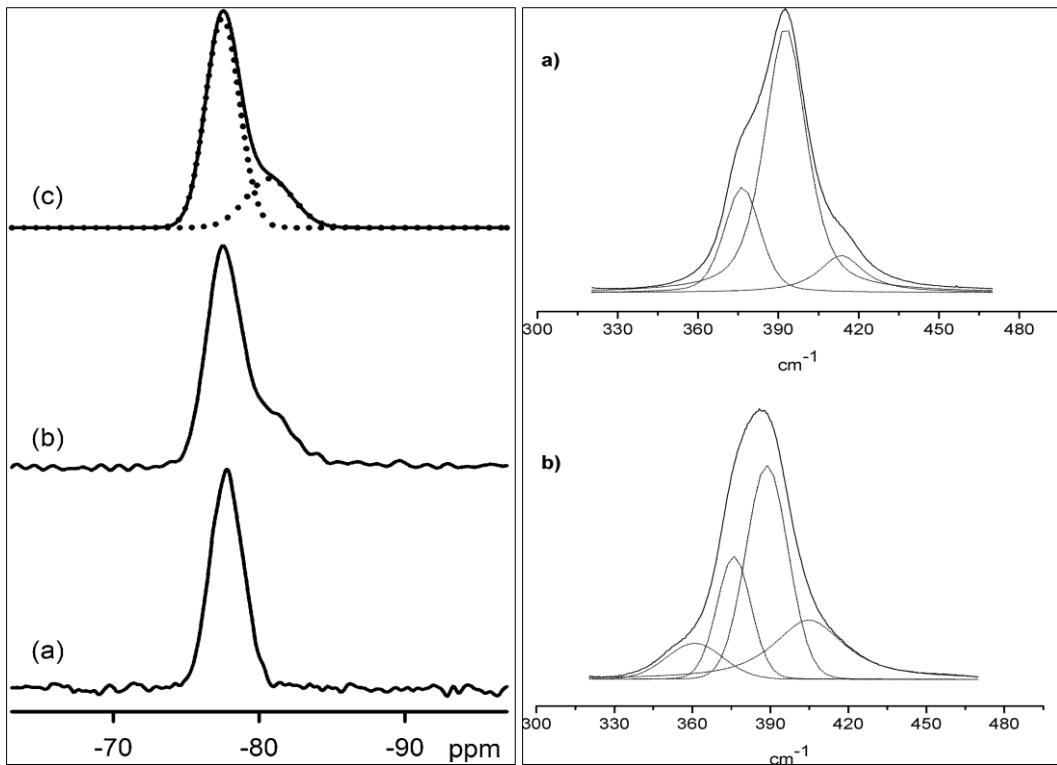


Figure I. 28. ^{29}Si NMR spectra (left) and Raman spectra results (right) for (a) $\text{La}_8\text{Sr}_2(\text{SiO}_4)_6\text{O}_2$, (b) $\text{La}_9\text{Sr}(\text{SiO}_4)_6\text{O}_{2.5}$, (c) deconvolution of the latter. [128, 129]

Considering the flexibility of the oxygen interstitial site, the interstitial conduction pathway is predicted in two process: a direct process (vacancy mechanism) and a complex sinusoidal process (interstitial mechanism) by atomistic simulation, as shown in figure I.29.

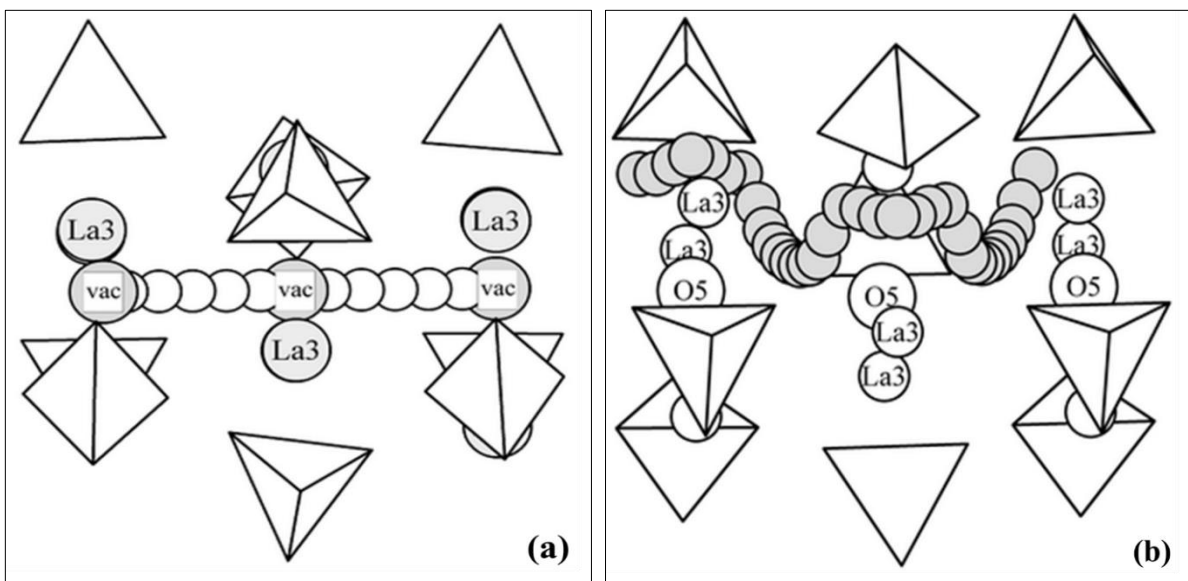


Figure I. 29. O5 oxygen vacancy migration along the O5 oxide channel (a), and interstitial oxygen migration viewed perpendicular to the O5 channel, showing a non-linear (sinusoidal-like) pathway (b), suggested for $\text{La}_8\text{Sr}_2(\text{SiO}_4)_6\text{O}_2$ and $\text{La}_{9.33}(\text{SiO}_4)_6\text{O}_2$ respectively

Based on the preliminaries, no doubt the major migration channel is located along c-axis. The experimental studies on detailed conductivity of single crystal have shown that the conductivity is anisotropic, with the conductivity parallel to c (the direction of the oxygen channels) significantly higher than that perpendicular (e.g. $\text{Nd}_{9.33}(\text{SiO}_4)_6\text{O}_2$, $\sigma_c = 6.4 \times 10^{-3} \text{ S cm}^{-1}$, $\sigma_{ab} = 1.3 \times 10^{-3} \text{ S cm}^{-1}$ at 500 °C, both activation energies are fairly similar around 0.6 eV) [130]. The results suggest that although the main conduction pathway is down the oxide-ion channels, there is also significant conduction perpendicular to the channels (i.e. inter-channel conduction).

Figure I.30 exhibits one possible explanation for inter-channel conduction [117, 131]. This shows that the local relaxation around the interstitial site leads to reduction in the distance to a neighboring SiO_4 unit. This could effectively create a pathway, whereby an interstitial oxide-ion is moved between adjacent channels by a series of two cooperative “ $\text{S}_{\text{N}}2$ ”-type processes ($\text{S}_{\text{N}}2$ = bimolecular nucleophilic substitution), with accompanying rotation of the tetrahedral.

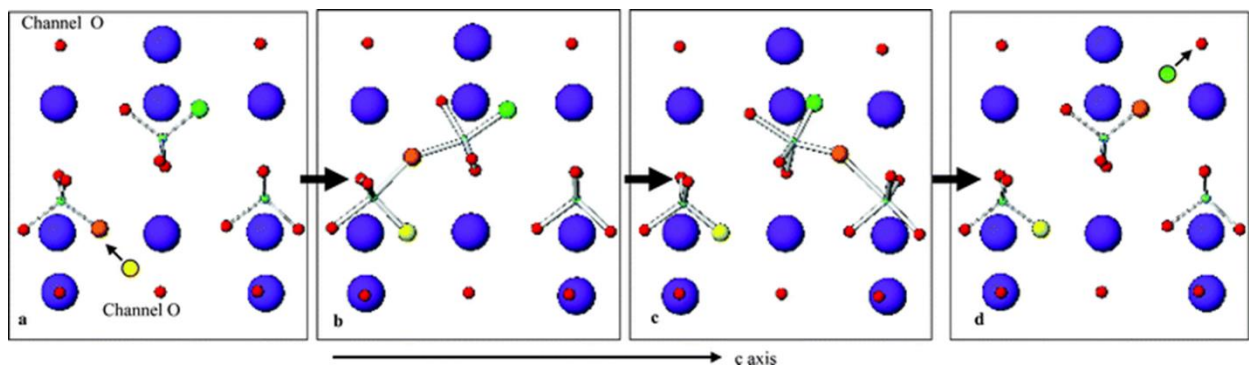


Figure I. 30. Proposed conduction pathway between adjacent oxide-ion channels via two “ $\text{S}_{\text{N}}2$ ”-type processes, with accompanying rotation of the silicate tetrahedra, obtained from computer simulation results of $\text{La}_{9.33}(\text{SiO}_4)_6\text{O}_2$. The incorporation of a periphery interstitial oxide-ion (yellow) (a) forces a silicate oxygen (orange) in between the two SiO_4 units forming an Si_2O_9 unit (b), the top silicate unit rotates to form an Si_2O_9 unit with a neighboring silicate unit (c), and an oxygen on the top silicate unit (green) is released as an interstitial in a different channel (d). [117, 131]

I.4.4 Influence of doping and substitution

Multiple metal elements can be good candidate to dope in the compounds LSO (ex. Mg, Ca, Sr, Co, Cu, Al, Zn, Mg, Ti, Ge, Fe ...) because they demonstrate the possibility to improve the properties of electrical conductivity. The dopants may in fact modify the electrical properties by changing the quantity of the charge carriers O^{2-} , tunnels size or some other factors.

There are three types of doping possibility according to the doping sites:

- La Site: Ca, Sr, Ba, Bi.
- Si Site: B, Al, Ga, Zn, Ti, Ge, Fe, P.
- La and Si sites: Mg, Mn, Ni, Cu, Co.

Table I.7 shows some comparison of electric properties of doped LSO [117, 123]. Apatites LSO, in which we substitute some dopant of Si^{4+} cations, have higher ionic conductivity and lower energy activation. These results are also depended on the purity of the phase by the synthesis process.

This doping influence has been reviewed by Emma Kendrick et al., as shown in Figure I.31. [117] They compare the influence in compounds with different interstitial oxygen ions. Elements doping in both cases have positive and negative effects.

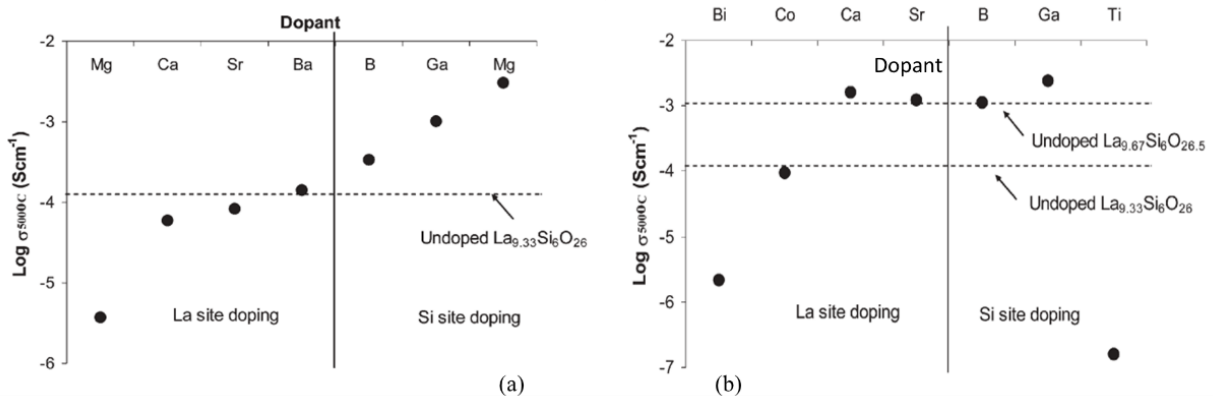


Figure I. 31. Comparison of the conductivities (500 °C) of oxygen stoichiometric samples with the same level of cation vacancies (a) and same level of oxygen excess – $O_{2.5}$ (b) [117]

Table I. 7. The apatite type LSO electrical properties doped by various elements

Doping site	formulas	Activation energy	Ionic conductivity (500 °C)
La site	$\text{La}_{8.67}\text{Ba}(\text{SiO}_4)_6\text{O}_2$	0.67	1.1×10^{-4}
	$\text{La}_{8.67}\text{Sr}(\text{SiO}_4)_6\text{O}_2$	0.87	8.3×10^{-5}
	$\text{La}_{8.67}\text{Mg}(\text{SiO}_4)_6\text{O}_2$	1.13	3.6×10^{-6}
	$\text{La}_{8.33}\text{Mg}_{1.5}(\text{SiO}_4)_6\text{O}_2$	1.23	1.2×10^{-6}
	$\text{La}_{8.67}\text{Ca}(\text{SiO}_4)_6\text{O}_2$	0.86	5.8×10^{-5}
	$\text{La}_9\text{Mg}_{0.5}\text{Si}_6\text{O}_{26}$	0.98	2.1×10^{-5}
Si site	$\text{La}_{8.67}\text{Ga}_{0.5}\text{Si}_{5.5}\text{O}_{26}$	0.67	4.6×10^{-4}
	$\text{La}_{10}\text{GaSi}_5\text{O}_{26}$	0.70	2.4×10^{-3}
	$\text{La}_{10}\text{BSi}_5\text{O}_{26.5}$	0.68	1.1×10^{-3}
	$\text{La}_{9.67}\text{Si}_{5.5}\text{Mg}_{0.5}\text{O}_{26}$	0.67	3.0×10^{-3}
	$\text{La}_{9.60}(\text{GeO}_4)_6\text{O}_{2.4}$	1.03	$2.0 \times 10^{-3*}$
	$\text{La}_{9.55}(\text{GeO}_4)_6\text{O}_{2.32}$	0.99	$1.6 \times 10^{-3*}$
	$\text{La}_{9.33}(\text{GeO}_4)_6\text{O}_2$	/	$2.9 \times 10^{-3*}$
La and Si site	$\text{La}_{9.33}\text{Mg}_{0.5}\text{Si}_{5.5}\text{Mg}_{0.5}\text{O}_{26}$	0.80	1.0×10^{-4}

*measured at 600 °C, ref [132]

I.5 Summary

In this chapter, a brief review from the principles to the materials of SOFC, especially electrolyte materials, is presented. As the basis of the present study, lanthanum silicates (LSO) system is introduced and discussed, including the structure, electric properties. The doping effects by multiple metal elements are reviewed to find proper candidate doped in our composition.

I.6 References

- [1] Badwal SPS, Foger K. Solid oxide electrolyte fuel cell review. *Ceram Int.* 1996;22:257-65.
- [2] Mahato N, Banerjee A, Gupta A, Omar S, Balani K. Progress in material selection for solid oxide fuel cell technology: A review. *Prog Mater Sci.* 2015;72:141-337.
- [3] Nesaraj AS. Recent developments in solid oxide fuel cell technology - a review. *J Sci Ind Res India.* 2010;69:169-76.
- [4] Steele BC, Heinzel A. Materials for fuel-cell technologies. *Nature.* 2001;414:345-52.
- [5] Möbius H-H. On the history of solid electrolyte fuel cells. *Journal of solid state electrochemistry.* 1997;1:2-16.
- [6] Grove WR. Mr. W. R. Grove on a new Voltaic Combination. *The London and Edinburgh Philosophical Magazine and Journal of Science.* 1838.
- [7] Grove WR. On Voltaic Series and the Combination of Gases by Platinum. *Philosophical Magazine and Journal of Science.* 1839;XIV:127-30.
- [8] Schönbein CF. On the Voltaic Polarization of Certain Solid and Fluid Substances. *The London and Edinburgh Philosophical Magazine and Journal of Science.* 1839, Retrieved October 2, 2013:43.
- [9] Robert. GW. On a gaseous voltaic battery. *Philosophical Magazine Series 3.* 1842;21:2F.
- [10] Nernst W. On the electrolytic conduction of solid bodies at high temperatures. *Z Electrochem.* 1899;6:41-3.
- [11] Nernst W. German Patent 104872 (6 July 1897) *Z. Elektrochem.* 1899;6:41.
- [12] Nernst W. Material for electric-lamp glowers. *Google Patents;* 1901.
- [13] Baur E, Preis H. Über Brennstoff-Ketten mit Festleitern. *Zeitschrift für Elektrochemie und angewandte physikalische Chemie.* 1937;43:727-32.
- [14] Baur E, Preis H. Fuel-gas cells with solid electrolytes. *Electrochem;* 1937.
- [15] Kiukkola K, Wagner C. Measurements on galvanic cells involving solid electrolytes. *Journal of the Electrochemical Society.* 1957;104:379-87.
- [16] Kubaschewski O, Evans A, Alcock CB. *Metallurgical thermochemistry.* 1967.
- [17] Etsell T, Flengas SN. Electrical properties of solid oxide electrolytes. *Chemical Reviews.* 1970;70:339-76.
- [18] Archer D, Sverdrup E, English W, Carlson W. AN INVESTIGATION OF SOLID-ELECTROLYTE FUEL CELLS. DTIC Document; 1963.
- [19] PALGUYEV S, VOLCHENKOVA Z. The electrical conductivity of solid oxide systems. ii. the system zirconium oxide- calcium oxide. electrical conductivity and transport(Conductivity and transport numbers for zirconium oxide-calcium oxide ceramic systems). 1962.
- [20] Palguyev S, Volchenkova Z. Das Problem der festen Elektrolyte für Brennstoffzellen. *Tr Inst Khim, Akad Nauk SSSR, Ural Filial.* 1958;2:183-200.
- [21] Binder H, Köhling A, Krupp H, Richter K, Sandstedt G. Elektrochemische oxydation von kohlenwasserstoffen in einer festelektrolytbrennstoffzelle bei temperaturen von 900–1000 °C. *Electrochimica Acta.* 1963;8:795-803.
- [22] Fabry P, Kleitz M, Déportes C. Sur l'Utilisation d'une electrode ponctuelle dans les cellules à oxyde electrolyte solide. II. Application a la détermination des tensions d'oxydoreduction des défauts ponctuels dans l'electrolyte. *Journal of Solid State Chemistry.* 1973;6:230-9.
- [23] Smith JG, Williams KR. Fuel cells with solid state electrolytes. *Google Patents;* 1969.
- [24] Broecker WS, Takahashi T. Calcium carbonate precipitation on the Bahama Banks. *Journal of Geophysical Research.* 1966;71:1575-602.

- [25] Takahashi T, Yamamoto O. Polarization of the solid-electrolyte cell Ag/Ag₃SI/I₂. *Electrochimica Acta*. 1966;11:911-7.
- [26] Ishihara T, Matsuda H, Takita Y. Doped LaGaO₃ perovskite type oxide as a new oxide ionic conductor. *Journal of the American chemical society*. 1994;116:3801-3.
- [27] Khan M, Islam M, Bates D. Dopant substitution and ion migration in the LaGaO₃-based oxygen ion conductor. *The Journal of Physical Chemistry B*. 1998;102:3099-104.
- [28] Ishihara T, Akbay T, Furutani H, Takita Y. Improved oxide ion conductivity of Co doped La_{0.8}Sr_{0.2}Ga_{0.8}Mg_{0.2}O₃ perovskite type oxide. *Solid State Ionics*. 1998;113:585-91.
- [29] Huang K, Tichy RS, Goodenough JB. Superior Perovskite Oxide-Ion Conductor; Strontium-and Magnesium-Doped LaGaO₃: I, Phase Relationships and Electrical Properties. *Journal of the American ceramic society*. 1998;81:2565-75.
- [30] Mu L, Rao AD, Brouwer J, Samuelsen GS. Design of highly efficient coal-based integrated gasification fuel cell power plants. *Journal of Power Sources*. 2010;195:5707-18.
- [31] Hassmann K. SOFC power plants, the Siemens-Westinghouse approach. *Fuel Cells*. 2001;1:78-84.
- [32] Suzuki T, Funahashi Y, Yamaguchi T, Fujishiro Y, Awano M. New Stack Design of Micro-tubular SOFCs for Portable Power Sources. *Fuel Cells*. 2008;8:381-4.
- [33] Suzuki M, Iwata S, Higaki K, Inoue S, Shigehisa T, Miyachi I, et al. Development and field test results of residential SOFC CHP system. *ECS Transactions*. 2009;25:143-7.
- [34] Staffell I, Green R, Kendall K. Cost targets for domestic fuel cell CHP. *Journal of Power Sources*. 2008;181:339-49.
- [35] Staffell I, Ingram A, Kendall K. Energy and carbon payback times for solid oxide fuel cell based domestic CHP. *international journal of hydrogen energy*. 2012;37:2509-23.
- [36] Bieberle-Hutter A, Beckel D, Muecke U, Rupp J, Infortuna A, Gauckler L. Micro-solid oxide fuel cells as battery replacement. *Mst News*. 2005;4:12.
- [37] Holtappels P, Stimming U. Solid oxide fuel cells (SOFC). *Handbook of Fuel Cells*. 2010.
- [38] Badwal S, Foger K. Solid oxide electrolyte fuel cell review. *Ceram Int*. 1996;22:257-65.
- [39] Ormerod RM. Solid oxide fuel cells. *Chemical Society Reviews*. 2003;32:17-28.
- [40] O'Hayre RP, Cha S-W, Colella W, Prinz FB. *Fuel cell fundamentals*: John Wiley & Sons New York; 2006.
- [41] Wachsman ED, Lee KT. Lowering the temperature of solid oxide fuel cells. *Science*. 2011;334:935-9.
- [42] Nørskov JK, Rossmeisl J, Logadottir A, Lindqvist L, Kitchin JR, Bligaard T, et al. Origin of the overpotential for oxygen reduction at a fuel-cell cathode. *The Journal of Physical Chemistry B*. 2004;108:17886-92.
- [43] Trasatti S. Chemical and electrochemical surface reactivity, role of the competition between solvent and reaction intermediate adsorption. *Proceedings of the Symposium on Electrocatalysis: The Electrochemical Society, Inc*; 1982. p. 2.
- [44] Jaksic JM, Ristic NM, Krstajic NV, Jaksic MM. Electrocatalysis for hydrogen electrode reactions in the light of fermi dynamics and structural bonding FACTORS—I. individual electrocatalytic properties of transition metals. *International journal of hydrogen energy*. 1998;23:1121-56.
- [45] Holton OT, Stevenson JW. The role of platinum in proton exchange membrane fuel cells. *Platinum Metals Review*. 2013;57:259-71.
- [46] Kharton V, Marques F, Atkinson A. Transport properties of solid oxide electrolyte ceramics: a brief review. *Solid State Ionics*. 2004;174:135-49.
- [47] Shaula A, Kharton V, Marques F. Oxygen ionic and electronic transport in apatite-type La_{10-x}(Si, Al)₆O_{26±δ}. *Journal of Solid State Chemistry*. 2005;178:2050-61.
- [48] Shaula A, Kharton V, Waerenborgh J, Rojas D, Marques F. Oxygen ionic and electronic transport in apatite ceramics. *Journal of the European Ceramic Society*. 2005;25:2583-6.

- [49] Xia C, Liu M. Low-temperature SOFCs based on $\text{Gd}_{0.1}\text{Ce}_{0.9}\text{O}_{1.95}$ fabricated by dry pressing. *Solid State Ionics*. 2001;144:249-55.
- [50] Mekhilef S, Saidur R, Safari A. Comparative study of different fuel cell technologies. *Renewable and Sustainable Energy Reviews*. 2012;16:981-9.
- [51] Taroco H, Santos J, Domingues R, Matencio T. *Ceramic Materials for Solid Oxide Fuel Cells*: INTECH Open Access Publisher; 2011.
- [52] Jin C-Q, Zhou J-S, Goodenough J, Liu Q, Zhao J, Yang L, et al. High-pressure synthesis of the cubic perovskite BaRuO_3 and evolution of ferromagnetism in ARuO_3 ($A = \text{Ca}, \text{Sr}, \text{Ba}$) ruthenates. *Proceedings of the National Academy of Sciences*. 2008;105:7115-9.
- [53] Button D, Archer D. Development of $\text{La}_{1-x}\text{Sr}_x\text{CoO}_3$ air electrodes for solid electrolyte fuel cells. Amer Ceram Soc Washington, Meeting May 1966.
- [54] Skinner SJ. Recent advances in perovskite-type materials for SOFC cathodes. *Fuel Cells Bulletin*. 2001;4:6-12.
- [55] Nielsen J, Hjelm J. Impedance of SOFC electrodes: A review and a comprehensive case study on the impedance of LSM: YSZ cathodes. *Electrochimica Acta*. 2014;115:31-45.
- [56] Shannon Rt. Revised effective ionic radii and systematic studies of interatomic distances in halides and chalcogenides. *Acta Crystallographica Section A: Crystal Physics, Diffraction, Theoretical and General Crystallography*. 1976;32:751-67.
- [57] Mizusaki J, Yonemura Y, Kamata H, Ohyama K, Mori N, Takai H, et al. Electronic conductivity, Seebeck coefficient, defect and electronic structure of nonstoichiometric $\text{La}_{1-x}\text{Sr}_x\text{MnO}_3$. *Solid state ionics*. 2000;132:167-80.
- [58] Martin C, Maignan A, Pelloquin D, Nguyen N, Raveau B. Magnetoresistance in the oxygen deficient $\text{LnBaCo}_2\text{O}_{5.4}$ ($\text{Ln} = \text{Eu}, \text{Gd}$) phases. *Applied physics letters*. 1997;71.
- [59] Grimaud A, Mauvy F, Bassat J, Fourcade S, Rocheron L, Marrony M, et al. Hydration properties and rate determining steps of the oxygen reduction reaction of perovskite-related oxides as H^+ -SOFC cathodes. *Journal of The Electrochemical Society*. 2012;159:B683-B94.
- [60] Tedmon C, Spacil H, Mitoff S. Cathode materials and performance in high-temperature zirconia electrolyte fuel cells. *Journal of The Electrochemical Society*. 1969;116:1170-5.
- [61] Spacil HS. Electrical device including nickel-containing stabilized zirconia electrode. Google Patents; 1970.
- [62] Ramirez-Cabrera E, Atkinson A, Chadwick D. Catalytic steam reforming of methane over $\text{Ce}_{0.9}\text{Gd}_{0.1}\text{O}_{2-x}$. *Applied Catalysis B: Environmental*. 2004;47:127-31.
- [63] Rasmussen JF, Hagen A. The effect of H_2S on the performance of Ni-YSZ anodes in solid oxide fuel cells. *Journal of Power Sources*. 2009;191:534-41.
- [64] Nikooyeh K, Clemmer R, Alzate-Restrepo V, Hill JM. Effect of hydrogen on carbon formation on Ni/YSZ composites exposed to methane. *Applied Catalysis A: General*. 2008;347:106-11.
- [65] Chen T, Wang WG, Miao H, Li T, Xu C. Evaluation of carbon deposition behavior on the nickel/yttrium-stabilized zirconia anode-supported fuel cell fueled with simulated syngas. *Journal of Power Sources*. 2011;196:2461-8.
- [66] Costa-Nunes O, Gorte RJ, Vohs JM. Comparison of the performance of Cu-CeO₂-YSZ and Ni-YSZ composite SOFC anodes with H_2 , CO, and syngas. *Journal of Power Sources*. 2005;141:241-9.
- [67] Lu C, Worrell W, Vohs J, Gorte R. A comparison of Cu-ceria-SDC and Au-ceria-SDC composites for SOFC anodes. *Journal of The Electrochemical Society*. 2003;150:A1357-A9.
- [68] Murray EP, Tsai T, Barnett S. A direct-methane fuel cell with a ceria-based anode. *Nature*. 1999;400:649-51.
- [69] Steele B. Appraisal of $\text{Ce}_{1-y}\text{Gd}_y\text{O}_{2-y/2}$ electrolytes for IT-SOFC operation at 500 C. *Solid state ionics*. 2000;129:95-110.

- [70] Omar S, Wachsman ED, Jones JL, Nino JC. Crystal structure–ionic conductivity relationships in doped ceria systems. *Journal of the American Ceramic Society*. 2009;92:2674-81.
- [71] Omar S, Wachsman ED, Nino JC. A co-doping approach towards enhanced ionic conductivity in fluorite-based electrolytes. *Solid State Ionics*. 2006;177:3199-203.
- [72] Omar S, Wachsman ED, Nino JC. Higher ionic conductive ceria-based electrolytes for solid oxide fuel cells. *Applied Physics Letters*. 2007;91:4106.
- [73] Gong M, Liu X, Tremblay J, Johnson C. Sulfur-tolerant anode materials for solid oxide fuel cell application. *Journal of Power Sources*. 2007;168:289-98.
- [74] Hui S, Petric A. Evaluation of yttrium-doped SrTiO₃ as an anode for solid oxide fuel cells. *Journal of the European Ceramic Society*. 2002;22:1673-81.
- [75] Hui S, Petric A. Electrical properties of yttrium-doped strontium titanate under reducing conditions. *Journal of The Electrochemical Society*. 2002;149:J1-J10.
- [76] Blennow P, Hansen KK, Wallenberg LR, Mogensen M. Electrochemical characterization and redox behavior of Nb-doped SrTiO₃. *Solid State Ionics*. 2009;180:63-70.
- [77] Deng Z, Niu H, Kuang X, Allix M, Claridge J, Rosseinsky M. Highly conducting redox stable pyrochlore oxides. *Chemistry of Materials*. 2008;20:6911-6.
- [78] Blundred GD, Bridges CA, Rosseinsky MJ. New oxidation states and defect chemistry in the pyrochlore structure. *Angewandte Chemie International Edition*. 2004;43:3562-5.
- [79] Subramanian M, Aravamudan G, Rao GS. Oxide pyrochlores—a review. *Progress in Solid State Chemistry*. 1983;15:55-143.
- [80] Modeshia DR, Walton RI. Solvothermal synthesis of perovskites and pyrochlores: crystallisation of functional oxides under mild conditions. *Chemical Society Reviews*. 2010;39:4303-25.
- [81] Kramer S, Spears M, Tuller H. Conduction in titanate pyrochlores: role of dopants. *Solid State Ionics*. 1994;72:59-66.
- [82] Kramer S, Tuller H. A novel titanate-based oxygen ion conductor: Gd₂Ti₂O₇. *Solid State Ionics*. 1995;82:15-23.
- [83] Porat O, Heremans C, Tuller H. Stability and mixed ionic electronic conduction in Gd₂(Ti_{1-x}Mo_x)₂O₇ under anodic conditions. *Solid State Ionics*. 1997;94:75-83.
- [84] Zhu W, Deevi S. Development of interconnect materials for solid oxide fuel cells. *Materials Science and Engineering: A*. 2003;348:227-43.
- [85] Akashi T, Maruyama T, Goto T. Transport of lanthanum ion and hole in LaCrO₃ determined by electrical conductivity measurements. *Solid State Ionics*. 2003;164:177-83.
- [86] Tietz F. Thermal expansion of SOFC materials. *Ionics*. 1999;5:129-39.
- [87] Yang Z, Weil KS, Paxton DM, Stevenson JW. Selection and evaluation of heat-resistant alloys for SOFC interconnect applications. *Journal of the Electrochemical Society*. 2003;150:A1188-A201.
- [88] Fergus J, Hui R, Li X, Wilkinson DP, Zhang J. *Solid oxide fuel cells: materials properties and performance*: CRC press; 2008.
- [89] Badwal S, Ciacchi F. Oxygen-ion conducting electrolyte materials for solid oxide fuel cells. *Ionics*. 2000;6:1-21.
- [90] Shuk P, Wiemhöfer H-D, Guth U, Göpel W, Greenblatt M. Oxide ion conducting solid electrolytes based on Bi₂O₃. *Solid State Ionics*. 1996;89:179-96.
- [91] Kharton VV, Naumovich EN, Yaremchenko AA, Marques FM. Research on the electrochemistry of oxygen ion conductors in the former Soviet Union. *Journal of Solid State Electrochemistry*. 2001;5:160-87.
- [92] Jiang N, Wachsman ED. Structural Stability and Conductivity of Phase-Stabilized Cubic Bismuth Oxides. *Journal of the American Ceramic Society*. 1999;82:3057-64.

- [93] Takahashi T, Iwahara H, Arao T. High oxide ion conduction in sintered oxides of the system Bi₂O₃-Y₂O₃. *Journal of Applied Electrochemistry*. 1975;5:187-95.
- [94] Zhao H, Feng S. Hydrothermal Synthesis and Oxygen Ionic Conductivity of Codoped Nanocrystalline Ce_{1-x} M_x BiO₃. 4O₂. 6-x, M= Ca, Sr, and Ba. *Chemistry of materials*. 1999;11:958-64.
- [95] Jung DW, Lee KT, Wachsmann ED. Terbium and Tungsten Co-doped Bismuth Oxide Electrolytes for Low Temperature Solid Oxide Fuel Cells. *Journal of the Korean Ceramic Society*. 2014;51:260-4.
- [96] Verkerk M, Keizer K, Burggraaf A. High oxygen ion conduction in sintered oxides of the Bi₂O₃-Er₂O₃ system. *Journal of applied electrochemistry*. 1980;10:81-90.
- [97] Kruidhof H, Bouwmeester H, De Vries K, Gellings P, Burggraaf A. Thermochemical stability and nonstoichiometry of erbia-stabilized bismuth oxide. *Solid State Ionics*. 1992;50:181-6.
- [98] Abraham F, Boivin J, Mairesse G, Nowogrocki G. The BIMEVOX series: a new family of high performances oxide ion conductors. *Solid State Ionics*. 1990;40:934-7.
- [99] Lazure S, Vernochet C, Vannier R-N, Nowogrocki G, Mairesse G. Composition dependence of oxide anion conduction in the BIMEVOX family. *Solid State Ionics*. 1996;90:117-23.
- [100] Iharada T, Hammouche A, Fouletier J, Kleitz M, Boivin J, Mairesse G. Electrochemical characterization of BIMEVOX oxide-ion conductors. *Solid State Ionics*. 1991;48:257-65.
- [101] Kilner JA, Skinner S, Irvine S, Edwards P. *Functional materials for sustainable energy applications*: Elsevier; 2012.
- [102] Radhakrishnan A, Rao PP, Linsa KM, Deepa M, Koshy P. Influence of disorder-to-order transition on lattice thermal expansion and oxide ion conductivity in (Ca_x Gd_{1-x})₂ (Zr_{1-x} M_x)₂ O₇ pyrochlore solid solutions. *Dalton Transactions*. 2011;40:3839-48.
- [103] Feng M, Goodenough J. A superior oxide-ion electrolyte. *European journal of solid state and inorganic chemistry*. 1994;31:663-72.
- [104] Cherry M, Islam MS, Catlow C. Oxygen ion migration in perovskite-type oxides. *Journal of Solid State Chemistry*. 1995;118:125-32.
- [105] TASCAN JM. Structure and reactivity of perovskite-type oxides. *Advances in catalysis*. 1989;36:237.
- [106] Anderson HU. Review of p-type doped perovskite materials for SOFC and other applications. *Solid State Ionics*. 1992;52:33-41.
- [107] Hayashi H, Inaba H, Matsuyama M, Lan N, Dokiya M, Tagawa H. Structural consideration on the ionic conductivity of perovskite-type oxides. *Solid State Ionics*. 1999;122:1-15.
- [108] Nomura K, Tanase S. Electrical conduction behavior in (La_{0.9} Sr_{0.1}) M_{III} O_{3-δ} (M_{III}= Al, Ga, Sc, In, and Lu) perovskites. *Solid State Ionics*. 1997;98:229-36.
- [109] Fisher CAJ. *Electrical conductivity of brownmillerite-structured oxide ceramics*: University of Oxford; 1996.
- [110] Ferguson J, Kim Y, Kourkoutis L, Vodnick A, Woll A, Muller D, et al. Epitaxial oxygen getter for a brownmillerite phase transformation in manganite films. *Advanced Materials*. 2011;23:1226-30.
- [111] Goodenough J, Ruiz-Diaz J, Zhen Y. Oxide-ion conduction in Ba₂ In₂ O₅ and Ba₃ In₂ MO₈ (M= Ce, Hf, or Zr). *Solid State Ionics*. 1990;44:21-31.
- [112] Schober T, Friedrich J, Krug F. Phase transition in the oxygen and proton conductor Ba₂ In₂ O₅ in humid atmospheres below 300 °C. *Solid State Ionics*. 1997;99:9-13.
- [113] Schober T, Friedrich J. The oxygen and proton conductor Ba₂ In₂ O₅: Thermogravimetry of proton uptake. *Solid State Ionics*. 1998;113:369-75.

- [114] Kakinuma K, Yamamura H, Haneda H, Atake T. Oxide-ion conductivity of the perovskite-type solid-solution system, $(\text{Ba}_{1-x}\text{Sr}_x\text{La}_y)_2\text{In}_2\text{O}_{5+y}$. *Solid State Ionics*. 2002;154:571-6.
- [115] Lacorre P. The LPS concept, a new way to look at anionic conductors. *Solid State Sciences*. 2000;2:755-8.
- [116] Marrero-López D, Pena-Martinez J, Ruiz-Morales J, Pérez-Coll D, Martín-Sedeno M, Nunez P. Applicability of $\text{La}_2\text{Mo}_2\text{W}_y\text{O}_9$ materials as solid electrolyte for SOFCs. *Solid State Ionics*. 2007;178:1366-78.
- [117] Kendrick E, Islam MS, Slater PR. Developing apatites for solid oxide fuel cells: insight into structural, transport and doping properties. *Journal of Materials Chemistry*. 2007;17:3104-11.
- [118] Nakayama S, Sakamoto M. Electrical properties of new type high oxide ionic conductor $\text{RE}_{10}\text{Si}_6\text{O}_{27}$ (RE= La, Pr, Nd, Sm, Gd, Dy). *Journal of the European Ceramic Society*. 1998;18:1413-8.
- [119] Nakayama S, Kageyama T, Aono H, Sadaoka Y. Ionic conductivity of lanthanoid silicates, $\text{Ln}_{10}(\text{SiO}_4)_6\text{O}_3$ (Ln= La, Nd, Sm, Gd, Dy, Y, Ho, Er and Yb). *Journal of Materials Chemistry*. 1995;5:1801-5.
- [120] Sun F. Caractérisation de revêtements de silicate de lanthane de structure apatite dopé au magnésium réalisés par projection plasma en vue d'application comme électrolyte de pile à combustible de type IT-SOFC: Université de Technologie de Belfort-Montbéliard; 2010.
- [121] León-Reina L, Porrás-Vázquez JM, Losilla ER, Aranda MA. Interstitial oxide positions in oxygen-excess oxy-apatites. *Solid State Ionics*. 2006;177:1307-15.
- [122] Nakayama S, Highchi M. Electrical properties of apatite-type oxide ionic conductors $\text{RE}_9.33(\text{SiO}_4)_6\text{O}_2$ (RE= Pr, Nd and Sm) single crystals. *Journal of materials science letters*. 2001;20:913-5.
- [123] Najib A, Sansom J, Tolchard J, Slater P, Islam M. Doping strategies to optimise the oxide ion conductivity in apatite-type ionic conductors. *Dalton Transactions*. 2004:3106-9.
- [124] Béchade E, Julien I, Iwata T, Masson O, Thomas P, Champion E, et al. Synthesis of lanthanum silicate oxyapatite materials as a solid oxide fuel cell electrolyte. *Journal of the European Ceramic Society*. 2008;28:2717-24.
- [125] Haile SM. Fuel cell materials and components. *Acta Materialia*. 2003;51:5981-6000.
- [126] Tolchard JR, Islam MS, Slater PR. Defect chemistry and oxygen ion migration in the apatite-type materials $\text{La}_{9.33}\text{Si}_6\text{O}_{26}$ and $\text{La}_8\text{Sr}_2\text{Si}_6\text{O}_{26}$. *Journal of Materials Chemistry*. 2003;13:1956-61.
- [127] Saiful Islam M. An apatite for fast oxide ion conduction. *Chemical communications*. 2003:1486-7.
- [128] Orera A, Sanjuán M, Kendrick E, Orera V, Slater P. Raman spectroscopy studies of apatite-type germanate oxide ion conductors: correlation with interstitial oxide ion location and conduction. *Journal of Materials Chemistry*. 2010;20:2170-5.
- [129] Orera A, Kendrick E, Apperley D, Orera V, Slater P. Effect of oxygen content on the ^{29}Si NMR, Raman spectra and oxide ion conductivity of the apatite series, $\text{La}_{8+x}\text{Sr}_{2-x}(\text{SiO}_4)_6\text{O}_{2+x/2}$. *Dalton Transactions*. 2008:5296-301.
- [130] Nakayama S, Sakamoto M, Highchi M, Kodaira K. Ionic conductivities of apatite type $\text{Nd}_X(\text{SiO}_4)_6\text{O}_{1.5X-12}$ (X= 9.20 and 9.33) single crystals. *Journal of materials science letters*. 2000;19:91-3.
- [131] León-Reina L, Losilla ER, Martínez-Lara M, Bruque S, Aranda MA. Interstitial oxygen conduction in lanthanum oxy-apatite electrolytes. *Journal of Materials Chemistry*. 2004;14:1142-9.

[132] León-Reina L, Martín-Sedeno M, Losilla E, Cabeza A, Martínez-Lara M, Bruque S, et al. Crystalchemistry and oxide ion conductivity in the lanthanum oxygermanate apatite series. *Chemistry of materials*. 2003;15:2099-108.

CHAPTER II. Fundamentals of Experimental, Calculation and Characterization

In this chapter, we present a brief review of synthesis methods, and describe the experimental techniques and characterization used in this study, including the synthesis methods, microstructure characterization (XRD, SEM) electrolyte properties measurement (ionic conductivity) and a brief introduction of the DFT (Density Functional Theory).

Since the quality of LSO material is of the essence for the highest performances of SOFC devices, we have paid the greatest attention to its synthesis process and explored a large variety of preparation methods and selected the most efficient one.

II.1. Synthesis methods

II.1.1 Dry pressing

Dry pressing is the technique of fabricating ceramic components by the compaction of flowable powders in a metal die set. This fabrication technology enables the manufacture of parts to accurate dimensional specifications and enables high volume production. There are three fundamental steps in dry pressing technology that include spray dried powder preparation, pressing and sintering. Dry pressing is simple, reproducible, and very cost-effective. Figure II.1 gives a schema of the dry pressing technology and devices. Dense electrolyte can be obtained by this technique. *Xia* and *Liu* reported that GDC ($\text{Gd}_{0.1}\text{Ce}_{0.9}\text{O}_{1.95}$) films were successfully fabricated by this dry-pressing process. SOFCs based on GDC films were tested having maximum power densities of 400 mW/cm^2 at $600 \text{ }^\circ\text{C}$ [1, 2].

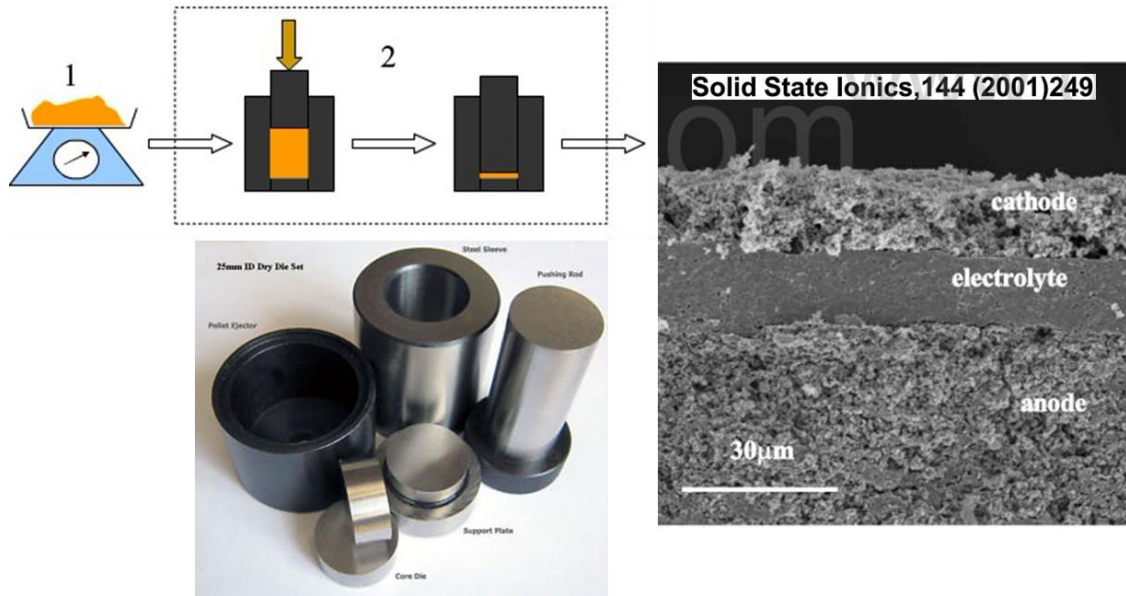


Figure II. 1. A schematic diagram for showing dry pressing process, devices and the electrolyte obtained by this technique.

II.1.2 Casting

Casting is a traditional ceramic manufacturing process in which a liquid material is usually poured into a mold, which contains a hollow cavity of the desired shape, and then allowed to solidify. The solidified part is also known as a casting, which is ejected or broken out of the mold to complete the process. It is low-cost and suitable for making thin wall products with complex shapes and has been used in fabricating yttria stabilized zirconia (YSZ) tubes and cone-shaped electrolyte cylinders. It is developed to adopt the fabrication of electrolyte into tape-casting, slip casting and vacuum casting et al.[3-6] A fair example of this technology is given by *N.O. Shanti* et al.[7] who reported that electrolyte of multiple layers with thickness ranging from 10 to 500 μm were produced with a single tape casting step for each layer. The assembled cells made with this technique have maximum current density and power density (1.76 A cm^{-2} and 425 mW cm^{-2} respectively), as shown in Figure II.2.

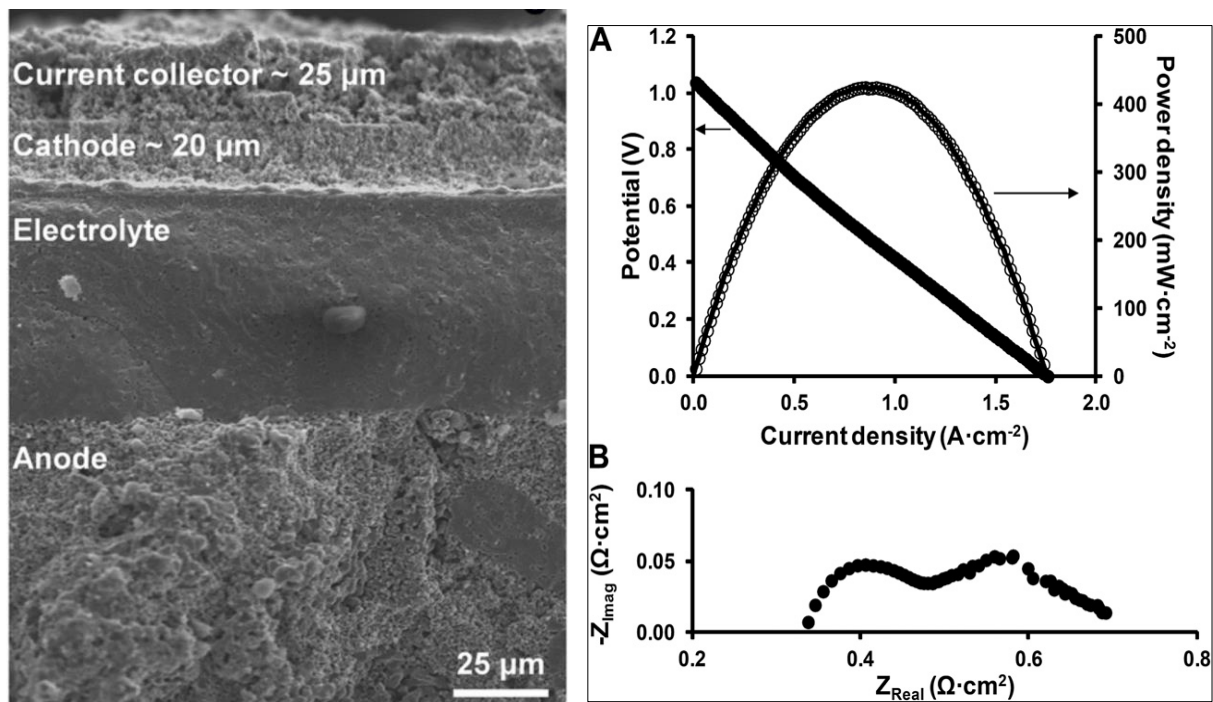


Figure II. 2. SEM micrographs of tape casting electrolyte using in SOFC and voltage-current, impedance spectrum characteristics of the cell operating at 800 °C.

II.1.3 Screen printing

Screen printing is an industrially used cost-effective method to fabricate homogeneous layers of pastes containing ceramic powders. Organic binder systems are frequently used for large-scale production such as lacquers because they are insensitive to seasonal changes of temperature and humidity compared to water-based dispersions. Compared with some other techniques, it is low-cost, easy to realize, and suitable for mass-production. A key step of this technology is the preparation of the raw material as the “printing ink”. [8, 9] All of precursor materials is uniformly dispersed in slushy solution. *M. Dudek* [10] developed the technology for SOFC fast fabrication, named inkjet printing. The printing technology offers excellent thickness and uniformity control of ceramic coating less than 10 μm thick. Figure II.3 gives the 8YSZ layers prepared with screen printing technology by *Peter Ried* et al. [11] With this technology, the inevitable emergence of a large number of pores leads to the conductivity is lower than for a dense YSZ pellet with same measure condition, as shown in Figure II.3.

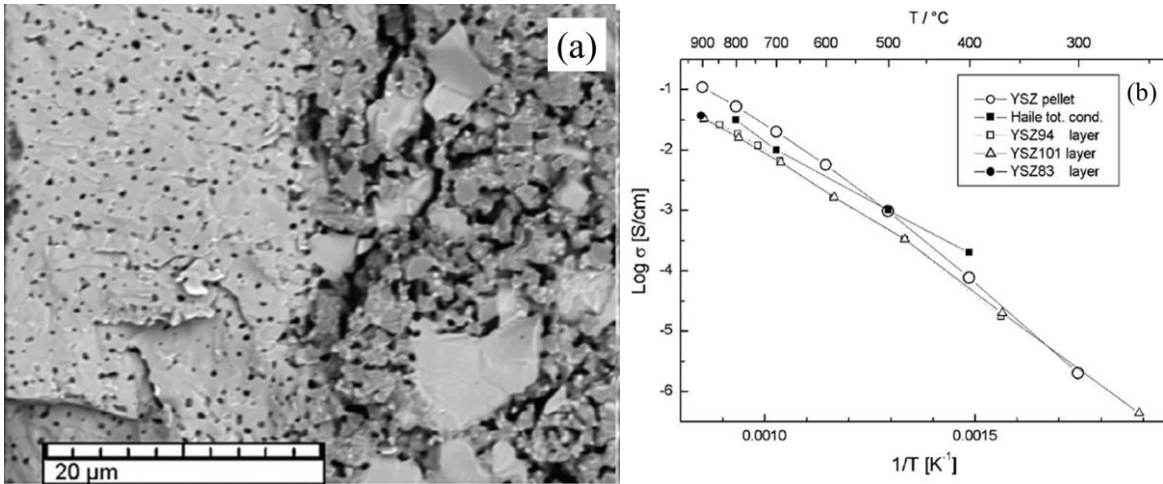


Figure II. 3. (a) SEM micrographs of electrolyte layer on the left and porous Ni–YSZ cermet on the right. (b) Specific resistance at different temperatures in comparison with YSZ pellet.

II.1.4 Physical vapor deposition (PVD)

PVD describes a variety of vacuum deposition methods which can be used to produce thin films. It uses physical process (such as heating, sputtering [12-16] or electron beam [17, 18] etc.) to produce a vapor of material, which is then deposited on the object which requires coating. It is used in the manufacture of electrolyte which require thin dense films for mechanical, chemical and electronic functions. The morphology of the electrolyte fabricated by PVD is shown in Figure II.4 by *H. Hidalgo* et al [19]. The dense, thin film is obtained with excellent electric performance. However the promotion of this technology is limited for its requirements of high vacuum and costly target materials.

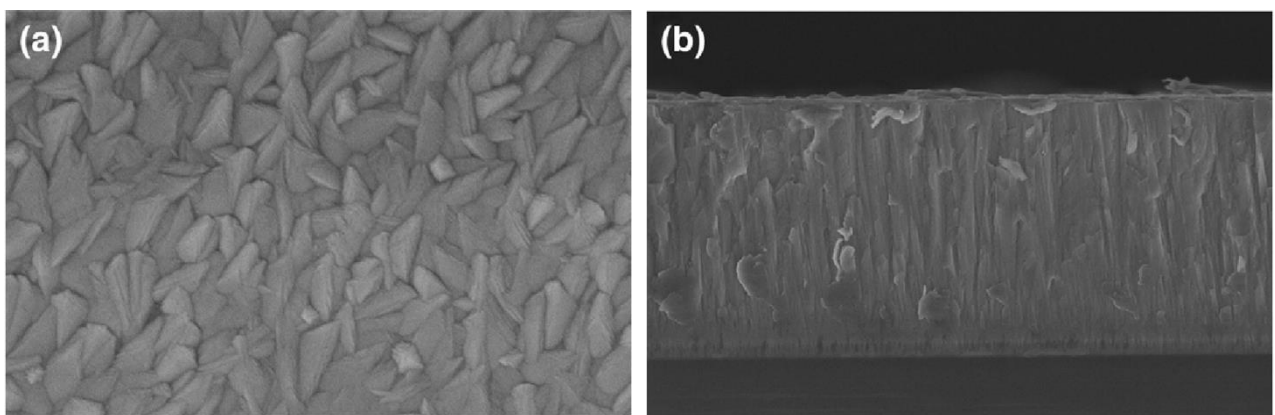


Figure II. 4. SEM micrographs of YSZ films grown by RMS (reactive magnetron sputtering) on (100) Si substrate at room temperature under 1 Pa: a) top view, b) cross-section.

II.1.5 Chemical vapor deposition (CVD)

CVD is a chemical process used to produce high quality, high-performance, solid materials. It is practiced in various formats. Some formats are usually used in the fabrication process of electrolytes, such as atomic-layer (AL) CVD, metal-organic (MO) CVD [20] and aerosol-assisted (AA) CVD etc [21]. Figure II.5 gives a schematic diagram of AACVD experimental setup and the electrolyte obtained by this technology [22].

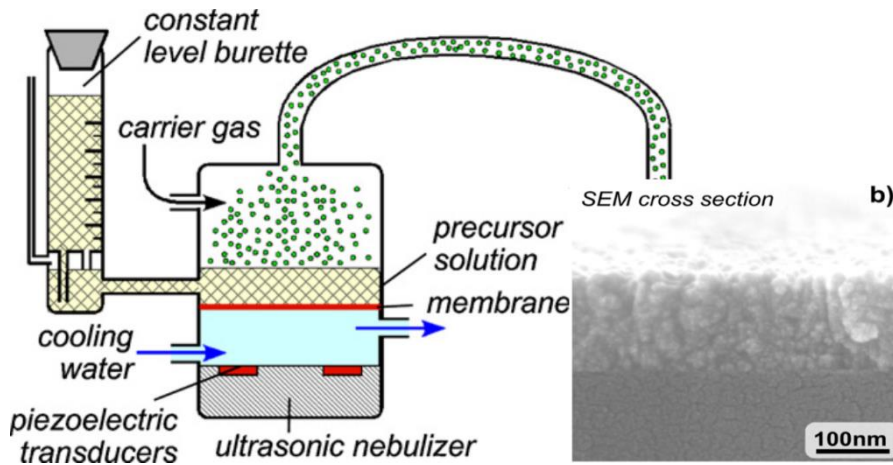


Figure II. 5. Experimental setup of ultrasonic aerosol assisted chemical vapor deposition at atmospheric pressure and the morphology of as obtained electrolyte

II.1.6 Thermal spray

Thermal spray is a generic term for a group of processes that utilize a heat source to melt material in powder, wire or rod form. The molten or semi-molten material is propelled toward a prepared surface by expanding process gases. The particles quench rapidly, upon impact with the surface, and bond with the part. Subsequent impacting particles create a coating buildup [23-25]. The coating and synthesis process of the fuel cell materials is investigated by the previous work in our laboratory [26-28]. Recently, *F. Sun* reported [29] that better performance and denser apatite products can be obtained by very low pressure plasma spraying (VLPPS)

than that by atmospheric plasma spraying (APS). A mount of microcracks can be detected in fracture surface of coating deposited by the latter. Figure II.6 shows the morphologies of the layer deposited by different types of thermal spray.

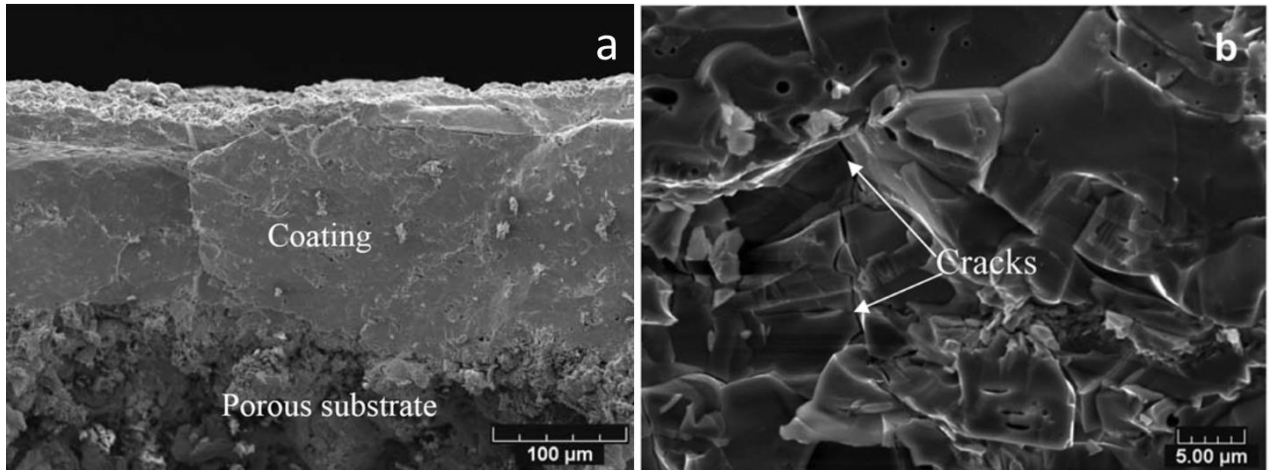


Figure II. 6. Micrographs of fracture surface of the $\text{La}_{10}\text{Si}_{5.8}\text{Mg}_{0.2}\text{O}_{26.8}$ coating deposited by VLPPS (a) and APS (b).

II.1.7 Chemical methods

A number of chemical methods are available for this synthesis of solid electrolyte:

- Conventional precipitation
- Reaction in molten salt medium
- HDP (“homogeneous deposition precipitation”)
- Combustion synthesis
- Sol-gel methods

In this thesis work, we have preliminarily investigated the first three methods in consideration of their relative simplicity.

When using conventional precipitation, one needs to perform the co-precipitation of the cationic part (lanthanum and possible substituting ions: Sr, Mn etc.) and the anionic part (silicate). This method has been explored and results are reported in Chapter IV.1 and IV.2.

The molten salt method has been lastly studied in Chapter IV.3 using various alkali salts (chlorides, nitrates and sulfates) as the molten media likely to favor the interaction between the lanthanum and silica. The main issues observed have been: i) high level of impurities present in the LSO product (due to the concentrations of the contaminants presents in the starting fusible salts) and ii) the release of heavy smoke in the case of ammonium nitrate.

The HDP method has also been evaluated as well (Chapter IV.4). Here some lanthanum hydroxide is deposited at very low rate on a quite separated silica substrate (silica gel). The essential advantage of this method lies in the fact that precipitate nuclei are extremely fine due to the very low change in the pH during the hydrolysis of urea. However, we have stated that the precipitated lanthanum hydroxide, although well distributed over the silica particles were not able to diffuse inside the very core of the grains, which led to incomplete reaction.

Finally, the sol-gel method proved to be the most adequate and has been selected as the actual synthesis path in this work.

The principle of the sol-gel method is to generate nano-size particles in which the reacting atoms (e.g. La and Si) are located in very close vicinity in a common molecule and are therefore likely to interact easily with each other. The method is used for the fabrication of metal oxides, especially the oxides of silicon and titanium. The process involves conversion of monomers into a colloidal solution (sol) that acts as the precursor for an integrated network (or gel) of either discrete particles or network polymers. The sol and gel formation process is shown in Figure II.7 and two critical steps (condensation and gelation) determine the character of products directly [30].

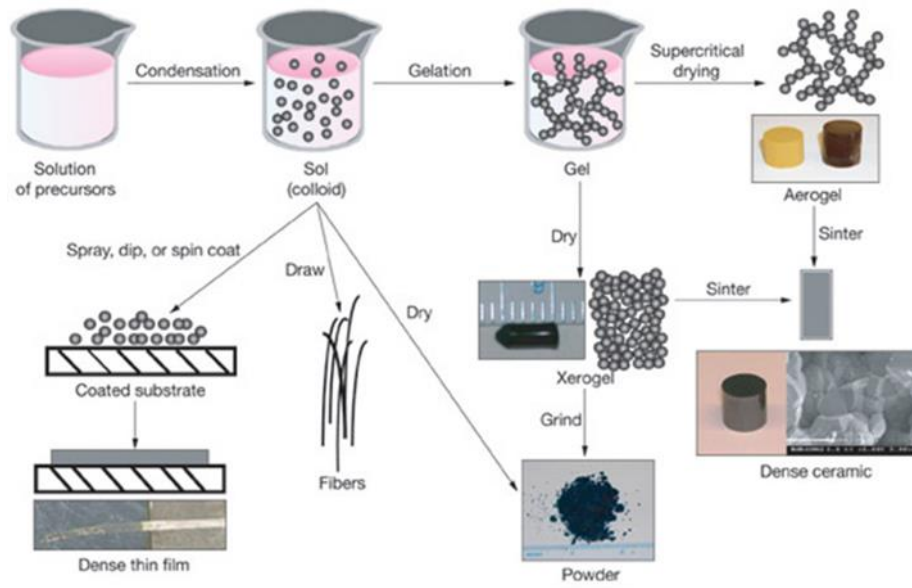


Figure II. 7. A schematic diagram of sol-gel process and its application ways (<https://str.llnl.gov/str/May05/Satcher.html>)

Sol-gel method is a quite efficient way to synthesize lanthanum silicates, the investigated object of this thesis work. *Tao et al.* [31] first reported the synthesis of apatite-type lanthanum silicates from TEOS and La_2O_3 using the sol-gel technique. According to the work, both $\text{La}_{10}(\text{SiO}_4)_6\text{O}_3$ and $\text{La}_{9.33}(\text{SiO}_4)_6\text{O}_2$ apatite-type lanthanum silicates form, with final heating at $1400\text{ }^\circ\text{C}$, pure apatite-type in good crystallization was achieved. *C'ardier et al.*[32] synthesized $\text{La}_{9.33}\text{Si}_6\text{O}_{26}$ nanocrystalline powders from route based on sol-gel process. High density (up to 90%) could be attained after attrition milling step of the powders. He concluded that the starting particles size and the sintering behavior have a great influence on the relative density of the ceramics. They have also studied the effect of several parameters, such as hydrolysis molar ratio ($\text{H}_2\text{O}/\text{SiO}_2$) ratio, volumetric ratio of catalyst to TEOS and silicon concentration, in gel formation[33]. Recently, *Qingle et al.* discussed the influence of pH value in the sol-gel process to obtain apatite-type $\text{La}_{9.33}\text{Si}_6\text{O}_{26}$. The single phase of apatite-type structure compound is formed and in good crystallization with specific surface area of $5.53\text{ m}^2\text{ g}^{-1}$ and the particle size around 200 nm.

Sol-gel method is employed as our major way to synthesize lanthanum silicates, thus we will give more details of this method. Doping elements were introduced in order to improve the performance of these compounds with this method. It was shown that substituting Al^{3+} for Si^{4+} in the SiO_4 tetrahedra of the oxyapatite structure increases its ionic conductivity[34, 35]. Recently *E. Jothinathan* et al.[36] prepared Al^{3+} , Fe^{3+} doped LSO using low temperature (900°C for 8h), fast and user-friendly sol-gel processing technique. The flowchart of the sol-gel process is given in Figure II.8. Then, *J. Zhou* et al.[37] synthesized $\text{La}_{9.67}\text{Si}_{6-x}\text{Al}_x\text{O}_{26.5-x/2}$ electrolyte with multiple Al proportion, however $\text{La}_{9.67}\text{Si}_6\text{O}_{26.5}$ ($x = 0$) among the series exhibits the highest electrical conductivity. By viewing the reports, the synthesis process seriously affects the performance of the compounds. The improvement of sol-gel process is necessary to achieve pure phase, high crystalline compounds.

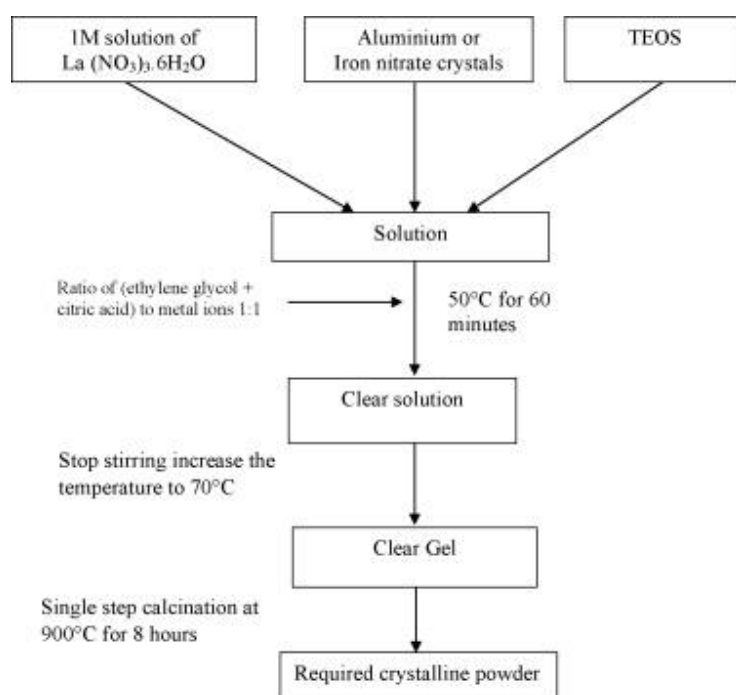


Figure II. 8. Flowchart of the process used in the preparation of doped and undoped lanthanum silicates.

Currently, some new techniques are derived from the traditional sol-gel technique, such as gel casting, gel printing, water-based sol gel, and so on.[8, 38]. These techniques have much advantage in the synthesis of this LSO series as following:

- User-friendly, easy realization;
- Low cost of the equipment required;
- Reaction complete;
- High purity of products;
- Fast preparation;
- High efficiency and usage of raw-materials;

II.2 Characterization

II 2.1 Density

Density is an important indicator to measure the performance of a sample. As electrolyte material in fuel cells, the samples should be as high as possible to isolate the gas flow between the two electrodes. The density of prepared samples is determined from measurements of the mass and volume, and calculated by the following equation.

$$\rho = \frac{m}{e \cdot \pi \cdot \frac{d^2}{4}} \quad \text{EQN II.1}$$

with, m - the mass of sample; d – the diameter and e – the thickness.

The theoretical value of lanthanum silicates is $5.4 \text{ g}\cdot\text{cm}^{-3}$ (evaluated through simulation methods). Higher calcination temperatures seem to lead to higher densities. Figure II.9 gives an example (Mg doped LSO) of the influence of calcination temperature to the density.[39]

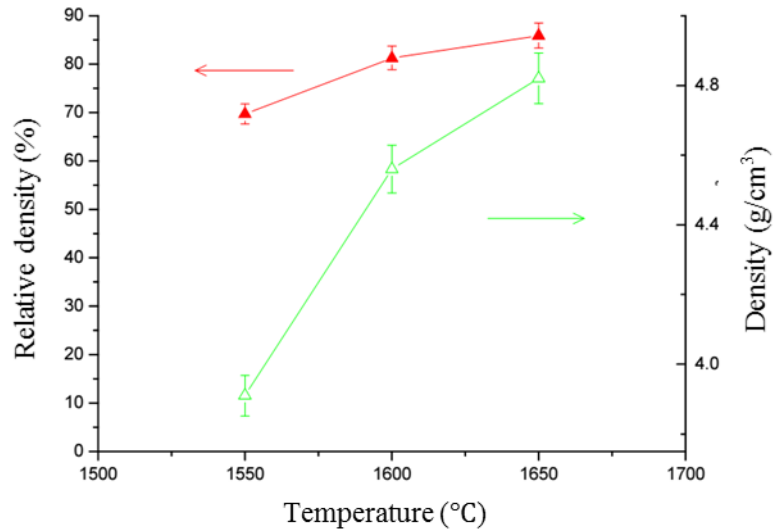


Figure II. 9. Density and relative density of sintered samples at different temperatures [39]

II.2.2 Phase

X-ray powder diffraction (XRD) is a rapid analytical technique primarily used for phase identification of a crystalline material and can provide information on unit cell dimensions. It is adopted in this work to determine the phase and to verify the purity of the obtained compounds. This technique allows, in the case of ceramics, whether the desired phase was obtained and the reaction was well taken place. It provides information on the purity, crystallinity and crystallographic parameters value. The equipment used in this study is branded of Bruker AXS D8 FOCUS. It is equipped with a curved counter, and allows measurements at a fixed incidence of 4° . The device is equipped with a cobalt anticathode ($\lambda = 0,17889\text{nm}$). Figure II.10 shows the equipment in which is the sample stage, and the detector / counter lies at the two sides of the stage.

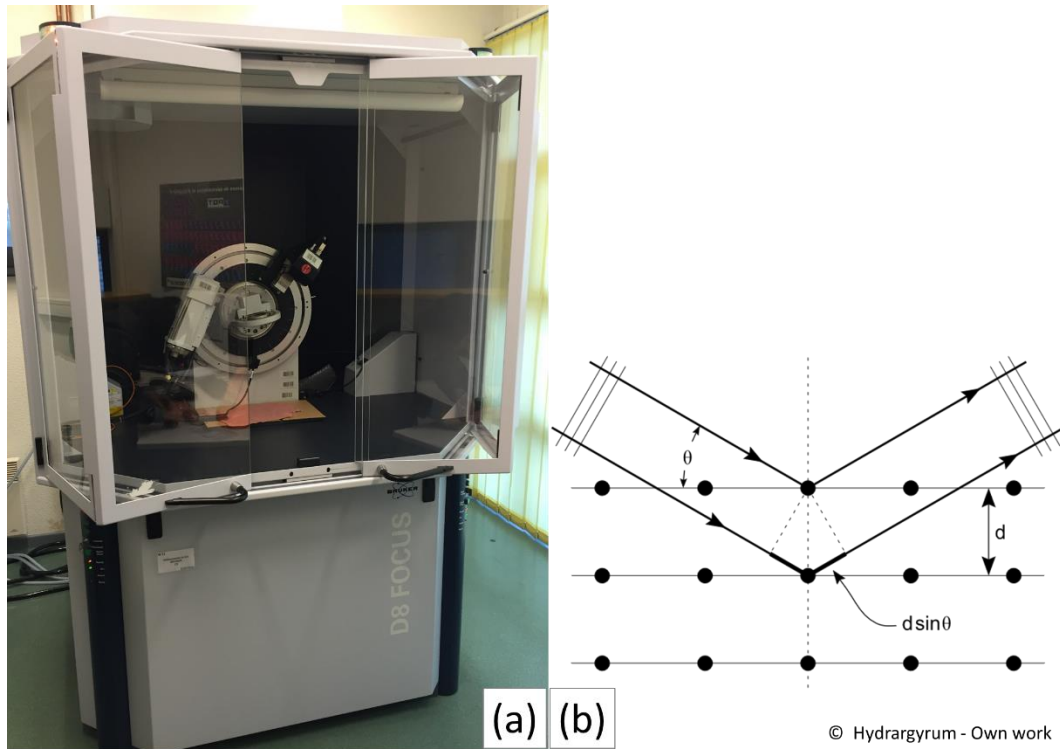


Figure II. 10. Photography and X-ray diffraction mechanism of Bruker-AXS D8 FOCUS Advanced Bragg-Brentano X-ray Powder Diffractometer

Crystals are regular arrays of atoms, and X-rays can be considered waves of electromagnetic radiation. An X-ray striking an electron produces secondary spherical waves emanating from the electron. This phenomenon is known as elastic scattering. A regular array of scatterers produces a regular array of spherical waves. Although these waves cancel one another out in most directions through destructive interference, they add constructively in a few specific directions, determined by Bragg's law:

$$n\lambda = 2d \sin \theta \quad \text{EQN II.2}$$

Each particular structure has specific directions which is called the high intensity diffraction position as well as the characteristic peaks of the compounds. The characteristic peaks of lanthanum silicate are shown in Figure II.11 [40]. This is used to identify the experimental diffraction pattern of the obtained samples.

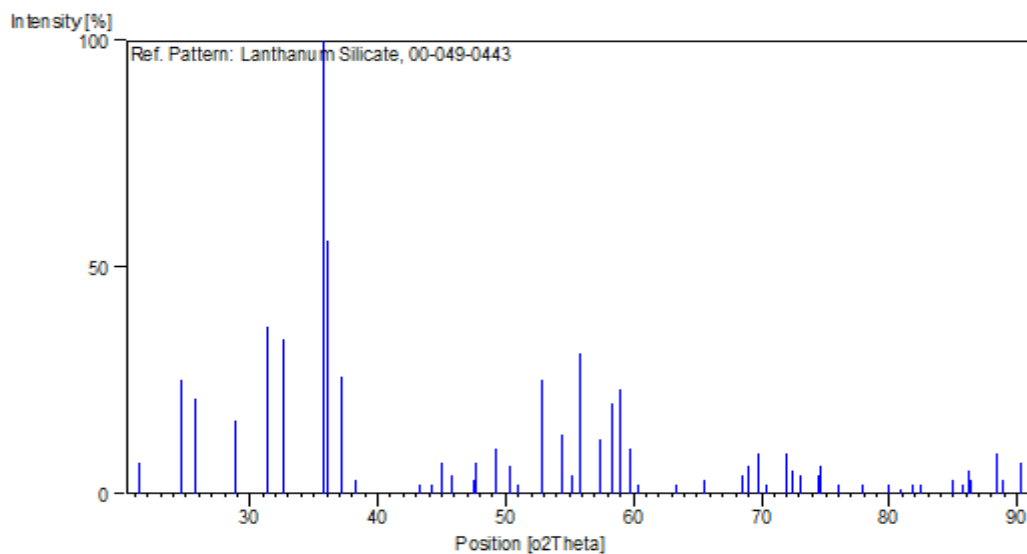


Figure II. 11. Stick pattern of high intensity diffraction for Lanthanum silicate (ref. 00-049-0443)

The compounds phases involved in our work are identified by comparison with the reference file ICDD (International Center for Diffraction Data). The files PDF (Powder Diffraction File) are used to identify synthesized components are reported in Table II.1.

Table II. 1. The PDF files of the compounds involved in this work

Compounds	Formula	Ref. code
Lanthanum silicate	$\text{La}_{9.33}\text{Si}_6\text{O}_{26}$	00-049-0443
Lanthanum silicate	La_2SiO_5	00-040-0234
Lanthanum silicate	$\text{La}_{10}\text{Si}_6\text{O}_{27}$	00-053-0291
Lanthanum oxide	La_2O_3	00-022-0641
Quartz	SiO_2	01-080-2148

II 2.3 Microstructure

A scanning electron microscope (SEM) is used in this study to determine the microstructure and the morphology of the obtained samples. It is a type of electron microscope that produces images of a sample by scanning it with a focused beam of electrons.



Figure II. 12. JSM-7800F field emission scanning electron microscope

The equipment is shown in Figure II.12, which is JSM-7800F field emission scanning electron microscope of JEOL Company. Due to the very narrow electron beam, SEM micrographs have a large depth of field yielding a characteristic three-dimensional appearance useful for understanding the surface structure of a sample. A wide range of magnifications is possible, and the range of this type of SEM is from about 50 times to more than 300,000 times, about 150 times the magnification limit of the best light microscopes.

Energy-dispersive X-ray spectroscopy (EDX) is usually equipped in this equipment used for the elemental analysis or chemical characterization of a sample. As the energies of the X-rays are characteristic of the difference in energy between the two shells and of the atomic structure

of the emitting element, EDS allows the elemental composition of the specimen to be measured.

Table II.2 gives characteristic X-ray energy of the elements involved in our study.

Table II. 2. Some elements' characteristic X-ray energy for EDX characterization

Elements	C	O	Si	Sr	La
X-ray energy				K α 14.140	La 4.650
(keV)	K α 0.277	K α 0.525	K α 1.739	La 1.806	M 0.833

II 2.4 Conductivity

The electrical conductivity of sintered material is a very important property for the use of the electrolyte. It can be measured by the DC method. The principle and the measuring device are presented to define the electrical conductivity. The DC method of four points is used to measure the electrical conductivity of the sample as shown in Figure II .13.

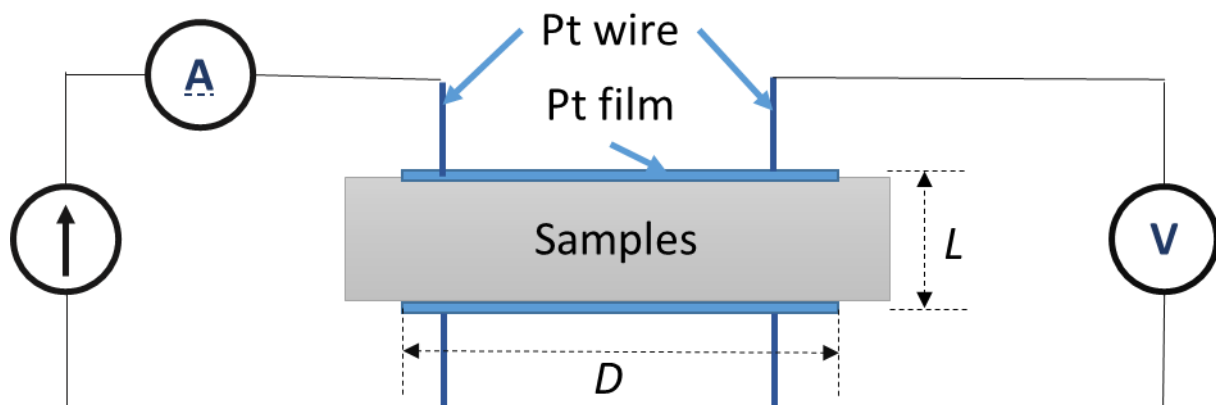


Figure II. 13. Diagram of the four-point method

This method avoids the influence of the electrodes resistance. During measurement, it is necessary to circulate a current and measure the resulting voltage between two points of the sample. The resistance which is the ability to oppose the flow of electric current, can be defined by the following formula. At the same time, it can be calculated by Ohm's law.

$$R = \rho \frac{L}{A} = \frac{U}{I} \quad \text{EQN II.3}$$

Among them, R - resistance of the sample (measured in ohms, Ω), ρ - the electrical resistivity ($\Omega \cdot \text{cm}$), L - the length of the piece of material (m), A - the cross-sectional area of the specimen (m^2), U - the voltage measured across the sample (V), I - the current through the sample (A).

Conductivity is the ability to allow electrical charges to move freely, in other words to allow the passage of electric current, which is the inverse of resistivity, thus,

$$\sigma = \frac{1}{\rho} = \frac{L}{R \cdot A} \quad \text{EQN II.4}$$

σ is the conductivity having SI units of Siemens per meter (S/m).

The resistance can be measured by the DC method. In order to completely understand the impedance of the sample, in our work, the method of electrochemical impedance spectroscopy (EIS) was applied for the electrochemical characterization of solid electrolytes. In fact, this method makes it possible to distinguish and identify the response of the electrolyte following the application of an alternating voltage disturbance with variable frequency and low amplitude around a stationary operating point. The voltage can be expressed as $E_t = E_0 \exp(j\omega t)$, which is a sinusoidal signal, as well as the current. The impedance, including resistance, capacitance and inductance, is given in EQN II.5.

$$Z(\omega) = \frac{E_t}{I_t} = \frac{E_0 \exp(j\omega t)}{I_0 \exp(j\omega t + \varphi)} = Z_0 \exp(j\varphi) = Z_0 \cos\varphi + jZ_0 \sin\varphi \quad \text{EQN II.5}$$

Z' and Z'' are employed to replace the real and imaginary parts to simplify the equation:

$$Z(\omega) = \text{Re}(Z) + j\text{Im}(Z) = Z' + Z'' \quad \text{EQN II.6}$$

The complex impedance is generally represented by Nyquist plot or Bode plot in measurement results. According to the results, the impedance can be fitted to a simple circuit. Figure II.14

shows an example of electrical circuit (a), corresponding Nyquist plot (b) and Bode plot (c). [41] In the representation of the Nyquist plane, the real part and the imaginary part of the impedance (Z' and Z'') are plotted respectively on the X and Y axis. Usually, electrochemistry takes the negative Y-axis to up as shown in Figure II. 14 (b). The impedances of low frequencies and high frequencies are located at right and left of the plot respectively. In the case of Bode plot, the logarithm of modulus $|Z|$ and / or variation of the argument of the phase (ϕ) are represented as a function of logarithmic angular frequency [$\log(|Z|) = f(\log\omega)$ or $\phi = f(\log\omega)$]. The advantage of such a representation (Figure II.14.c) is to identify directly the frequency spectrum corresponding to each measured result.

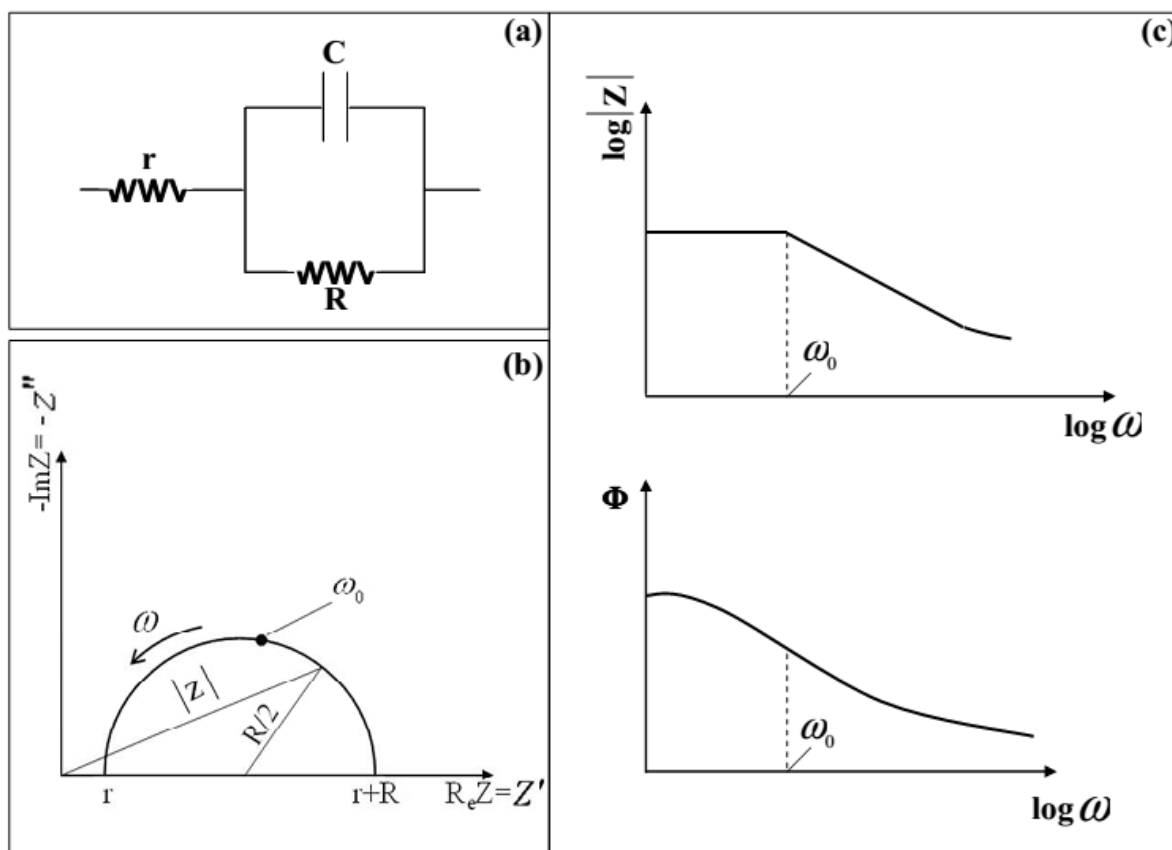


Figure II. 14. Representation of an electric circuit impedance diagram. (a) Electrical circuit, (b)Complex impedance diagram corresponding to a Nyquist plot and (c) in a Bode plot.

The ionic conductivity can be presented by the analysis of Nyquist plot. The total ionic conductivity of a polycrystalline electrolyte depends upon the contribution from both grain and grain boundary. The separate resistive contributions of both grain interior and the grain boundaries towards the total resistivity can be obtained using AC impedance spectroscopy technique.

Fig. II.15 a shows the schematic of an impedance plot of a polycrystalline sample with electrode (i.e., containing both grains and grain boundaries) of thickness L, and cross-sectional electrode area A. Its corresponding analog equivalent electrical circuit is shown in Fig. II. 15 b, where the total electrical conductivity (σ_t) can be obtained from the following expression[42]:

$$\frac{1}{\sigma_t} = \frac{1}{\sigma_g} + \frac{1}{\sigma_{gb}} \tag{EQN II.7}$$

where σ_g and σ_{gb} are the conductivities of grain interior and grain boundary, respectively.

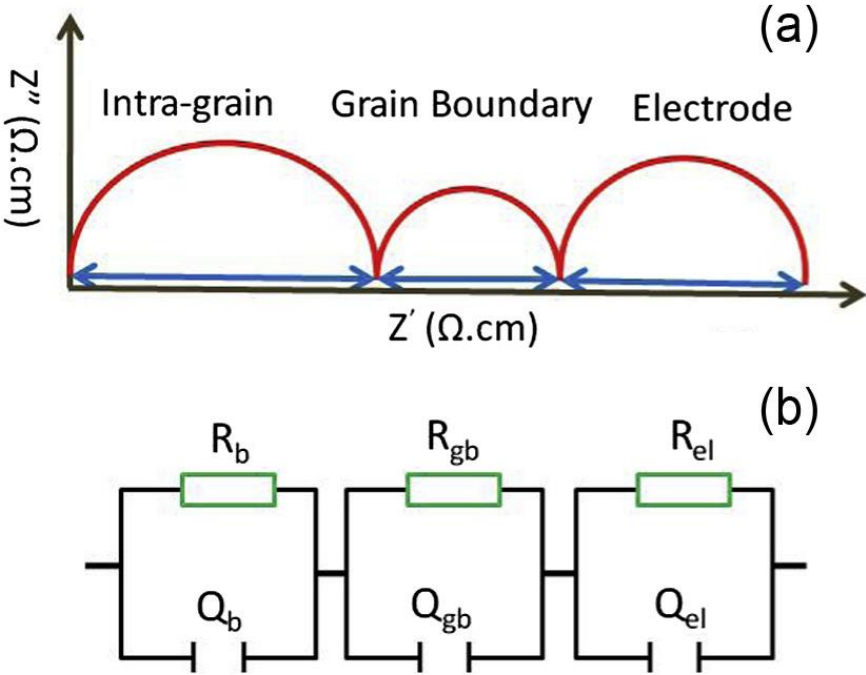


Figure II. 15. Schematic of an impedance plot for an electroded polycrystalline sample with an analog equivalent electric circuit.

In measurement, Pt film is deposited on the two sides of our samples as current collector by the PVD technique. The studied electrolyte is composed to the following structure:

Humid air / electrode (Pt) / electrolyte LSO / electrode (Pt) / Humid air

The electrical properties were measured as a function of temperature by complex impedance spectroscopy, using a Solartron 1260A frequency response analyzer (FRA) in the frequency range 5 Hz - 15 MHz, under static air. The measurements were performed at the open circuit voltage as well as with an applied AC voltage of 100 mV. The impedance diagrams were recorded from 673 K to 1273 K with thermal steps and stabilization times of about 25 K and 20 minutes respectively.

Figure II.16. shows the ionic conductivity measurement device (a samples furnace equipped with Agilent 3458A Multimeter and Solartron 1260A frequency response analyzer) applied in this work.

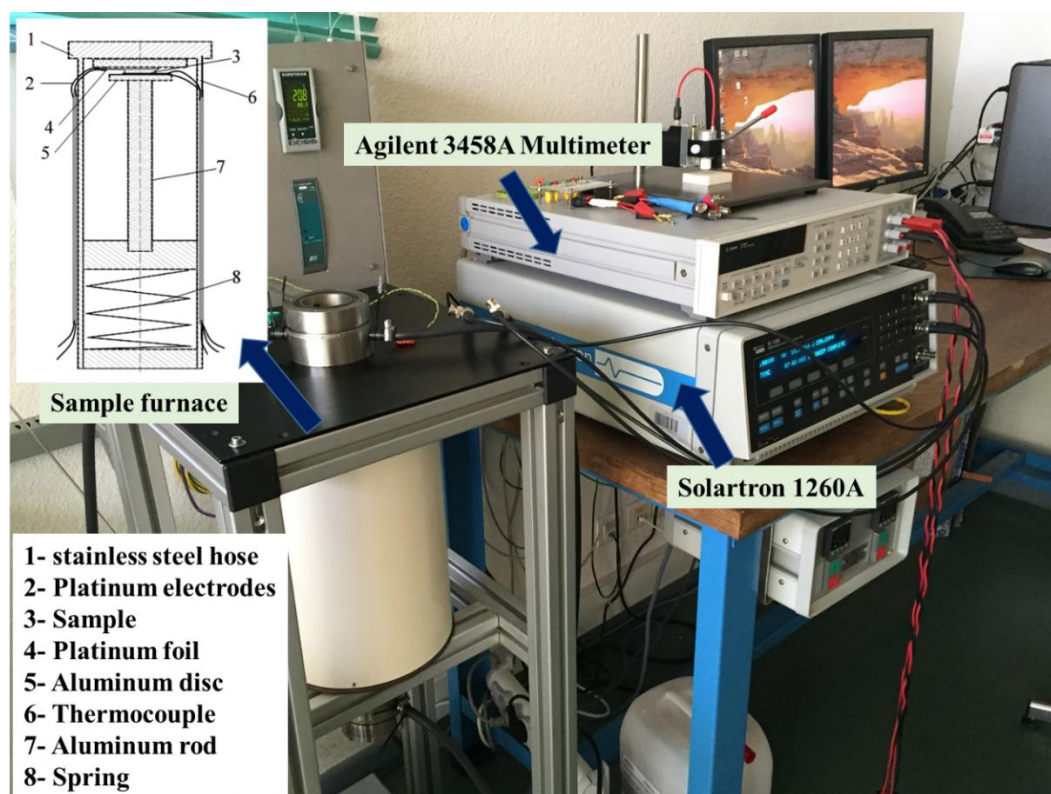


Figure II. 16. Devices for measuring the conductivity (the inset is the structure of sample furnace)

A flow of nitrogen gas is maintained over the samples to create a reproducible and dry atmosphere. The nitrogen atmosphere also eliminates air oxidation of the samples at high temperatures. The sample is sealed into a small aluminum pan. The reference is usually an empty pan and cover. The pans hold up to about 10 mg of material. We choose the linear temperature scan rate. The triangles are amplifiers that determine the difference in the two input signals. The sample heater power is adjusted to keep the sample and reference at the same temperature during the scan.

In our study, this technique is employed to determine the content of crystal water in raw material for precise experiments. Then, the calcination process of our apatite-type LSO is investigated by this technique because the heat flow would be affected with the phase transitions or chemical reactions.

II.3. Ab initio calculations modeling

II.3.1 Introduction of ab initio calculation

The underlying physical laws necessary for the mathematical theory of a large part of physics and the whole of chemistry are thus completely known and the difficulty is only that the exact application of these laws leads to equations much too complicated to be soluble ---P.A.M. Dirac, Proc. Roy. Soc. (London), 123 714 (1929)

Ab initio (or first-principles) calculation[44-46] is one of the most commonly used quantum methods in the fields of solid state physics and quantum chemistry for determination of physical and quantum factors of systems. The objective of most ab initio approaches based on fundamental quantum theory is to calculate stationary states of electrons in the electrostatic field of atomic nuclei, i.e., the electronic structure. The energy of this ground state can then serve as a basis for investigation of displacements of the nuclei which leads to determination of

many macroscopic properties important in technology. The calculation scale and time lies in an extremely small scale. It can deal with system of a single molecule, a group of molecules, a liquid or solid, as shown in Figure II.18 of the compassion of different simulation methods.

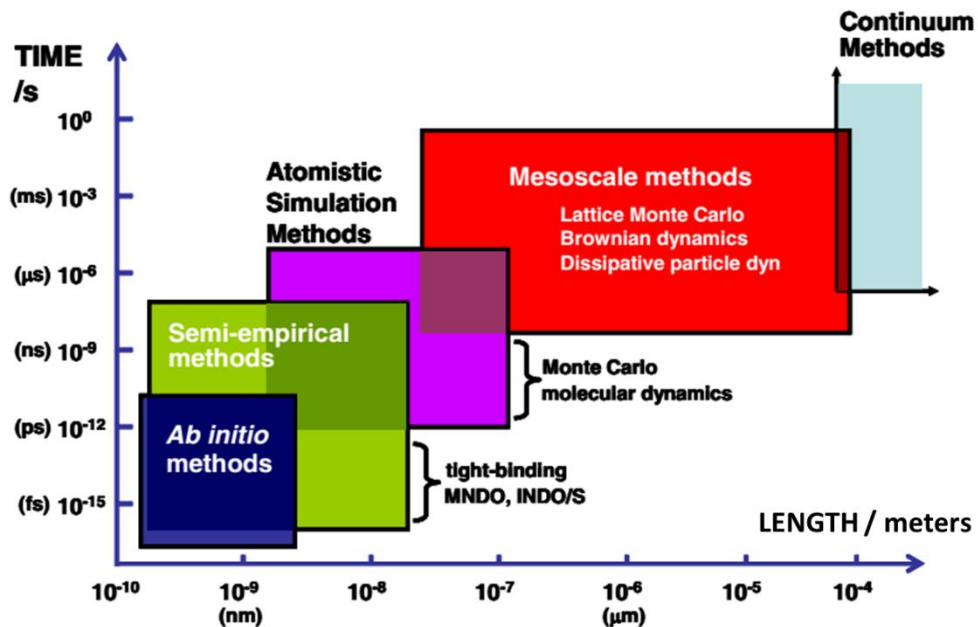


Figure II. 18. Schematic illustration of the simulation methods for different length and time scales

This calculation is based on the Schrödinger equation, firstly formulated in late 1925, and immediately first attempts to develop applicable theories were made. However, a really successful approach providing a solution of this equation for many-body problem that is relevant to solids was done almost 50 years later. The density functional theory (DFT) was invented to include correlation effects without using the very costly wave function methods. Nowadays, most ab initio methods used in materials science and solid state physics are based on the DFT.

The main advantage of ab initio approach is its independence on experimental data. Unlike in the case of semi-empirical methods, there is no need for calibration or fitting parameters. Thus, ab initio methods can also be used for calculations of some structural and mechanical

characteristics of hypothetical systems, i.e., for prediction of properties of materials that have not yet been developed. Meanwhile, such investigations can provide a better understanding of micro mechanisms of materials.

II.3.2 Density functional theory (DFT)

Density functional theory (DFT) is a computational quantum mechanical modelling method used in physics, chemistry and materials science to investigate the electronic structure (principally the ground state) of many-body systems, in particular atoms, molecules, and the condensed phases. In many cases the results of DFT calculations for solid-state systems agree quite satisfactorily with experimental data. Computational costs are relatively low when compared to traditional methods, such as Hartree–Fock theory and its descendants based on the complex many-electron wavefunction.

II.3.2.1 Fundamental Principles

DFT methods model all the electrons in a system, and the zero energy corresponds to having all nuclei and electrons at an infinite distance from one another. Quantum mechanics (QM) is the correct mathematical description of the behavior of electrons and thus of chemistry. In theory, QM can predict any property of an individual atom or molecule exactly. In practice, the QM equations have only been solved exactly for one electron systems. These approximations can be very useful, but this requires an amount of sophistication on the part of the researcher to know when each approximation is valid and how accurate the results are likely to be.

The Schrödinger equation, shown in EQN II.8, was devised as an equivalent formulation of QM and it is the basis for nearly all computational chemistry methods.

$$\hat{H}\Psi = E\Psi \qquad \text{EQN II.8}$$

where \widehat{H} is the Hamiltonian operator, Ψ a wave function, and E the energy. The wave function C is a function of the electron and nuclear positions. As the name implies, this is the description of an electron as a wave. The Hamiltonian operator \widehat{H} is, in general,

$$\widehat{H} = -\sum_{\alpha=1}^N \left\{ \frac{\hbar^2}{2M_{\alpha}} \nabla_{\alpha}^2 \right\} - \sum_{i=1}^n \left\{ \frac{\hbar^2}{2m_i} \nabla_i^2 \right\} - \sum_{\alpha,i} \frac{Z_{\alpha} e^2}{r_{\alpha i}} + \sum_{\alpha, \beta \neq \alpha} \frac{Z_{\alpha} Z_{\beta} e^2}{R_{\alpha \beta}} + \sum_{i, j \neq i} \frac{e^2}{r_{ij}} \quad \text{EQN II.9}$$

where $\nabla_{i/\alpha}^2$ is the Laplacian operator acting on particles of electrons/nuclei. M/m is the mass of the particles.

It can be simply expressed focusing on the expression of energy,

$$\widehat{H} = \widehat{T}_{\alpha} + \widehat{T}_e + \widehat{V}_{\alpha\alpha} + \widehat{V}_{\alpha e} + \widehat{V}_{ee} \quad \text{EQN II.10}$$

Where,

$\widehat{T}_{\alpha}, \widehat{T}_e$ - Kinetic energies of the electrons and nuclei;

$\widehat{V}_{\alpha\alpha}, \widehat{V}_{\alpha e}, \widehat{V}_{ee}$ - Potential energy of nuclei-nuclei, electrons-nuclei, electrons-electrons interaction;

The eigenvalues of equation cannot be calculated accurately in the case of hydrogen-like systems. In the case of a multi-electronic system, because of electronic interactions, there is no exact analytical solution of Schrödinger equation. In order to find acceptable solution of the equation, we need to make approximations of Hamiltonian operator. The first approximation is the Born-Oppenheimer approximation [47].

II.3.2.2 Born-Oppenheimer approximation

All methods of solving the Schrödinger equation based on this approximation, where its authors (Born and Oppenheimer) assume that there is a time scale difference between the electronic and nuclear motions due to a big difference in mass between the nuclei and electrons. Therefore, it

is possible to decouple the movement of the nuclei and the electrons, then to write the wave function into two wave functions: nuclei and electrons.

$$\Psi(\vec{r}, \vec{R}) = \Psi_\alpha(\vec{R}) + \Psi_e(\vec{r}, \vec{R}) \quad \text{EQN II.11}$$

Where $\Psi_\alpha(\vec{R})$ is the wave function associated to the nuclei and $\Psi_e(\vec{r}, \vec{R})$ is the wave function associated to the electrons and the nuclei are fixed in the position of \vec{R} . The total energy is then written as the sum of a nuclear and electronic contribution.

$$E = E_\alpha(\vec{R}) + E_e(\vec{R}) \quad \text{EQN II.12}$$

This approximation is known as the Born-Oppenheimer adiabatic approximation. The position of the nuclei in the field is supposedly fixed. The parameter of nuclei kinetic energies in Hamiltonian operator can be omitted.

$$(\hat{T}_e + \hat{V}_{\alpha\alpha} + \hat{V}_{\alpha e} + \hat{V}_{ee})\Psi_e(\vec{r}, \vec{R}) = E_e(\vec{R})\Psi_e(\vec{r}, \vec{R}) \quad \text{EQN II.13}$$

Some methods are employed for the solution of this equation. The premier effective method is that of Hartree-Fock based on the assumption of free electrons. This method is quite useful to quantum chemistry to treat the atoms and molecules, but they are less accuracy for solids calculation. The DFT is proved probably to be a more modern and powerful method due to the two theorems by Hohenberg and Kohn [48] established in 1964. These authors have demonstrated that all aspects of the electronic structure of a system in a non-degenerate ground state is completely determined by its electron density instead of its wave function.

II.3.2.3 Hohenberg and Kohn theorems

The Hohenberg and Kohn theorems relate to any system consisting of electrons moving under the influence of an external potential $v_{\text{ext}}(\mathbf{r})$. Stated simply they are as follows:

Theorem 1:

The electron density $\rho(\mathbf{r})$ determines the external potential $v_{\text{ext}}(\mathbf{r})$. The energy functional $E[\rho(\mathbf{r})]$ alluded to in the first Hohenberg-Kohn theorem can be written in terms of the external potential $v_{\text{ext}}(\mathbf{r})$ in the following way:

$$E[\rho(\vec{r})] = F[\rho(\vec{r})] + \int \rho(\vec{r})v_{\text{ext}}(\vec{r}) d\vec{r} \quad \text{EQN II.14}$$

Where $\int \rho(\vec{r})v_{\text{ext}}(\vec{r}) d\vec{r}$ represents the core-electron interaction. $F[\rho(\vec{r})]$ is a function of density $\rho(\vec{r})$ independent of external potential $v_{\text{ext}}(\vec{r})$; it contains the contributions of kinetic and coulomb energy:

$$F[\rho(\vec{r})] = T[\rho(\vec{r})] + V_{ee}[\rho(\vec{r})] = T[\rho(\vec{r})] + E_H[\rho(\vec{r})] + E_{xc}[\rho(\vec{r})] \quad \text{EQN II.15}$$

Where $T[\rho(\vec{r})]$ is the kinetic energy of the electron system and $V_{ee}[\rho(\vec{r})]$ is the term electron-electron interaction that includes Hartree energy $E_H[\rho(\vec{r})]$ (the Coulomb repulsive of electron-electron) and the exchange and correlation energy $E_{xc}[\rho(\vec{r})]$.

In this theorem, stated simply, the electrons determine the positions of the nuclei in a system, and also all ground state electronic properties, because $v_{\text{ext}}(\mathbf{r})$ and N completely define H in N -electron systems.

Theorem 2:

For a given external potential and a fixed number of electrons, the ground state energy can be obtained variationally: the ground state of the system is the global minimum of the functional $E[\rho(\vec{r})]$ and density which minimizes this function is the density of the ground state $\rho_0(\vec{r})$.

$$\frac{[\partial E[\rho(\vec{r})]]}{\partial \rho(\vec{r})} \Big|_{\rho(\vec{r})=\rho_0(\vec{r})} = 0 \quad \text{EQN II.16}$$

Although the Hohenberg-Kohn theorems are extremely powerful, they do not offer a way of computing the ground-state density of a system in practice. About one year after the seminal DFT paper by Hohenberg and Kohn, Kohn and Sham[49] designed a simple method for

carrying-out DFT calculations, that retains the exact nature of DFT. This method is described in next.

II.3.2.4 The Kohn-Sham Formulation

The Kohn-Sham formulation centers on mapping the full interacting system with the real potential, onto a fictitious non-interacting system whereby the electrons move within an effective "Kohn-Sham" single-particle potential $v_{KS}(r)$. The Kohn-Sham method is still exact since it yields the same ground state density as the real system, but greatly facilitates the calculation.

The Kohn-Sham potential $v_{KS}(r)$ is given by,

$$v_{KS}(r) = v_{ext}(r) + v_H(r) + v_{xc}(r) \quad \text{EQN II.17}$$

with the Hartree potential $v_H(r)$,

$$v_H(r) = \frac{\partial E_H[\rho(r)]}{\partial \rho(r)} = \int \frac{\rho(r')}{|r-r'|} dr' \quad \text{EQN II.18}$$

and the exchange-correlation potential $v_{xc}(r)$

$$v_{xc}(r) = \frac{\partial E_{xc}[\rho(r)]}{\partial \rho(r)} \quad \text{EQN II.19}$$

The ground state density is obtained in practice by solving the one-electron Schrödinger equations,

$$\left[-\frac{\hbar^2}{2m_i} \nabla_i^2 + v_{ext}(r) + v_H(r) + v_{xc}(r) \right] \psi_i(\vec{r}) = E_i \psi_i(\vec{r}), i = 1, \dots, N \quad \text{EQN II.20}$$

Determining the ground state of the system, then returning to solve, with self-consistent manner, the set of equations (EQN II.20) is known as Kohn-Sham equation. The sum of three $v_{ext}(r) + v_H(r) + v_{xc}(r)$ is an effective potential $v_{KS}(r)$ which can be characterized as it depends only on the parameter r . This method is formally correct, but for the practical calculation, the exchange

and correlation energy, which is a density functional, requires the introduction of some approximations.

II.3.2.5 The exchange-correlation functionals

The fact that the DFT gives no information on the form of the exchange-correlation functional $E_{xc}[\rho(r)]$, meanwhile the approximation have to be introduced for its determination must be applicable to different systems. The actual calculation of the energy and the potential for exchange-correlation is based on a number of approximations.

Local-density approximation (LDA)

The local-density approximation (LDA) relies on the assumption that the electron density varies slowly in space and therefore the exchange-correlation terms depend only on the local value of $\rho(r)$; that is to say, it deals with a non-homogeneous system as being locally homogeneous. In this regard, LDA is generally synonymous with functional based on the homogeneous electron gas (HEG) approximation, which are then applied to realistic systems (molecules and solids).

In general, for a spin-unpolarized system, a local-density approximation for the exchange-correlation energy is written as

$$E_{xc}^{LDA}[\rho(\vec{r})] = \int \rho(\vec{r}) \varepsilon_{xc}[\rho(\vec{r})] d\vec{r} \quad \text{EQN II.21}$$

Where $\varepsilon_{xc}[\rho(\vec{r})]$ is the exchange-correlation energy per particle of a homogeneous electron gas of charge density $\rho(\vec{r})$.

The exchange-correlation energy is decomposed into exchange and correlation terms linearly,

$$E_{xc}^{LDA}[\rho(\vec{r})] = E_x^{LDA}[\rho(\vec{r})] + E_c^{LDA}[\rho(\vec{r})] \quad \text{EQN II.22}$$

The exchange-energy density of a HEG is known analytically. The LDA for exchange employs this expression under the approximation that the exchange-energy in a system where the density is not homogeneous, is obtained by applying the HEG results pointwise, yielding the expression

$$E_x^{LDA}[\rho(\vec{r})] = -\frac{3}{4}\left(\frac{3}{\pi}\right)^{1/3} \int \rho(\vec{r})^{4/3} d\vec{r} \quad \text{EQN II.23}$$

Accurate quantum Monte Carlo simulations for the energy of the HEG have been performed for several intermediate values of the density, in turn providing accurate values of the correlation energy density $E_c^{LDA}[\rho(\vec{r})]$. The most popular LDA's to the correlation energy density interpolate these accurate values obtained from simulation while reproducing the exactly known limiting behavior. Various approaches, using different analytic forms for $E_c^{LDA}[\rho(\vec{r})]$, have generated several LDA's for the correlation functional, including Vosko-Wilk-Nusair (VWN)[50]; Perdew-Zunger (PZ81)[51]; Cole-Perdew (CP)[52]; Perdew-Wang (PW92)[53].

The LDA can only describe the ground state of electronic systems but not the excited states. The wide band gap of semiconductors and insulator are underestimated in this approximation. For certain strong correlation effects systems, LDA approximation does not properly describe the system properties. In particular, the transition metal compounds of insulating type Mott-Hubbard insulating or charge transfer are predicted metal.

The extension of density functional to spin-polarized systems is straightforward for exchange, where the exact spin-scaling is known, but for correlation further approximations must be employed. A spin polarized system in DFT employs two spin-densities, $\rho_\alpha(\vec{r})$ and $\rho_\beta(\vec{r})$ with $\rho(\vec{r}) = \rho_\alpha(\vec{r}) + \rho_\beta(\vec{r})$, and the form of the local-spin-density approximation (LSDA) is

$$E_{xc}^{LSDA}[\rho_\alpha(\vec{r}), \rho_\beta(\vec{r})] = \int \rho(\vec{r}) \varepsilon_{xc}[\rho_\alpha(\vec{r}), \rho_\beta(\vec{r})] d\vec{r} \quad \text{EQN II.24}$$

Generalized gradient approximations (GGA)

The Generalized gradient approximations bring an improvement compared to the LDA. In the local approximation, the exchange and correlation potential depends only on the density, whereas in the GGA approximation, the potential is expressed as a function of local electron density and its gradient.

$$E_{xc}^{GGA}[\rho(\vec{r})] = \int \rho(\vec{r}) f[\rho(\vec{r}), \nabla\rho(\vec{r})] d\vec{r} \quad \text{EQN II.25}$$

Where, $f[\rho(\vec{r}), \nabla\rho(\vec{r})]$ was the function of exchange energy and dependent correlation of the electron density and its gradient.

There are several versions of GGA most frequently used which are introduced by Perdew and Wang (PW91), Perdew, Burke and Ernzerhof.

In many cases, the GGA approximation provides better results than LDA for total energy, cohesive energies, the volumes to balance and incompressibility modules. However the systems with strong correlations are poorly described.

Hubbard-corrected energy functionals (LDA+U, GGA+U)

The basic idea behind DFT+U is to treat the strong on-site Coulomb interaction of localized electrons, which is not correctly described by LDA or GGA, with an additional Hubbard-like term. The on-site Coulomb interactions are particularly strong for localized d and f electrons, but can be also important for p localized orbitals. The strength of the on-site interactions is usually described by parameters U (on site Coulomb) and J (on site exchange). Hubbard correction is added to the energy functional in order to overcome the imprecision of the strong correlations systems calculation.

$$E_{DFT+U} = E_{DFT} + \sum_a \frac{U-J}{2} (\rho_a - \rho_a^2) \quad \text{EQN II.26}$$

where ρ_a is the atomic orbital occupation matrix.

II.3.2.6 Solving equations

To solve the equations of Kohn-Sham, a basic status has been chosen to represent the electron density $\rho(r)$, the potential $V(r)$ and Kohn-Sham orbitals. The process of the resolution is shown in Figure II.19.

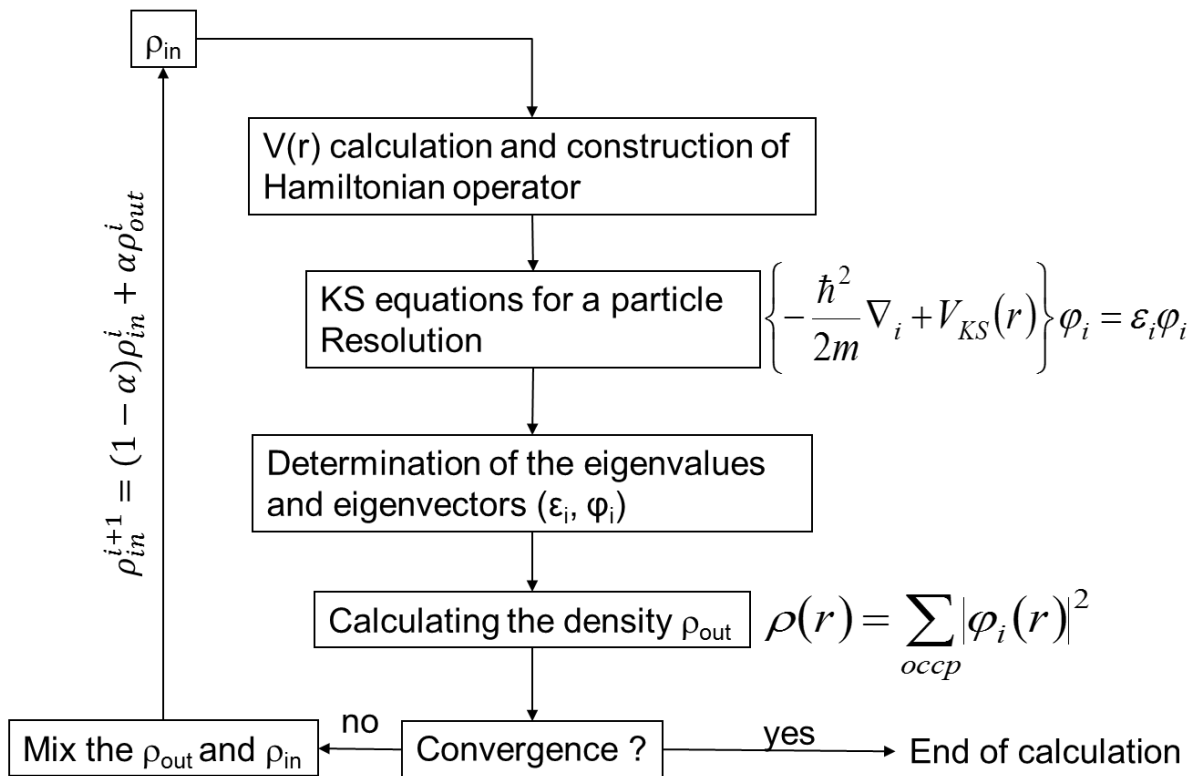


Figure II. 19. Flowchart of a self-consistent calculation in a method based on the DFT calculation

Conveniently, the value of forces on the atoms can be get at the end of each self-consistent electronic cycle and use of conjugate gradient algorithms, for minimizing the energy and determining the optimum geometry or performing the calculations molecular dynamics.

II.3.3 The pseudopotentials

The pseudopotential is used as an approximation for the simplified description of complex systems. It is an attempt to replace the complicated effects of the motion of the core (i.e. non-

valence) electrons of an atom and its nucleus with a pseudopotential, so that the Schrödinger equation contains a modified effective potential term instead of the Coulombic potential term for core electrons normally found in the Schrödinger equation.

Some pseudopotentials probably employed in our calculation are introduced as follows:

Norm-conserving pseudopotentials (NCP)

The necessary characteristics for the construction of a pseudopotential of Norm-conserving pseudopotentials were proposed by Hamann et al. 1979 [54]. It should satisfy four properties:

- Real and Pseudo states have the same eigenvalues (for a given configuration);
- Real and Pseudo wavefunctions agree beyond a cut-off radius;
- The integrals from 0 to r of the real and pseudo charge densities agree for $r > r_c$ (Norm-Conserving condition)

$$4\pi \int_0^R |\varphi_{real}(r)|^2 r^2 dr = 4\pi \int_0^R |\varphi_{ps}(r)|^2 r^2 dr \quad \text{EQN II.27}$$

- The logarithmic derivatives and their first energy derivative of real and pseudo wavefunctions match at the cut-off radius.

Ultrasoft pseudopotentials (USPP)

Many modern pseudopotential calculations use a generalisation of the Kleinman-Bylander form known as “ultrasoft” pseudopotentials, which were developed by Vanderbilt in the early 1990s [55]. As the name suggests, ultrasoft pseudopotentials attain much smoother (softer) pseudo-wavefunctions so use considerably fewer plane-waves for calculations of the same accuracy.

Projector augmented wave method (PAW)

Valence wavefunctions tend to have rapid oscillations near ion cores due to the requirement that they are orthogonal to core states; this situation is problematic because it requires many Fourier components (or in the case of grid-based methods, a very fine mesh) to describe the

wavefunctions accurately. The PAW approach addresses this issue by transforming these rapidly oscillating wavefunctions into smooth wavefunctions which are more computationally convenient, and provides a way to calculate all-electron properties from these smooth wavefunctions. [56]

The wave function is rewritten as follows:

$$|\psi\rangle = |\psi^{ps}\rangle - \sum_i |\phi_i^{ps}\rangle c_i + \sum_i |\phi_i\rangle c_i \quad \text{EQN II.28}$$

Where $\sum_i |\phi_i^{ps}\rangle c_i$ is the development of the base $|\psi^{ps}\rangle$ on a pseudo partial waves and $\sum_i |\phi_i\rangle c_i$ is the development of $|\psi\rangle$ on a basis of partial waves, within the volume of spheres $\Omega_{\vec{R}}$ around atomic sites indicated by \vec{R} . The coefficients c_i are scalar products of wave functions and pseudo-projection functions within the area $\Omega_{\vec{R}}$.

$$c_i = \langle p_i | \phi_i^{ps} \rangle \quad \text{EQN II.29}$$

It works with three objects:

1. Partial wave $|\phi_i\rangle$ obtained by radial integration of the Schrödinger equation for atomic energy ε_i which are orthogonal to the functions of the core;
2. The pseudo partial wave $|\psi^{ps}\rangle$ coincides with the exact partial wave to the outside of the core area;
3. The projection function of each partial wave $|p_i\rangle$, shown in region $\Omega_{\vec{R}}$ which satisfies the relationship $\langle p_i | \phi_i^{ps} \rangle = \delta_{ij}$.

II.3.4 Computational application

The DFT calculation is widely used as an efficient and economical way to get crystal parameters, electronic structures, total energy and magnetic properties etc., summarized as ground state

properties. At the same time, it can meet various requirements of material properties. Figure II.20 shows the most common applications with DFT calculation.

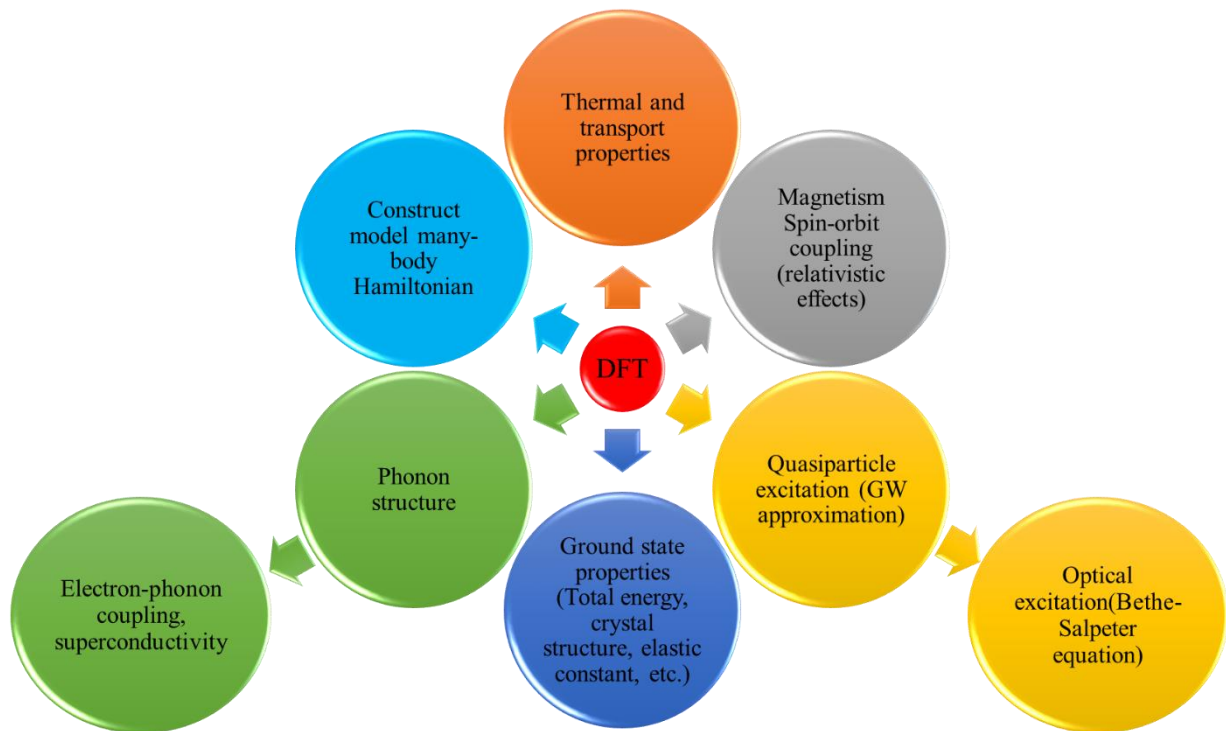


Figure II. 20. Material properties studies with DFT calculation

II.3.5 Vienna Ab initio Simulation Package (VASP)

The Vienna Ab initio Simulation Package (VASP) [57] is a computer program for atomic scale materials modelling, e.g. electronic structure calculations and quantum-mechanical molecular dynamics, from first principles. It computes an approximate solution to the many-body Schrödinger equation, either within density functional theory (DFT), solving the Kohn-Sham equations.

In our work, the VASP is adopted to study the structural and electronic properties, including the Fermi energy, the density of states, band structure etc., of the Sr, Ge doped apatite-type lanthanum silicates LSO. This code is known for good parallelization which authorizes the calculation on more than one hundred atoms systems. It provides accuracy and efficiency for computer simulation ab initio and for these reasons it has become a widely used code.

The wave functions used in the VASP are developed on a plane wave basis adapted to the periodic calculation and have the advantage of being easily implemented with calculations using USPP of Vanderbilt and PAW. Blöchl and Kresse et al. [58] showed that the PAW method is especially good for the transition metal oxides, lanthanides, actinides and magnetic systems. So we used the PAW method for all of our work.

The wave functions which developed in reciprocal space are defined for an infinite number of points k in the Brillouin zone, and each point contributes to the electronic potential. In order to numerically evaluate the integrals on the occupied states of each point, the calculation is performed with a grid of points k finite size. To automatically generate this grid points k in the VASP, the method of Monkhorst and Pack [59] is used. The integration of occupied states may be achieved by the method of the tetrahedra (Jepsen et al.[60]), with the corrections of Blöchl et al. [61]. The VASP code uses conjugate gradient type algorithms to relax the structures. In practice, to relax an atomic structure, we minimize Hellmann-Feynman forces until the residual force on each atom fall below 0.08 eV/\AA .

II.4 References

- [1] Xia C, Liu M. Low-temperature SOFCs based on Gd 0.1 Ce 0.9 O 1.95 fabricated by dry pressing. *Solid State Ionics*. 2001;144:249-55.
- [2] Chen G, You H-X, Kasai Y, Sato H, Abudula A. Characterization of planer cathode-supported SOFC prepared by a dual dry pressing method. *Journal of Alloys and Compounds*. 2011;509:5159-62.
- [3] Wang Z, Qian J, Cao J, Wang S, Wen T. Multilayer tape-casting method for anode-supported planar SOFCs. *Fuel Cells Bulletin*. 2007;2007:12-5.
- [4] He T, Lu Z, Huang Y, Guan P, Liu J, Su W. Characterization of YSZ electrolyte membrane tubes prepared by a vacuum casting method. *Journal of alloys and compounds*. 2002;337:231-6.
- [5] Jing S, Lifeng D, Jiang L. Cone-shaped cylindrical Ce 0.9 Gd 0.1 O 1.95 electrolyte prepared by slip casting and its application to solid oxide fuel cells. *Journal of Rare Earths*. 2012;30:53-6.
- [6] Wang Z, Qian J, Cao J, Wang S, Wen T. A study of multilayer tape casting method for anode-supported planar type solid oxide fuel cells (SOFCs). *Journal of Alloys and Compounds*. 2007;437:264-8.
- [7] Shanti N, Bierschenk D, Barnett S, Faber K. Direct lamination of solid oxide fuel cell anode support, anode, and electrolyte by sequential tape casting of thermoreversible gel slips. *Journal of Power Sources*. 2012;212:43-6.
- [8] Hansch R, Chowdhury MRR, Menzler NH. Screen printing of sol-gel-derived electrolytes for solid oxide fuel cell (SOFC) application. *Ceramics International*. 2009;35:803-11.
- [9] Zhao L, Huang X, Zhu R, Lu Z, Sun W, Zhang Y, et al. Optimization on technical parameters for fabrication of SDC film by screen-printing used as electrolyte in IT-SOFC. *Journal of Physics and Chemistry of Solids*. 2008;69:2019-24.
- [10] Dudek M, Tomov R, Wang C, Glowacki B, Tomczyk P, Socha R, et al. Feasibility of direct carbon solid oxide fuels cell (DC-SOFC) fabrication by inkjet printing technology. *Electrochimica Acta*. 2013;105:412-8.
- [11] Ried P, Lorenz C, Brönstrup A, Graule T, Menzler NH, Sitte W, et al. Processing of YSZ screen printing pastes and the characterization of the electrolyte layers for anode supported SOFC. *Journal of the European Ceramic Society*. 2008;28:1801-8.
- [12] Nagata A, Okayama H. Characterization of solid oxide fuel cell device having a three-layer film structure grown by RF magnetron sputtering. *Vacuum*. 2002;66:523-9.
- [13] Mahieu S, Ghekiere P, De Winter G, Depla D, De Gryse R, Lebedev O, et al. Influence of the Ar/O₂ ratio on the growth and biaxial alignment of yttria stabilized zirconia layers during reactive unbalanced magnetron sputtering. *Thin Solid Films*. 2005;484:18-25.
- [14] Wanzenberg E, Tietz F, Panjan P, Stöver D. Influence of pre-and post-heat treatment of anode substrates on the properties of DC-sputtered YSZ electrolyte films. *Solid State Ionics*. 2003;159:1-8.
- [15] Fondard J, Billard A, Bertrand G, Briois P. Synthesis and characterization of La₂NiO_{4+δ} coatings deposited by reactive magnetron sputtering using plasma emission monitoring. *Solid State Ionics*. 2014;265:73-9.
- [16] Fondard J, Billard A, Bertrand G, Fourcade S, Batocchi P, Mauvy F, et al. Effect of total pressure on La₂NiO₄ coatings deposited by reactive magnetron sputtering using plasma emission monitoring. *Surface and Coatings Technology*. 2015.
- [17] He X, Meng B, Sun Y, Liu B, Li M. Electron beam physical vapor deposition of YSZ electrolyte coatings for SOFCs. *Applied Surface Science*. 2008;254:7159-64.

- [18] Uhlenbruck S, Jordan N, Serra J, Buchkremer H, Stöver D. Application of electrolyte layers for solid oxide fuel cells by electron beam evaporation. *Solid State Ionics*. 2010;181:447-52.
- [19] Hidalgo H, Reguzina E, Millon E, Thomann A-L, Mathias J, Boulmer-Leborgne C, et al. Yttria-stabilized zirconia thin films deposited by pulsed-laser deposition and magnetron sputtering. *Surface and Coatings Technology*. 2011;205:4495-9.
- [20] Garcia G, Caro J, Santiso J, Pardo JA, Figueras A, Abrutis A. Pulsed injection MOCVD of YSZ thin films onto dense and porous substrates. *Chemical Vapor Deposition*. 2003;9:279-84.
- [21] Kim JW, Jang DY, Kim M, Choi HJ, Shim JH. Nano-granulization of gadolinia-doped ceria electrolyte surface by aerosol-assisted chemical vapor deposition for low-temperature solid oxide fuel cells. *Journal of Power Sources*. 2016;301:72-7.
- [22] Schlupp M, Prestat M, Martynczuk J, Rupp J, Bieberle-Hütter A, Gauckler L. Thin film growth of yttria stabilized zirconia by aerosol assisted chemical vapor deposition. *Journal of Power Sources*. 2012;202:47-55.
- [23] Hui R, Wang Z, Kesler O, Rose L, Jankovic J, Yick S, et al. Thermal plasma spraying for SOFCs: Applications, potential advantages, and challenges. *Journal of Power Sources*. 2007;170:308-23.
- [24] Zhang S-L, Li C-X, Li C-J, Yang G-J, Liu M. Application of high velocity oxygen fuel flame (HVOF) spraying to fabrication of La_{0.8}Sr_{0.2}Ga_{0.8}Mg_{0.2}O₃ electrolyte for solid oxide fuel cells. *Journal of Power Sources*. 2016;301:62-71.
- [25] Li C-J, Li C-X, Ning X-J. Performance of YSZ electrolyte layer deposited by atmospheric plasma spraying for cermet-supported tubular SOFC. *Vacuum*. 2004;73:699-703.
- [26] Zhang C, Li C-J, Zhang G, Ning X-J, Li C-X, Liao H, et al. Ionic conductivity and its temperature dependence of atmospheric plasma-sprayed yttria stabilized zirconia electrolyte. *Materials Science and Engineering: B*. 2007;137:24-30.
- [27] Rampon R, Marchand O, Filiatre C, Bertrand G. Influence of suspension characteristics on coatings microstructure obtained by suspension plasma spraying. *Surface and Coatings Technology*. 2008;202:4337-42.
- [28] Marchand O, Bertrand P, Mougín J, Comminges C, Planche M-P, Bertrand G. Characterization of suspension plasma-sprayed solid oxide fuel cell electrodes. *Surface and Coatings Technology*. 2010;205:993-8.
- [29] Sun F, Zhang N, Li J, Liao H. Preparation of dense silicate electrolyte coating with low pressure plasma spraying and very low pressure plasma spraying for intermediate-temperature solid oxide fuel cells. *Journal of Power Sources*. 2013;223:36-41.
- [30] Satcher J. *Novel Materials from Sol-Gel Chemistry*. *Science & Technology Review*. 2005;925:422-7794.
- [31] Tao S, Irvine JT. Preparation and characterisation of apatite-type lanthanum silicates by a sol-gel process. *Materials research bulletin*. 2001;36:1245-58.
- [32] Celerier S, Laberty-Robert C, Ansart F, Calmet C, Stevens P. Synthesis by sol-gel route of oxyapatite powders for dense ceramics: Applications as electrolytes for solid oxide fuel cells. *Journal of the European Ceramic Society*. 2005;25:2665-8.
- [33] Celerier S, Laberty C, Ansart F, Lenormand P, Stevens P. New chemical route based on sol-gel process for the synthesis of oxyapatite La_{9.33}Si₆O₂₆. *Ceramics International*. 2006;32:271-6.
- [34] Takeda N, Itagaki Y, Sadaoka Y. Relationship between Pre-Exponential Factor and Activation Energy of Conductivity in Sintered Ln_{9.33+x/3}Si_{6-x}M_xO₂₆ (Ln= La, Nd, Sm, M= Al, Gd) with Apatite-like Structure. *Journal of the Ceramic Society of Japan*. 2007;115:643-7.

- [35] Abram E, Sinclair D, West A. A novel enhancement of ionic conductivity in the cation-deficient apatite $\text{La}_{9.33}(\text{SiO}_4)_6\text{O}_2$. *Journal of Materials Chemistry*. 2001;11:1978-9.
- [36] Jothinathan E, Vanmeensel K, Vleugels J, Van der Biest O. Synthesis of nano-crystalline apatite type electrolyte powders for solid oxide fuel cells. *Journal of the European Ceramic Society*. 2010;30:1699-706.
- [37] Zhou J, Ye X, Li J, Wang S, Wen T. Synthesis and characterization of apatite-type $\text{La}_{9.67}\text{Si}_{6-x}\text{Al}_x\text{O}_{26.5-x/2}$ electrolyte materials and compatible cathode materials. *Solid State Ionics*. 2011;201:81-6.
- [38] Zhang L, He HQ, Wu H, Li C-Z, Jiang SP. Synthesis and characterization of doped $\text{La}_9\text{ASi}_6\text{O}_{26.5}$ (A= Ca, Sr, Ba) oxyapatite electrolyte by a water-based gel-casting route. *international journal of hydrogen energy*. 2011;36:6862-74.
- [39] Sun F. Caract érisation de rev êtements de silicate de lanthane de structure apatite dop é au magn ésium r éalis és par projection plasma en vue d'application comme électrolyte de pile à combustible de type IT-SOFC: Universit é de Technologie de Belfort-Montbéliard; 2010.
- [40] Kolitsch U, Seifert H, Aldinger F. The Identity of Monoclinic La_2O_3 and Monoclinic Pr_2O_3 with $\text{La}_{9.33}(\text{SiO}_4)_6\text{O}_2$ and $\text{Pr}_{9.33}(\text{SiO}_4)_6\text{O}_2$, Respectively. *Journal of Solid State Chemistry*. 1995;120:38-42.
- [41] D éportes C, Duclot M, Fabry P. *Electrochimie des solides*: Presses universitaires de Grenoble; 1994.
- [42] Aoki M, Chiang YM, Kosacki I, Lee L, Tuller H, Liu Y. Solute Segregation and Grain-Boundary Impedance in High-Purity Stabilized Zirconia. *Journal of the American ceramic society*. 1996;79:1169-80.
- [43] Coats A, Redfern J. Thermogravimetric analysis. A review. *Analyst*. 1963;88:906-24.
- [44] Cramer CJ. *Essentials of computational chemistry: theories and models*: John Wiley & Sons; 2013.
- [45] Jensen F. *Introduction to computational chemistry*: John Wiley & Sons; 2013.
- [46] Young D. *Computational chemistry: a practical guide for applying techniques to real world problems*: John Wiley & Sons; 2004.
- [47] Born M, Oppenheimer R. Zur quantentheorie der molekeln. *Annalen der Physik*. 1927;389:457-84.
- [48] Hohenberg P, Kohn W. Inhomogeneous electron gas. *Physical review*. 1964;136:B864.
- [49] Kohn W, Sham LJ. Self-consistent equations including exchange and correlation effects. *Physical Review*. 1965;140:A1133.
- [50] Vosko S, Wilk L, Nusair M. Accurate spin-dependent electron liquid correlation energies for local spin density calculations: a critical analysis. *Canadian Journal of physics*. 1980;58:1200-11.
- [51] Perdew JP, Zunger A. Self-interaction correction to density-functional approximations for many-electron systems. *Physical Review B*. 1981;23:5048.
- [52] Cole LA, Perdew J. Calculated electron affinities of the elements. *Physical Review A*. 1982;25:1265.
- [53] Perdew JP, Wang Y. Accurate and simple analytic representation of the electron-gas correlation energy. *Physical Review B*. 1992;45:13244.
- [54] Hamann D, Schl üter M, Chiang C. Norm-conserving pseudopotentials. *Physical Review Letters*. 1979;43:1494.
- [55] Vanderbilt D. Soft self-consistent pseudopotentials in a generalized eigenvalue formalism. *Physical Review B*. 1990;41:7892.
- [56] Bl öchl PE. Projector augmented-wave method. *Physical Review B*. 1994;50:17953.
- [57] Kresse G, Furthmüller J. *VASP the Guide*. Computational Physics, Faculty of Physics, Universität Wien, Sensengasse. 2001;8.

- [58] Kresse G, Joubert D. From ultrasoft pseudopotentials to the projector augmented-wave method. *Physical Review B*. 1999;59:1758.
- [59] Monkhorst HJ, Pack JD. Special points for Brillouin-zone integrations. *Physical Review B*. 1976;13:5188.
- [60] Jepson O, Anderson O. The electronic structure of hcp Ytterbium. *Solid State Communications*. 1971;9:1763-7.
- [61] Blöchl PE, Jepsen O, Andersen OK. Improved tetrahedron method for Brillouin-zone integrations. *Physical Review B*. 1994;49:16223.

CHAPTER III. Ab initio study of $\text{La}_{10-x}\text{Sr}_x(\text{Si,Ge})_6\text{O}_{27-0.5x}$ apatite for SOFC electrolyte

In this chapter, we present the ab-initio calculation on Sr, Ge-doped lanthanum silicates LSO. The calculation is based on the density functional theory (DFT) with the code VASP. Two doping positions, Sr dopant at La position and Ge dopant at Si position, have been investigated. Doped LSO conductivity is studied by the parameters of lattice constant, electronic properties, and formation energies.

III.1 Introduction

Many contributions of numerical modeling and simulations are quite important for the understanding and technological improvement of SOFC. They incorporate the known physical and chemical phenomena occurring inside SOFC to predict its performance. The simulation work is speedy and relatively easy once the model is programmed and validated.

Some common simulation methods for predicting the performance of SOFCs or the materials are summarized from the open literatures: artificial intelligence, finite element and finite volume methods, molecular dynamics, ab initio calculation etc.

S.O.T. Ogaji et al [1] reported that both computation methods and novel approaches based on artificial intelligence techniques can provide similar accuracy in the modeling of a SOFC. The operating voltage, the operating efficiency, the power output and the temperature generated of fuel cells are evaluated with this simulation method. However the prediction of the materials characteristics with this method is relatively rare in the literatures.

Finite element methods [2] and finite volume methods [3] are employed to analyze thermal pressing, electrochemical oxidation of fuel composition and some output characteristics of a SOFC. It is demonstrated to be an efficient way to predict and evaluate the performance of a SOFC system.

Molecular dynamic is a numerical simulation method for the physical/chemical phenomena in complex systems, which may involve thermal management, mass and charge transport, together

with internal reforming reactions and electrochemical reactions in the SOFC. It is the most widely used method to investigate the performance of fuel cell system, as well as the materials' properties. As for the electrolyte, molecular dynamics techniques are employed to explore the diffusion of oxide ions, then to approximate the ionic conductivity of the electrolyte materials. C.W. Huang et al [4] reported the simulation work on ionic conduction process of oxygen in $Ce_{1-x}M_xO_{2-x/2}$. The ionic conductivity was evaluated from the self-diffusivity of oxygen ions, described by the Nernst–Einstein (N–E) relation. The self-diffusivity can be related with mean-square displacement (MSD) which can be acquired by the molecular dynamics simulation. The simulation illustrates quite few electronic features which can be completed by ab initio calculation.

Ab initio calculation of the SOFC electrolyte is rarely reported in literatures. Recently Sha Xue et al [5] investigated the atomic and electronic structures of the battery electrolyte. It shows this calculation can be well applied in the investigation of fundamental properties of the materials.

III.2 $La_{10-x}Sr_x(Si,Ge)_6O_{27-0.5x}$ apatite study

Since rare earth silicates with a general formula of $RE_{10-x}Si_6O_{27-1.5x}$ were used as an electrolyte in a SOFC by Nakayama et al[6] for the first time, they have attracted considerable attention due to their higher oxide ionic conductivity and lower activation energy. Among these, $La_{10}Si_6O_{27}$ series is more promising due to the higher ionic conductivity compared to some other rare earth apatite.[7] Their properties can be modified by various doping methods. Currently, the two major applied doping methods are element substitution at the La position and Si position. Mg, Sr, Ba as alkaline earth metal are widely used to substitute the La position, and Sr is the most common element due to its similar chemical properties with La. As an example of Sr substitution is the Sr-doped apatite-type lanthanum silicates ($La_9Sr_1Si_6O_{26.5}$) synthesized by Bonhomme et al.[8] A large number of works are also focused on the Si position doping. S. Nakayama et al investigated the Ge substitution at Si position and A. Orera et al.[9,

10] further expanded the substitution element from Ge to other different elements doping. Table III.1 summaries the ionic conductivities and activation energy obtained from the previous literature. As can be seen, the ionic conductivities show a significant decrease with increasing the ratio of Sr-doping while the amount of La and Sr remains unchanged. Besides, it is also seen that Ge substitution apatite electrolyte has a lower ionic conductivity compared to the Si substitution.

Table III. 1. Experimental ionic conductivities and activation energy of Ge, Sr substitution LSO apatite. $(La_{10-x}Sr_x)(Si,Ge)_6$ in the table represents $La_{10-x}Sr_x(Si,Ge)_6O_{27-0.5x}$ for short, similarly hereinafter)

	$(La_{10}Sr_0)Ge_6$ [10]	$(La_{10}Sr_0)Si_6$ [11, 12]	$(La_9Sr_1)Si_6$ [8]	$(La_8Sr_2)Si_6$ [11, 12]
Ionic conductivity ($S \cdot cm^{-1}$, 700 °C)	$5 \sim 8 \times 10^{-3}$	$10.8 \sim 20 \times 10^{-2}$	$2.4 \sim 2.6 \times 10^{-3}$	2.9×10^{-7}
Activation energy(eV)	-	0.47	0.78	1.34
Electronic conductivity($k\Omega$)	1.2 (500 °C)	0.19	-	-

Calculation methods based on the first principle was also widely used to analyze the material microstructure, properties and performances. Meanwhile, the oxygen diffusion in different types of electrolyte including LSO electrolyte has been summarized by A. Chronos et al.[13], and the ionic transportation mechanism has been widely studied using atomistic simulation. However, only few studies focusing on the apatite electrolyte for SOFC using DFT are available. In the current work, based on DFT, systematic computational results of Sr, Ge - doped LSO apatite for SOFC electrolyte are presented and doping position effect on the ionic conductivity and activation energy are also studied. Calculation results are also compared to previous experimental results.

III.2.1 Calculation details

Ultrasoft pseudo potential [14] method based on density functional theory (DFT) in the generalized gradient approximation (GGA) proposed by Perdew et al was used to perform the

calculations[15]. The Vienna ab initio simulation package (VASP) [16-18] was used to explore the influence of doping positions by applying a plane-wave basis within the projector augmented-wave method. The DFT is an efficient method to predict the ground state properties and thus to analyze the properties of materials. As a first step, a single apatite cell was built to obtain the DOS (Density of States) calculation results through the structure optimization and static calculation. The Brillouin zone scale was set to $3 \times 3 \times 3$ gamma centered k-point mesh in the Monkhorst-Pack scheme. Nevertheless, the k-point was changed to $7 \times 7 \times 7$ in the DOS calculation. An energy cut-off of 380 eV was used in all of our calculations.

The activation energy of each group is calculated with a model of oxygen migration along the ionic channel. For the considered doping effect, the migration channel can be supposed directly along c-axis. The energy barrier of oxygen migration could be also approximated as the activation energy.

To start the calculation, four important input files are necessary: INCAR, POSCAR, POTCAR and KPOINTS. INCAR is the central input file which determines 'what to do and how to do it', and contains a relatively large number of parameters. POSCAR contains the lattice geometry and the ionic positions. POTCAR file contains the pseudopotential for each atomic species used in the calculation. KPOINTS must contain the k-point coordinates and weights or the mesh size for creating the k-point grid. A calculation period costs several hours to one or two days and the code VASP is run at the Mésocentre de calcul de Franche-Comté

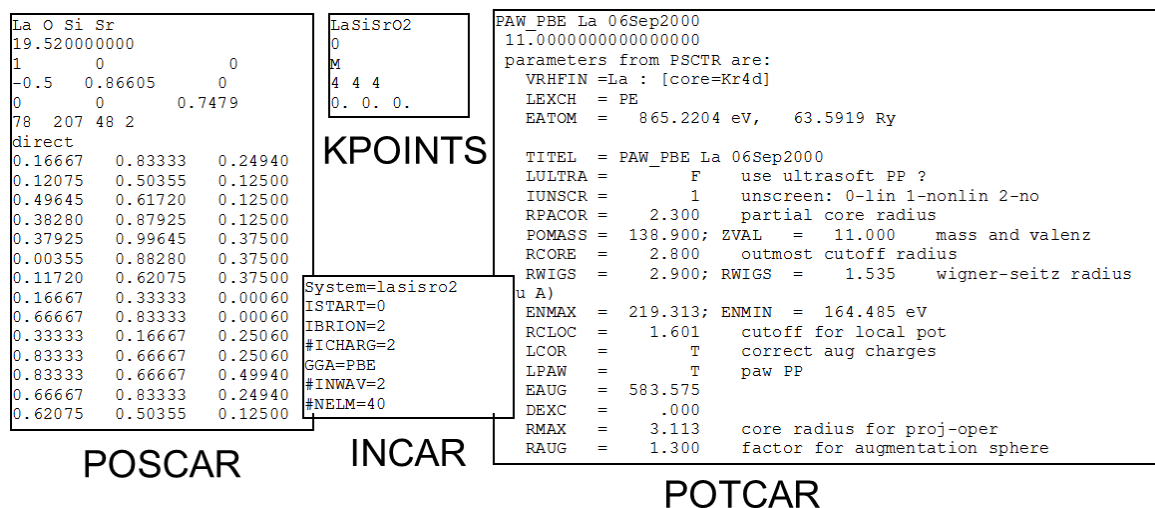


Figure III. 1. Schematic diagram of the input files for VASP

III.2.2 Structure properties

Table III.2 gives the lattice parameter [19] of an apatite structure $\text{La}_{10}\text{Si}_6\text{O}_{27}$ in p63/m group to build structure $\text{La}_{10-x}\text{Sr}_x(\text{Si},\text{Ge})_6\text{O}_{27-0.5x}$. The oxygen ion migrates in LSO materials, thus the amount of oxygen atoms frequently changes. If the position and La/Sr and Si/Ge ratios are given, the Si-O tetrahedron and crystal frame will be determined. In this work, the calculation takes into account the relative number between La/Sr and Si/Ge.

Table III. 2. The atoms coordinate of lanthanum-silicon apatite structure

Coordinate	La1	La2/Sr	Si/Ge	O1	O2	O3	O4
X	0.2289	0.3333	0.4020	0.3224	0.5965	0.3443	0
Y	-0.0125	0.6667	0.3718	0.4847	0.4731	0.2549	0
Z	0.2500	-0.0007	0.2500	0.2500	0.2500	0.0701	0.2500

III.3 Sr-doped LSO study

III.3.1 electronic properties

Figure III.2 shows the LSO apatite structure and the oxygen migration channel. As it can be seen, there is a large number of atoms in each single cell of the apatite structure. In order to check the accuracy of the calculation, the lattice constant values in each apatite cell are set as $a=b=9.9000 \text{ \AA}$ and $c=7.3294 \text{ \AA}$, which slightly differs from the experimental values.

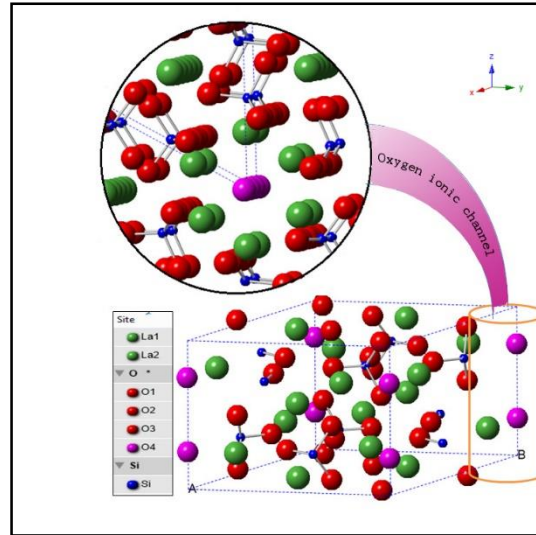


Figure III. 2. Schematic diagram of lanthanum-silicon apatite structure

Table III.3 lists the results of the calculated and experimental lattice parameters [10, 11]. It is noted that the results are in good agreement with the experimental ones, and more accurate than previous calculations. As the amount of Sr dopant increases, both experimental and calculated cell size increases along the c-axis. However, in a- and b- axis directions, the variation is quite low. This phenomenon has some effects on the oxygen migration which was discussed by J.R. Tolchard et al. Our work gives some deep effects on the density of states and total energy which directly impact the ionic conductivity.

Table III. 3. Calculated and experimental lattice constants and internal parameters of LSOs and LGO

	Experiment		This work		Previous calculations	
	a/Å	c/Å	a/Å	c/Å	a/Å	c/Å
(La ₁₀ Sr ₀)Si ₆	9.7248/9.7173	7.1895/7.1800	9.6759	7.1889	9.7607	7.1189
(La ₉ Sr ₁)Si ₆	9.7072	7.1979	9.6924	7.1918	/	/
(La ₈ Sr ₂)Si ₆	9.7083	7.2377	9.6760	7.2341	9.8053	7.1558
(La ₁₀ Sr ₀)Ge ₆	9.910	7.270	9.9036	7.3420	/	/

Different ratios of Sr-doping in La position are calculated in this part using the GGA method. Indeed, it has been reported that the ionic conductivity significantly decreases by partly substituting La by Sr specially for a ratio of La(Sr):Si=10:6.

Figure III.3 shows the calculation results (including the Fermi level, total energy and formation energy) for each material, compared to the experimental ones (the ionic conductivity value has been treated logarithmically, $\text{S}\cdot\text{cm}^{-1}$). The formation energy is calculated by the following equation (EQN III.1)

$$E_{\text{formation}} = E_{\text{Total}(\text{La}_{10}\text{Si}_6\text{O}_{27})} - 10E_{\text{Total}(\text{La})} - 6E_{\text{Total}(\text{Si})} - 27E_{\text{Total}(\text{O})} \quad \text{EQN III.1}$$

The total energy of each atom is calculated and the values are as follows, La -0.53686 eV; Si -0.16432 eV; O -0.15510 eV; Sr -0.06825 eV; Ge -0.16010 eV.

It is noted that the Fermi level changes correspondingly with ionic conductivity. According to the the doping ratio increase, the Fermi level decreases gradually and thus the ionic conductivity shows a significant decrease. A lower Fermi level leads to a wider band gap. Hence, it is really difficult for an electron to make a transition to the conduction band, which means that the material have higher electron insulation. Furthermore, a wider band gap presents a lower electron delocalization which results in fewer obstacles to the oxygen ion migration. The formation energy can be also observed in Figure III.3, the less doping LSO has a lower formation energy. It can be deduced that the apatite would be more stable without doping.

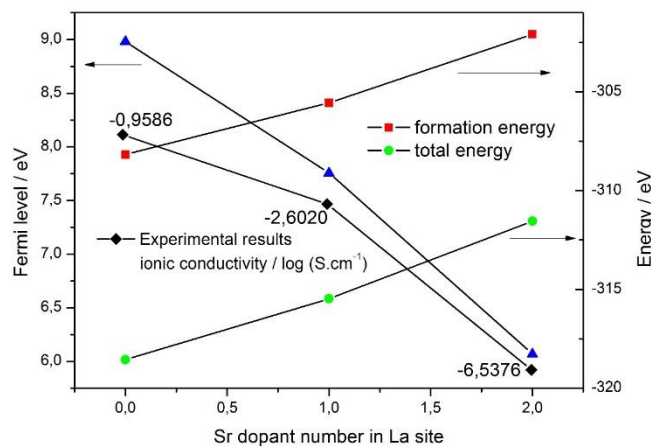


Figure III. 3. Different Sr dopant ratio effects on the electronic properties compared to ionic conductivity

Figure III.4 shows a diagram of electronic distribution curve for analyzing the mechanism of Fermi energy changes with doping. As can be observed, the LSO causes an excess of electrons in each molecule. In this case, the initial state can be considered as n-type semiconductor. The substitution of Sr^{2+} in the La^{3+} position is quite similar with a p-type doping process which can lead to a decrease of Fermi level. Besides, a higher Fermi level results in a narrower energy gap, because the electrons occupy a higher level above the valence band.

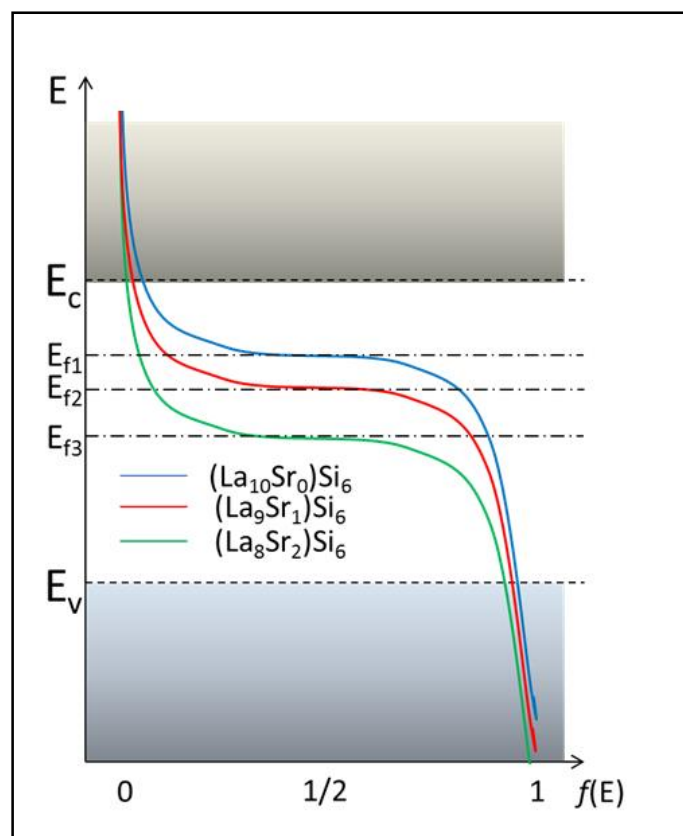


Figure III. 4. Effect of Sr dopant on the Fermi level

III.3.2 Density of states and band structure

The total density of states (DOS) and different atoms DOS (Partial DOS, PDOS) results are shown in Figure III.5. The three DOS Fermi energies are set as zero point energy ($E_f=0$).

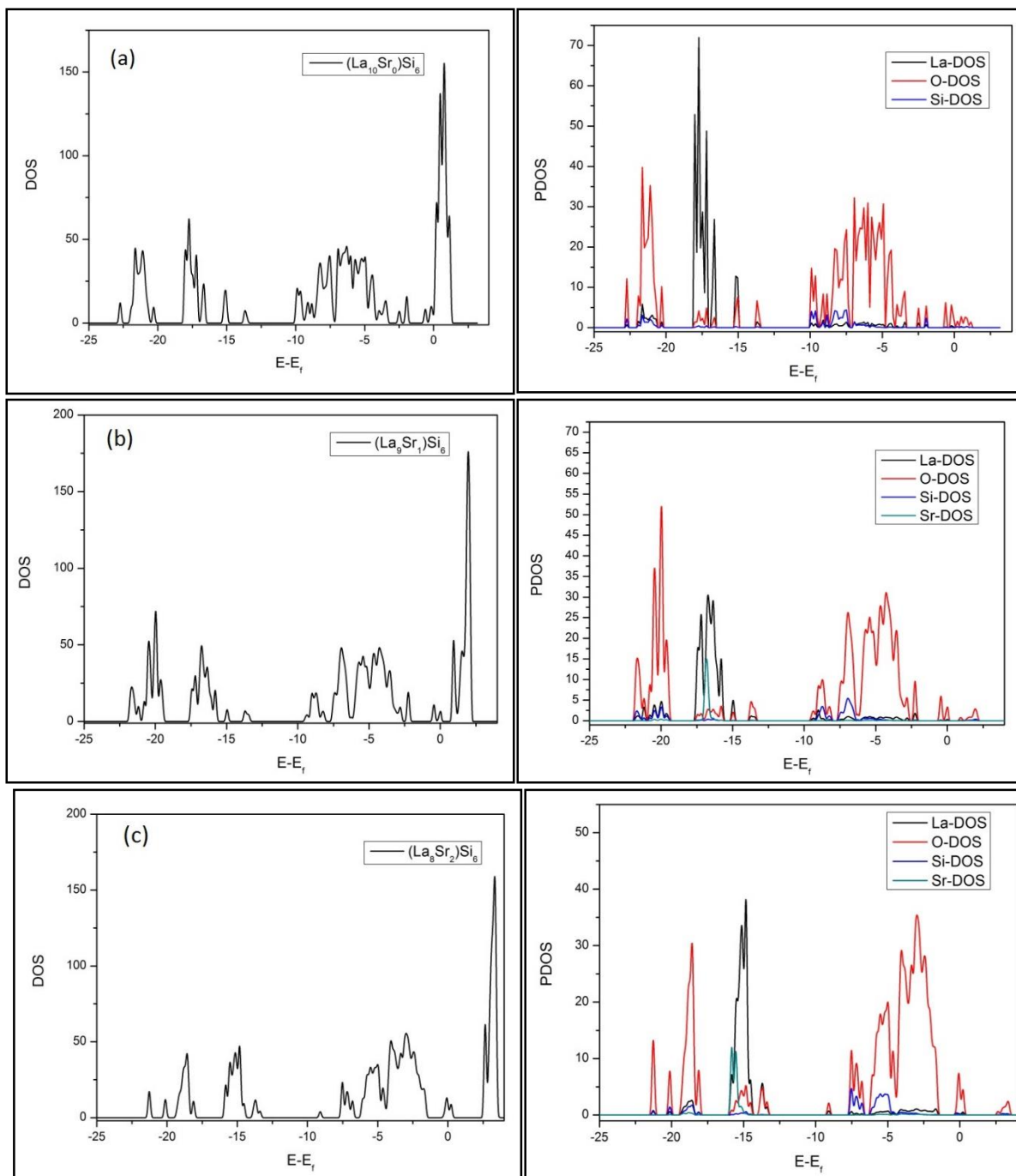


Figure III. 5. Total DOS (left) and partial DOS (right) of LSO with different Sr dopant ratios in (a) La:Sr = 10:0 (b) La:Sr = 9:1 (c) La:Sr = 8:2

The DOS figure shows sharp and multi peaks which mean electron delocalization is weak, therefore the oxygen ions can easily pass through the LSO which is suitable as an oxygen ion conductor. The PDOS also shows that different atoms DOS occupies different energy levels with little overlap. The band between atoms is ionic, thus the LSO can be considered as an ionic crystal which is a basic requirement for an electrolyte in a SOFC. Furthermore, the oxygen

states below Fermi level occupy higher energy level which means that oxygen electron transition to the conduction band is easier. Then, oxygen atoms can be ionized more easily than other atoms, hence this material is very appropriate to transfer the oxygen ions as an electrolyte.

In order to compare the distances between the bottom level conduction band and Fermi level, the three Sr doping ratios DOS are plotted and shown in Figure III.6. With Sr doping, the states around Fermi energy has significant shifting toward higher energy, therefore the material has a wider energy gap.

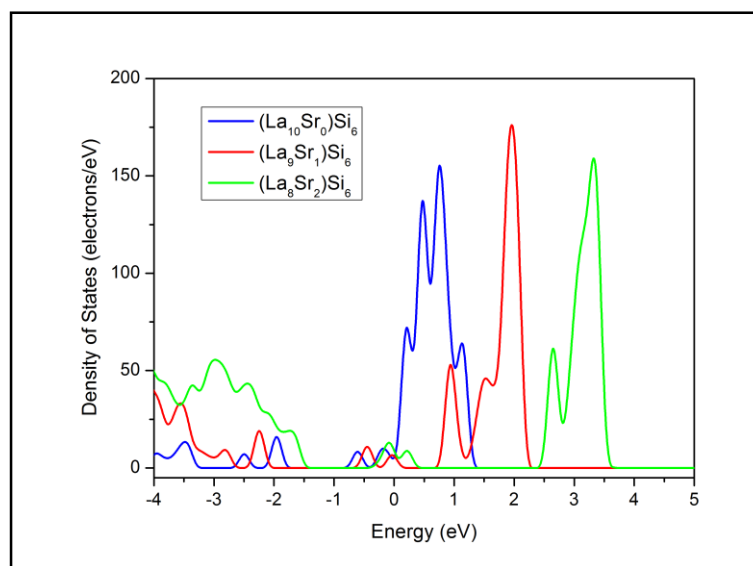


Figure III. 6. Comparison among the different Sr-doping ratios

In order to further understand the Sr doping impact on the DOS, figure III.7 shows partial DOS curves. It can be observed that the Sr 5s states occupy a higher energy with two doped Sr in one molecule (red curve) than that with one doped Sr (blue curve) which results in the La 5d-6s states moving outward. The La 5s-4d-5p states of La₁₀Sr₀ have a larger quantity of PDOS than the other two doping ratios (black curve at the left part of the figure). If Sr substitutes La position, the states which originally belong to La will shift to a higher energy. The calculation results indicate that Sr-doping has the ability to change the DOS.

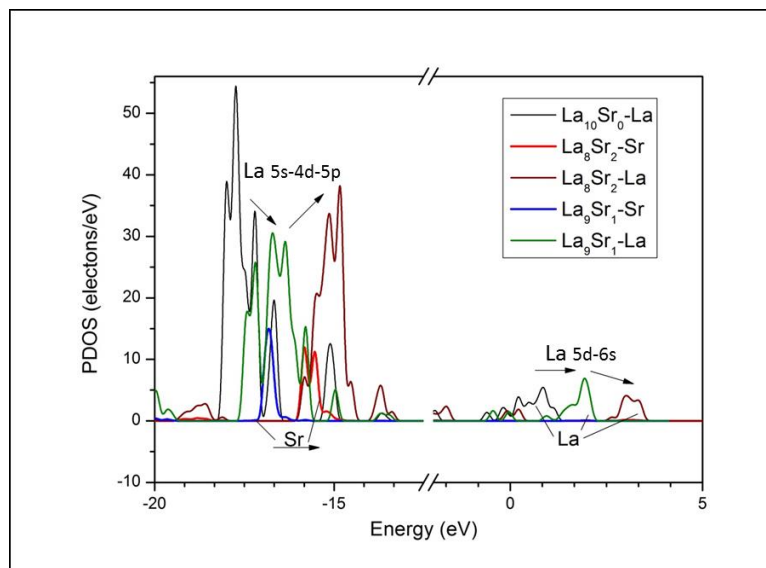


Figure III. 7. PDOS curves analysis for different La and Sr doping ratios

$\text{La}_{10}\text{Si}_6\text{O}_{27}$ is selected to show the band structure change for apatite with Sr doping and without doping. The LSO band structure is shown in Figure III.8.

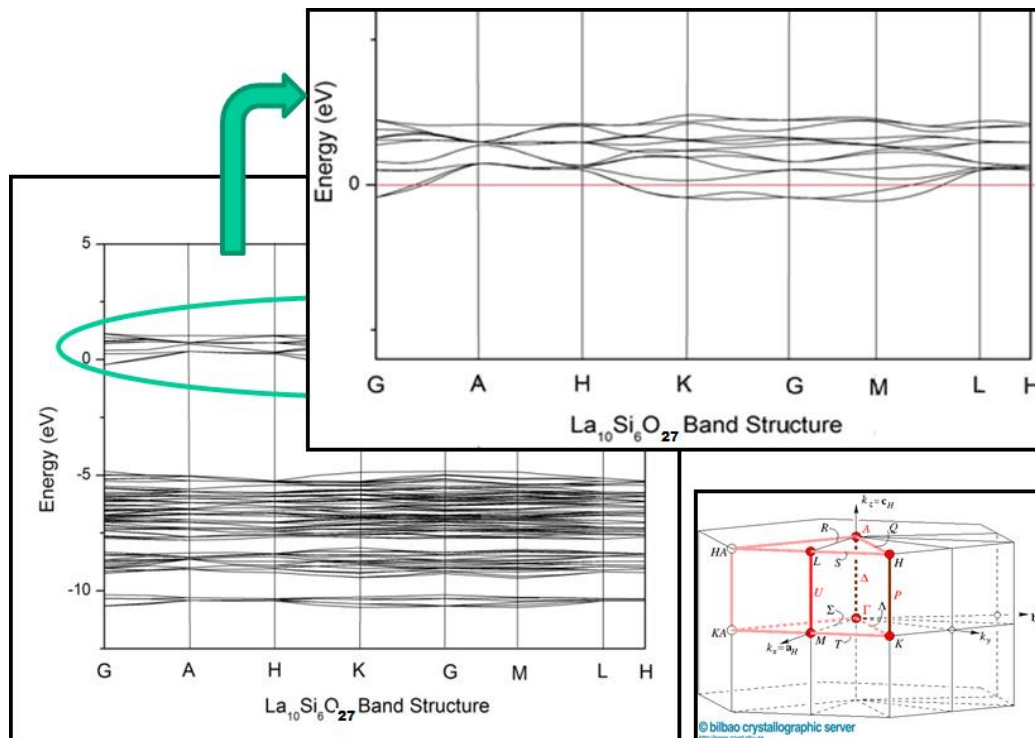


Figure III. 8. Calculated band structure of $\text{La}_{10}\text{Si}_6\text{O}_{27}$

Few band overlaps can be observed, which suggests a poor bonding between atoms. The oxygen ions can easily pass through the atoms interspace with lower electron blocking. Indeed, there is no band crossing the zero energy in AH, KG, GM zone around the Fermi level, which means there is a low electronic conductivity of the crystal along these directions[20, 21]. These results confirm that apatite materials are very suitable as an electrolyte in a SOFC.

III.4 Ge-doped LSO study

In order to compare the influence of different doped positions, Ge substitution at Si position is used as a common dopant element at Si position due to their similar electron orbits. Firstly, the complete substitution of Ge at Si position is calculated to obtain the DOS. The DOS of LSO and $\text{La}_{10}\text{Ge}_6\text{O}_{27}$ (LGO) are shown in Figure III.9. It is clear that the two curves overlap. It can be deduced that the Fermi levels of the two materials are almost the same as in our previous analysis. The bonding orbitals of Si and Ge are the same $(3,4)s^2 (3,4)p^2$, hence it has little influence on DOS and electronic transitions with Ge substitution. In this case, the calculation of different Ge doping ratios is omitted.

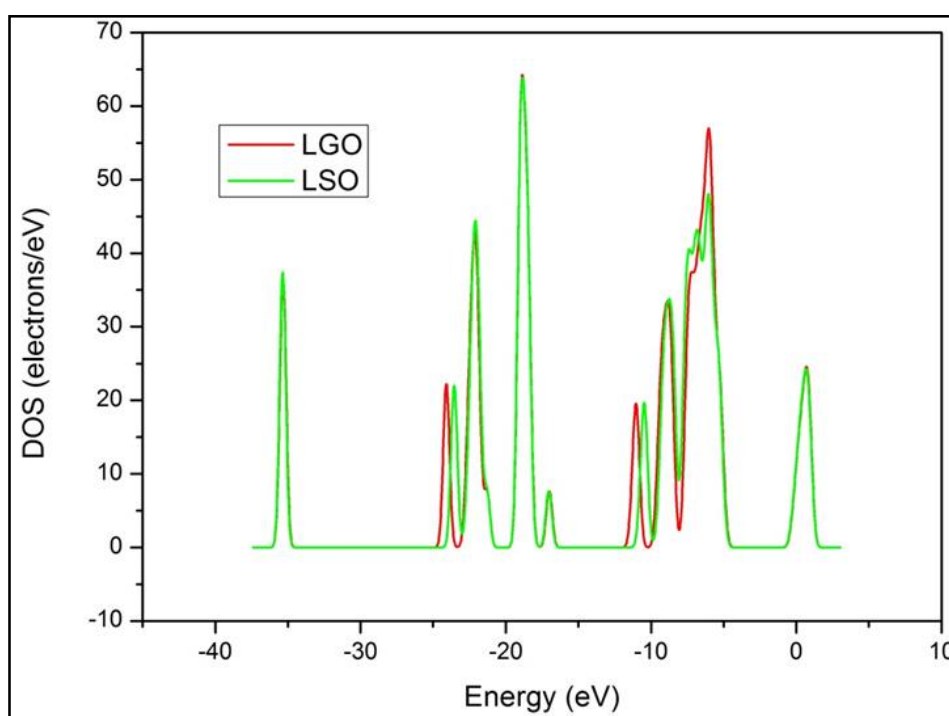


Figure III. 9. The DOS comparison between LSO and LGO

To explain the difference of LGO ionic conductivity from LSO in the experimental results, the electron density was calculated in Figure III.10. The oxygen on the cell edge can be treated as an ion transporter if it can move freely with low resistance, thus it can be observed in the figure where the cell edge channels are excellent candidates to transfer the ions. Comparing the two electron distributions, it can be seen that the oxygen is more influential with La in LGO than that in LSO, hence the oxygen ions are difficult to pass through the channel. The reason for this fact can be attributed to the different electron binding forces of different atoms. This is why the experimental ionic conductivity of LGO is lower than LSO even though they have the similar DOS curve patterns. The oxygen transfer channel can be influenced by Ge substitution, which has a different mechanism from the Sr-doping in La position.

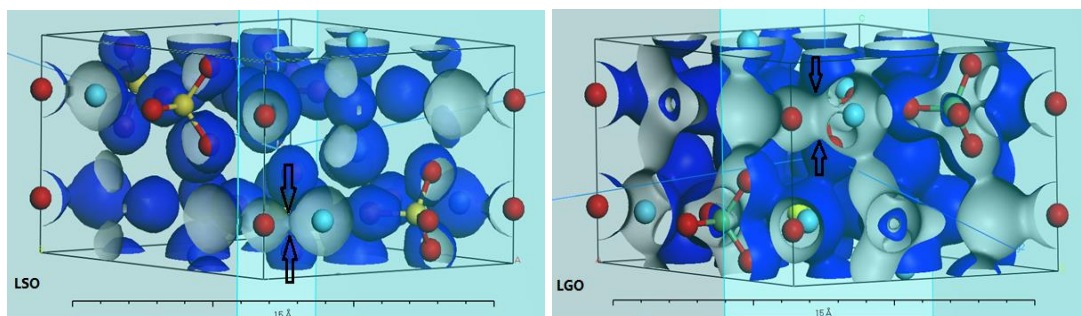


Figure III. 10. The calculated electron density of LSO and LGO

III.5 Effect of doping on activation energy

There are two La positions in this crystal structure: 4f, sited away from migration channel, and 6h, sited near to migration channel. Thus, two situations (far, near) appear in one Sr doping at La position and three situations (far-far, near-far and near-near) appear in two Sr doping at La position. Figure III.11 shows the calculation results of LSO energy barriers with different Sr doping ratios. Each figure shows the oxygen migration channel and Sr substitution position. The total energy is obtained as a function of one oxygen's position, which can be seen more

clearly in Figure 11 (f) – perpendicular to c -axis. The O_1 position (O_1-O_1') is the chosen independent variable of the function. The energy barriers are obtained from the energy difference, exhibited in figures as the activation energies.

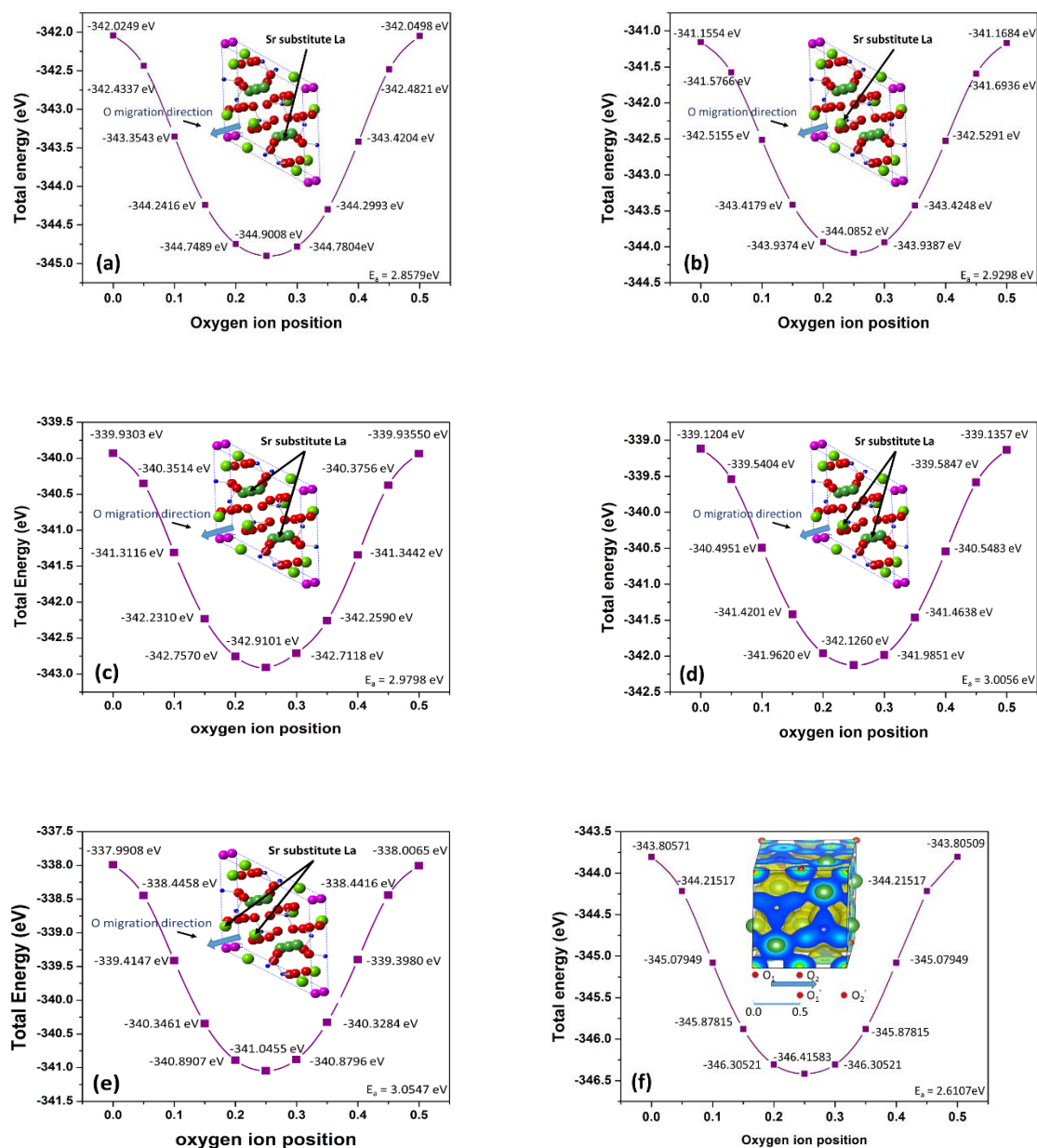


Figure III. 11. The calculated energy barriers along c -axis for activation energy of LSO with different Sr doping ratios and positions (a ~ b, $La_9SrSi_6O_{26.5}$ with Sr position near to (a) and far from (b) migration channel; c ~ e, $La_8Sr_2Si_6O_{26}$ with two Sr positions near to (c), near-far from (d) and far-far from (e) migration channel; f, $La_{10}Si_6O_{27}$)

In addition, the activation energy of Ge substitution LGO apatite is calculated under the same conditions. Figure III.12 (a) shows the calculation results. Relatively high total energy is presented in this group which means that LGO structure has a lower stability compared to LSO. The activation energies of each group are compared in Figure III.12 (b). The activation energy changes slightly when Ge totally substitutes Si positions. Thus, calculations for different Ge doping ratios are not useful. However, the Sr doping effect on the activation energy seems more significant. Indeed, more Sr doping ratio leads to higher activation energy, which is not suitable for electrolyte performances in SOFC. This phenomenon is also consistent with the experimental results (shown in Table III.1). It also can be noted that the doping effect is more significant for the substitution at La 6h position (near the migration channel) than that at La 4f position (far from the migration channel). The Sr doping actually affects the migration channel and the results depend on the distance to the channel. However, Ge effect, covered by Ge-O tetrahedron, is not obvious even all Si positions are substituted by Ge.

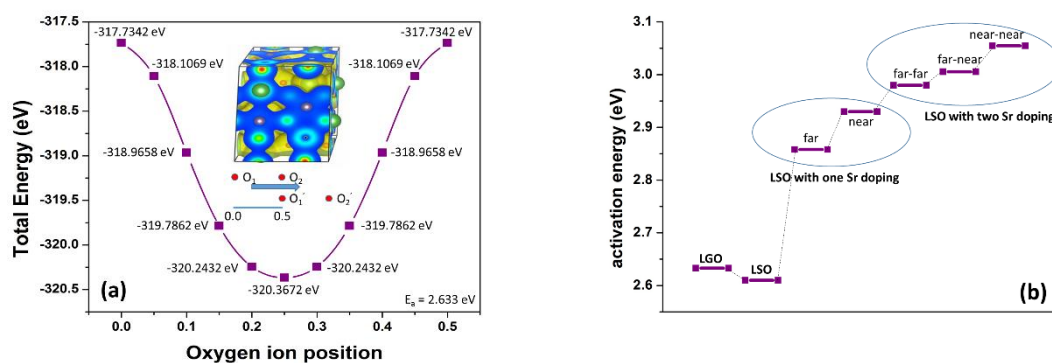


Figure III. 12. The calculated energy barriers along c-axis for activation energy of LGO (a) and the activation energy of each group (b).

III.6 Influence of doping positions on lattice parameters

From the calculation results, the two doping positions show different effects on the ionic conductivity. Based on the structure optimization results, the atom positions of each material and lattice parameter are obtained. The modeling results of XRD patterns for different dopant

apatites are shown Figure III.13 (a). It is found that the Sr doping influences the intensity of (0 0 2) direction, but it has a slight effect on the main peak. The lattice parameters change slightly after Sr-doping. However, in the case of Ge doping, the main (2 1 1) peak moves to a lower angle, thus the lattice parameter is higher than LSO. This results are confirmed by the experimental diffraction patterns showed in Fig.12 (b). The powders using in the diffraction are synthesized by sol-gel method and measured with Co target (this leads the shift of high intensity diffraction peaks). The lattice parameter of Sr doping LSO increases slightly by seeing the peak shift a little to a low angle. However, the parameter changes significantly by Ge substituting at Si position. These two elements (Sr and Ge) show different impacts on the ionic conductivity. The main influence of La position dopant is the change in Fermi level and DOS results, which can affect the activation energy. However, the Si position substitution changes lattice parameter, which sharply affects the electron distribution around the oxygen channel instead of the Fermi energy.

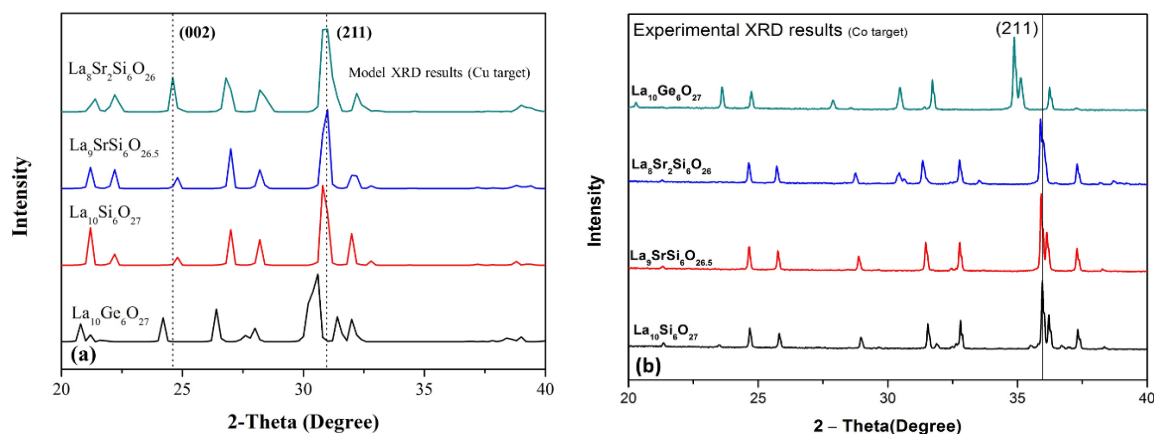


Figure III. 13. $\text{La}_{10-x}\text{Sr}_x(\text{Si,Ge})_6\text{O}_{27-0.5x}$ XRD patterns: (a) modeled and (b) experimental, versus different doping ratios

III.7 Summary

In this work, the influence of different doping positions on the apatite materials $\text{La}_{10-x}\text{Sr}_x(\text{Si,Ge})_6\text{O}_{27-0.5x}$ in SOFC were investigated using DFT calculation. Sr-doping at La site has

been discussed and the calculation results are in good agreement with the experimental results. The ionic conductivity has been correlated with the Fermi level. This latter decreased sharply as the Fermi level moves to lower energies with Sr substitution which is the main factor that affects ionic conductivity. The activation energy is also simulated by the energy barriers along the migration channel. The effect of Sr doping on the activation energy is clear and the decrease is more obvious while the doping position is near to the migration channel. As to Ge doping, the affects slightly both activation energy and DOS diagram.

III.8 References

- [1] Ogaji S, Singh R, Pilidis P, Diacakis M. Modelling fuel cell performance using artificial intelligence. *Journal of Power Sources*. 2006;154:192-7.
- [2] Vaidya S, Kim J-H. Finite element thermal stress analysis of solid oxide fuel cell cathode microstructures. *Journal of Power Sources*. 2013;225:269-76.
- [3] Spallina V, Mastropasqua L, Iora P, Romano M, Campanari S. Assessment of finite volume modeling approaches for intermediate temperature Solid Oxide Fuel Cells working with CO-rich syngas fuels. *International Journal of Hydrogen Energy*. 2015;40:15012-31.
- [4] Huang C, Wei W, Chen C, Chen J. Molecular dynamics simulation on ionic conduction process of oxygen in $Ce_{1-x}M_xO_{2-x/2}$. *Journal of the European Ceramic Society*. 2011;31:3159-69.
- [5] Xue S, Liu Y, Dang H, Li Y, Teeters D, Crunkleton DW, et al. Ab initio calculations of the atomic and electronic structures of crystalline PEO 3: LiCF₃SO₃ electrolytes. *Computational Materials Science*. 2016;112:170-4.
- [6] Nakayama S, Kageyama T, Aono H, Sadaoka Y. Ionic conductivity of lanthanoid silicates, Ln₁₀(SiO₄)₆O₃ (Ln= La, Nd, Sm, Gd, Dy, Y, Ho, Er and Yb). *Journal of Materials Chemistry*. 1995;5:1801-5.
- [7] Yoshioka H, Nojiri Y, Tanase S. Ionic conductivity and fuel cell properties of apatite-type lanthanum silicates doped with Mg and containing excess oxide ions. *Solid State Ionics*. 2008;179:2165-9.
- [8] Bonhomme C, Beaudet-Savignat S, Chartier T, Maître A, Sauvet A-L, Soulestin B. Sintering kinetics and oxide ion conduction in Sr-doped apatite-type lanthanum silicates, La₉Sr₁Si₆O_{26.5}. *Solid State Ionics*. 2009;180:1593-8.
- [9] Orera A, Baikie T, Panchmatia P, White T, Hanna J, Smith ME, et al. Strategies for the Optimisation of the Oxide Ion Conductivities of Apatite-Type Germanates. *Fuel Cells*. 2011;11:10-6.
- [10] Higuchi Y, Sugawara M, Onishi K, Sakamoto M, Nakayama S. Oxide ionic conductivities of apatite-type lanthanum silicates and germanates and their possibilities as an electrolyte of lower temperature operating SOFC. *Ceramics International*. 2010;36:955-9.
- [11] Tolchard JR, Islam MS, Slater PR. Defect chemistry and oxygen ion migration in the apatite-type materials La_{9.33}Si₆O₂₆ and La₈Sr₂Si₆O₂₆. *Journal of Materials Chemistry*. 2003;13:1956-61.
- [12] Sansom J, Slater P. Oxide ion conductivity in the mixed Si/Ge apatite-type phases La_{9.33}Si_{6-x}Ge_xO₂₆. *Solid State Ionics*. 2004;167:23-7.
- [13] Chroneos A, Yildiz B, Tarancón A, Parfitt D, Kilner JA. Oxygen diffusion in solid oxide fuel cell cathode and electrolyte materials: mechanistic insights from atomistic simulations. *Energy & Environmental Science*. 2011;4:2774-89.
- [14] Vanderbilt D. Soft self-consistent pseudopotentials in a generalized eigenvalue formalism. *Physical Review B*. 1990;41:7892.
- [15] Kohn W, Sham LJ. Self-consistent equations including exchange and correlation effects. *Physical Review*. 1965;140:A1133.
- [16] Kresse G, Joubert D. From ultrasoft pseudopotentials to the projector augmented-wave method. *Physical Review B*. 1999;59:1758.
- [17] Kresse G, Furthmüller J. Efficiency of ab-initio total energy calculations for metals and semiconductors using a plane-wave basis set. *Computational Materials Science*. 1996;6:15-50.
- [18] Kresse G, Furthmüller J. Efficient iterative schemes for ab initio total-energy calculations using a plane-wave basis set. *Physical Review B*. 1996;54:11169.

- [19] Le ón-Reina L, Porras-V ázquez JM, Losilla ER, Aranda MA. Interstitial oxide positions in oxygen-excess oxy-apatites. *Solid State Ionics*. 2006;177:1307-15.
- [20] Aroyo MI, Orobengoa D, de la Flor G, Tasci ES, Perez-Mato JM, Wondratschek H. Brillouin-zone database on the Bilbao Crystallographic Server. *Acta Crystallographica Section A: Foundations and Advances*. 2014;70:126-37.
- [21] Lacroix-Orio L, Tillard M, Belin C. Synthesis, crystal and electronic structure of Li₁₃Ag₅Si₆, a potential anode for Li-ion batteries. *Solid State Sciences*. 2008;10:5-11.

Chapter IV: Preliminary experimental exploration
for synthesizing pure $\text{La}_{10}\text{Si}_6\text{O}_{27}$ apatites

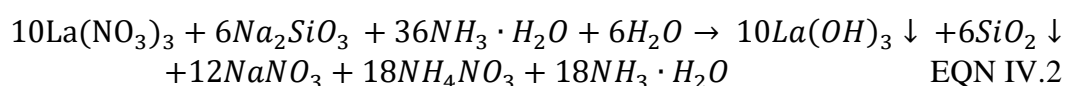
In this chapter, some preliminary methods for synthesizing pure phase apatite type $\text{La}_{10}\text{Si}_6\text{O}_{27}$ are explored. They include co-precipitation, melting salt, homogeneous deposition precipitation (HDP). Particularly, the first attempt of co-precipitation gave some interesting results despite some homogeneity issues.

IV.1 Co-precipitation method

The present work explores a modified co-precipitation method based on novel chemical reaction to synthesize apatite-type $\text{La}_{10}\text{Si}_6\text{O}_{27}$ (LSO) fine powder. With which the apatite phase can be achieved with a relatively facile procedure at low temperature.

IV.1.1 Sample preparation

$\text{La}_{10}\text{Si}_6\text{O}_{27}$ powders are synthesized by co-precipitation method based on novel chemical reaction using $\text{La}(\text{NO}_3)_3 \cdot 6\text{H}_2\text{O}$, Na_2SiO_3 (both from sigma-Aldrich, 99.9%) as raw materials and ammonia ($\text{NH}_3 \cdot 6\text{H}_2\text{O}$) solution as auxiliary. $\text{La}(\text{NO}_3)_3 \cdot 6\text{H}_2\text{O}$ is characterized with ATG to verify the number of crystal water. The reactions involved in the synthesis process as follows:



A certain excess ammonia is used in this reaction to control the pH unchanged at 8.5~9.5. It is clear that too acid or too alkaline environments would affect the precipitation of $\text{La}(\text{OH})_3$ and SiO_2 . Only complete precipitation of the two compounds leads to stoichiometric reaction during calcination to obtain pure phase apatite LSO. In order to increase the duration of mixing process, we design the reaction under control as figure IV.1 shows.

Figure IV.1 gives the schema of the equipment that the reaction takes place in ammonia solution to provide a weak alkaline environment. The two solutions drop into ammonia slowly and it is

stirring continuously. Once the reaction is completed, the suspension is filtrated to obtain the calcination precursors.

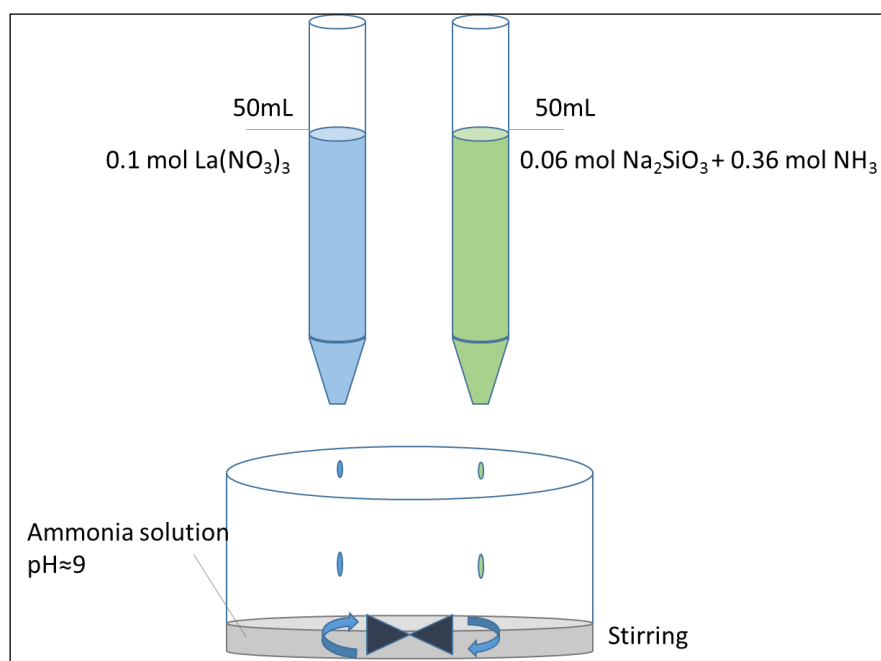


Figure IV. 1. co-precipitation reaction equipment design (Acid burette – left; alkaline burette – right)

The precursors are calcined with the temperature from 700°C to 1100°C for 6h. After the characterization to identify the product, they are sintered with 1500°C for 2h to densify the samples for SOFC application.

IV.1.2 Co-precipitation process and calcination

The pH and temperature value is closely monitored during synthesis process. Table IV.1 gives these values in the reaction.

Table IV. 1. The pH and temperature values during the co-precipitation process

Test Time	PH	Temperature (°C)
Start reaction	8.9	40
5min	9.1	50
10min (reaction end)	9.0	55
30min after reaction	8.5	64
60min	8.6	60

The temperature is controlled at about 40~60°C to accelerate the reaction and it is also found that the pH value keeps little change during the reaction, thus the reaction is complete of each drop arrives the ammonia solution , meanwhile it takes place as planned.

Figure IV.2 exhibits the XRD analysis of different groups of powders with different calcination temperatures treatment. We can find there is no diffraction intensity of La_2O_3 or SiO_2 in the XRD pattern before calcination, which tends indicate that the absence of agglomeration of any oxide in the mixture.

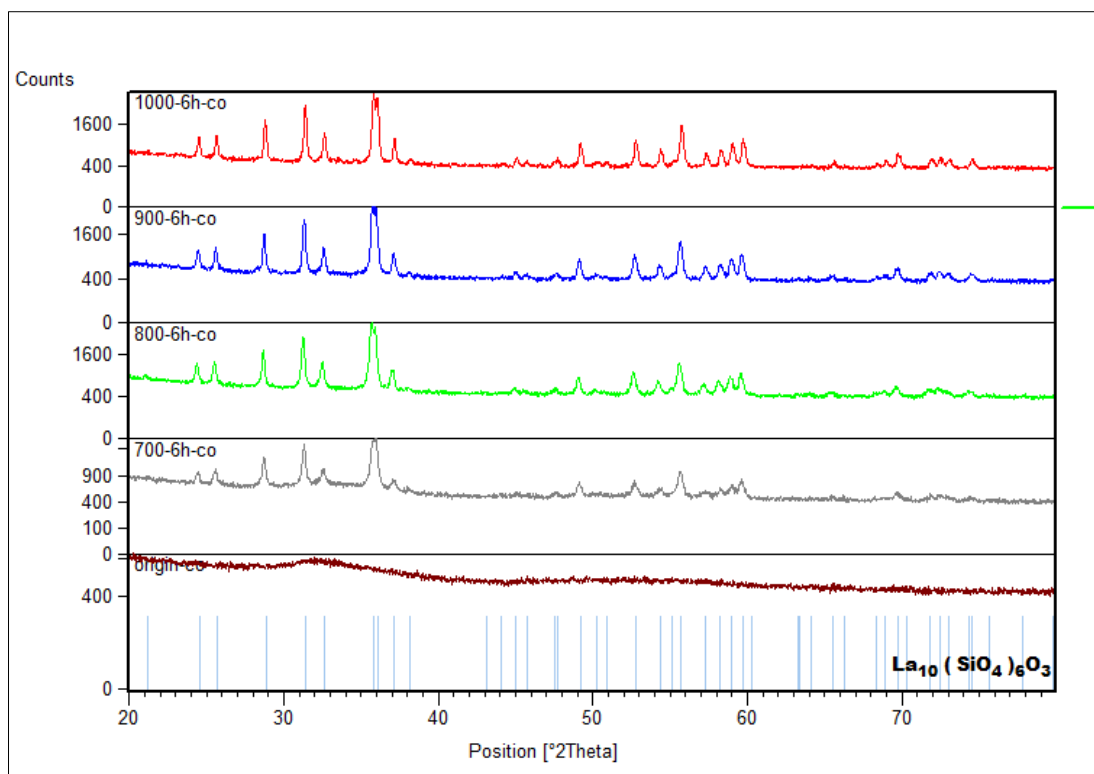


Figure IV. 2. X-ray diffraction patterns of different groups of compounds synthesized with different calcination temperature

All the calcined powders show pure apatite phase without any impurities (Fig. IV.2), indicating that the apatite structure has been formed basically at 700 °C. This formation temperature of apatite phase LSO is much lower than that via the methods in the existing reports, which is usually higher than 900°C even with kinds of auxiliary agents (ethylene glycol et al.) in preparation process. Especially, there is an indeterminate high intensity diffraction existing in the groups with the treatment of 1100°C, as shown in Figure IV.3. It is inferred that the impurity is La_2O_3 or La_2SiO_5 . *B. Li et al* [1] have reported that the formation temperature of La_2SiO_5 is higher than that of oxy-apatite phase, and the presence of La_2O_3 at lower temperature leads to the formation of La_2SiO_5 phase at higher temperature, and the formation temperature is between 1000°C and 1100°C. This result corroborates our inference. This undesirable by-product would affect the performance of ionic conductivity. Further work would be necessary to solve this issue.

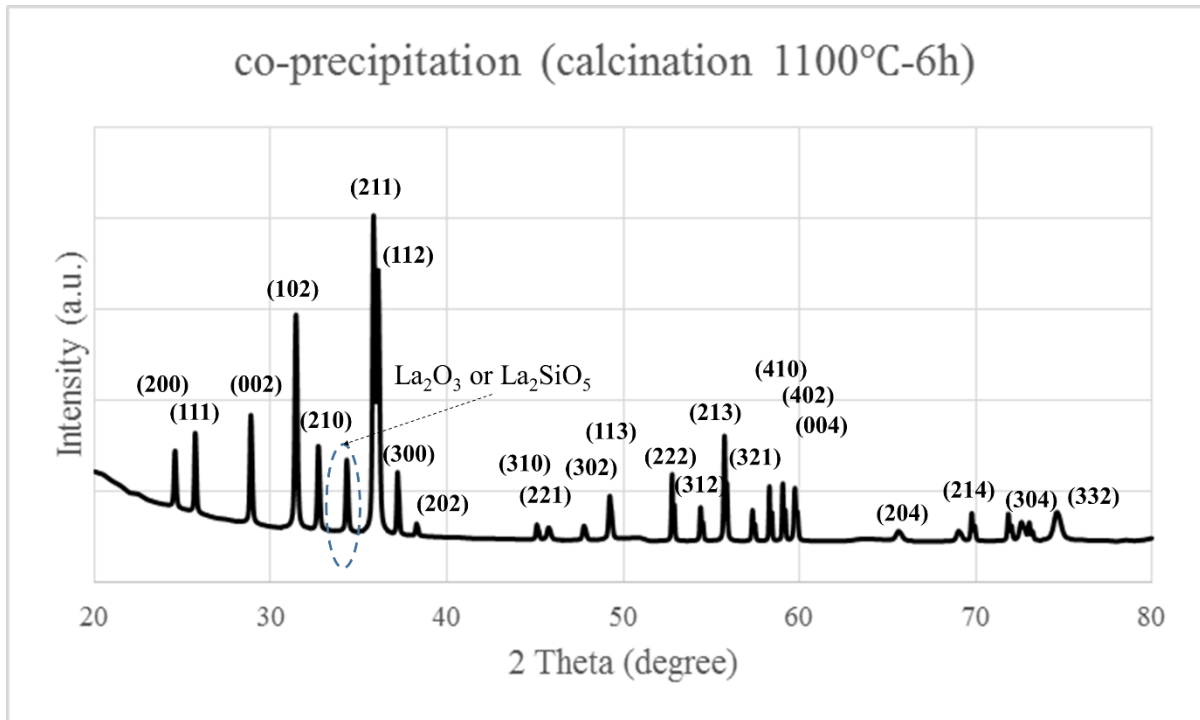


Figure IV. 3. X-ray diffraction patterns the group of compounds synthesized with 1000°C calcination temperature (the miller indices of lanthanum silicate is shown in the figure)

To investigate the calcination process, Figure IV.4 gives the TG and DSC analysis curves. While the calcination temperature is about below 300°C, water gets out from the precipitate. And then, $\text{La}(\text{OH})_3$ starts decomposition by seeing the significant peak of the DSC curve. Concurrently, LSO formation process occurs with the temperature continuous increase. The total mass loss is 88.4% during $\text{La}(\text{OH})_3$ decomposition to the final, which corresponds the change of $10\text{La}(\text{OH})_3 + 6\text{SiO}_2$ (expected precipitates) to $5\text{La}_2\text{O}_3 + 6\text{SiO}_2$. We have noted some endothermic peaks exist in the DSC curve above 900°C, which is due to the entropy change of apatite LSO grain growth process, instead of the formation process reported in some previous work.

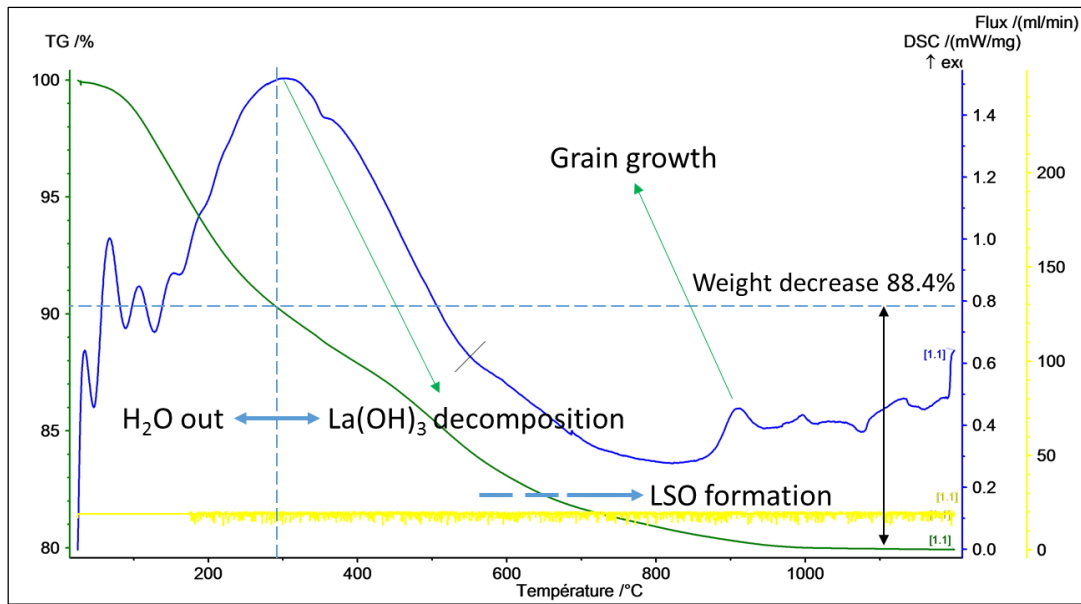


Figure IV. 4. TG/DSC curves of precipitant to analyze the calcination process

Figure IV.5 shows the morphologies of different groups of samples treated by different calcination temperatures. The figure IV.5 (a) gives the morphology of original powder without calcination treatment. The particles agglomerate into cauliflower-like, large ones and the average size is to 0.5-1 μm comparing with that of a single particle of 20nm. Figure IV.5 (b~e) show the morphologies of the samples treated with 700°C to 1000°C. The crystallization process can be discovered with the calcination temperature increasing. Small grains have formed starting from 700°C and they become bigger and more distinct by higher temperature treatment. Meanwhile, more grain shapes change to hexagonal from the treatment of 900°C, which infers that the grains belong to apatite-type LSO structure.

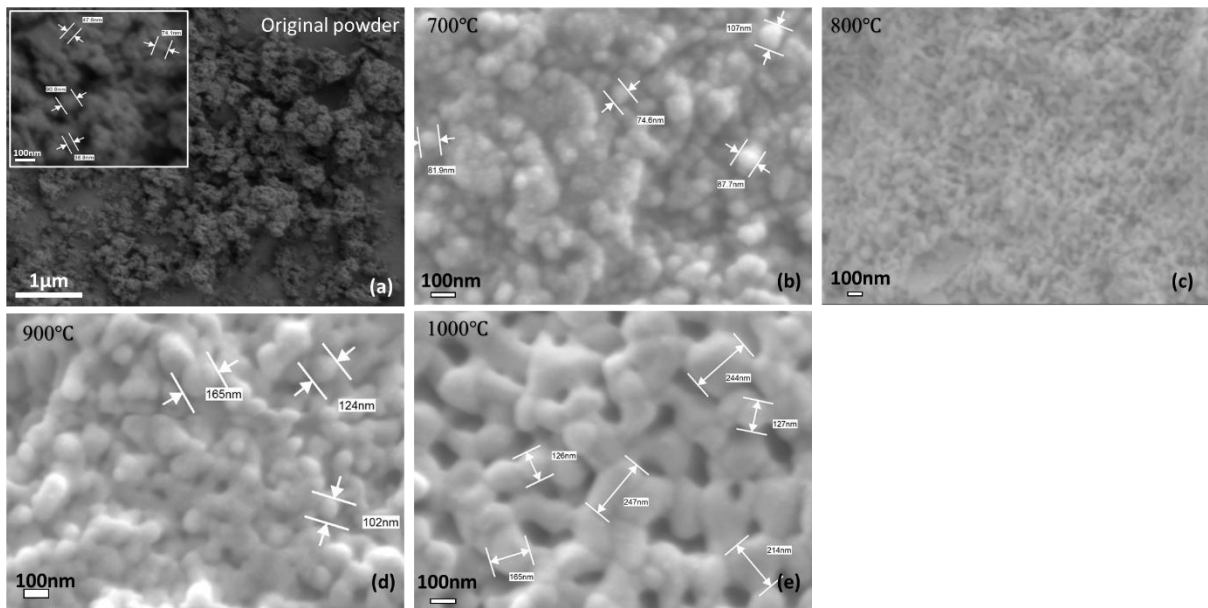


Figure IV. 5. The morphologies of samples with different calcination temperatures treatment by SEM analysis

The grain sizes are measured and summarized in figure IV.6, it can be seen the grain sizes have significant increase which is helpful to enhance the density of sample bulks.

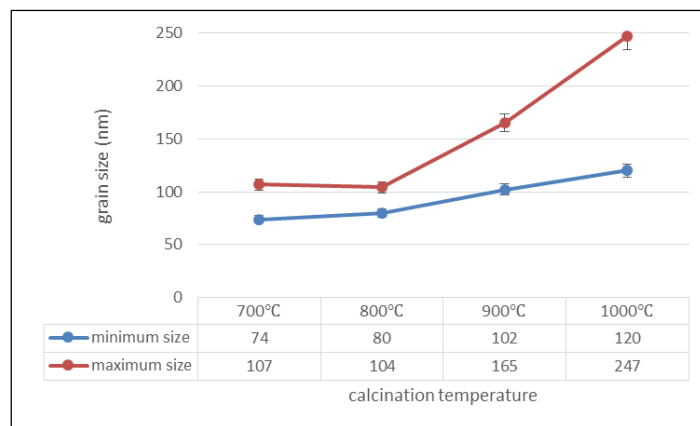


Figure IV. 6. The grain sizes of samples treated with different temperatures by analyzing SEM photos

Figure IV.7 gives the EDX results of the samples. The group with 1000°C calcination treatment is selected as an example due to the result of each group pretty much the same. In each group measurement, three different zones are detected to verify the homogenization of the sample. It can be found the three curves coincide perfectly. Meanwhile, in the curves, there are no peaks

pointing to the elements of Na or N which have existed in the precursor solution and it means the auxiliary agents are easily removed in our preparation process. Considering the accuracy limitation of this EDX technology, the mean value of silicon-oxygen ratio is quite close to 6/10 which is the theory ratio of them.

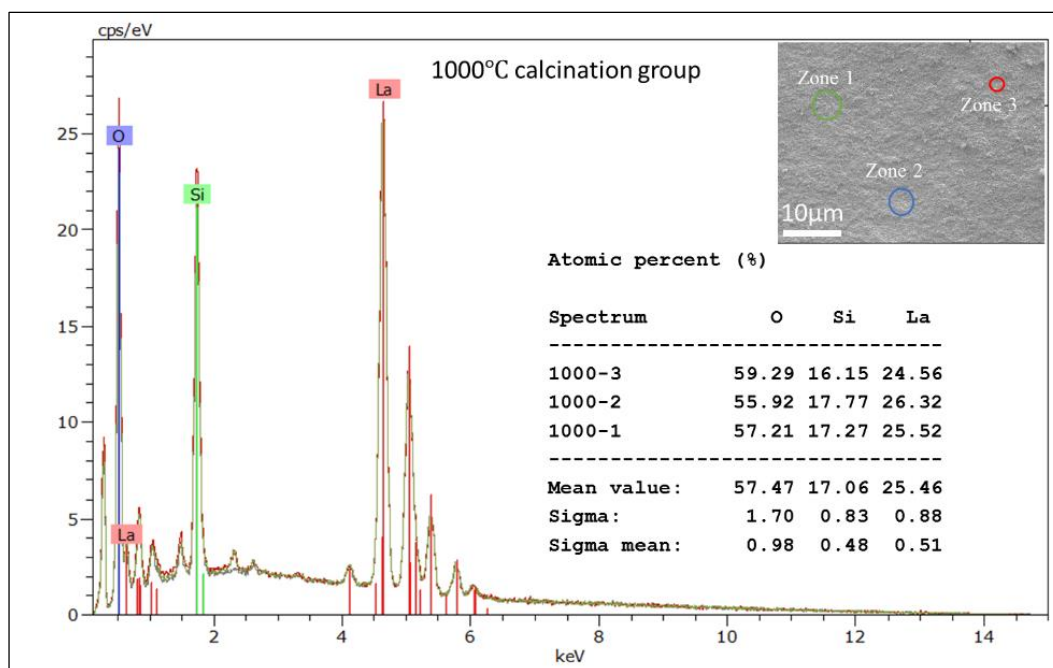


Figure IV. 7. EDX analysis curve of the obtained sample in three different zones (1000°C group as an example)

IV.1.3 Sintering process and characterization

Figure IV.8 shows the XRD patterns of all the samples after sintering at 1500°C for 2h.

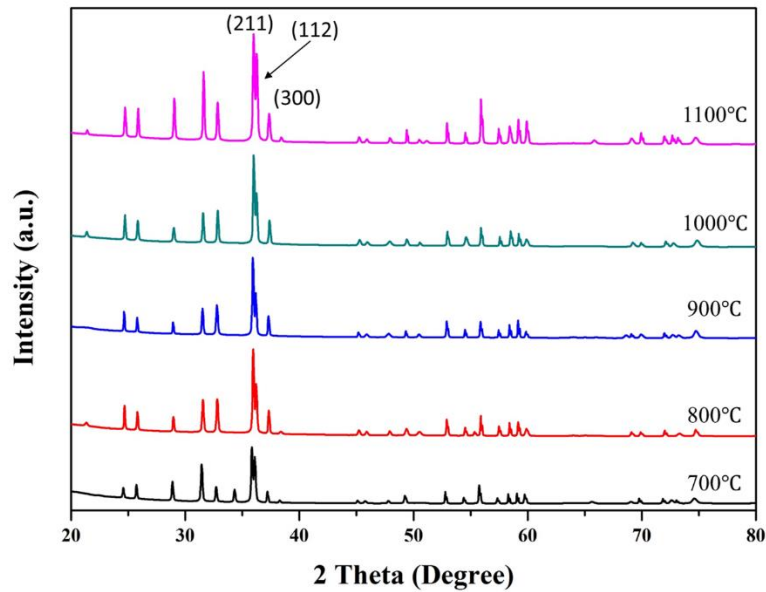


Figure IV. 8. X-ray diffraction patterns of different groups with further sintering treatment at 1500°C for 2h

They all keep the diffraction peaks matching the apatite structure and the intensity diffraction of the samples tend to become identical, even some secondary peaks disappeared. The intensity of the diffraction peaks effect becomes more marked after sintering. The peaks become sharper and stronger as compared to the ones before the treatment, and the average FWHM changes from 0.1376° - 0.2362° to 0.0984° - 0.1181° . The diffraction peaks have more details (close peaks can be separated) in each peak. The samples have been well crystallized and the crystal grains increase with the high temperature treatment. This result also evidences the favorable effect of sintering on the degree of crystallization of the apatites.

Figure IV.9 shows the SEM microstructure of some synthesized apatites after sintering.

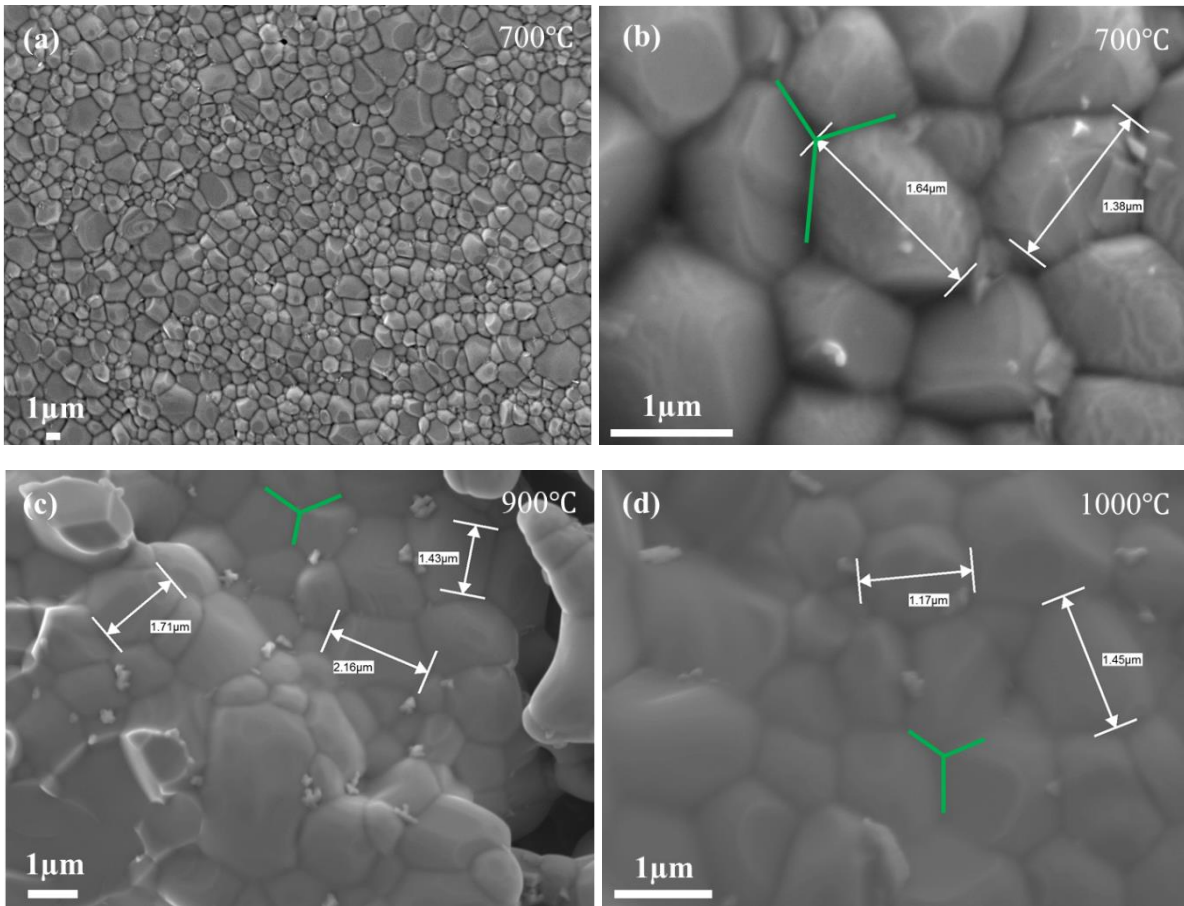


Figure IV. 9. Typical SEM micrographs of samples sintered at 1500°C for 2h

The crystal grains significantly increase up from the nanometer scale (before sintering) to 1-3 μm and they get closely connected to each other, as well as in large scale shown in figure IV.9(a). The sintering treatment obviously densifies the apatite materials which is beneficial in the prospect of SOFC electrolytes applications. The grains have the appearance of hexagons and one sees some of the boundary angles equaling 120° , which is congruent with the crystal structure of our previous discusses. As far as the calcination temperature is concerned, it seems that it does not affect significantly the grain size. Globally we can note that the sintered apatite materials, as characterized in this section, will be suitable candidates as electrolytes in SOFC.

IV.1.4 Electrical characterization

Before the electrical measurement, we have deposited a Pt collector by magnetron sputtering on each face of the sample to obtain a good current collector. The thickness of Pt coating is around 200 nm to avoid the Ostwald Ripening mechanism with the temperature. The experimental points were fitted by a least-squares procedure using an equivalent electrical circuit in order to extract the electrical features of the ceramic. The circuit consisted in one parallel (R//CPE) contributions to account for high and medium frequency processes (where R is a pure resistance and CPE is a Constant Phase Element $Z_{CPE} = 1/Y_0(j\omega)^p$ with Y_0 the module of the CPE element and p a parameter taking into account the depressing of the semi-circle. The capacitive effect deduced from the R and CPE values is given by:

$$C = R^{\left(\frac{1-p}{p}\right)} \times CPE^{\left(\frac{1}{p}\right)} \quad \text{EQN. IV.3}$$

The figure IV.10 shows a nyquist diagram of the sample registered at 500°C, for our samples it's very difficult to distinguish the bulk and the grain boundary contributions. The resistance of the pellet increase with the calcination treatment, this result is very surprising because the increasing of the calcination temperature increase the density and the grain size of the pellets. This comportment is certainly induced by the presence of the impurity phase with the temperature.

The electrical conductivity of samples is presented in figure IV.11 in an Arrhenius plot. The ionic conductivity is relatively low between 0.06 to 7.73 mS.cm⁻¹ at 675 °C. The linear evolution of ionic conductivity indicate that the conductivity is thermally activate and the activation energy is respectively 1.04, 1.28, 0.98 eV for sample annealed at 800, 900 and 1000°C. The value is relatively high in comparison with the literature data (0.5 to 0.9 eV without impurity phase)[2]. The capacity of the sample calcined at low temperature is close to 10⁻¹⁰/10⁻⁹ F.cm⁻¹. According to the work of Tao et al[3], the ionic conductivity is dominated by the grain

boundaries contributions. For the pellet annealed at 1000 °C, the capacity is of the order 10^{-11} F.cm⁻¹, in this case the ionic conductivity is controlled by the grain contribution[3]. Nevertheless, this analysis indicates that the poor conductivity of the pellet most probably originates from an interfacial blocking effect and/or the presence of the impurity phase.

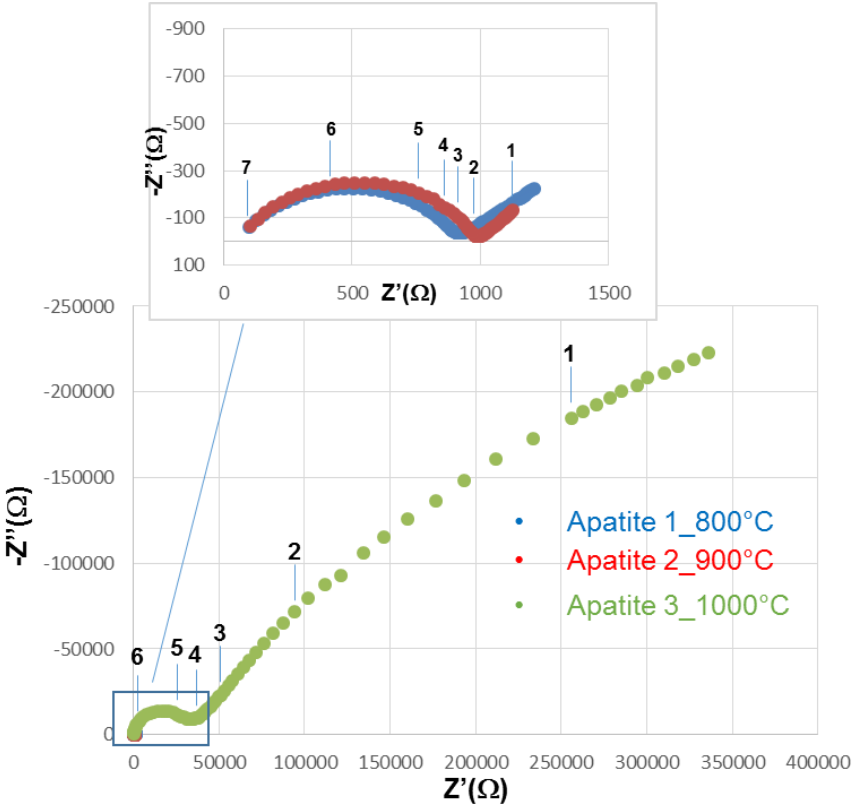


Figure IV. 10. Impedance diagram in Nyquist representation registered at 773 K under static air on apatite pellet. Frequency logarithms are represented

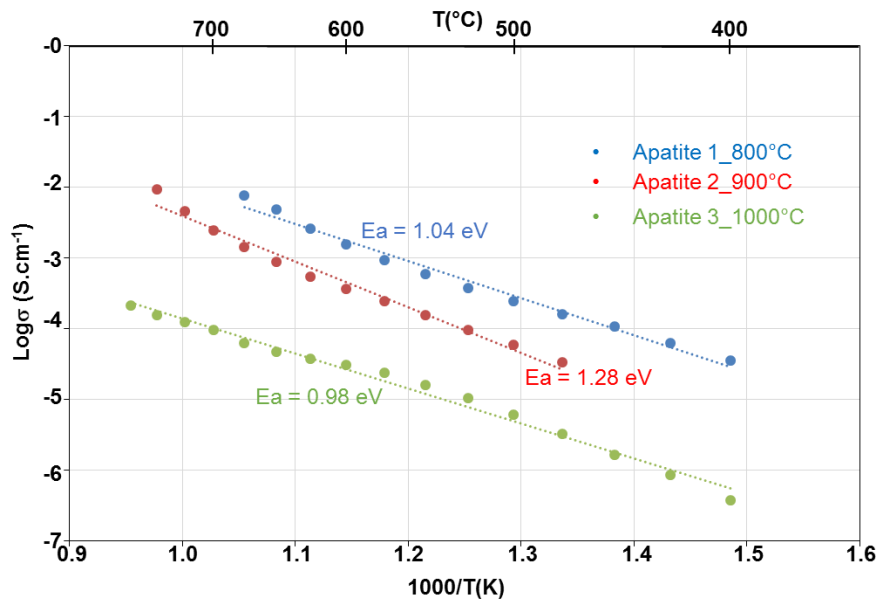


Figure IV. 11. Arrhenius plot of ionic conductivity

In summary, the first attempt of a novel method, based on direct chemical reaction, is realized to synthesize apatite type lanthanum silicates as electrolyte in IT-SOFC. Suitable stoichiometric precursors are generated at the same time, and this is beneficial to the formation reaction of LSO. The apatite phase composition is obtained from quite moderate temperature of 700°C for 6h. After the densification process of 1500°C for 2h, the samples exhibit acceptable performance of ionic conductivity of 7.73 mS.cm⁻¹ at 675 °C. This novel method is worth to development due to it is facile to implement and low cost. The replacement of the chemicals in the reaction can satisfy some other synthesis requirements. It is noted that the impurity in the composition affects the conductivity performance, and it will be modified in future work by introducing different dispersants.

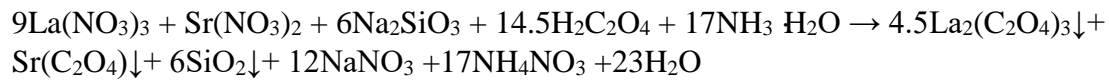
IV.2 Sr, Mn-doping LSO with co-precipitation method design

IV.2.1 Sr-doping LSO

In order to dope Sr into LSO composition, a new chemical reaction for co-precipitation is developed. The difficulty for Sr-doping is that Sr(OH)₂ is highly soluble in water, thus we have

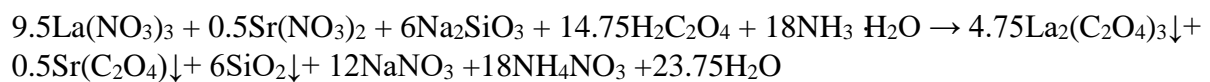
to introduce new reactant oxalic acid $\text{H}_2\text{C}_2\text{O}_4$. The solubility product constant K_s of SrC_2O_4 is as low as 5×10^{-8} , meanwhile, the solubility of $\text{La}_2(\text{C}_2\text{O}_4)_3$ is 2.08mg/L, equals 3.8×10^{-6} mol/L.

The main reactions is as follows:



EQN IV.4

and



EQN IV.5

for different Sr doping ratios. Adding excess of ammonia solution to increase the PH, $\text{Sr}(\text{C}_2\text{O}_4)$ precipitation reaction is more complete. However, it affects SiO_2 precipitation. In this case, we have to keep the pH around 7, thus we choose $\text{CH}_3\text{COONH}_4$ (ammonium acetate) as a pH buffer.

Figure IV.12 gives the schema of the equipment that the reaction is taken place in ammonium acetate solution to provide a neutral environment. The three solutions drop into ammonium acetate slowly and it is stirring continuously. Once the reaction is completed, the suspension is filtrated to obtain the calcination precursors.

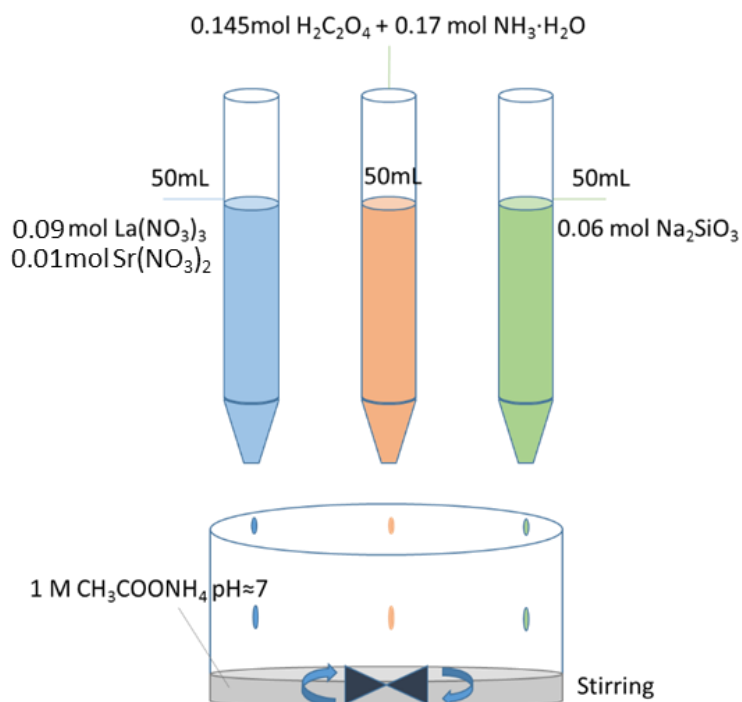


Figure IV. 12. Sr-doping LSO co-precipitation reaction equipment design

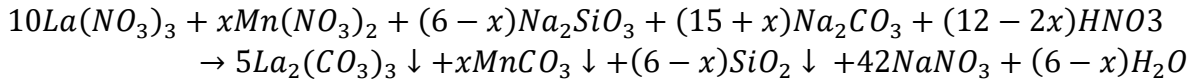
The experimental results show the precipitation is quite fast, and the agglomeration is obvious. Thus the obtained LSO has much impurity. The pH value is the key factor to affect the precipitation. The ammonium oxalate as an alternative can be employed to replace the oxalic acid- ammonia system.

IV.2.2 Mn-doping LSO

Manganese (Mn) doping in LSO composition can effectively improve its conductivity performance.[4] Mn ion has various valence of +2, +3, +4, +6, and +7 under certain condition. If the valence of Mn ion is +4, it will occupy Si site and the trivalent Mn prefers La site.

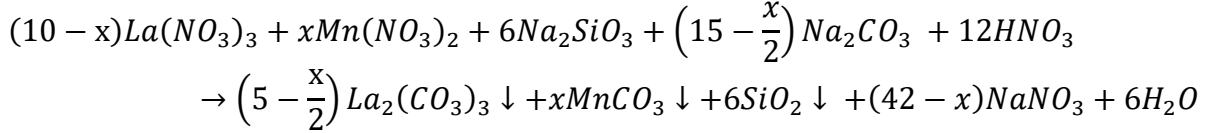
Main reactions:

Mn (IV) at Si position, $\text{La}_{10}\text{Si}_{(6-x)}\text{Mn}_x\text{O}_{27}$ ($x=0.5, 1, 1.5$)



EQN IV.6

Mn (III) at La position, $La_{10-y}Mn_ySi_6O_{27}$ ($x=0.5, 1, 1.5$)



EQN IV.7

In order to keep the pH value about 9~10, 0.05M Na_2CO_3 and $NaHCO_3$ solution is used as the buffer solution. The experimental equipment and process is shown in figure IV.13.

Si position	La position
Adding H_2O_2 solution to oxidize Mn^{2+} at $20^\circ C$	/
Filtering the solution, keep the residue	Filtering the solution, keep the residue
Washing the residue with ammonia solution (pH=9.7~10)	Washing the residue with ammonia solution (pH=9.7~10)
Drying the products ($80^\circ C$ -10h)	Drying the products ($80^\circ C$ -10h)
Compress to discs (200MPa for 20s)	Compress to discs (200MPa for 20s)
<p>Calcination procedure</p>	<p>Calcination procedure</p>

Figure IV. 13. Experimental equipment and process of Mn-doping LSO with co-precipitation

Wherein, the difference calcination processes in the table are employed to control the valence of Mn. The MnO-Mn₂O₃-MnO₂ phase diagram is shown in Figure IV.14. As for Si site doping, the calcination temperature is maintained at 300 °C for 10h to generate the tetravalent Mn (MnO₂).

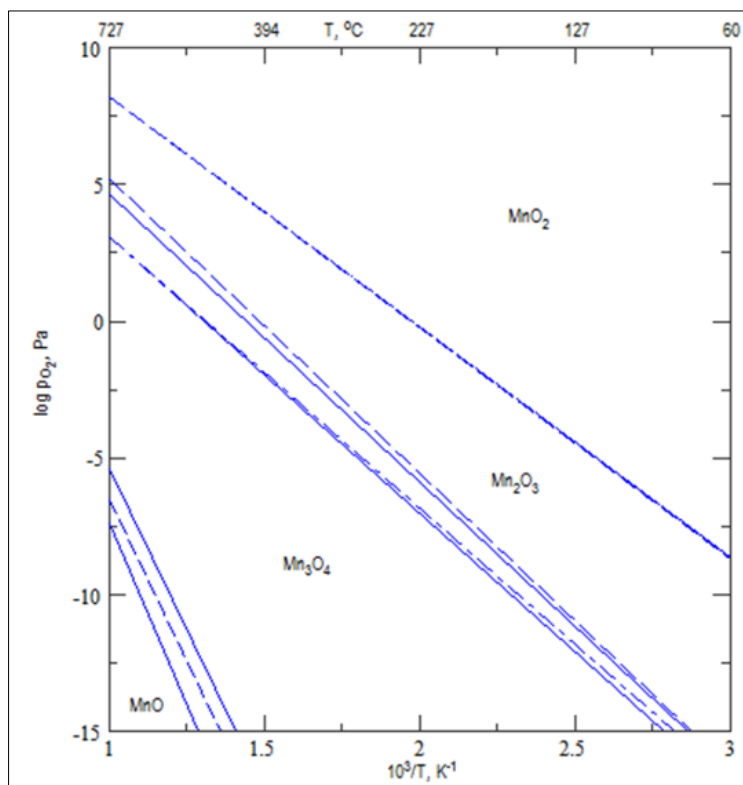


Figure IV. 14. the phase diagram of the MnO-Mn₂O₃-MnO₂ system[5]

The XRD diffraction patterns of the powder before calcination and the sample after calcination are shown in Figure IV.15. By seeing the diffraction pattern of the powder before calcination, some high intensity diffraction peaks existing in the pattern means the crystallization and agglomeration takes place in precipitation process. Comparing with the experiment without Mn-doping, this precipitation reaction rate is much higher. The reaction product has no time to disperse. The introduction of dispersant can perhaps improve this circumstance. After calcination, the principal peaks indicate the apatite phase LSO. It is noted that the impurity in

La site doping groups is inferred to Mn_2O_3 and La_2O_3 , which suggests the agglomerated chemicals is difficult to react with silica with heat treatment. As for the Si site doping group, the abundance of La_2O_3 is even higher. Probably, this is due to the influence of H_2O_2 . Further investigation should be explored to remove the impurity in the product.

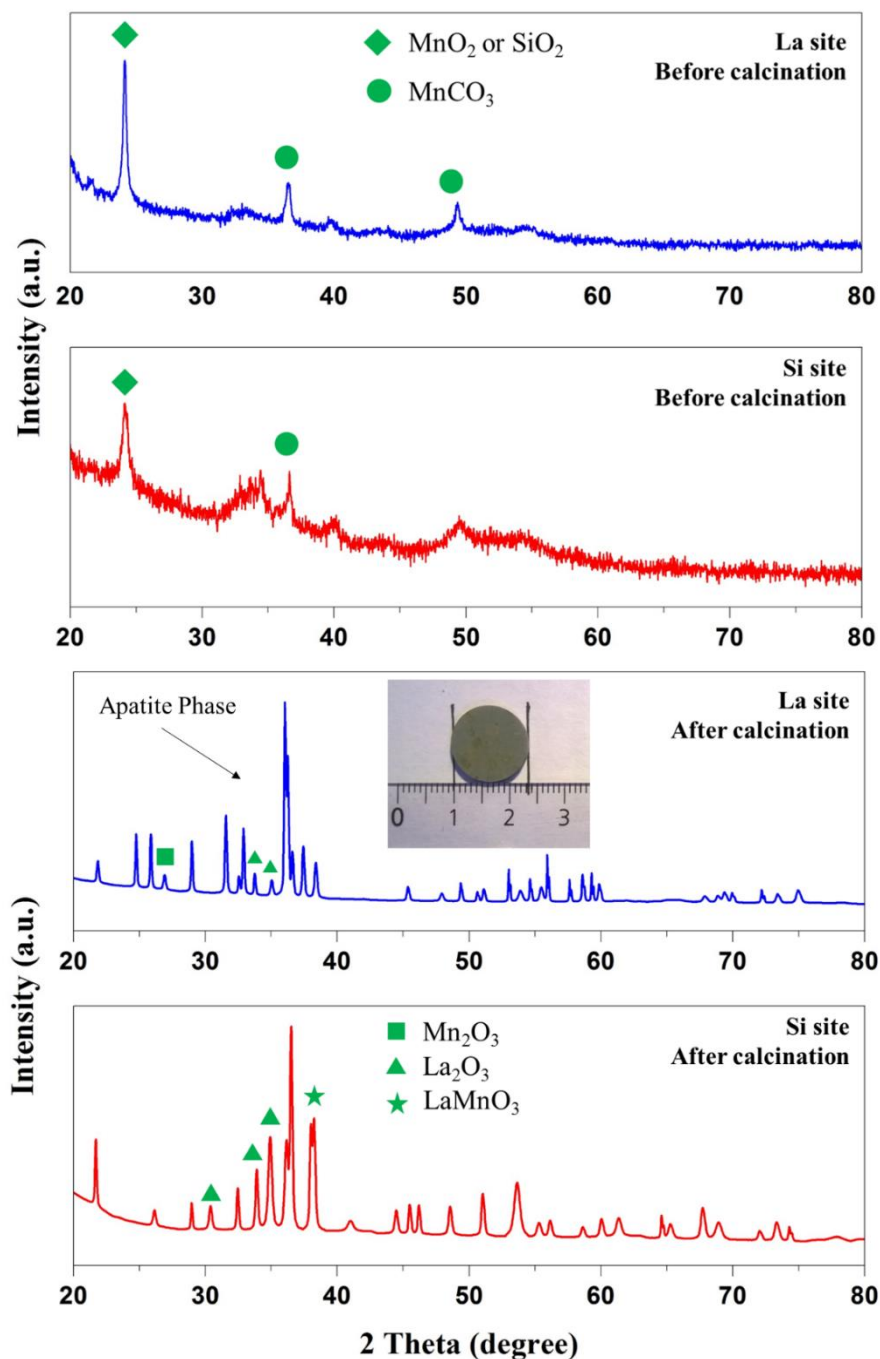


Figure IV. 15. The XRD diffraction patterns of the powder before calcination and the sample after calcination (the inset shows the sample appearance)

IV.3 Molten salt

This section presents the attempt to prepare LSO powders by molten salt method for solid electrolyte application. According to the report of Buyin LI et al.,[6] the reactants in the molten salt have a high reactivity and mobility, and react easily and completely, which can greatly reduce the synthesis temperature. Moreover the product powders have a better uniformity and fewer agglomerates. They successfully synthesized LSO powders with pure apatite phase at relatively low temperature of 900°C. In order to further reduce the synthesis temperature, multiple salts as flux are employed in our investigation.

- NH_4NO_3

Considering the low melting point of NH_4NO_3 ($T_{\text{mp}}=140^\circ\text{C}$), it is adopted as flux of the first attempt. Figure IV.16 gives the flow chart of this molten salt method. In order to ensure all the precursor easy to melting, lanthanum nitrate ($\text{La}(\text{NO}_3)_3 \cdot 6\text{H}_2\text{O}$) and metadisilicic acid [7] ($\text{SiO}_2 \cdot 0.5\text{H}_2\text{O}$) were employed in this method. The mixed salts were melted at 180°C for 4h. After washing, filtering, the residue is dried as the target product.

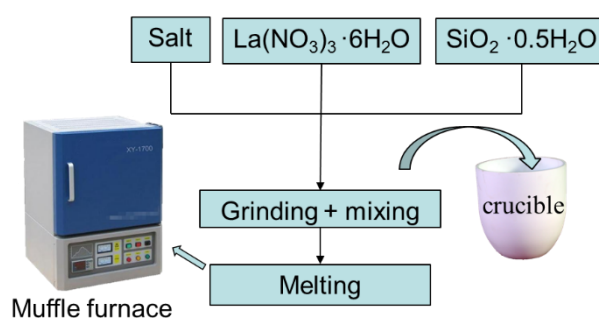


Figure IV. 16. Flow chart of molten salt method for LSO synthesis

The XRD pattern is used to identify the composition. Figure IV.17 shows the diffraction pattern of the product by molten NH_4NO_3 method. The resulting mixture is amorphous. At this stage, it has not been possible to state the reaction was taken place or not and further work would have been necessary. However, during the calcination, an intense emission of smoke was observed which led us to discard this method for environmental reason.

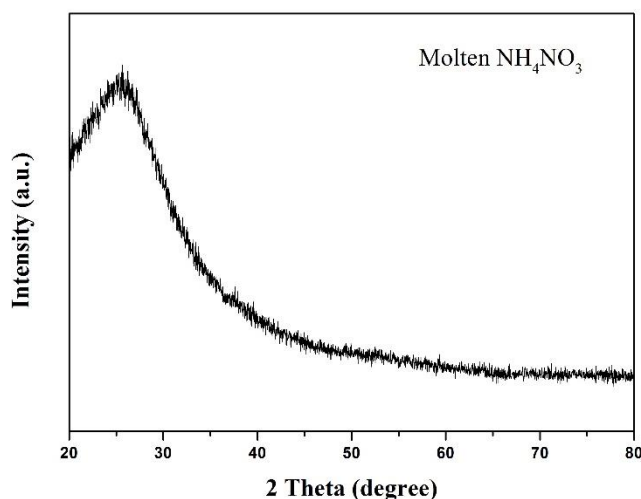


Figure IV. 17. XRD diffraction pattern of the composition synthesized by molten NH_4NO_3 method

- Eutectic mixture of alkali chlorides

Based on the paper reporting successful synthesis of LSO with molten NaCl , a eutectic mixture of alkali chlorides has been employed to develop the synthesis process, in order to decrease the temperature. NaCl - KCl eutectic is firstly used as the flux. Figure IV.18 gives the phase equilibrium diagram of the KCl - NaCl system. [8] According to the diagram, KCl (50.6%)- NaCl eutectic is prepared, then mixed to the $\text{La}(\text{NO}_3)_3 \cdot 6\text{H}_2\text{O} + \text{SiO}_2 \cdot 0.5\text{H}_2\text{O}$ with the mass ratio of 3:1.

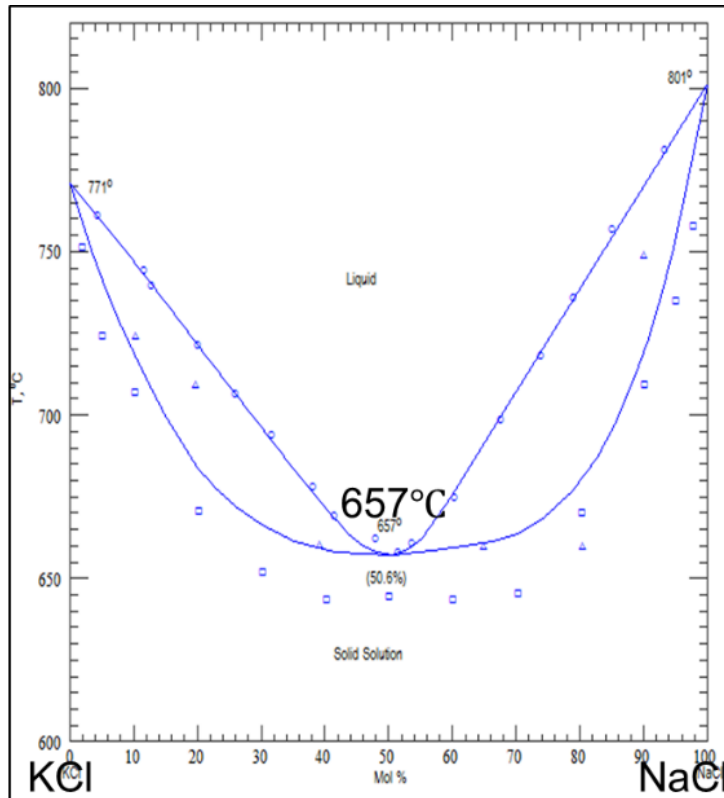


Figure IV. 18. The phase equilibrium diagram of the KCl-NaCl system

Four comparison syntheses were realized with different heating temperature 700°C, 800°C, 850°C and 950°C for 4h respectively. Among them, the products of the 850°C and 950°C experiments had a pre-heating treatment at 200°C for 6h to remove water from the salts. Figure IV.19 gives the XRD results of the composition. Unexpectedly, the principal high intensity diffraction peaks indicates that the main part of the composition is the lanthanum oxychloride (LaOCl). This material has no ability to transfer oxygen ions. In addition, the properties determine the difficulty to remove it from the product: the low solubility in water or alcohol; its thermally stable properties at temperatures as high as 1000 °C [9]. By comparing different groups, higher abundance of LaOCl exists in the groups treated with higher temperature. It can be seen the apatite phase almost disappears at 1000°C treatment, while the abundance of LSO phase has

significant increase at 800°C. As for the 700°C group, it is inferred the mixture is not completely melted by the experimental observation. Thus the formation of LSO is impeded.

To achieve pure phase LSO product, two ways are taken to solve the LaOCl problem: washing with citric acid solution and reduce the heating temperature.

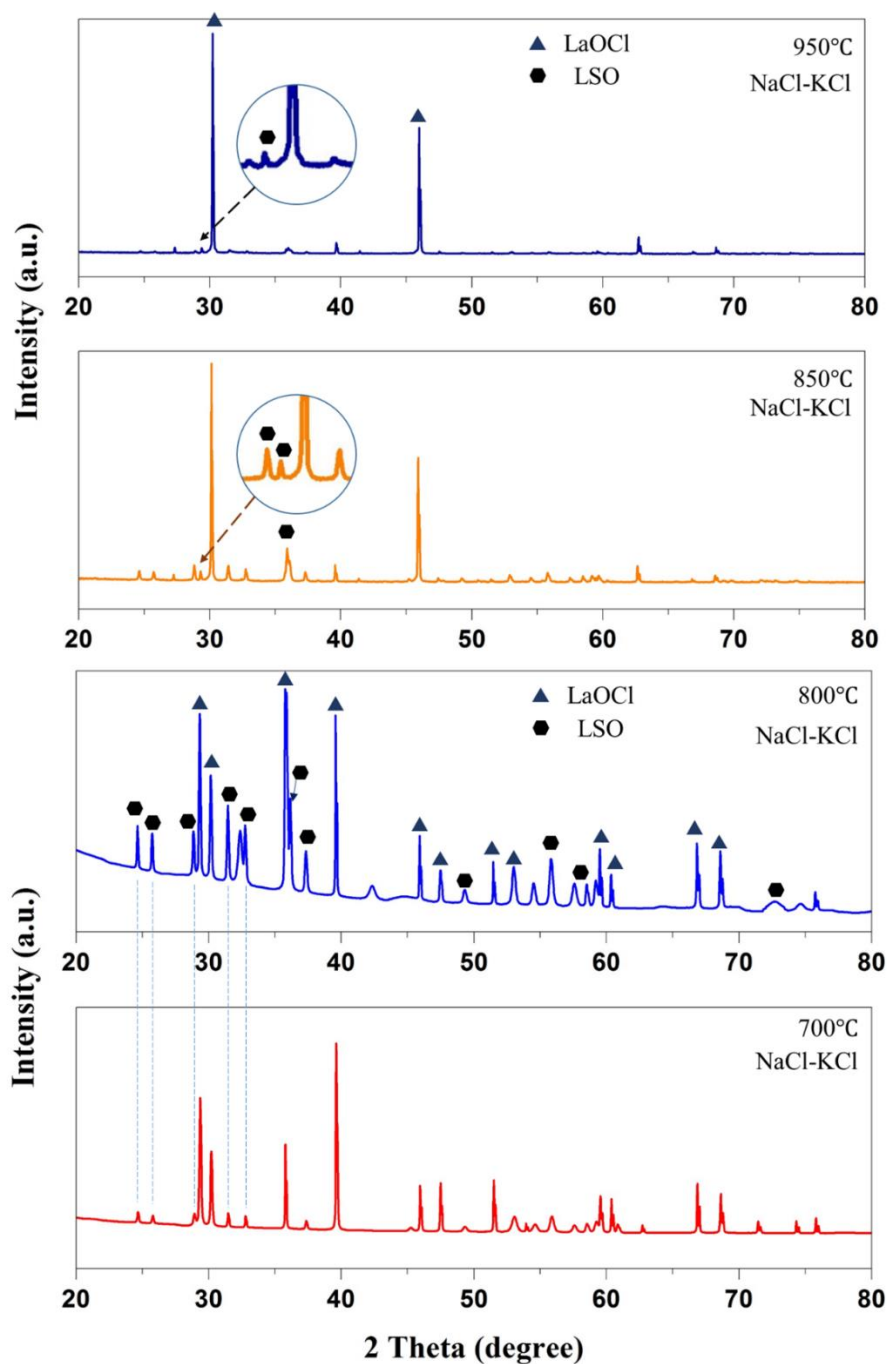


Figure IV. 19. XRD results of the product with NaCl-KCl eutectic method by multiple temperature

Figure IV.20 illustrates the diffraction pattern comparison between the products before and after the citric acid washing. After the washing process, the only remaining peaks of LSO phase disappear. The acid solution has an effect contrary to the one aimed since the LSO is dissolved rather than LaOCl.

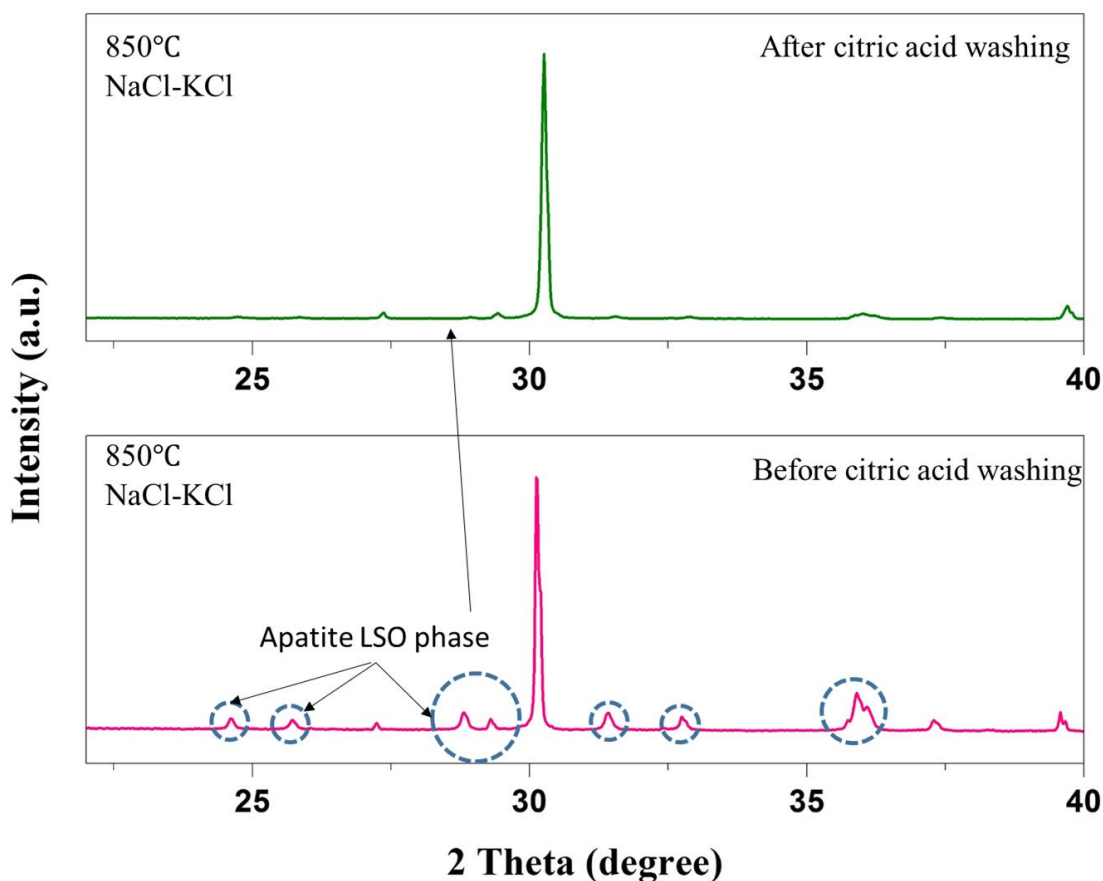


Figure IV. 20. The diffraction pattern of the 850°C group before and after the citric acid washing

In order to reduce the reaction temperature, the KCl-LiCl eutectic was chosen in turn as an alternative fluxing system. The phase equilibrium diagram of this system is shown in Figure IV.21.[10] According to the diagram, the reaction temperature is set as 450°C for 10h. The diffraction pattern of the product is shown in Figure IV.22. The principal high intensity

diffraction peaks still indicates the main product is still LaOCl, and it can be formed at the temperature as low as 450°C. The temperature is not enough to form the LSO apatite phase. Chloride and lanthanum ions can easily react with each other in molten salt environment. To avoid the emergence of LaOCl, chloride salts were discarded as potential fluxing agents in our following investigations.

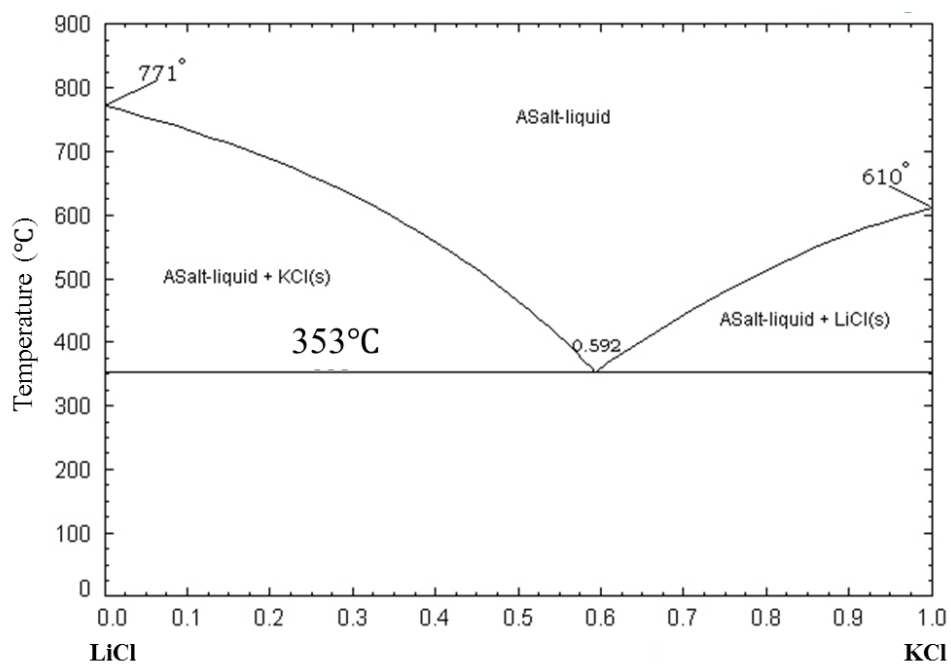


Figure IV. 21. The phase equilibrium diagram of the KCl-LiCl system

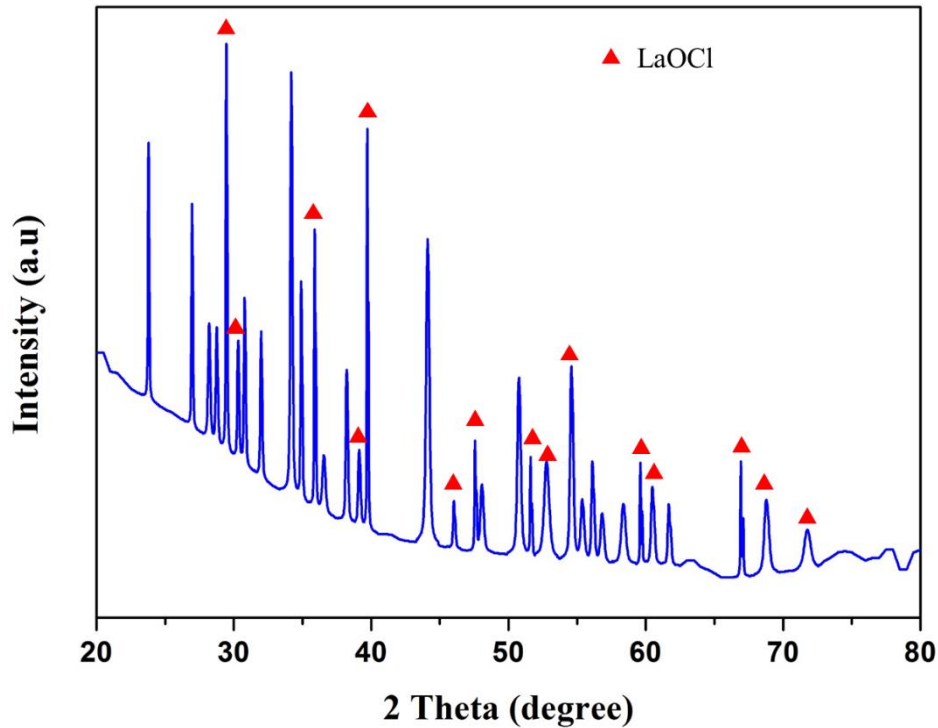


Figure IV. 22. XRD results of the product with LiCl-KCl eutectic method at 450°C for 10h

- Eutectic mixture of alkali sulfates

Sulfates are chosen as the flux to develop the molten salt method. The $\text{Li}_2\text{SO}_4\text{-K}_2\text{SO}_4$ system has a relatively low melting point, which is suitable in this attempt. The phase equilibrium diagram of this system is shown in Figure IV.23. The synthesis process is similar to the previous experiments, including the mass ratio of the flux and reactants. Two reaction temperatures are used in this section: 700°C and 900°C for 4h respectively.

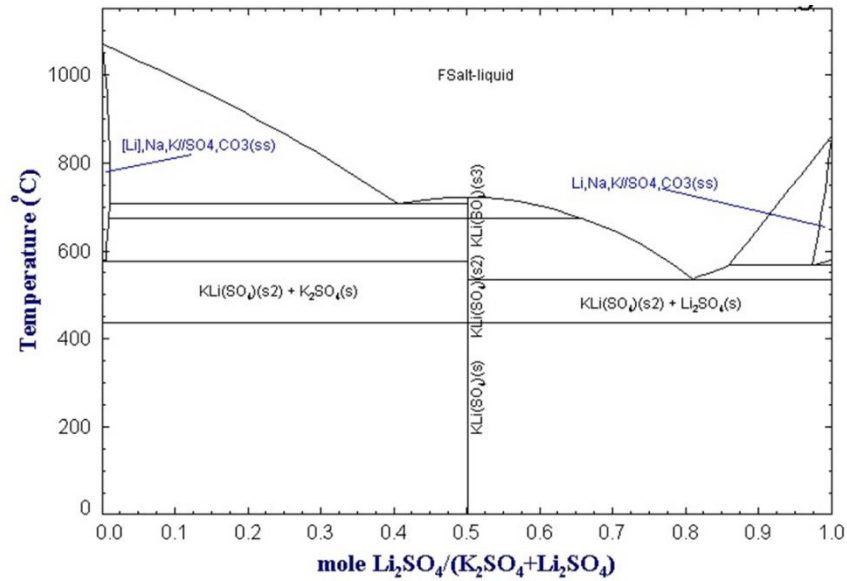


Figure IV. 23. The phase equilibrium diagram of the $\text{Li}_2\text{SO}_4\text{-K}_2\text{SO}_4$ system (data from FTsalt)

The XRD results are shown in Figure IV.24. A new impurity consisting in $(\text{LaO})_2\text{SO}_4$ appears in the product and it is in higher abundance than LSO composition. Therefore, when using the sulfate path, the LSO phase can be found in the product but, at the same time, another impurity is also introduced.

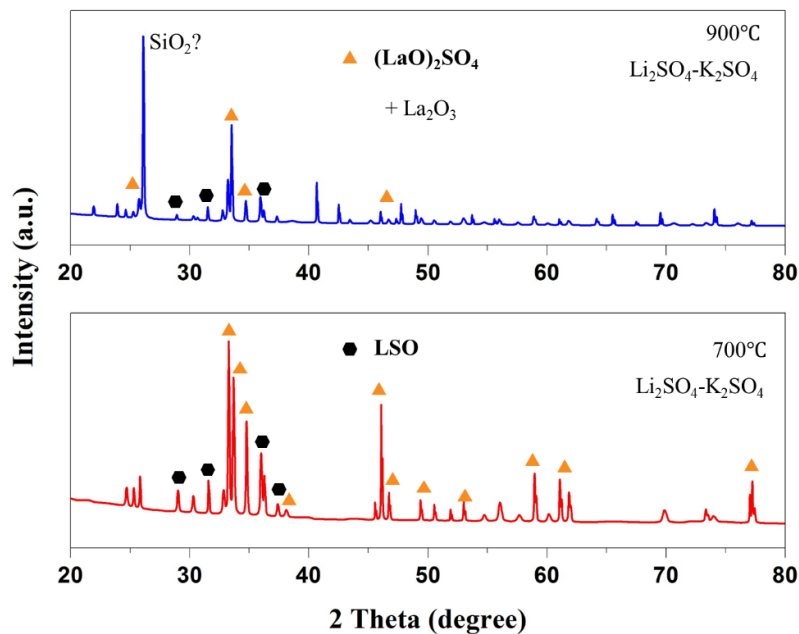
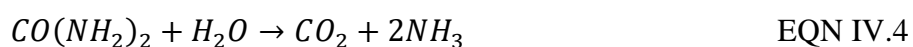


Figure IV. 24. XRD results of the product with $\text{Li}_2\text{SO}_4\text{-K}_2\text{SO}_4$ eutectic method at 700°C and 900°C

In summary, the molten salt method would need further important development to become effective.

IV.4 Homogeneous deposition precipitation (HDP)

Homogeneous deposition precipitation (HDP) method has also been tested for the synthesis of apatite phase LSO. Figure IV.25 gives the schematic diagram of the equipment. Stoichiometric lanthanum nitrate, silica gel and urea are dissolved in water. With stirring and heating, the hydrolysis reaction of urea takes place in the flask slowly.



The solution gradually becomes alkaline with the CO_2 being evolved outside the solution and ammonia being created. Therefore, lanthanum hydroxide can be deposited slowly and homogeneously on the silica gel particles and react with them.

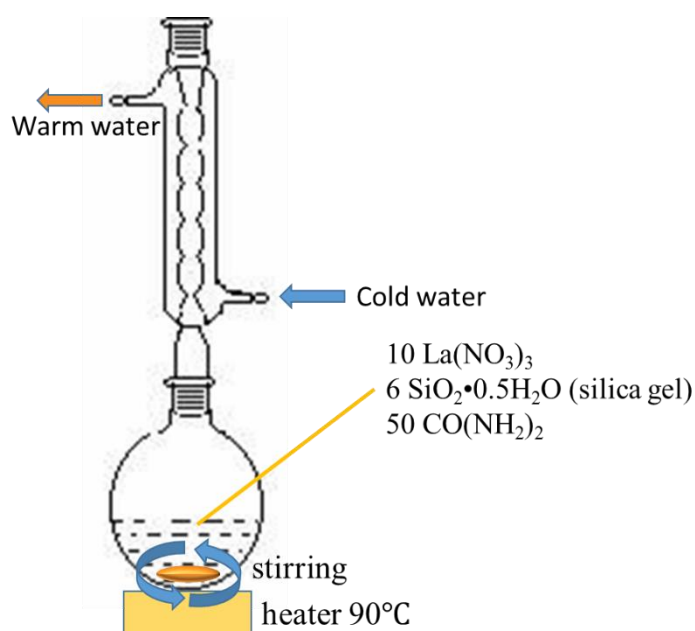


Figure IV. 25. Schematic diagram of homogeneous deposition precipitation method equipment for synthesizing LSO compounds

After filtering the obtained suspension, it is calcined at 800°C for 2h. The XRD results are shown in Figure IV.26. Almost all the high intensity diffraction peaks indicate lanthanum oxide (La_2O_3) which means that the lanthanum hydroxide has been actually deposited in this method. However, the formation reaction of LSO has not taken place in the process.

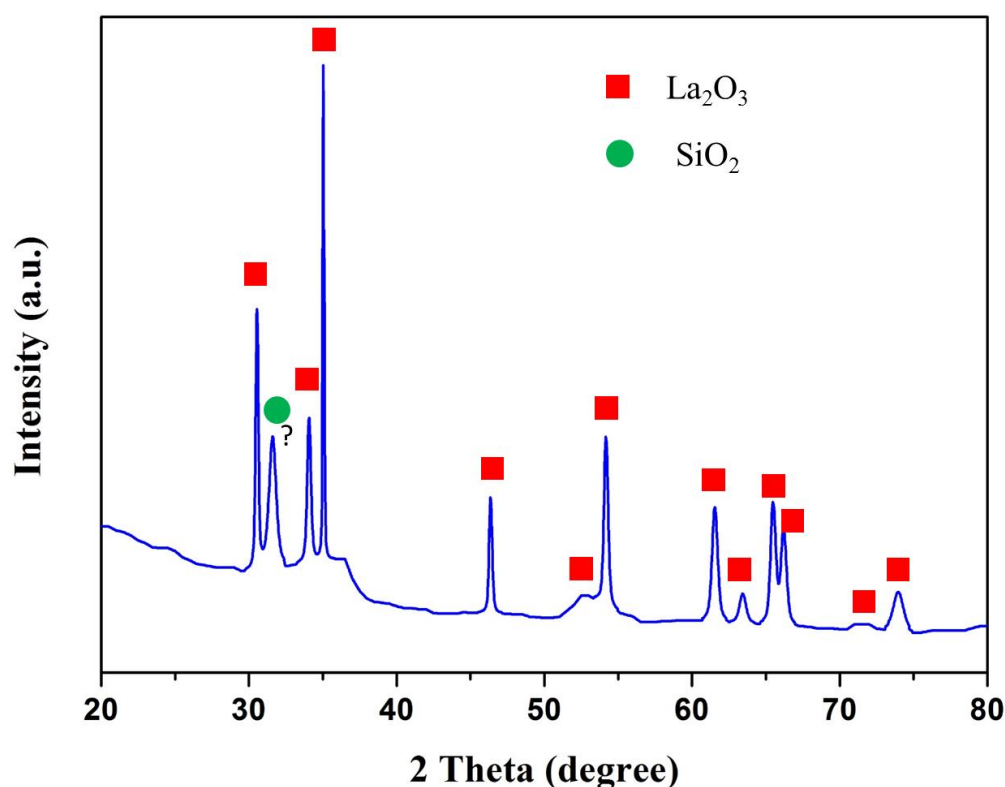


Figure IV. 26. XRD results of the product with HDP method with calcination temperature of 800°C for 2h

In order to explore the reasons of the absence of LSO phase formation, the morphology of the product has been examined by SEM in Figure IV.27. It is shown that the micron level hexagonal crystals exist in the powder, which is inferred as La_2O_3 for it has hexagonal crystal structure (P-3m1). This proves that the La_2O_3 got agglomerated during the deposition process. This agglomeration process is faster than the reaction with silica gel, which leads to an incomplete reaction to form apatite phase.

The hydrolysis process is still too fast in comparison with the $\text{La}_2\text{O}_3\text{-SiO}_2$ reaction. Some dispersant or TEOS could be introduced in deposition process to prevent the agglomeration but this assumed relatively important further investigations.

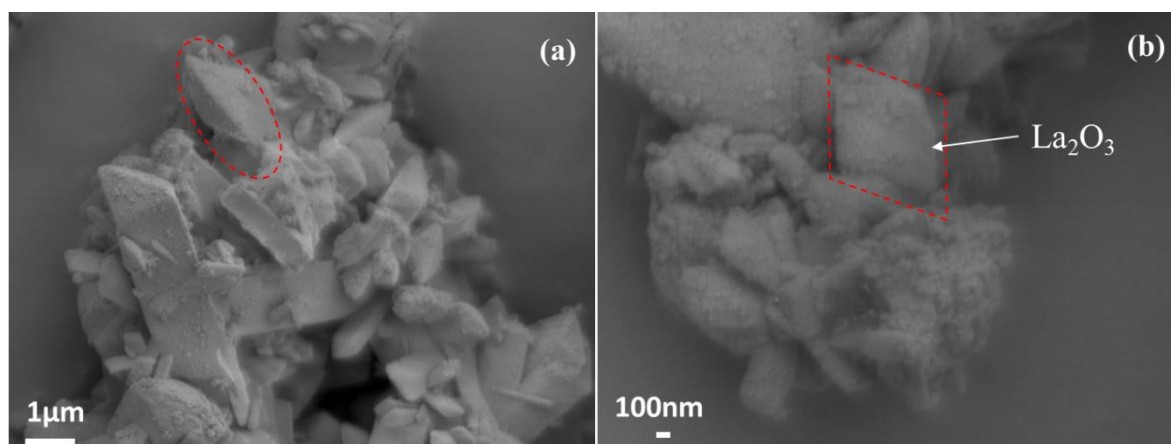


Figure IV. 27. The morphologies of the powder with HDP method calcined at 800°C for 2h by SEM analysis

IV.5 Summary

In this chapter, we have reported several preliminary attempts to prepare LSO with alternative chemical methods. The co-precipitation method proved to be the most effective since the apatite phase composition could be successfully obtained from quite moderate temperature of 700°C for 6h. However after the sintering treatment of 1500°C for 2h, the samples exhibit mediocre performance in terms of ionic conductivity ($7.73 \text{ mS}\cdot\text{cm}^{-1}$ at 675 °C). The other routes explored would need substantial improvements to become effective.

For these reasons, we finally selected the sol-gel method which gave high purity apatite samples with pretty good electric performances as developed in chapter V.

IV.6 References

- [1] Li B, Liu W, Pan W. Synthesis and electrical properties of apatite-type $\text{La}_{10}\text{Si}_6\text{O}_{27}$. *J Power Sources*. 2010;195:2196-201.
- [2] Briois P, Mazataud C, Fourcade S, Mauvy F, Grenier J-C, Billard A. Synthesis and characterization of apatite structure sputter deposited coatings dedicated to intermediate temperature solid oxide fuel cells. *Journal of The Electrochemical Society*. 2011;158:B1479-B84.
- [3] Tao SW, Irvine JTS. Preparation and characterisation of apatite-type lanthanum silicates by a sol-gel process. *Mater Res Bull*. 2001;36:1245-58.
- [4] Maruyama H, Kishimoto H, Yasui M, Horita T, Yamaji K, Yamazaki A. Conductivity Enhancement of Apatite-Type Doped Lanthanum Silicates.
- [5] Birkner N, Navrotsky A. Thermodynamics of manganese oxides: Effects of particle size and hydration on oxidation-reduction equilibria among hausmannite, bixbyite, and pyrolusite. *American Mineralogist*. 2012;97:1291-8.
- [6] Li B, Liu J, Hu Y, Huang Z. Preparation and characterization of $\text{La}_{9.33}\text{Si}_6\text{O}_{26}$ powders by molten salt method for solid electrolyte application. *Journal of Alloys and Compounds*. 2011;509:3172-6.
- [7] Rochow EG. *The Chemistry of Silicon: Pergamon International Library of Science, Technology, Engineering and Social Studies*: Elsevier; 2013.
- [8] Coleman D, Lacy P. The phase equilibrium diagram for the KCl-NaCl system. *Materials Research Bulletin*. 1967;2:935-8.
- [9] Imanaka N, Okamoto K, Adachi Gy. Water-Insoluble Lanthanum Oxychloride-Based Solid Electrolytes with Ultra-High Chloride Ion Conductivity. *Angewandte Chemie International Edition*. 2002;41:3890-2.
- [10] Janz GJ. *Molten salts handbook*: Elsevier; 2013.

Chapter V Synthesis of Pure $\text{La}_{10-x}\text{Sr}_x\text{Si}_6\text{O}_{27-0.5x}$
Apatites Using an Optimized Sol-Gel Process

In this chapter, the synthesis process of Sr-doped $\text{La}_{10}\text{Si}_6\text{O}_{27}$ through optimizing a water-based sol-gel method is studied. The relevant synthesis parameters have been investigated to get pure, highly crystalline powders. The mechanisms occurring in the sol-gel reactions are discussed. Pure apatite powders have been obtained by calcination from a temperature as low as 800°C for 2h and they have considerable performance as electrolyte material in IT-SOFC.

V.1 Parameters investigation

The influences of multiple elements doping were studied to modify the apatite $\text{La}_{10}\text{Si}_6\text{O}_{27}$ performance as an electrolyte. Generally elements Ge, Mn, Al, Fe, etc [1-5] are chosen to dope at Si site. Sr has been chosen as suitable element doping at La site due to the similar chemical properties with La.

V.1.1 Synthesis process

Two sources of lanthanum consisting of: La_2O_3 (Aldrich 99.9%) and $\text{La}(\text{NO}_3)_3 \cdot x\text{H}_2\text{O}$ (Aldrich 99.0%), TEOS (tetraethyl orthosilicate, Aldrich 99.9%) and strontium nitrate : $\text{Sr}(\text{NO}_3)_2$ (Aldrich 99.0%) were used as starting materials. The synthesis procedure is shown in Figure V.

1. Dilute ammonia and nitric acid were used to adjust the pH.

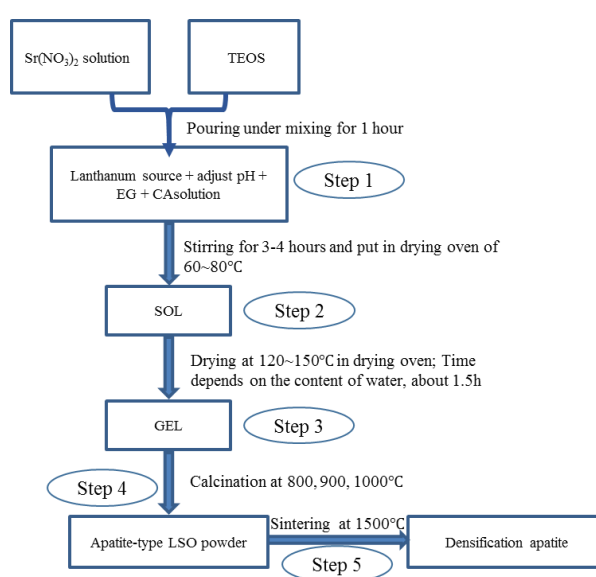


Figure V. 1. Flow chat of the process used for the preparation of doped and undoped lanthanum silicates

Lanthanum nitrate that had been previously studied by TGA in order to determine its hydration degree “ $x = 6$ ” (shown in Figure V. 2), was dissolved in deionized water (solution A). Alternatively, La_2O_3 was calcined at 800°C and dissolved in dilute HNO_3 to obtain a clear solution (solution B). Solutions A and B were used as La sources.

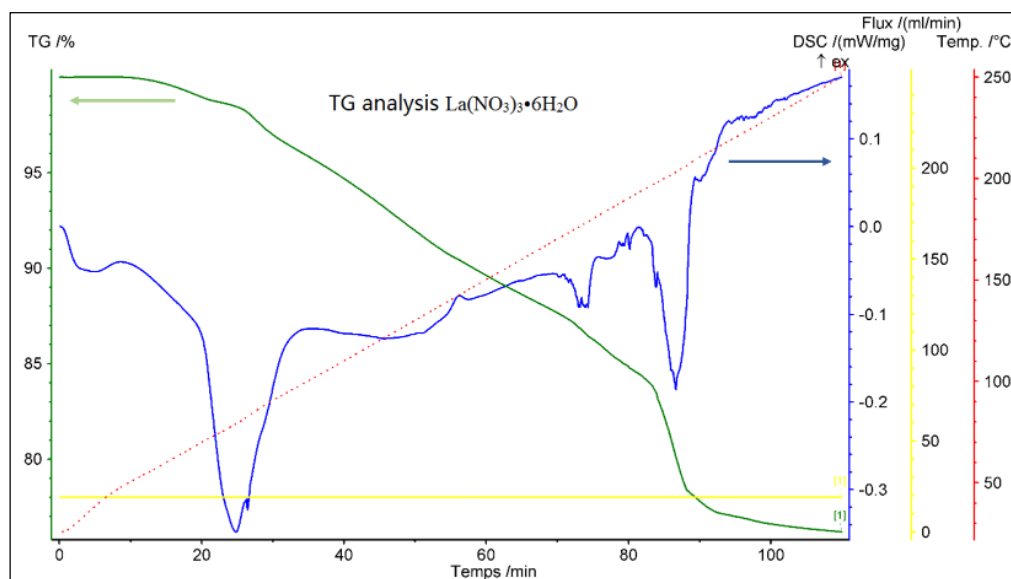


Figure V. 2. TG/DSC curves of $\text{La}(\text{NO}_3)_3 \cdot x\text{H}_2\text{O}$ as raw material to verify the number of crystal water in a molecular

Ethylene glycol (EG) and citric acid (CA) were added to the above solution yielding solution A1 or B1 in which the ratio between the (EG+CA) mixture (in 1:1 molar proportion) and the $(\text{La}^{3+} + \text{Sr}^{2+})$ moles equaled one. TEOS and $\text{Sr}(\text{NO}_3)_2$ were mixed separately with deionized water leading to two mixtures; in step 1, this two mixtures were added into the solution A1 or B1 under mixing. After adjusting the pH with nitric acid or ammonia solution, the resulting solution was stirred for 3-4 h to form the sol (step 2), then the latter was dried in an oven at 80°C yielding a dry gel (step 3). The dry gels were pressed under 200 MPa for 40s to form disks of 1.5cm diameter. Once the disks were obtained, they were calcined in air at 800°C , 900°C and

1000°C, with a heating ramp of 10°C/min and then freely cooled (step4). A final sintering (step 5) was performed at a temperature up to 1500°C for 2h in order to obtain densified LSO.

In this work, the doping ratios of Sr, which occupies some La sites, were set as Sr/La = 0/10, 1/9 and 2/8 by atom, leading to three distinct “groups” of apatites having the theoretical formulas: $\text{La}_{10}\text{Si}_6\text{O}_{27}$ (undoped), $\text{La}_9\text{SrSi}_6\text{O}_{26.5}$ (1-Sr dope) and $\text{La}_8\text{Sr}_2\text{Si}_6\text{O}_{26}$ (2-Sr dope) respectively.

V.1.2 Effect of Sr-doping

The use of solution B as La source led to white sticking powders after the drying step at 120°C-150°C. The three groups of apatite as defined above were prepared using this solution B. The XRD patterns obtained after sintering are shown in Figure V. 3.

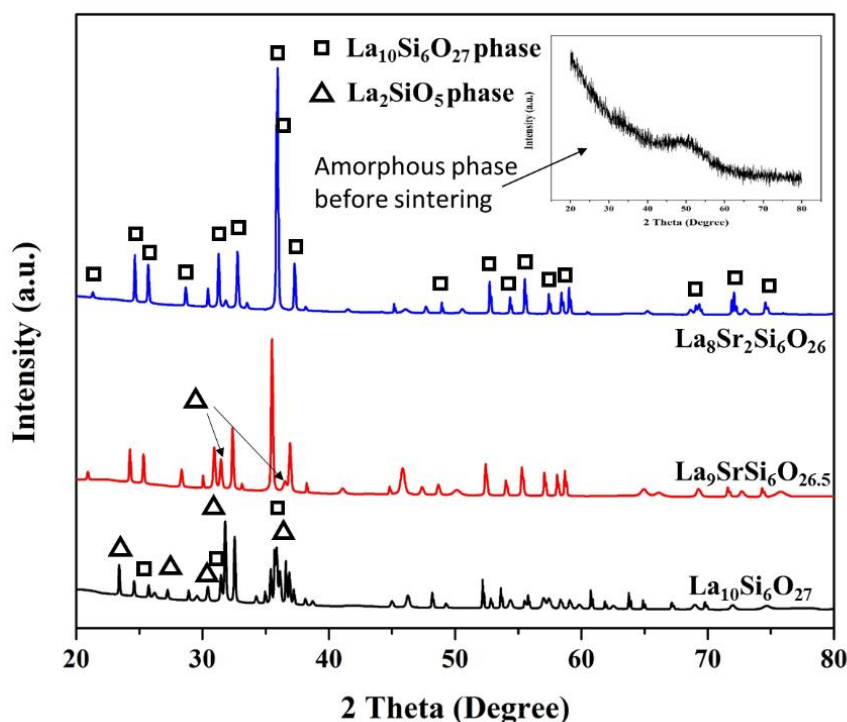


Figure V. 3. Diffraction patterns of lanthanum silicates corresponding to the three Sr-doping ratios after sintering (1500°C, 4h). The inset shows the pattern of dry gel before sintering

All the dry gels are amorphous. Indeed atoms of La, Si and Sr (when present) lie in quite close vicinity of each other in the gel which is conducive to the complete reaction in the sintering step and yields the apatite phase. The XRD patterns after calcination at 800°C and sintering at 1500°C show that the 2-Sr doped apatite group exhibits the highest crystallinity: as the doping ratio increases, the degree of crystallinity becomes higher with larger grains being formed. The undoped group shows major peaks of La_2SiO_5 which comes from a reaction between SiO_2 and La_2O_3 in zones. The latter is locally in excess with a $\text{La}_2\text{O}_3/\text{SiO}_2$ ratio higher than 5/6 which corresponds $\text{La}_{10}\text{Si}_6\text{O}_{27}$ product. Based on the atoms balance, it can be inferred that some amorphous SiO_2 is present in the undoped apatite. The addition of strontium atoms that compete with lanthanum in the reaction with silicon tends to alleviate this effect. Thus, the Sr-doping has a certain positive influence for obtaining pure apatite in our sol-gel process. There is still a small amount of La_2SiO_5 detected in “1-Sr doped” group which almost disappears in “2-Sr doped” group that exhibits narrow and sharp diffraction peaks. Neither Sr oxide nor silicate can be detected in the two groups of Sr doped apatite which indicated that Sr has been fully incorporated into the apatite structure. This positive effect of the Sr doping in the sol gel process is also probably due to the strong alkaline character of this metal that readily reacts with the silicate ion. Nevertheless, some very tiny secondary peaks persist even in the “2-Sr doped” group. In order to increase the purity, we decided to assess the effect of pH.

V.1.3 Study of the influence of pH

In this section, we prepared three reaction media having different pH:

- Solution A1 as such was taken as near-neutral medium (pH = 5.2)
- Solution B1 adjusted to pH 0.2 with HNO_3 was taken as acidic medium;
- Solution A1 adjusted to pH 8.3 with $\text{NH}_3 \cdot \text{H}_2\text{O}$ was taken as alkaline medium.

The synthesis procedure was then conducted as shown in figure V.1.

chains is a kind of alcoholysis, and the hydroxyl group original from silanol, the product of previous hydrolysis reaction. This leads to form silicon-oxygen chains. There are unreacted hydroxyl group still at the ends of the chains, which keep the chains soluble in water. Thus, the solution contains both chelating metal ions chains and hydrophilic silicon chains that are intertwined due to Van der Waals attraction (dotted line in step 3). Such solution that contains randomly distributed ionic reagents favors an efficient gelation process, which prevents the formation of unwanted single oxide phases in the next calcination treatment.

Because the first solution is too acidic, the citric acid ionization is inhibited leading the chelation inoperative. Conversely, in the alkaline solution, the metal ions get preferentially associated with hydroxide ions, resulting in insoluble alkali hydroxide being precipitated without any gelation process leading to turbid solution: after 1h standing, the liquid appears stratified and the deposition can be found in bottom. The near-neutral group possess clear, stable and viscous solution. The acidic group exhibits not so clear, but stable solution.

Figure V. 5 (a) and (b) show the morphologies of two dry gels, prepared with “non optimized” (alkaline pH) and optimized (near neutral pH) gelation conditions respectively. When using the “non optimized” gelation conditions, the agglomeration and crystallization of the precursors seem to start before the calcinations step: the micro-sized particles having regular shapes are probably separated La_2O_3 or SiO_2 phases. However, with the optimized gelation conditions, the average size of the particles is in dozens nm: there is apparently neither partial crystallization nor agglomeration. The presence of such nano-particles is favorable for the formation of the apatite structure.

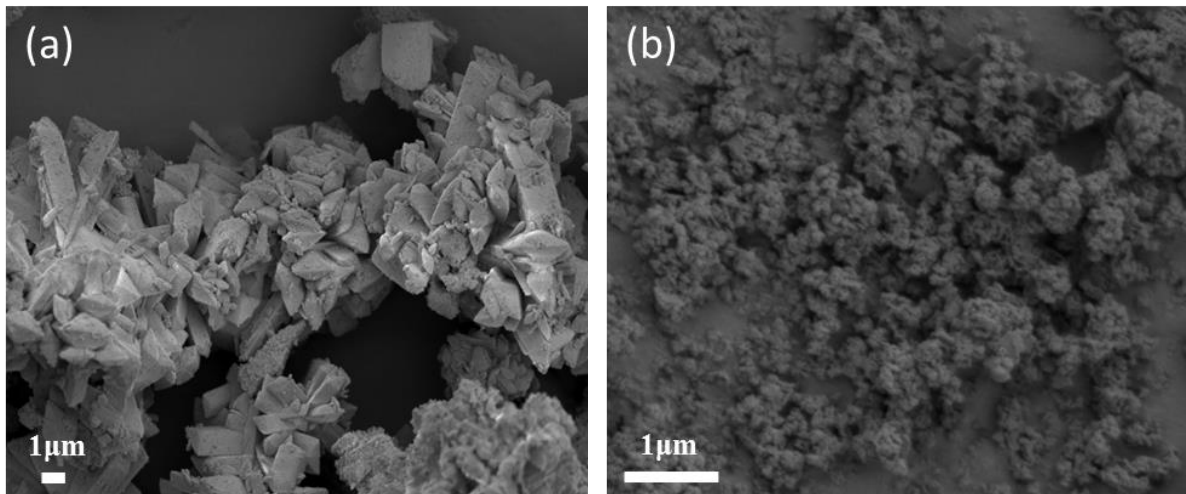


Figure V. 5. SEM figures of the morphologies of the obtained compounds with optimized process (a, dry gel before calcination with unsuitable pH; b, dry gel before calcination with optimized pH.)

V.1.4 Effect of the calcination condition

In this section, we will focus on the undoped LSO obtained through “near-neutral solution” as it appears to be the most difficult apatite to synthesize. The investigated parameters were the calcination temperature and duration with the objective to identify the most suitable conditions. Three calcination temperatures (800°C, 900°C and 1000°C) and times (2h, 4h and 8h) have been explored. Firstly we noted that the formation of apatite is not satisfactory below 800°C. The influence of the calcination parameters is visible in Figure V. 6 that shows the useful portion of the X-ray diffraction range. The calcination temperature has a much stronger effect on the crystallization process than the duration. As we can see in the diagram (a), the diffraction peaks become sharper and narrower when the temperature increases. The sample calcined at high temperature displays peaks with low FWHM (Full width at half maximum) data, which means that it contains bigger grains of greater crystallinity. In addition, the two overlapping peaks [Miller indices of (211) and (112)] are increasingly separated when passing from 800 to 1000°C.

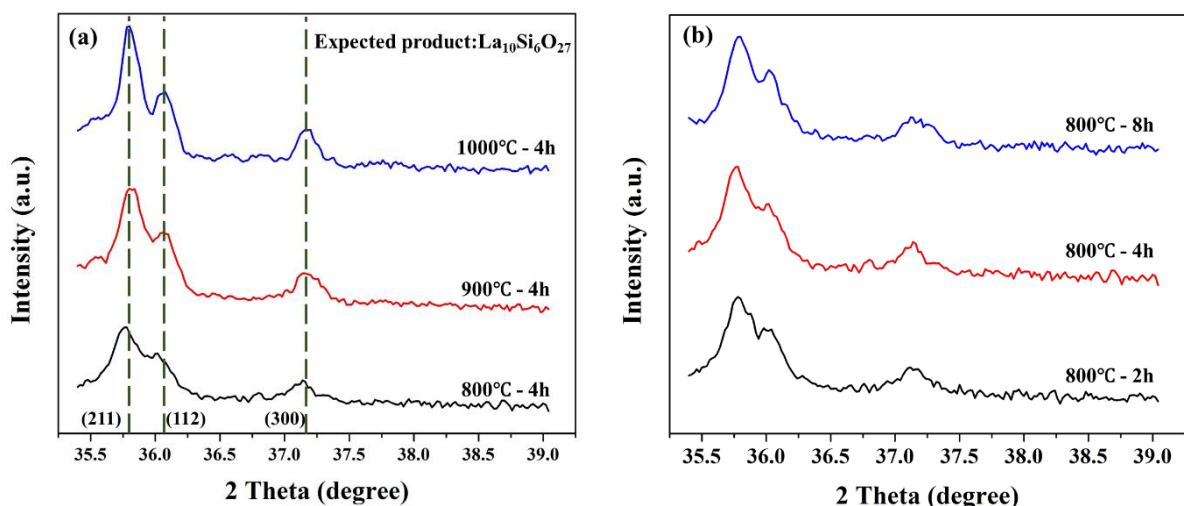


Figure V. 6. Diffraction patterns of the obtained powders for the sintering time (a) and temperature (b) studies

The influence of the calcination duration is shown in the diagram (b): one does not see any significant effect of this parameter. We can conclude that, while the formation of the amorphous apatite molecule is a rather fast process which can be completed with an 800°C-2h calcination treatment, the crystallization process is a substantially activated process.

Therefore, besides a nearly neutral pH, the most favorable condition is a minimum calcination, temperature of 800°C with a duration 2 hours being sufficient.

V.2 Optimized synthesis study

V.2.1 Calcination study

Based on the discussion, the $\text{La}_{10-x}\text{Sr}_x\text{Si}_6\text{O}_{27-0.5x}$ ($x=0, 1, 2$) apatites are synthesized through the water-based sol-gel technique using $\text{La}(\text{NO}_3)_3 \cdot 6\text{H}_2\text{O}$, $\text{Sr}(\text{NO}_3)_2$ and TEOS (tetraethyl orthosilicate) as raw materials. Ethylene glycol (EG) and citric acid (CA) were used - in equimolar ratio - as they are reputed to generate good quality sols according to the Pechini process. The ratio between the number of moles of the (EG+CA) mixture to that of ($\text{La}^{3+} + \text{Sr}^{2+}$) equals one. TEOS is first added in a stirred solution of $\text{Sr}(\text{NO}_3)_2$ in deionized water and the

mixture is added under stirring into the above (EG+CA) solution. During the process of sol formation, the pH value is controlled around 4~6 (we had studied the influence of pH value in previous work). The sols obtained are dried at 120-150 °C, yielding dry gels. These are compacted at 200 MPa for 30s, calcined in air at different temperatures: 800°C, 900°C and 1000°C for 2h with a heating rate of 10°C/min and are finally freely cooled.

Table V.1 shows the XRD analyses of different “groups” of powders synthesized using different doping ratios and calcination temperatures. We call hereafter Group 1, Group 2 and Group 3 the synthesized LSO apatites having the respective molar Sr/La ratio of: 0, 1:9 and 2:8, each group comprising three “individual materials” that have been calcined at 800, 900 and 1000°C respectively.

Table V. 1. XRD analyses of powders obtained with different Sr doping ratios and calcination temperatures

	Solution status	Expected products formulas	Sintering parameters	Tag in this study	XRD analysis results
Group 1		$\text{La}_{10}\text{Si}_6\text{O}_{27}$	800°C-2h	800-1	Apatite structure
			900°C-2h	900-1	
			1000°C-2h	1000-1	
Group 2	Clear and jelly-like	$\text{La}_9\text{SrSi}_6\text{O}_{26.5}$	800°C-2h	800-2	
			900°C-2h	900-2	
			1000°C-2h	1000-2	
Group 3		$\text{La}_8\text{Sr}_2\text{Si}_6\text{O}_{26}$	800°C-2h	800-3	
			900°C-2h	900-3	
			1000°C-2h	1000-3	

It can be seen that all powders obtained have the apatite structure even with a calcination temperature as low as 800°C. Figure V. 7 shows a typical XRD patterns for dry gels before calcination.

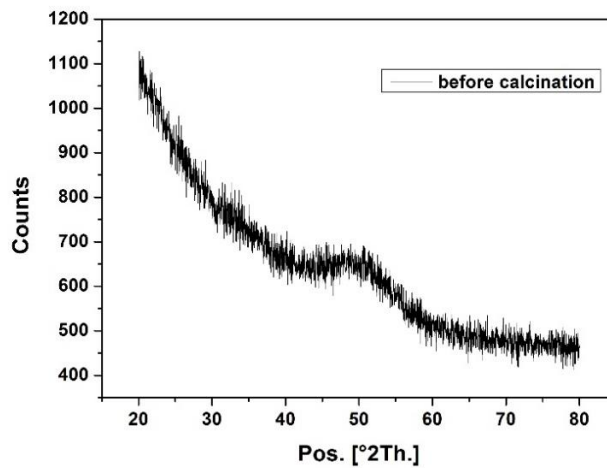


Figure V. 7. Typical XRD pattern of a dry gel before calcination

The virtual absence of high intensity diffraction peak in the diagram means that the dry gel is amorphous. Similar XRD results were obtained for all groups. The XRD patterns of the nine individual materials after calcination are shown in Figure V. 8.

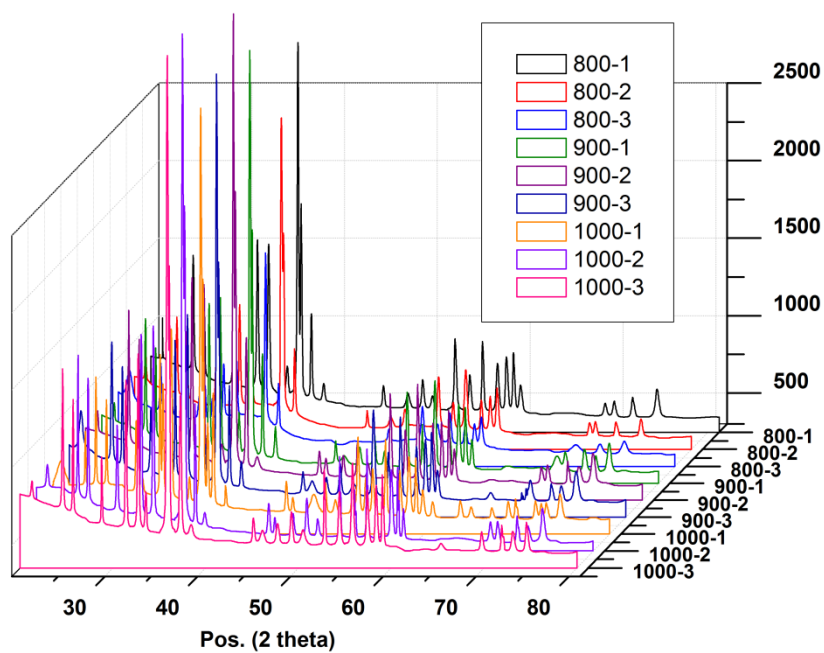


Figure V. 8. XRD patterns obtained with different calcination temperature and Sr doping (no sintering)

All the high-intensity reflections correspond accurately to the apatite phase $\text{La}_{10}\text{Si}_6\text{O}_{27}$ (pdf ref. code: 00-053-0291) composition and no secondary phases are detected, including Sr doping cases (groups 2 and 3). This indicates that pure apatite can be formed at 800°C even for 2h. In addition the XRD patterns of group 2 and 3 do not show any peak pertaining to any Sr compound. Thus, it can be said that the Sr atoms have been well incorporated inside the apatite crystal structure.

Figure V. 9 shows the $30\text{-}40^\circ$ portions of the XRD diagrams relating to different calcination temperatures and doping ratios.

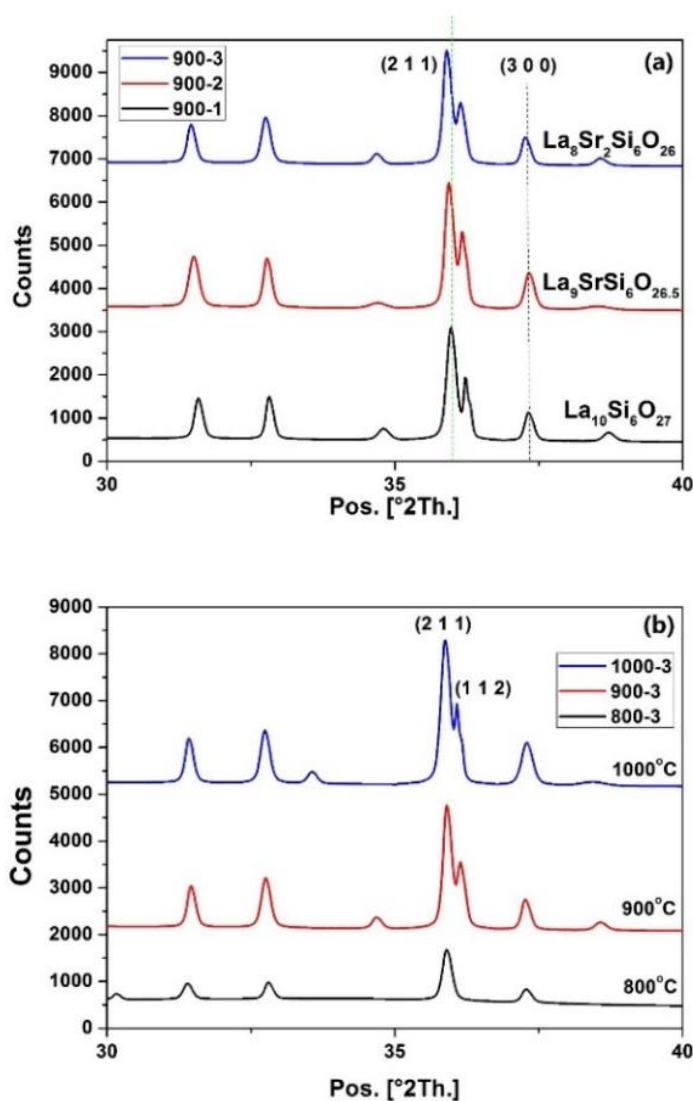


Figure V. 9. Local XRD patterns corresponding to three Sr doping ratios (a) and three calcination temperatures (b) (no sintering)

Figure V. 9 (a) shows that the diffraction intensity is virtually the same irrespective of the doping ratio. However, the diffraction peak corresponding to the (2 1 1) Miller index shows an increasing shift towards the low angles with increasing Sr doping ratios. This effect is not perceptible with the (3 0 0) lattice plane. Based on a previous simulation work, we infer that the lattice of $\text{La}_{10}\text{Si}_6\text{O}_{27}$ gets expanded along the c -axis direction as the Sr dopant occupies some La sites, while the crystal lattice size does not change significantly along the a and b -axes. The reason of this very minor change in crystal geometry lies in the close ionic radii of Sr^{2+} (1.32\AA) and La^{3+} (1.17\AA).

The calcination temperatures slightly affect the lattice parameters as it can be seen in Figure V. 9 (b) which shows the diffraction patterns under different calcination temperatures at constant doping ratio. However, as expected, the diffraction intensity grows with the calcination temperature since the degree of crystallization increases. A close examination of these peaks shows average FWHM (width at half maximum) data ranging between 0.1181° and 0.2362° , which corresponds to rather small grains.

The microstructure of the LSO compounds impacts also on the ionic conductivity in SOFC applications. For example the degree of compactness of the bulk which reflects the crystallization degree, impacts the conductivity since the conductivity of the boundary zones is different from that of the crystal bulk. It also affects the isolation conditions of the gas fluxes, which is of prime importance within SOFC applications. Figure V. 10 shows typical SEM microstructures of various synthesized apatites. Figure V. 10 (a) shows agglomerated blocks and some smaller, dispersed particles, the average size of the blocks being in the order of magnitude of $10\text{--}50\mu\text{m}$.

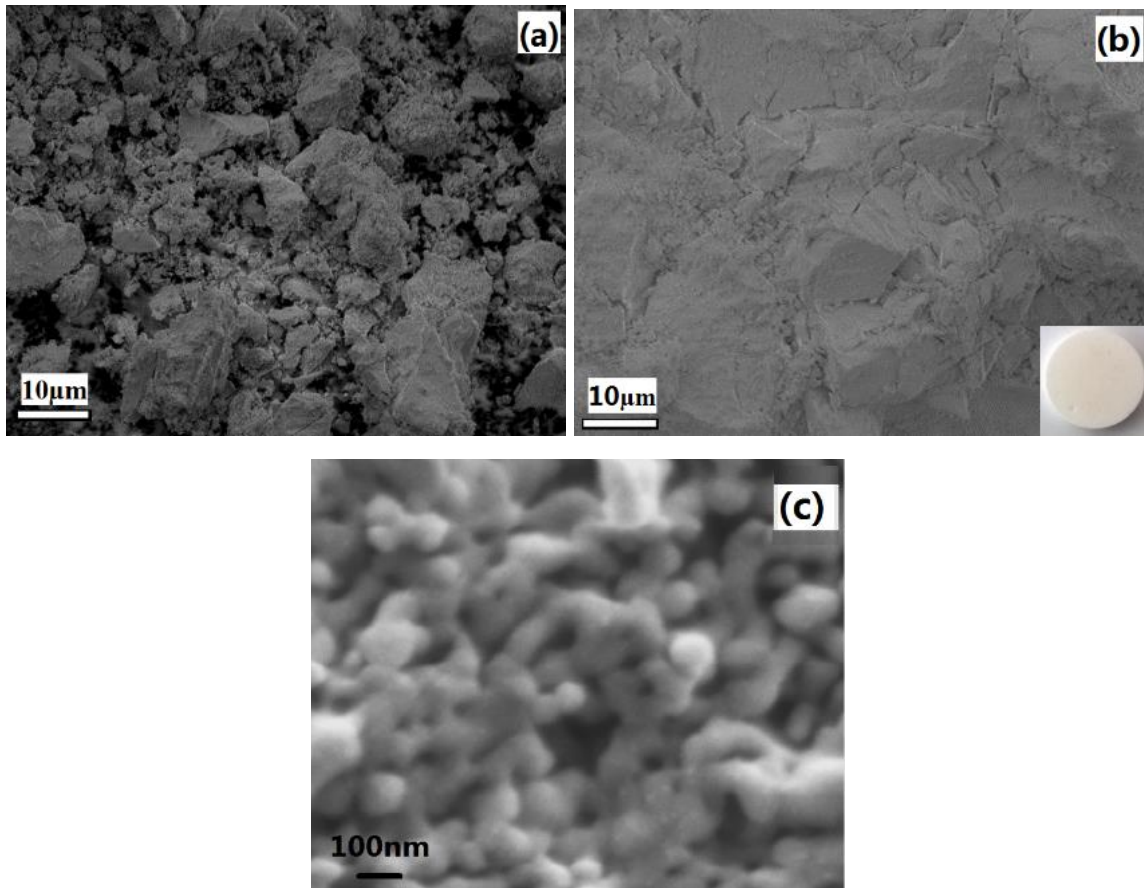


Figure V. 10. SEM micrographs of calcined (no sintering) samples (a, 900 °C-3; b, 1000 °C-3; c, 1000 °C-3)

Figure V. 10 (b) shows the morphology of compacted compound (the inset shows the final pellet): it is visible that the solid particles connect each other in a quite tight way which leads to a good isolation of the gas fluxes. However some micro-cracks are visible among the blocks which slightly affect the density of the sample and create a risk of direct contact between air and fuel. Nanoscale microstructures are observed in Figure V. 10 (c) and show grain sizes in the 80~150 nm range. Despite the resolution limit of the SEM apparatus, a nanoscale porous structure is perceptible on the surface. Globally, it can be said that the microstructures are not yet optimized for SOFC applications. The sintering process is therefore required to densify the samples and make them suitable SOFC electrolytes.

The density has been determined in function of the Sr doping. The results are summarized in Figure V. 11. High calcination temperature as well as higher Sr-doping ratios are of course favorable to obtain high density samples. The average density of the samples is $2.5 \text{ g}\cdot\text{cm}^{-3}$: there is a quite high gap with the theoretical value of $5.4 \text{ g}\cdot\text{cm}^{-3}$ (evaluated through simulation methods). It can be inferred that some micro-cracks exist in the synthesized compounds despite their high purity and crystallinity. Since it is not unfavorable for the flow isolation in a real SOFC, a further densification process based on a sintering at high temperature has to be applied.

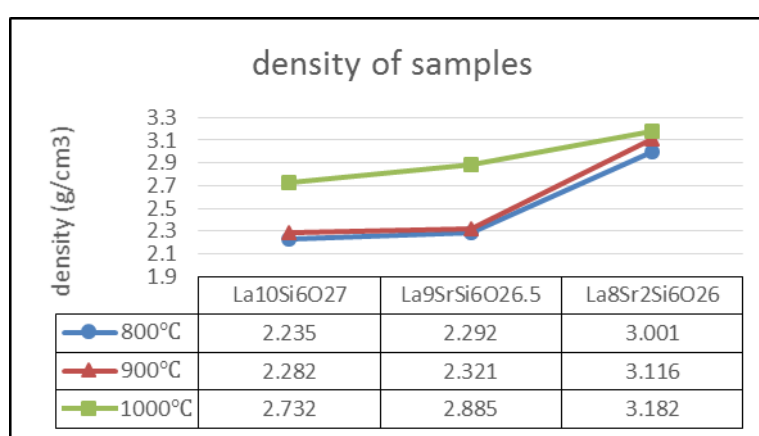


Figure V. 11. The sample density of each group by the optimized process

V.2.2 Sintering study

A further sintering step at a temperature of 1500°C for 2h is applied in order to densify the samples. The density data of the samples also evolve. Figure V. 12 shows the change in size of a particular sample after sintering. The volume resulting from this reduced geometry gets decreased by 73%, so that the density increased by the same amount.

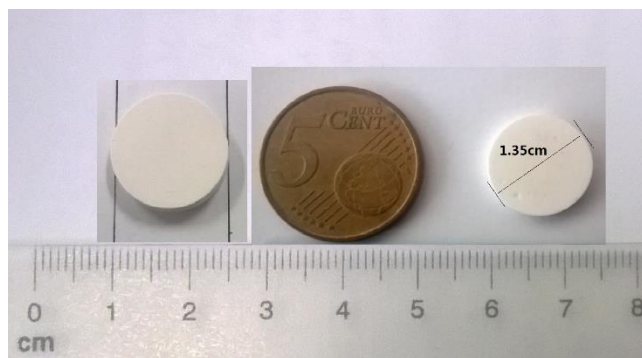


Figure V. 12. The size change of the sample before and after sintering at 1500°C

Figure V. 13 shows the XRD patterns of all the samples after sintering at 1500°C for 2h. They all keep the diffraction peaks matching the apatite structure and the intensity diffraction of the samples tend to become identical irrespective of their composition. While it has been seen that the positions of the diffraction peaks after the pre-calcination step are slightly affected by the Sr doping, this effect becomes more marked after sintering.

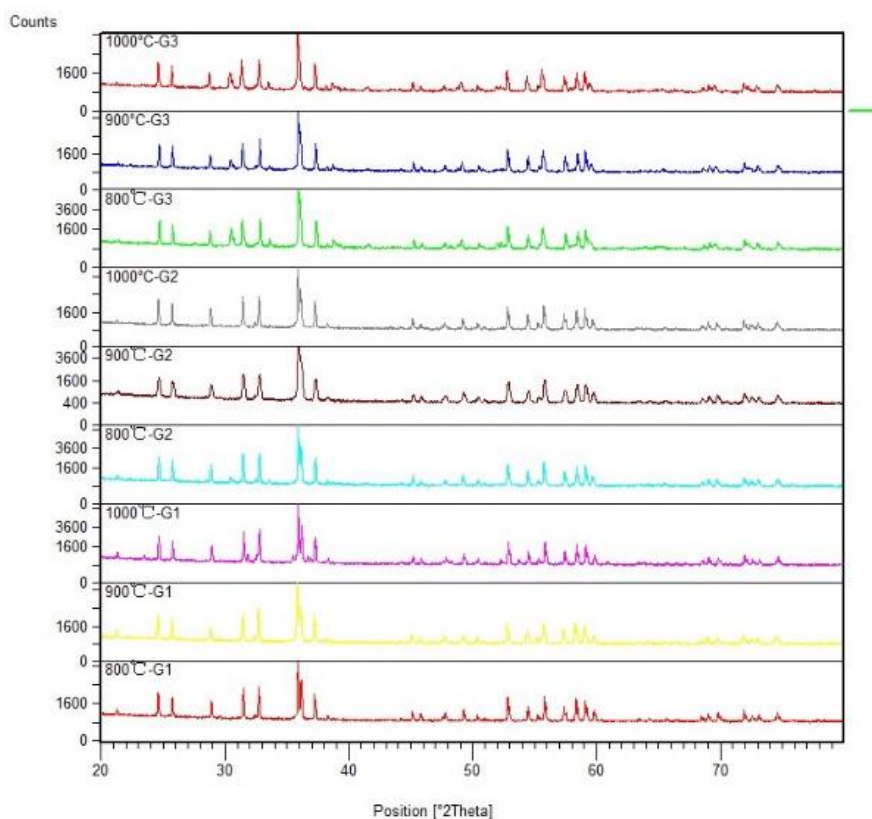


Figure V. 13. XRD patterns of the sintered samples (groups 1 to 3 having different calcination temperatures and Sr doping)

As an example, in Figure V. 14 where the pre-calcination was performed at 1000°C, it can be seen that the main peak (2 1 1) shifts towards lower angles as the doping ratio increases. It implies that the corresponding dimension of the crystal cell still increases with the sintering treatment. The peaks become sharper and stronger as compared to the ones before the treatment, and the average FWHM changes from 0.1181 ° - 0.2362 ° to 0.048 ° - 0.098 °. Figure V. 14 (b) allows particularly to compare the 30-40 ° portions of the XRD diagram before and after sintering treatment. It is obvious that the diffraction peaks become higher and there are more details (close peaks can be separated) in each peak. The samples have been well crystallized and the crystal grains increase with the high temperature treatment. This result also evidences the favorable effect of sintering on the degree of crystallization of the apatites.

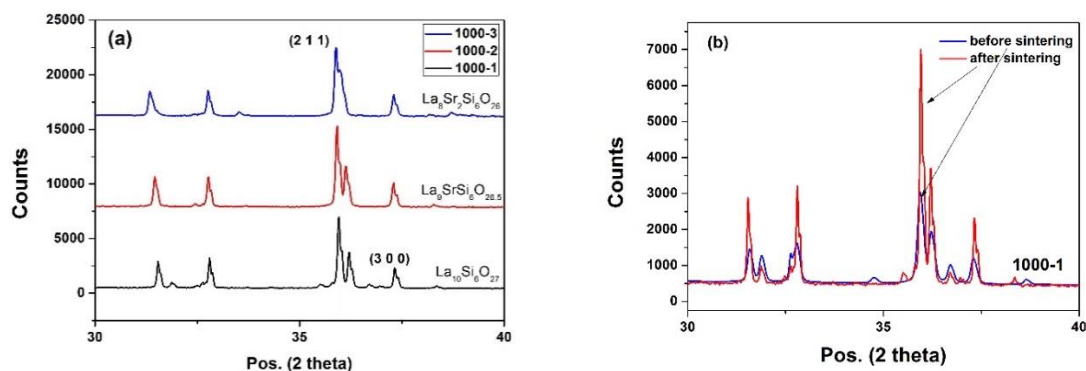


Figure V. 14. Local XRD patterns of the group 1 to 3 having different Sr doping proportion (a); influence of sintering temperature (b)

Figure V. 15 shows the SEM microstructure of some synthesized apatites after sintering. The crystal grains significantly increase up from the nanometer scale (before sintering) to 2-3 μm and they get closely connected to each other. The sintering treatment obviously densifies the apatite materials which is beneficial in the prospect of SOFC electrolytes applications. The grains have the appearance of hexagons and one sees some of the boundary angles equaling 120°, which is congruent with the crystal structure previously discusses. Specifically, a typical

crystal grain exhibiting a regular hexagon shape is visible in the image of the 800-3 sample. As far as the calcination temperature is concerned, it seems that it does not affect significantly the grain size. Globally we can note that the sintered apatite materials, as characterized in this section, will be suitable candidates as electrolytes in SOFC.

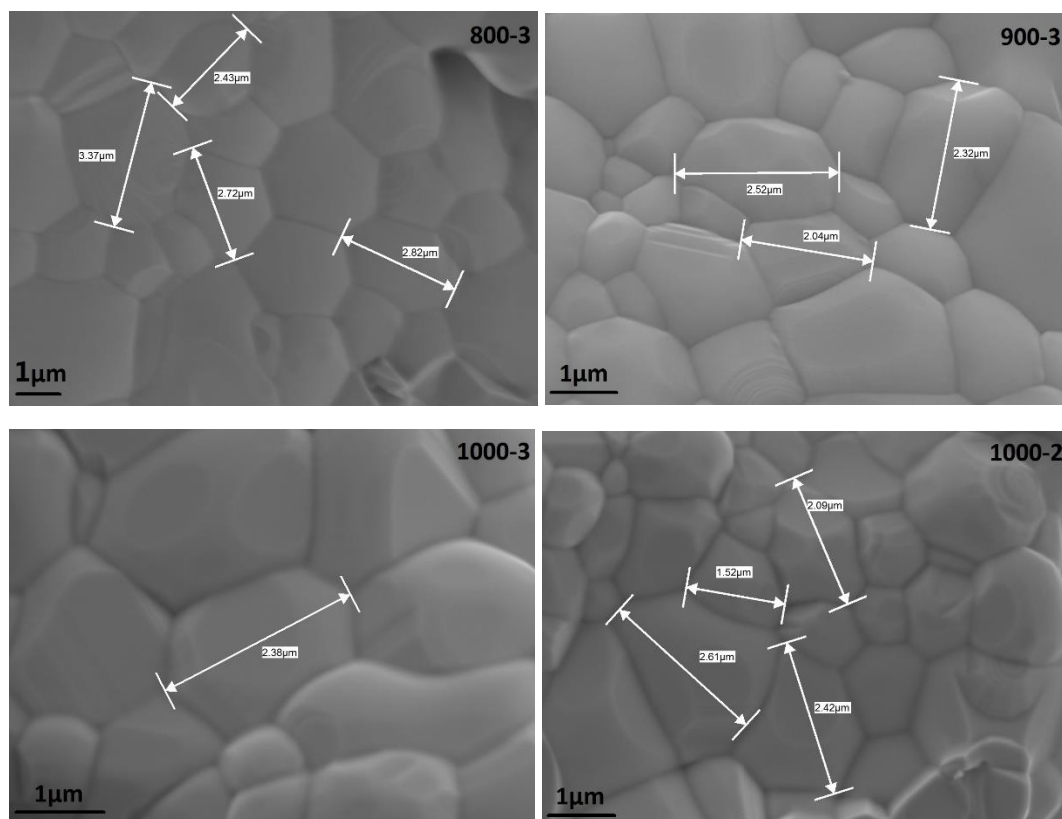


Figure V. 15. SEM micrographs of samples sintered at 1500°C for 2h

The EDS analyses of various samples are shown in Figure V. 16. To check the composition uniformity of the samples we analyzed two zones of each of them. As an example, the samples selected in Figure V. 16 had undergone a calcination at 1000°C. It can be seen that (i) the peaks match well with the expected elements and (ii) the spectra of the two zones coincide well, particularly in the high energy area, which means the samples are uniform and the elements are homogeneously distributed in the material.

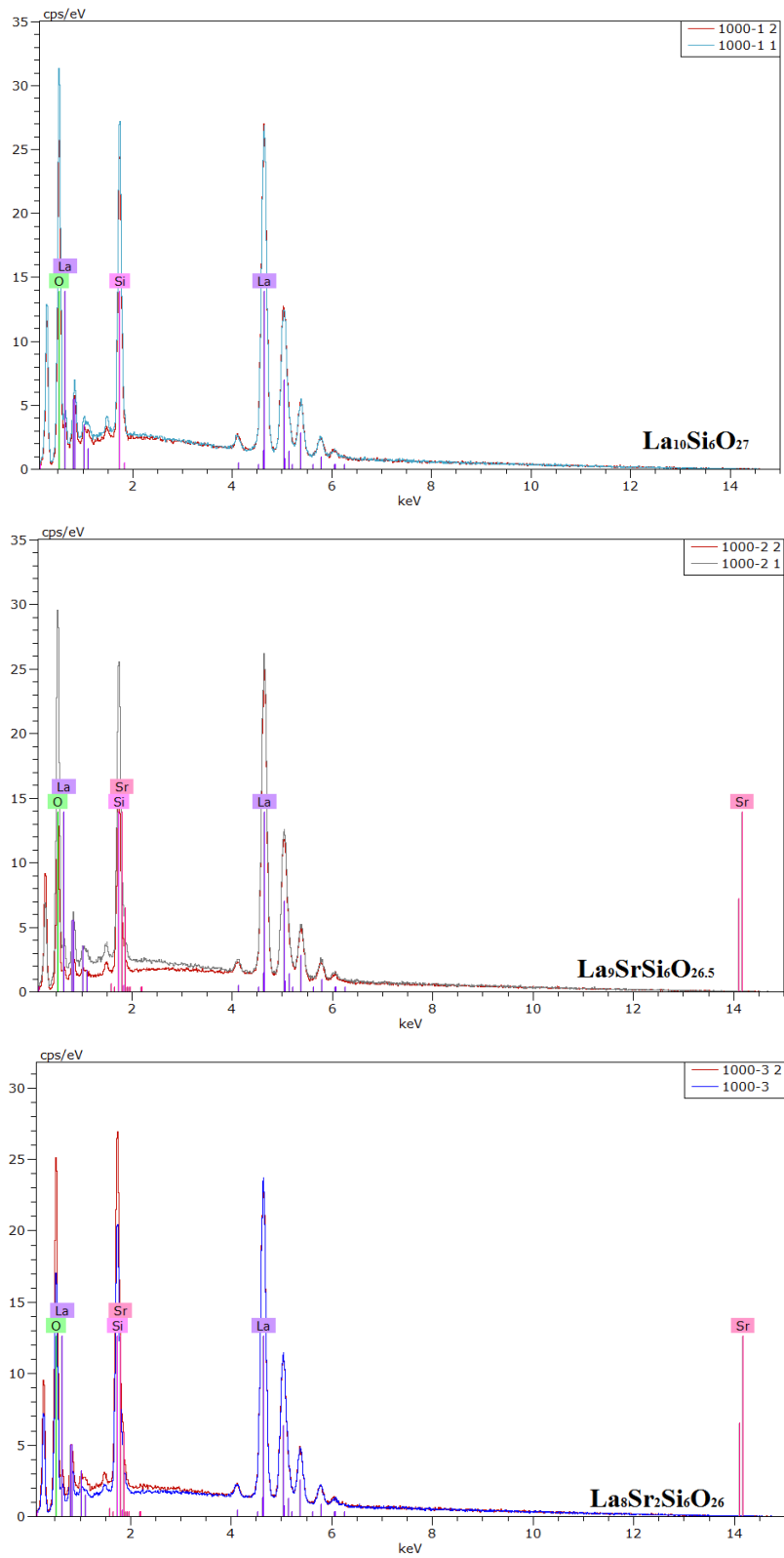


Figure V. 16. EDS spectra of sintered samples with different Sr doping ratios

The abundances of each elements are summarized in Table V.2. Since the EDS signals of the light elements are not very accurate, the formula computed from the EDS diagram is of course semi-quantitative. The value of La(Sr):Si ratio is close to 10:6, which is the theoretical value, and with the increase of the Sr doping ratio, the EDS spectra show a correlative increase of the Sr/La ratio. Consequently, based on the XRD results set out previously which demonstrated the formation of the apatite structure and the absence of any other Sr containing phase, we can now conclude that Sr has been well incorporated in the apatite network.

Table V. 2. Composition estimates based on the results of EDS

Group 1	Series	unn. C [wt.%]	norm. C [wt.%]	Atom. C [at.%]	Approximated formula
Oxygen (O)	K-series	18.13	18.88	57.85	La ₁₀ Si _{6.71} O _{22.9}
Silicon (Si)	K-series	9.32	9.70	16.94	
Lanthanum (La)	L-series	68.59	71.42	25.21	
	Total	96.04	100.00	100.00	
Group 2	Series	unn. C [wt.%]	norm. C [wt.%]	Atom. C [at.%]	Approximated formula
Oxygen (O)	K-series	20.74	21.42	61.18	La ₉ Sr _{0.45} Si _{6.14} O _{25.1}
Silicon (Si)	K-series	9.37	9.68	15.75	
Strontium (Sr)	L-series	2.02	2.08	1.09	
Lanthanum (La)	L-series	64.71	66.82	21.98	
	Total	96.84	100.00	100.00	
Group 3	Series	unn. C [wt.%]	norm. C [wt.%]	Atom. C [at.%]	Approximated formula
Oxygen (O)	K-series	15.47	15.61	51.01	La ₈ Sr _{0.65} Si _{6.29} O _{15.5}
Silicon (Si)	K-series	10.97	11.07	20.60	
Strontium (Sr)	L-series	3.55	3.58	2.13	
Lanthanum (La)	L-series	69.12	69.74	26.25	
	Total	99.10	100.00	100.00	

V.2.3 Conductivity study

Figure V. 17 shows the results of the measurement of the electrical conductivity for each group. All the groups exhibit considerable ionic conductivities at intermediate temperature which make them fair candidates as electrolytes in IT-SOFC. The progressive change in conductivity with the temperature means that the synthesized apatites are suitable to work in a wide

temperature range. From this figure, it can be found that Sr dopes affect the ionic conductivity more than the calcination temperature: while a Sr/La doping ratio of 1/9 (Group 2) is beneficial, the incorporation of more Sr (Sr/La = 2/8; Group 3) tends to decrease the conductivity. This non-trivial result is consistent with the findings of: (i) Zhang[6] who reported an improvement of the ionic conductivity from 4.3×10^{-3} to $1.68 \times 10^{-2} \text{ S}\cdot\text{cm}^{-1}$ at 500°C when passing from the $\text{La}_{10}\text{Si}_6\text{O}_{27}$ to the $\text{La}_9\text{SrSi}_6\text{O}_{26.5}$ apatite and (ii) A. Orera et al [7] who showed that the ionic conductivity decreases from 1×10^{-2} to $2.6 \times 10^{-7} \text{ S}\cdot\text{cm}^{-1}$ at 800°C when passing from the $\text{La}_9\text{SrSi}_6\text{O}_{26.5}$ to the $\text{La}_8\text{Sr}_2\text{Si}_6\text{O}_{26}$ apatite. As for the calcination step, a high calcination temperature helps to improve the ionic conductivity, nevertheless this influence is not so marked.

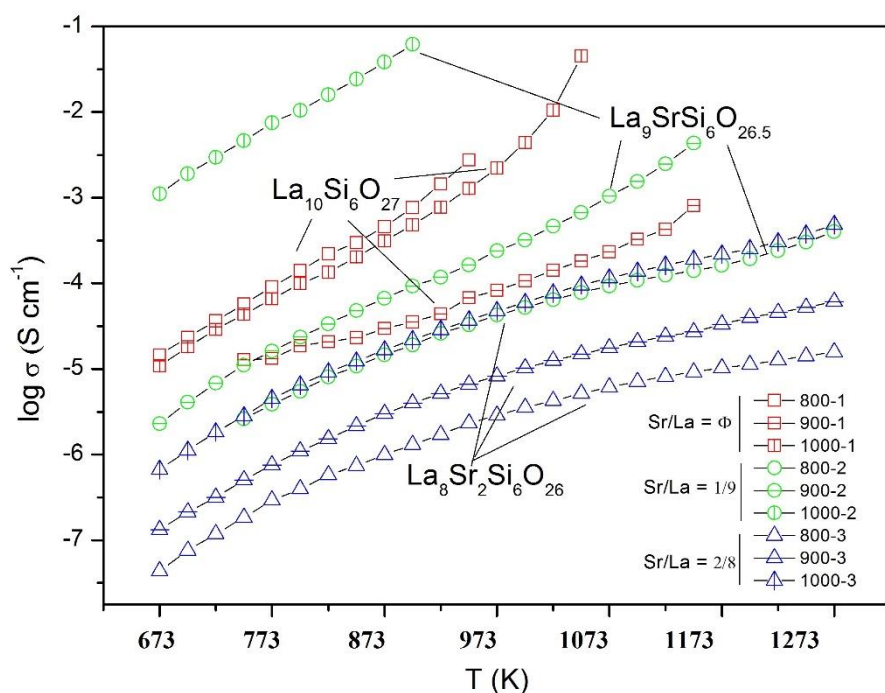


Figure V. 17. Ionic conductivities of the groups obtained with different Sr dopings and pre-calcination temperatures

Figure V. 18 summarizes the influence of the Sr doping and calcination temperature on the conductivity. The Groups 2, having one Sr atom incorporated into the apatite lattice exhibits the highest conductivity and its superiority gets enhanced with a higher calcination temperature.

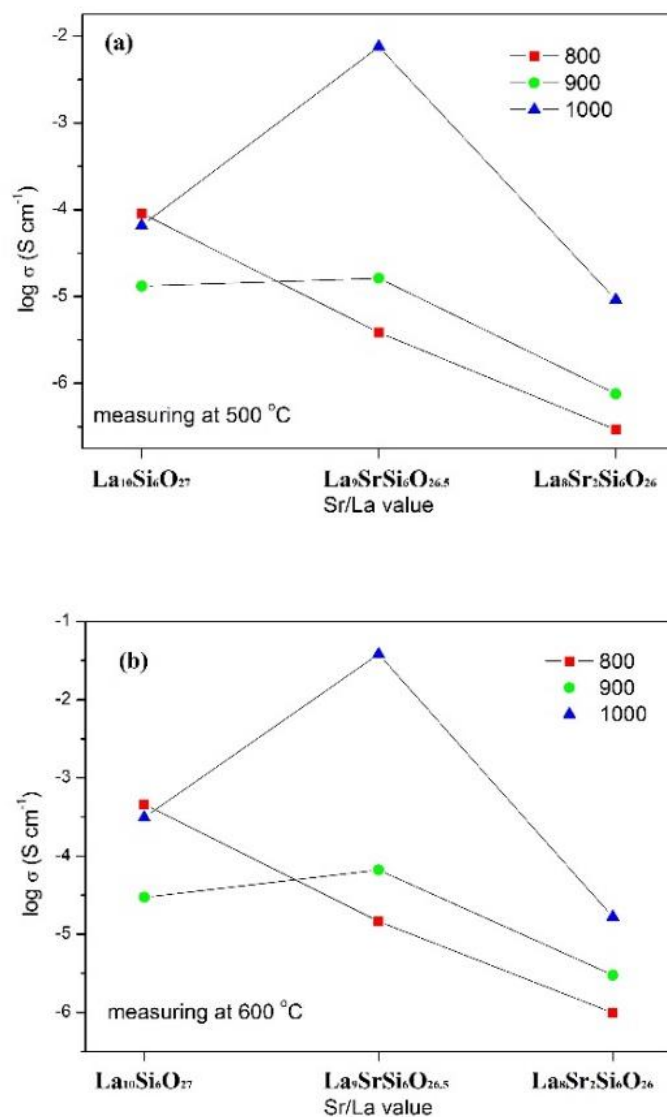


Figure V. 18. Ionic conductivities for different Sr ratios, measured at 500°C (a) and 600°C (b)

The respective influences of the Sr doping and calcination temperature are compared in Figure V. 19 in the form of Arrhenius plots.

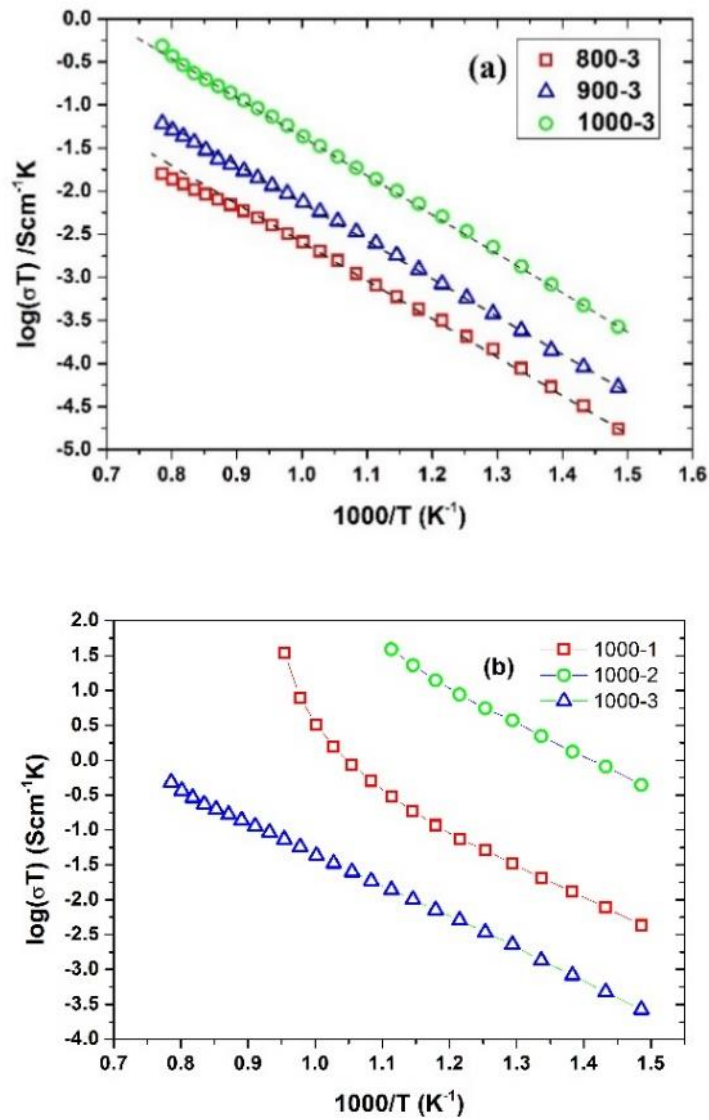


Figure V. 19. Arrhenius plots of samples calcined at three temperatures ($\text{La}_9\text{Sr}_2\text{Si}_6\text{O}_{27}$ as an example) (a) with different Sr doping ratios (1000-1: $\text{La}_{10}\text{Si}_6\text{O}_{27}$, 1000-2: $\text{La}_9\text{SrSi}_6\text{O}_{27}$ and 1000-3: $\text{La}_9\text{Sr}_2\text{Si}_6\text{O}_{27}$) (b)

High calcination temperature and the “medium Sr doping” are both beneficial. The conductivity σ of these apatite electrolytes can be written

$$\sigma = \frac{\sigma_0}{T} \exp\left(-\frac{E_a}{kT}\right) \quad \text{EQN V.1}$$

where σ_0 , E_a , k and T are the pre-exponential factor, activation energy, Boltzmann constant ($8.62 \times 10^{-5} \text{ eV} \cdot \text{K}^{-1}$) and absolute temperature. After a simple arrangement, this equation can be written as:

$$\log(\sigma T) = -\frac{E_a}{k} \cdot \frac{1}{T} + \log(\sigma_0) \quad \text{EQN V.2}$$

Table V.3 gives the calculated values of the activation energies as well as the densities that are closed to the theoretical values. This table shows in quantitative terms the positive effect of the calcination temperature on the activation energy and the densification of the samples. The activation energy for the oxygen ionic conduction of the synthesized apatites is in the range of 1.38 to 2.13 eV. The doping with Sr has therefore a medium effect on the energy barrier for the migration of interstitial oxygen between two SiO_4 tetrahedrons.

Table V. 3. Density and conductivity properties of the LSOs obtained after sintering

Samples	Calcination Temp.-time	Sintering Temp.-time	Density ($\text{g} \cdot \text{cm}^{-3}$)	Conductivity ($\text{mS} \cdot \text{cm}^{-1}$)			E_a (eV)
				400	600	800	
$\text{La}_{10}\text{Si}_6\text{O}_{27}$ (Gtoup1)	800°C-2h	1500°C-2h	3.44	0.0146	0.459	N/A	1.84
	900°C-2h		3.51	0.0128	0.030	0.233	1.49
	1000°C-2h		4.20	0.0108	0.312	45.0	1.38
$\text{La}_9\text{Sr}_1\text{Si}_6\text{O}_{26.5}$ (Gtoup2)	800°C-2h		3.53	0.0026	0.0146	0.095	1.41
	900°C-2h		3.57	0.0230	0.068	1.04	1.46
	1000°C-2h		4.44	1.11	38.3	N/A	1.49
$\text{La}_8\text{Sr}_2\text{Si}_6\text{O}_{26}$ (Gtoup3)	800°C-2h		4.62	4.35E-5	9.93E-4	6.13E-3	2.13
	900°C-2h		4.79	1.323E-4	3.01E-3	1.77E-2	1.81
	1000°C-2h		4.89	6.67E-4	1.67E-2	0.115	1.43

The best conductivity at intermediate temperature is obtained for the $\text{La}_9\text{SrSi}_6\text{O}_{26.5}$ apatite formula with the calcination temperature of 1000°C, the corresponding conductivity (38.3 $\text{mS} \cdot \text{cm}^{-1}$ at 600°C) being significantly higher than the general conductivity levels reported in previous works using traditional synthesis methods [6, 8]. This “medium Sr doped” LSO is therefore suitable for low temperature SOFC applications. Note worthily the undoped $\text{La}_{10}\text{Si}_6\text{O}_{27}$ apatite have also a very high conductivity (45 $\text{mS} \cdot \text{cm}^{-1}$) at 800°C which confirms

the favorable effect of this sol gel synthesis method. The Sr doping ratios in LSO need to be investigated more deeply in the 0 and 2/8 range to accurately determine the best performance Sr/La ratio.

V.3 Summary

Lanthanum silicate oxides with and without Sr-doping have been synthesized using a facile, water-based sol-gel method for potential applications as oxygen ion conducting electrolytes in IT-SOFCs. The effects of various parameters, namely the pH value, the doping ratio, the calcination temperature and time have been investigated. We found that the most effective process to synthesize pure apatite consists in (i) a near-neutral medium for the gelation step and (ii) a heat treatment at 800°C for 2h for the calcination step. The Sr-doping proved helpful to complete the gelation and crystallization steps. The synthesized apatite samples have been characterized by XRD and its degree of crystallization has been studied in function of the calcinations temperature in the perspective of a real SOFC application.

A subsequent sintering heat treatment has been used to densify the samples, resulting in a highly crystallized variety of apatite that well fits the requirements of an SOFC application. The XRD, SEM and EDS results confirm that the compounds obtained are pure, well crystallized apatites and that Sr is well incorporated in the structure. Both the effects of the calcination temperature and Sr doping ratios have been investigated. The proposed synthesis method enables alleviating calcination and sintering conditions and provides fairly good SOFC electrolyte candidates even after calcination at 800°C and sintering at 1500°C for 2h. While a higher calcination temperature slightly improves the conduction performances, a medium Sr doping (Sr/La = 1/9) procures a substantial improvement. Indeed a remarkable, intermediate temperature conductivity of 38.3 mS•cm⁻¹ is obtained at 600°C with the La₉SrSi₆O_{26.5} formula, that represents therefore a suitable

candidate for low temperature SOFC applications. Meanwhile, the non-doped $\text{La}_{10}\text{Si}_6\text{O}_{27}$ exhibited an ionic conductivity of $45 \text{ mS}\cdot\text{cm}^{-1}$ at 800°C , which confirms the suitability of the optimized sol gel process for the synthesizing of LSO with and without Sr doping. Further work should be carried out to accurately identify the doping ratio that yields the best conduction performance.

V.4 References

- [1] Argirusis C, Jothinathan E, Sourkouni G, Van der Biest O, Jomard F. Oxygen self-diffusion and conductivity measurements in apatite type electrolyte materials for SOFCs. *Solid State Ionics*. 2014;257:53-9.
- [2] McFarlane J, Barth S, Swaffer M, Sansom J, Slater P. Synthesis and conductivities of the apatite-type systems, $\text{La}_{9-33+x}\text{Si}_{6-y}\text{M}_y\text{O}_{26+z}$ (M= Co, Fe, Mn) and $\text{La}_8\text{Mn}_2\text{Si}_6\text{O}_{26}$. *Ionics*. 2002;8:149-54.
- [3] Gasparyan H, Neophytides S, Niakolas D, Stathopoulos V, Kharlamova T, Sadykov V, et al. Synthesis and characterization of doped apatite-type lanthanum silicates for SOFC applications. *Solid State Ionics*. 2011;192:158-62.
- [4] Zhou J, Ye X, Li J, Wang S, Wen T. Synthesis and characterization of apatite-type $\text{La}_{9.67}\text{Si}_{6-x}\text{Al}_x\text{O}_{26.5-x/2}$ electrolyte materials and compatible cathode materials. *Solid State Ionics*. 2011;201:81-6.
- [5] Shi Q, Lu L, Jin H, Zhang H, Zeng Y. Electrical properties and thermal expansion of cobalt doped apatite-type lanthanum silicates based electrolytes for IT-SOFC. *Materials Research Bulletin*. 2012;47:719-23.
- [6] Zhang L, He HQ, Wu H, Li C-Z, Jiang SP. Synthesis and characterization of doped $\text{La}_9\text{ASi}_6\text{O}_{26.5}$ (A= Ca, Sr, Ba) oxyapatite electrolyte by a water-based gel-casting route. *international journal of hydrogen energy*. 2011;36:6862-74.
- [7] Orera A, Kendrick E, Apperley DC, Orera VM, Slater PR. Effect of oxygen content on the Si-29 NMR, Raman spectra and oxide ion conductivity of the apatite series, $\text{La}_{8+x}\text{Sr}_{2-x}(\text{SiO}_4)_6\text{O}_{2+x/2}$. *Dalton T*. 2008:5296-301.
- [8] Bonhomme C, Beaudet-Savignat S, Chartier T, Geffroy P-M, Sauvet A-L. Evaluation of the $\text{La}_{0.75}\text{Sr}_{0.25}\text{Mn}_{0.8}\text{Co}_{0.2}\text{O}_{3-\delta}$ system as cathode material for ITSOFCs with $\text{La}_9\text{Sr}_1\text{Si}_6\text{O}_{26.5}$ apatite as electrolyte. *Journal of the European Ceramic Society*. 2009;29:1781-8.

Conclusion

In this thesis, apatite type lanthanum silicate ($\text{La}_{10}\text{Si}_6\text{O}_{27}$, LSO) as electrolyte material in IT-SOFC has been investigated by both simulation and experimental work. Partial elements (Sr/Ge) doping/ substitution to the material affects the electronic properties, which is examined by the simulation work. Meanwhile, Sr-doping LSO has been realized by sol-gel method in experimental work. The results demonstrate the potential of the material to be used as the electrolyte materials in IT-SOFC. The experimental study is also developed by some new synthesis methods and attempts, which further assist to simplify experimental process, reduce production cost. Important findings and conclusion by this research are summarized as the followings:

The influence of different doping positions on the apatite materials $\text{La}_{10-x}\text{Sr}_x(\text{Si,Ge})_6\text{O}_{27-0.5x}$ in SOFC were investigated using DFT calculation. Sr-doping at La site has been discussed and the calculation results are in good agreement with the experimental results. We firstly discussed the relationship between the microscopic electronic properties and macroscopic electric performances. The ionic conductivity has been correlated with the Fermi level. This conductivity decreased sharply as the Fermi level moves to lower energies with Sr substitution which is the main factor that affects ionic conductivity.

The activation energy is also simulated by the energy barriers along the migration channel. The effect of Sr doping on the activation energy is clear and the decrease is more obvious while the doping position is near to the migration channel. However, Ge doping affects deeply electrons distribution rather than both activation energy and DOS diagram.

Lanthanum silicate oxides with and without Sr-doping have been synthesized using a facile, water-based sol-gel method for potential applications as oxygen ion conducting electrolytes in

IT-SOFCs. The effects of various parameters, namely the pH value, the doping ratio, the calcination temperature and time have been investigated. We found that the most effective process to synthesize pure apatite consists in (i) a near-neutral medium for the gelation step and (ii) a heat treatment at 800°C for 2h for the calcination step. The Sr-doping proved helpful to complete the gelation and crystallization steps. The synthesized apatite samples have been characterized by XRD and its degree of crystallization has been studied in function of the calcinations temperature.

A subsequent sintering heat treatment has been used to densify the samples, resulting in a highly crystallized variety of apatite that well fits the requirements of an SOFC application. The XRD, SEM and EDS results confirm that the compounds obtained are pure, well crystallized apatites and that Sr is well incorporated in the structure. The proposed synthesis method enables alleviating calcination and sintering conditions and provides fairly good SOFC electrolyte candidates even after calcination at 800°C and sintering at 1500°C for 2h. While a higher calcination temperature slightly improves the conduction performances, a medium Sr doping (Sr/La = 1/9) procures a substantial improvement. Indeed a remarkable, intermediate temperature conductivity of 38.3 mS•cm⁻¹ is obtained at 600°C with the La₉SrSi₆O_{26.5} formula, that represents therefore a suitable candidate for low temperature SOFC applications. Meanwhile, the non-doped La₁₀Si₆O₂₇ exhibited an ionic conductivity of 45 mS•cm⁻¹ at 800°C, which confirms the suitability of the optimized sol gel process for the synthesizing of LSO with and without Sr doping.

With the experimental results, Sr dopes affect the ionic conductivity more than the calcination temperature: while a Sr/La doping ratio of 1/9 (Group 2) is beneficial, the incorporation of more Sr (Sr/La = 2/8; Group 3) tends to decrease the conductivity. This non-trivial result is consistent with the findings of: (i) Zhang who reported an improvement of the ionic conductivity from 4.3×10^{-3} to 1.68×10^{-2} S•cm⁻¹ at 500°C when passing from the La₁₀Si₆O₂₇ to the La₉SrSi₆O_{26.5}

apatite and (ii) A. Orera et al who showed that the ionic conductivity decreases from 1×10^{-2} to $2.6 \times 10^{-7} \text{ S}\cdot\text{cm}^{-1}$ at 800°C when passing from the $\text{La}_9\text{SrSi}_6\text{O}_{26.5}$ to the $\text{La}_8\text{Sr}_2\text{Si}_6\text{O}_{26}$ apatite. As for the calcination step, a high calcination temperature helps to improve the ionic conductivity, nevertheless this influence is not so marked. Further work should be carried out to accurately identify the doping ratio that yields the best conduction performance.

In addition, alternatives synthesis routes have been investigated: molten salts, HDP and co-precipitation. While the molten salts route led to major difficulty resulting from the high reactivity of lanthanum with chloride and sulfate ions, the precipitation routes are proved more promising: the HDP (homogeneous deposition precipitation) method could be improved by using the extremely divided silica (e.g. colloidal SiO_2 obtained by fresh precipitation) and the co-precipitation could be revisited while exploring the effect of temperature and pH. These alternatives synthesis ways are worth further experimental work.

For the co-precipitation method, the apatite phase composition is obtained from quite moderate temperature of 700°C for 6h. After the densification process of 1500°C for 2h, the samples exhibit acceptable performance of ionic conductivity of $7.73 \text{ mS}\cdot\text{cm}^{-1}$ at 675°C . This novel method is worth to development due to it is facile to implement and low cost.

In the meantime, there are several issues that are particularly interesting to the current study, which can be further investigated:

For the simulation work, the further work can focus on the molecular dynamic calculation to confirm the oxygen ion migration pathway in the crystal structure. At the same time, it can precise the DFT activation energy calculation. In addition, more elements doping can be applied in this simulation work to predict the electric performance which is possible to reduce the experimental cost.

It is worthy to assemble the electrodes to a complete cell for the Sr-doping LSO samples obtained by sol-gel method. The considerable conductivity performance makes them to be alternatives of the current commercial electrolytes.

The co-precipitation method for Sr, Mn doping LSO should be developed with the introduction of dispersant, which may effectively reduce the agglomeration rate in the precipitation process. Thus, it is possible to acquire the pure phase, well doped LSO. This modification is possible to extend to the homogeneous deposition precipitation (HDP) method.

Annex I. List of publications and conferences

Publications:

- **Y. Ma**, N. Fenineche, O. Elkedim, Ab initio study of $\text{La}_{10-x}\text{Sr}_x(\text{Si},\text{Ge})_6\text{O}_{27-0.5x}$ apatite for SOFC electrolyte, Computational Materials Science, 2015, 109:25–33.
- **Y. Ma**, N. Fenineche, O. Elkedim, M. Moliere, P. Briois. Synthesis of Pure $\text{La}_{10-x}\text{Sr}_x\text{Si}_6\text{O}_{27-0.5x}$ Apatites Using an Optimized Sol-Gel Process. ECS Transactions, 2015, 68(1):509-522.
- **Y. Ma**, N. Fenineche, O. Elkedim, M. Moliere, H. Liao, P. Briois. “Synthesis of apatite type $\text{La}_{10-x}\text{Sr}_x\text{Si}_6\text{O}_{27-0.5x}$ powders for IT-SOFC using sol-gel process” International Journal of Hydrogen Energy, accepted.
- **Y. Ma**, M. Moliere, N. Fenineche, O. Elkedim. “Novel chemical reaction co-precipitation method for the synthesis of apatite-type lanthanum silicate as an electrolyte in SOFC” In process.

Conferences:

- Y. Ma, N. Fenineche, O. Elkedim, H. Liao. Ab-initio Study On $\text{La}_{10-x}\text{Sr}_x(\text{Si},\text{Ge})_6\text{O}_{26}$ Apatite Electrolyte for IT-SOFC. Ingédoc 2014, troisièmes Journées des jeunes chercheurs à l’UTBM, Sévenans, France.
- Y. Ma, N. Fenineche, O. Elkedim. “Ab-initio study of apatite type $\text{La}_{10-x}\text{Sr}_x\text{Si}_6\text{O}_{27-0.5x}$ and the oxygen ion adsorption ability for SOFC electrolyte (poster)” 2ème REUNION PLENIERES du GdR HySPàC, Oct. 14-16. 2015, Porticcio, France.
- Y. Ma, N. Fenineche, M. Moliere, O. Elkedim, P. Briois. “Preparation and optimization of pure phase apatite type $\text{La}_{10-x}\text{Sr}_x\text{Si}_6\text{O}_{27-0.5x}$ powders for electrolyte of IT-SOFC (oral)” 2ème REUNION PLENIERES du GdR HySPàC, Oct. 14-16. 2015, Porticcio, France.
- Y. Ma, N. Fenineche, O. Elkedim. “Electrons behavior of different doping positions in $\text{La}_{10-x}\text{Sr}_x(\text{Si},\text{Ge})_6\text{O}_{26}$ apatite electrolyte of SOFC with DFT calculations” IDHEA Conference (May 12-14, 2014) Nantes, France.
- Y. Ma, N. Fenineche, O. Elkedim, M. Moliere, P. Briois. "Synthesis of Pure $\text{La}_{10-x}\text{Sr}_x\text{Si}_6\text{O}_{27-0.5x}$ Apatites Using an Optimized Sol-Gel Process." ECS Conference on Electrochemical Energy Conversion & Storage with SOFC-XIV (July 26-31, 2015). Ecs, 2015.Glasgow, UK.
- Y. Ma, N. Fenineche, O. Elkedim. "Oxygen Ion Adsorption Studies on $\text{La}_{10}\text{Si}_6\text{O}_{27}$ (001) Surface with DFT Calculation for SOFC Electrolyte" ECS Conference on Electrochemical Energy Conversion & Storage with SOFC-XIV (July 26-31, 2015). Ecs, 2015.Glasgow, UK.
- Y. Ma, N. Fenineche, O. Elkedim, M. Moliere. “Synthesis of Apatite Type $\text{La}_{10-x}\text{Sr}_x\text{Si}_6\text{O}_{27-0.5x}$ Powders Based on Sol-Gel Process Optimization for IT-SOFC” CIMATEN2014, 3^{ème} Conférence Internationale sur les MATériaux et l’ÉNERgie (Dec. 14-16, 2014) Sousse, Tunisie.

- Y. Ma, N. Fenineche, O. Elkedim, M. Moliere, H. Liao. “Synthesis of apatite type $\text{La}_{10-x}\text{Sr}_x\text{Si}_6\text{O}_{27-0.5x}$ powders for IT-SOFC using sol-gel process” mESC-IS2015, international symposium on Materials for Energy Storage and Conversion. (Sept. 7-9, 2015) METU, Ankara, Turkey.
- Y. Ma, N. Fenineche, O. Elkedim, M. Moliere, P. Briois. “Sr-doping effect on apatite type $\text{La}_{10}\text{Si}_6\text{O}_{27}$ electrolyte: experiments and ab-initio calculation” ICREGA 2016, 4th International Conference on Renewable Energy: Generation and Applications (Feb. 8-10, 2016) Belfort, France (Best presentation awards in SS09)

Abstract:

The Solid Oxide Fuel Cell (SOFC) defined by its ceramic and oxide electrolyte, is an electrochemical energy conversion device that produces electricity directly from the chemical reaction of fuel. Nowadays, apatite type rare earths silicates and germaniums attract many interests as the solid electrolyte due to the superior transport properties with high ionic conductivity and low activation energy. They can operate stably at intermediate temperature over a wide oxygen partial pressure range and maintain excellent performances, being considered as a candidate for IT-SOFC electrolytes. Among this series of conductors, the La-Si-O type has a higher conductivity and the performance would be modified by different doping elements.

The objective of this thesis is to study the effects of element substitution/doping and synthesis methods on the structural and conductivity properties of apatite type lanthanum silicates. In this study, we use a double approach: a simulation approach and an experimental approach to optimize the electrolyte materials purity and performance.

Using simulation approach, a first principle calculation based on DFT (Density Functional Theory) was carried out to investigate the effect on doping positions: Sr dopant at La position and Ge dopant at Si position. The calculation results give a connection to the ionic conductivity obtained by experiments.

With experimental approach, we present the synthesis and characterization of Sr-doped $\text{La}_{10}\text{Si}_6\text{O}_{27}$ (LSO) prepared through an optimized water-based sol-gel process. The results show that the ionic conductivity is thermally activated and values lies between 4.5×10^{-2} and $1 \times 10^{-6} \text{ Scm}^{-1}$ at 873 K as a function of the composition and powder preparation conditions.

KEY WORDS: apatite type lanthanum silicates; sol-gel; co-precipitation; DFT calculation; SOFC; electrolyte

Résumé:

Les piles à combustibles à électrolyte solide de type SOFC permettent de transformer directement l'énergie de la réaction chimique de formation de l'eau à partir de l'hydrogène et de l'oxygène, en énergie électrique. De nos jours, les apatites de type silicates de terres rares présentent beaucoup d'intérêt comme électrolyte solide en raison de leurs propriétés de transport élevées avec une forte conductivité ionique et une faible énergie d'activation. Ils peuvent fonctionner de manière stable à une température intermédiaire sur une large plage de pression partielle d'oxygène en maintenant d'excellentes performances. Ils sont ainsi considérés comme de bons candidats pour les électrolytes de piles de type IT-SOFC. Parmi cette série de conducteurs, le type La-Si-O possède une conductivité plus élevée et leur performance serait modifiée par différents éléments dopants.

L'objectif de cette thèse est d'étudier les effets des éléments de substitution / dopage ainsi que les méthodes de synthèse sur les propriétés structurales ainsi que sur la conductivité des apatites de type silicates de lanthane. Dans cette étude, nous utilisons une double approche: une approche de simulation et une approche expérimentale pour optimiser la pureté et les performances des matériaux d'électrolyte.

Dans l'approche de simulation, le calcul basé sur la DFT (Théorie de la fonctionnelle de la densité) a été réalisé en vue d'étudier l'effet des positions de dopage: dopant Sr à la position de La et dopant Ge à la position de Si. Les résultats obtenus par le calcul concernant la conductivité ionique sont en bon accord avec ceux obtenus par l'expérience.

Avec l'approche expérimentale, nous présentons la synthèse et la caractérisation de $\text{La}_{10}\text{Si}_6\text{O}_{27}$ (LSO) dopé par Sr et élaboré par les procédés sol-gel optimisés. Les résultats montrent que la conductivité ionique est activée thermiquement avec des valeurs comprises entre $4,5 \times 10^{-2}$ et $1 \times 10^{-6} \text{ S cm}^{-1}$ à 873 K et dépend des conditions d'élaboration et de la composition de la poudre.

Mots Clés : apatite de type silicates de lanthane, procédés sol-gel, co-précipitation, DFT, pile SOFC, électrolyte.

SPIM

■ École doctorale SPIM - Université de Technologie Belfort-Montbéliard

F - 90010 Belfort Cedex ■ tél. +33 (0)3 84 58 31 39

■ ed-spim@univ-fcomte.fr ■ www.ed-spim.univ-fcomte.fr

